LASER ASSISTED MICRO MILLING OF HARD MATERIALS

A Thesis
Presented to
The Academic Faculty

by

Mukund Kumar

In Partial Fulfillment
of the Requirements for the Degree
Doctor of Philosophy in the
School of Mechanical Engineering

Georgia Institute of Technology
August 2011

LASER ASSISTED MICRO MILLING OF HARD MATERIALS

Approved by:

Dr. Shreyes Melkote, Advisor
School of Mechanical Engineering
Georgia Institute of Technology

Dr. Steven W. Johnson
School of Materials Science and Engineering
Georgia Institute of Technology

Dr. Steven Y. Liang
School of Mechanical Engineering
Georgia Institute of Technology

Dr. Roshan J. Vengazhiyil
Industrial and Systems Engineering
Georgia Institute of Technology

Dr. Rhett J. Mayor
School of Mechanical Engineering
Georgia Institute of Technology

Date Approved: June 27, 2011

To Amma, Appa and Friends

ACKNOWLEDGEMENTS

I would like to extend my thanks to the following people. Thanks to my advisor, Prof. Shreyes N. Melkote, for his mentorship and the support during the course of my study at Georgia Tech. I would also like to thank all my committee members, Prof. Steven Y. Liang, Prof. Rhett J. Mayor, Prof. Steven W. Johnson and Prof. Roshan J. Vengazhiyil for overlooking my thesis work. Special thanks to my professors in my undergraduate school who kindled my interest to do research in manufacturing. I would also extend my thanks to the support provided by National Science Foundation and Woodruff School for making this possible. Special thanks to Mr. Steven Sheffield for his support in building my experimental setup and Mr. John Graham for his help with the machine shop. Thanks to Pam Rountree for her support in administrative issues. And finally, thanks to my mom, dad and all my friends here and back home in India for their great support.

TABLE OF CONTENTS

LIST OF TABLES

LIST OF FIGURES

SUMMARY

Recent innovations in micro manufacturing processes have enabled the fabrication of micro and meso scale structures and devices utilizing a wide range of engineering materials. One approach that has been researched extensively in recent years is mechanical micromachining (e.g. micro milling), which has distinct advantages over photolithography-based micromachining methods. However, certain factors limit the types of workpiece materials that can be processed using mechanical micromachining methods. These limitations include low material removal rates, rapid tool wear/failure, and poor part feature accuracy, especially when cutting hard materials such as tool and die steels and ceramics. Because of these limitations, there is a need to develop new micro manufacturing processes that are capable of generating accurate three dimensional micro scale features in hard-to-machine materials in an economical and efficient manner. This thesis presents an investigation of novel laser assisted micromachining methods that address the limitations of micromachining of hard-to-machine materials. The main focus of this thesis is on the development and study of a Laser Assisted Micro Milling (LAMM) process for micro-cutting of hard metals. In addition, a laser assisted micro grinding process is investigated for high strength ceramics.

For hard metals such as A2 tool steel (62 HR_c), the basic approach involves localized thermal softening of the workpiece material by focusing a solid-state continuous wave near infra-red laser beam in front of the micro milling tool (end mills of 0.1 to 0.5 mm diameter). By suitably controlling the laser power, spot size and scan

speed, it is possible to produce a sufficiently large reduction in the flow strength of the work material and consequently the cutting forces and tool deflections. The results indicate that material removal rates can be increased substantially (up to six times) for the hard metal investigated. Tool wear is reduced with laser assist resulting in more accurate groove geometries. Burr heights are found to increase with laser assist due to thermal softening of the workpiece. A force model is developed to predict the cutting forces in LAMM of hard metals and is shown to yield predictions that are in good agreement (<15% peak-to-peak error) with measurements.

For high strength ceramics such as reaction-sintered silicon nitride, the approach involves use of a two step process. In the first step, thermal cracks are generated in a confined volume by the steep thermal gradients generated by laser irradiation of the workpiece. In the second step, the weakened region is removed by a micro grinding tool. Both analytical and finite element models are developed to predict the size of the thermally cracked region in the first step. The results indicate that reductions in the average grinding forces of up to 43% are obtained with laser assist.

In addition, LAMM experiments are carried out to evaluate the wear behavior of several types of coated micro milling tools including TiCN, TiAlN, Al_2O_3 and Al_2O_3 +ZrN. The results indicate that delamination is the principal wear mechanism for most of the coated tools under conditions investigated in this study. It is also found that TiAlN and Al_2O_3 + ZrN coated tools perform the best in terms of flank wear.

In summary, this thesis describes the investigation of new laser assisted micro milling and grinding processes capable of creating micro scale features in difficult-to-cut

materials such as hardened steels and high strength ceramics. The characterization and modeling of the processes serve as a basis for users to select optimal process parameters.

CHAPTER 1

INTRODUCTION

1.1 Micromachining

The growing demand for miniaturization of electromechanical devices and systems for applications in biomedical, aerospace and defense industries is a key driver for the development of new micro manufacturing processes. Currently, photolithography-based processes and molding techniques are used to manufacture high aspect ratio structures, but only in a limited range of materials like silicon, copper and Ni alloys, and polymers. Unlike photolithography-based processes, mechanical micromachining processes such as micro milling are capable of generating three-dimensional free-form surfaces in a wide range of metals, ceramics and polymers [1-6].

Mechanical micromachining is a micro cutting process. A schematic of the cutting process that involves the shearing of a soft work material using a hard tool, is shown in Fig. 1.1. Mechanical micromachining is gaining popularity for its ability to produce parts with three-dimensional features ranging in size from a few micrometers to a few millimeters across a wide range of materials [7]. Figures 1.2 and 1.3 show examples of components manufactured using mechanical micromachining processes. Examples of different micromachining processes include micro milling, micro EDM, and micro grooving, the most versatile being the micro milling process.

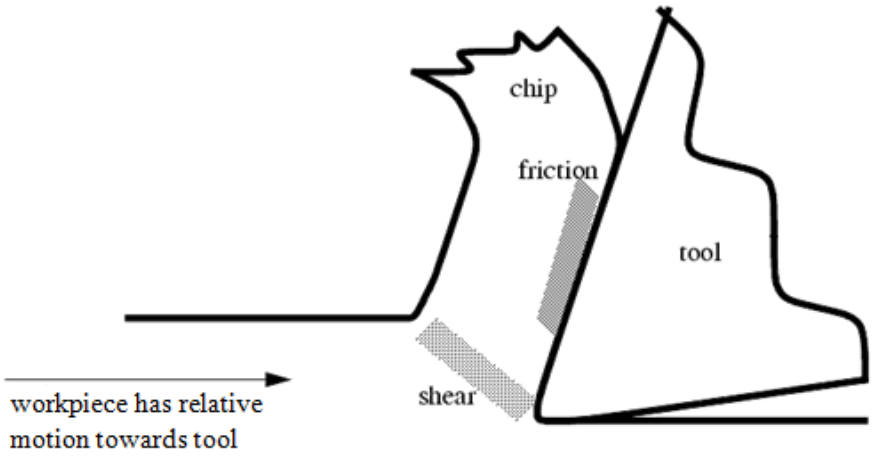

Figure 1.1: Orthogonal cutting process.

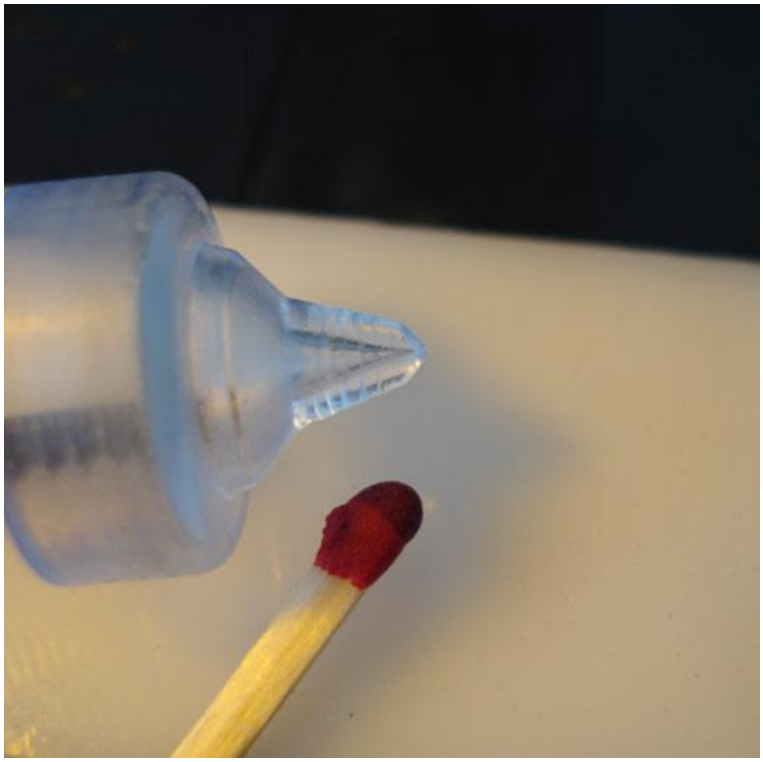

Figure 1.2: Micro milled orifice (0.07 mm diameter) in a nozzle for use in biomedical applications (Microlution, Inc.).

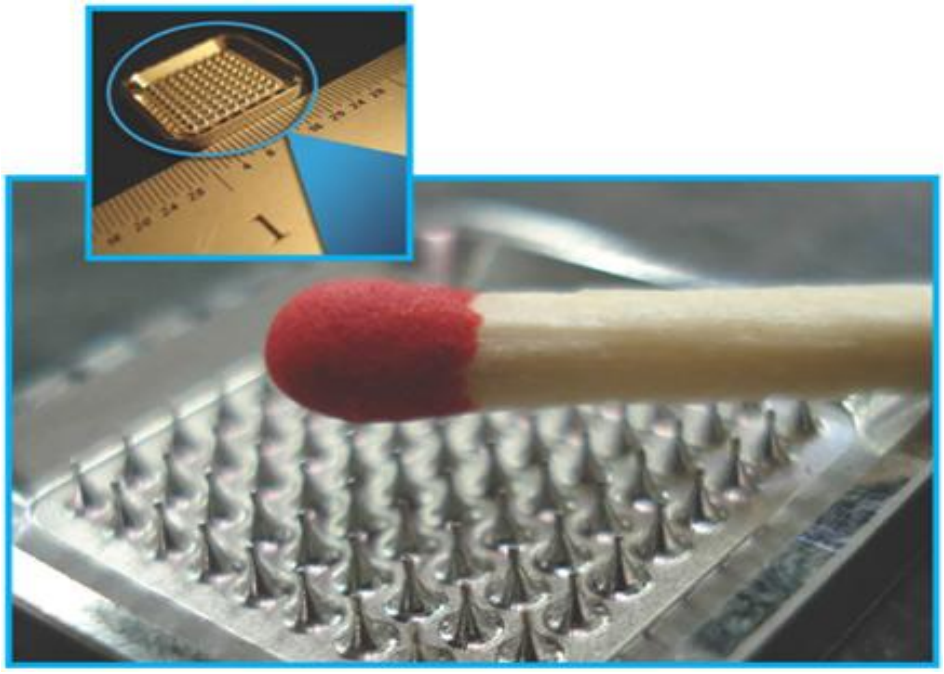

Figure 1.3: Micro milled contoured arrays (conical posts of height 1.5 mm, diameter at the top: 0.2 mm, diameter at the bottom: 0.5 mm) in 440C stainless steel (Microlution, Inc.).

1.2 Limitations of Micromachining

In spite of the advantages of micromachining, there are significant limitations of the process, particularly when machining materials such as hardened mold and die steels (60-65 HR_c), and sintered ceramics (1300-1500 HV). These limitations include low material removal rates, rapid tool wear/failure, and poor part feature accuracy especially when cutting hard materials [8-10]. These limitations, in turn, are due to the small size of the cutting tools, which have low stiffness and strength compared to conventional scale tools. A typical 40 μm micro end mill made of tungsten carbide is shown in Fig. 1.4. Specifically, the lower stiffness of these tools results in catastrophic failure of the micro tool because of the bending stresses generated by the cutting forces in the machining

process. In addition, tool wear becomes significant when machining hard materials. Because of the small size of these tools, a few microns of tool wear will cause a large deviation in the finished dimensions of the machined surface.

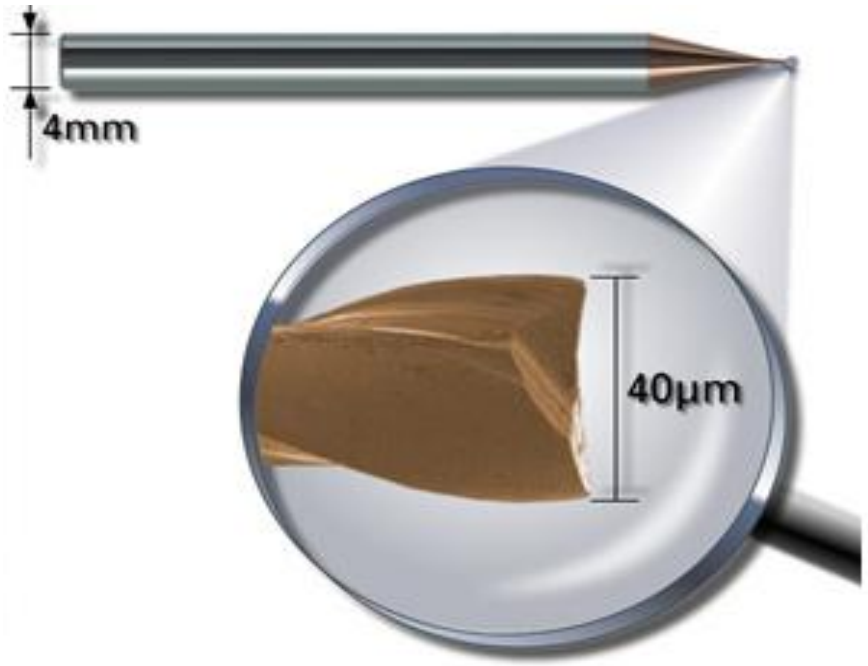

Figure 1.4: 40 µm tungsten carbide end mill (Hitachi Tool Engineering, Ltd.).

A few approaches have been proposed to overcome these limitations. The first approach involves the use of cutting fluids to provide cooling and lubrication. The idea is to minimize the friction at the tool-workpiece interfaces thereby reducing tool wear and cutting forces. However, it is very difficult to transport the cutting fluid to the cutting zone and tool-workpiece interfaces due to the high cutting speeds and the small size of the contact zone [11]. This limitation is also true to a great extent in macroscale machining. The second approach involves the application of coatings on the micro tool surfaces to reduce wear. This approach is routinely adopted at the macroscale to enhance

tool life. Although a few researchers have demonstrated that coatings prolong micro tool life to an extent [1], detailed tool wear studies on coated micro tools are limited.

The third approach to overcoming these limitations is to develop hybrid processes. One such hybrid process is Laser Assisted Machining (LAM). This process seeks to reduce the strength of the hard workpiece material through localized thermal softening with the aid of laser irradiation [12, 13]. By suitably controlling the laser power, spot size and scan speed, it is possible to substantially lower the flow strength of the work material, thereby lowering the cutting forces, preventing catastrophic tool failure, and/or minimizing tool deflections [12, 13]. The LAM process has been successfully applied at the macroscale for machining features in hard metals and ceramics. But, a systematic investigation of the LAM process at the microscale is lacking. Furthermore, laser assisted micromachining processes for ceramics have not been developed.

1.3 Research Approach

In light of the aforementioned limitations, this study aims to develop new laser assisted micromachining processes that addresses the limitations of micromachining of hard-to-machine materials. This research focuses on developing and studying laser assisted machining processes for two main classes of materials,

1. Hard metals (e.g. tool and die steels), and
2. Ceramics.

Two different approaches to laser assisted micromachining are adopted for these materials:

1. Thermal softening for hard metals

2. Thermal cracking for ceramics

For micromachining hard metals, the basic idea involves focusing a relatively low power continuous wave laser to induce highly localized thermal softening of the material immediately in front of the cutting tool. This process is schematically illustrated for the laser assisted micro milling process in Fig. 1.5. When the distance 'd' is less than a critical distance 'd_{crit}', the thermal effects of the laser beam are still felt by the material in contact with the micro tool. In the heated region, the micro tool is cutting through a softer material thereby generating lower cutting forces. To optimize the process, an understanding of the effects of laser parameters on the cutting process is essential. Hence, in this thesis, both experimental characterization and analytical force modeling of the Laser Assisted Micro Milling (LAMM) process are pursued. The model presented in the thesis can be used to establish optimal LAMM process parameters.

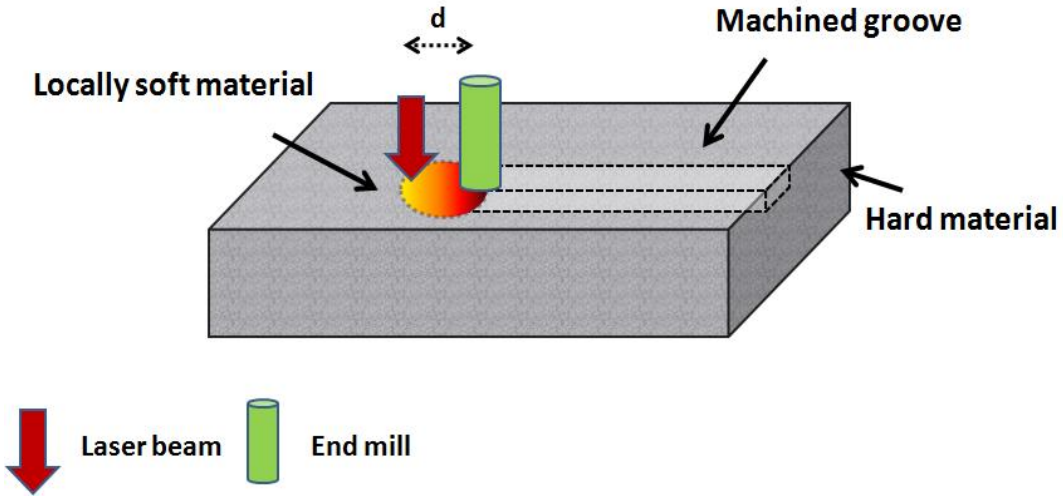

Figure 1.5: Schematic of the laser assisted micro milling process for hard metals ($d<d_{crit}$).

Another key limitation of the LAMM process today, especially when machining hard metals, is the lack of affordable cutting tool materials that can withstand the high temperatures generated in the process and at the same time yield economical tool life. One approach to reducing tool wear is to apply temperature resistant coatings to the cutting surfaces of the tool. However, tool coatings used in conventional macro and micro milling processes may not be suitable for LAMM, since the tool temperatures in LAMM can be significantly higher (300-400 ºC depending on the laser parameters) than in the micro milling process. Consequently, a study to evaluate tool wear behavior of both uncoated and coated tools in LAMM is needed in order to guide the development of suitable wear resistant tool coatings for the process.

Machining of hard ceramics like silicon nitride poses a significant challenge since these materials retain their strength up to 1000 ºC. Currently, the only reliable method, especially at the macroscale, is to use diamond wheel grinding, which tends to be a relatively slow and inefficient process. Although laser assisted machining of ceramics has been successfully demonstrated at the macroscale, its use at the microscale is limited by the lack of inexpensive micro tools that can withstand the stresses and high temperatures developed in the laser assisted process. Hence, this thesis investigates the development of a new laser-assisted process for micromachining of high strength ceramics like silicon nitride (flexural strength of 700 MPa up to 600 ºC). The proposed approach is to introduce thermal cracks in the ceramic by laser irradiation, thereby weakening the workpiece material. By suitably adjusting the laser power, spot size and scan speed, it is possible to create and confine the cracks to a specified volume of material. This material volume is then removed by a micro grinding tool as illustrated in Fig. 1.6. Note that

unlike Fig. 1.5, the distance '*d*' here is greater than the critical distance 'd_{crit}', indicating that laser scanning and micro grinding processes can be carried out independently.

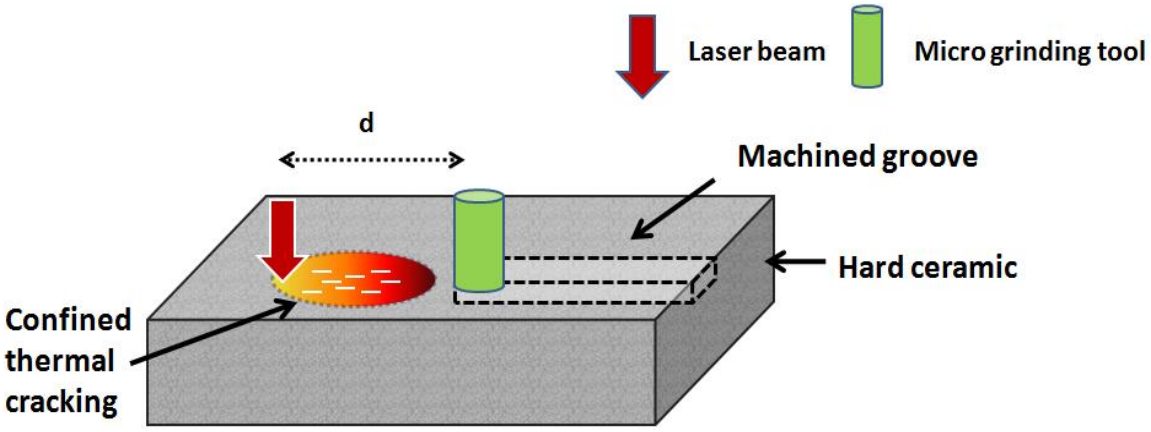

Figure 1.6: Approach for laser assisted micromachining of ceramics ($d>d_{crit}$)**.**

A fundamental understanding of the process variables and their effects on key process responses in each of the aforementioned approaches are crucial to develop and optimize the laser assisted micromachining process.

Consequently, the primary objectives of this thesis are:

1. To investigate the effects of laser assist on cutting forces, tool wear, surface quality, and material removal rates in micro milling of a hard metal through experimentation and modeling.
2. To experimentally investigate the wear mechanisms of uncoated and coated tools in LAMM of a hard metal.
3. To investigate the effects of laser assist on forces, tool wear, and surface quality in micro grinding of a high strength ceramic.

The stated research objectives are accomplished through several scientific investigations described in the subsequent chapters of the thesis.

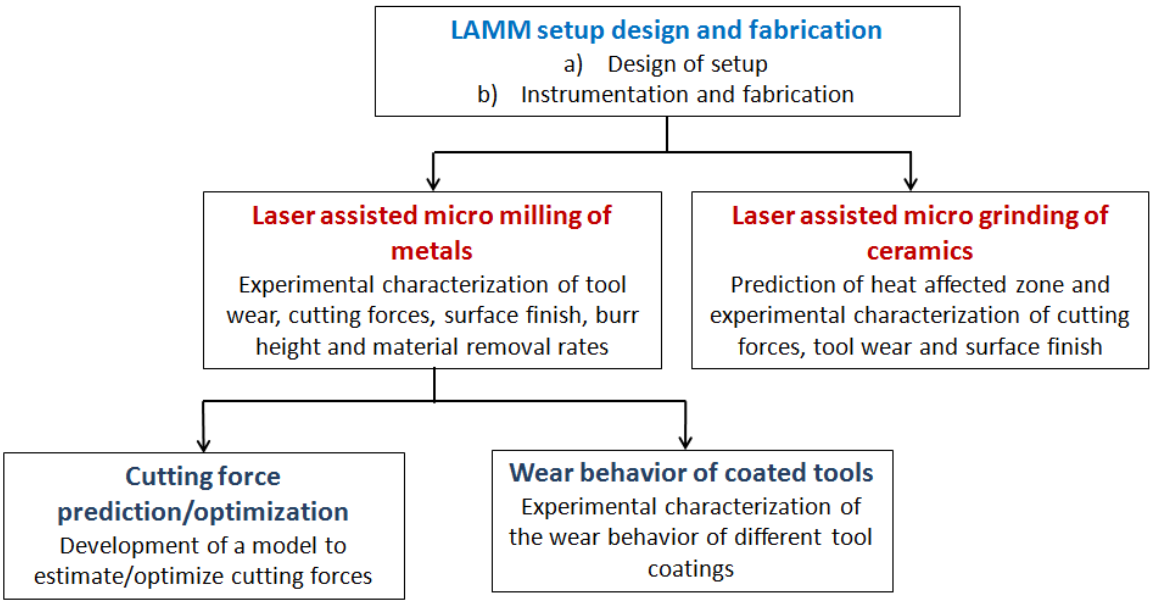

Figure 1.7: Overall research plan.

1.4 Dissertation Outline

Figure 1.7 shows the overall research plan with each block representing a specific research task. Chapter 3 focuses on the design and fabrication of the experimental setup. Chapter 4 describes an experimental study of LAMM of a hard metal designed to investigate the effects of laser assist on tool wear, surface finish, cutting forces and burr height. Chapter 5 presents the development of a mechanistic model to predict cutting forces in LAMM of a hard metal. Chapter 6 describes the approach used for laser assisted micro grinding of ceramics and presents the results of an experimental and modeling study of the approach applied to a sintered ceramic. Chapter 7 focuses on an experimental evaluation of the wear behavior of different commercially available and customized tool

coatings in LAMM. The main conclusions and original contributions of the thesis are summarized and suggestions for future work are presented in Chapter 8.

CHAPTER 2

LITERATURE REVIEW

Lasers are commonly used to create features at the macroscale. The various laser-based manufacturing processes are classified according to the power density of the laser as shown in Fig. 2.1. Lasers are increasingly being used to machine features at the microscale.

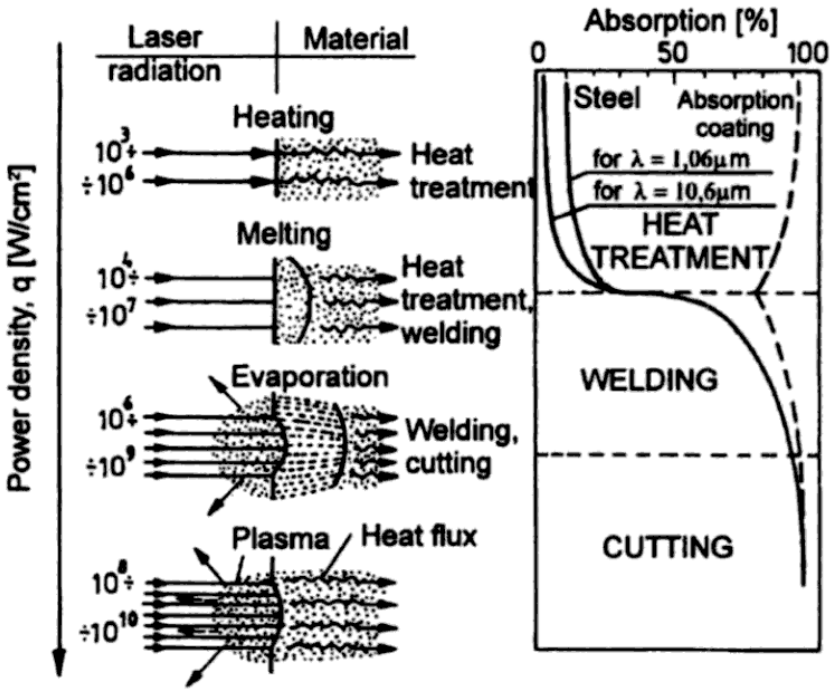

Figure 2.1: Different laser-based manufacturing processes as a function of power density [14].

High powered lasers with a small spot size are generally used for machining a variety of materials and features. Laser machines have been developed for performing drilling and cutting operations in a wide range of metals [15]. Simple three dimensional

features can be manufactured using laser configurations involving two beams as shown in Fig. 2.2.

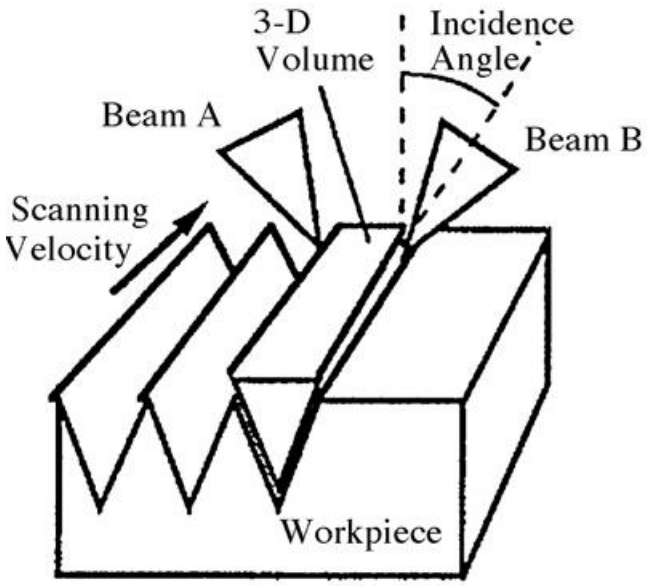

Figure 2.2: Laser milling of three dimensional features using two laser beams A and B oriented at an angle to each other [16].

Laser based machining processes have been analyzed and modeled extensively [17, 18]. In addition, laser assisted machining of metals and ceramics at the macroscale has been studied in detail [19-22]. However, limited work has been reported on laser assisted micromachining processes for hard metals and ceramics. Furthermore, laser assisted micromachining of metals has been analyzed by only a few researchers [12, 13, 23, 24]. This chapter reviews prior work in the relevant areas of laser machining at the microscale, mechanical micromachining, laser assisted macro/micro machining of metals and ceramics, and cutting tool coatings.

2.1 Laser Machining at the Microscale

Laser machining of microscale and macroscale features employs the ablation mechanism for material removal. Some of the key factors to be considered for the selection of lasers for machining include: wavelength, beam power, spot size, mode of operation, efficiency and maintenance requirements [15, 25]. The absorptivity characteristics of each material is a direct function of the wavelength of the laser beam which is well documented in literature for all the common types of lasers [15, 25]. The beam power and spot size control the intensity of the laser beam incident on the workpiece. Lasers can be operated either continuously (CW) or in pulses ranging in duration from milliseconds to a few femtoseconds [15, 25]. Lasers are mostly operated in continuous mode in hardening applications and in pulsed mode in machining applications. The most commonly used industrial lasers are excimer, CO_2, Nd:YAG and some of the commonly used applications of these lasers are drilling of nozzles for inkjet printers, micromachining of biomedical devices and MEMS [26]. Zhang et al. [27, 28] used Nd:YAG lasers for micromachining glass and ceramics and presented a detailed investigation of the laser induced plasma ablation process. Figure 2.3 shows a microfluidic device micro machined in a alumina substrate using a 190 nm UV laser while Fig. 2.4 shows a pattern of micro holes drilled in polyimide.

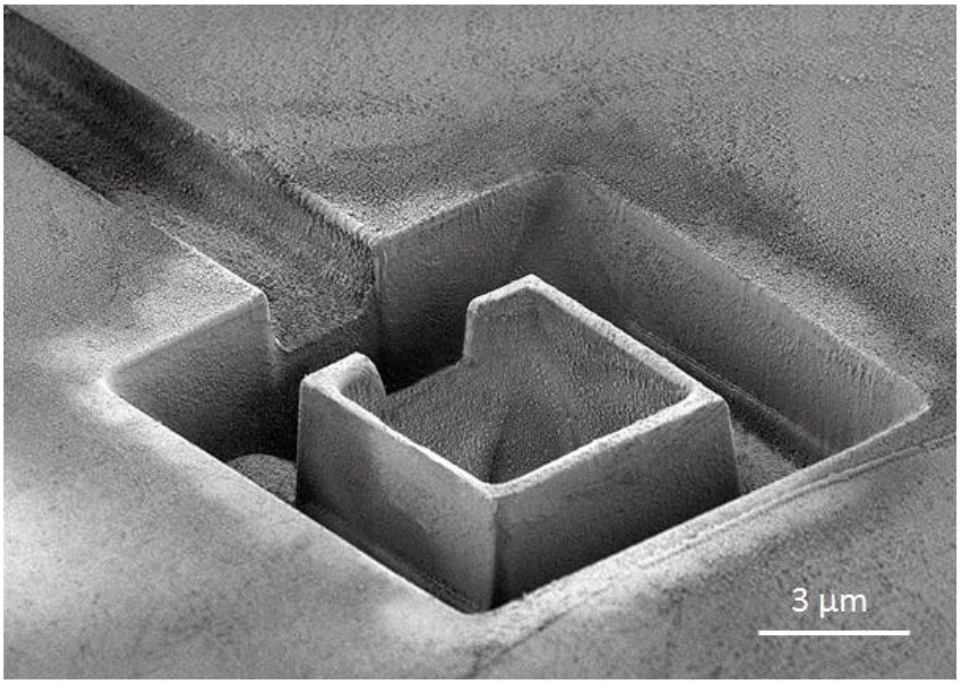

Figure 2.3: Microfluidic device micro machined in a alumina substrate using a UV laser (JPSA Laser Company).

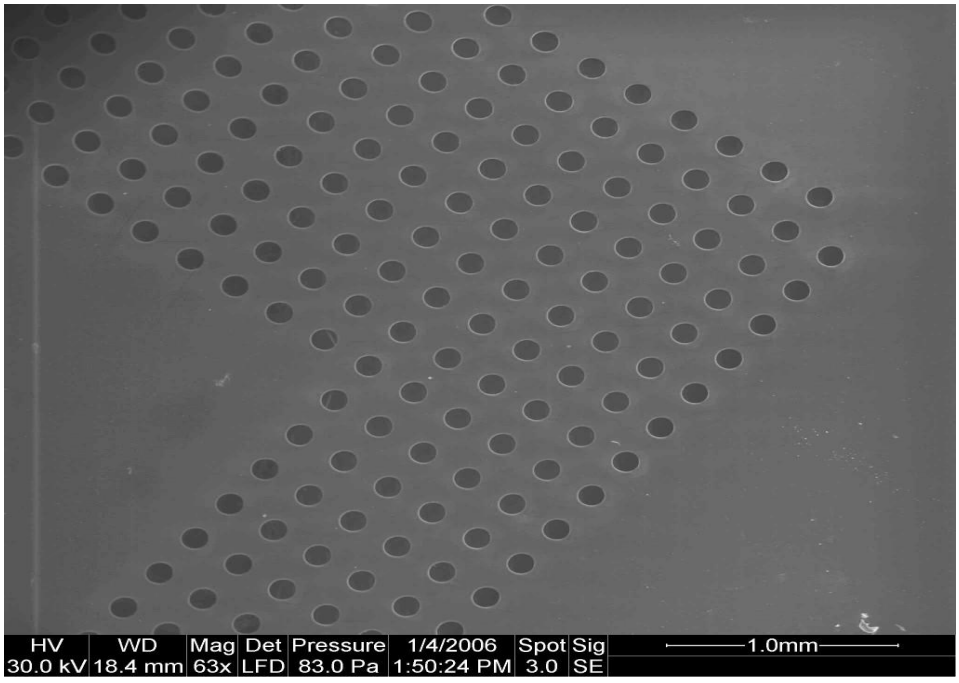

Figure 2.4: Micro holes laser machined in polyimide using a UV laser (Potomac Photonics).

In addition, laser micromachining of ceramics such as silicon nitride and alumina was studied by Hellrung et al. [29] and micro-patterns on silicon were created by Yang et al. [30]. Pfleging et al. [31] focused their studies on the use of laser micromachining for the manufacture of mold inserts in Poly Methyl Methacrylate (PMMA).

The use of ultra short pulsed lasers to create micro features has drawn the attention of researchers in recent years. Because of small spot sizes, and high peak powers, they enable the creation of micro features, which can find applications in microfluidics [32]. In addition, ultrafast lasers enable efficient ablation of materials since they induce minimum thermal damage in the surrounding work material [33].

In spite of all the advantages of laser micromachining, its material removal rate is a significant limiting factor when micromachining metals and ceramics. Processing of hard metals like WC-Co using femtosecond lasers have been reported. The reported material removal rates are on the order of 0.1 mm^3/min for deep drilling in hardened steel and 1 mm^3/min in PMMA [34]. In contrast, the material removal rates in mechanical micromachining processes such as micro milling are typically on the order of 25 to 50 mm^3/min [5]. Hence, pure laser based processes are slower and better suited for the manufacture of small features when the high cost of ultrafast high power lasers can be offset by the product cost. The ability to create features in a wide range of materials is a significant advantage of mechanical micromachining processes over pure laser based machining processes [2].

2.2 Mechanical Micromachining

Mechanical micromachining is used extensively in the manufacture of microscale products because of its advantages over pure laser based material processing as discussed in the earlier section. Research has been focused on both experimental and modeling aspects of micromachining process, specifically micro milling. Micro factories, micro and ultra-precision machine tools have been designed and developed for micromachining applications [35, 36] . Numerical and analytical modeling of different aspects of micro milling have been carried out extensively in the last decade [5, 37-46]. Some of the key research papers on modeling of micro milling include the work by Vogler et al. [39, 40] on modeling of cutting forces when micro milling a multiphase material and a review on the dynamics of the end milling process by Miao et al. [47]. The effect of edge radii on specific cutting energy has been modeled extensively using the finite element method, slip line field theories and molecular dynamic (MD) simulations [48, 49]. Figure 2.5 shows a schematic of the model used in the MD simulation of aluminum. Liu et al. [44] focused their efforts on modeling the elastic recovery effects in micro end milling.

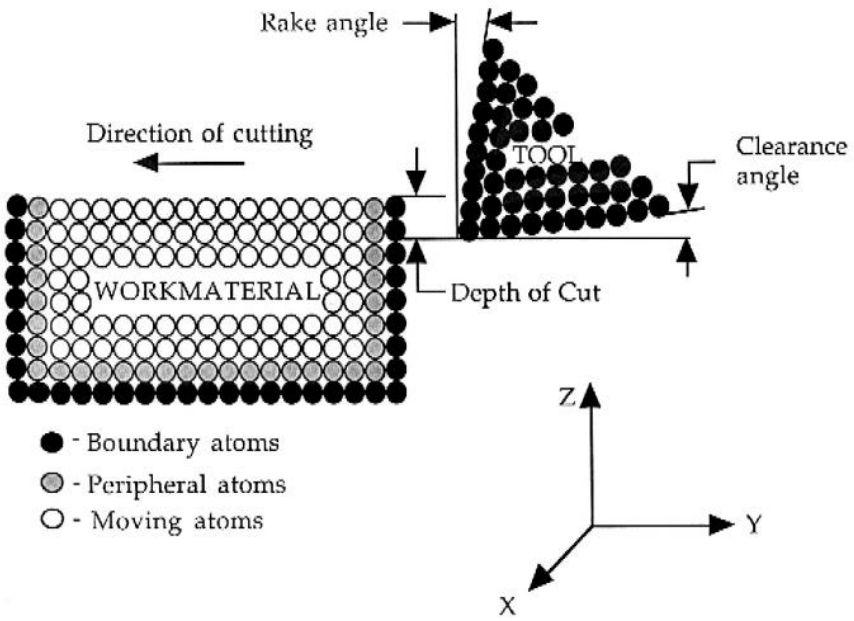

Figure 2.5: Schematic of the model used in the MD simulation of nanometric cutting of single crystal aluminum [48, 49].

The smallest commercially available micro end milling tool is ~5 μm in diameter which limits the feature size that can be produced by the micro milling process. A number of researchers have focused their experimental efforts in the last decade on fabricating features at the microscale. Friedrich et al. [50-52] made features as small as 22 μm in PMMA, which was used for the production of photolithography masks. Schaller et al. [53] investigated the machinability characteristics of non-ferrous materials like copper and aluminum. Rahman et al. [46] and Filiz et al. [54] focused their research on studying the material removal and tool wear mechanisms when micro milling copper. Figure 2.6 shows a turbine inlet structure micro machined in brass by Fleischer et al. [55]. Filiz et al. [56] used the micro milling process to manufacture microbarbs for use in implantable medical devices.

Most of the previous research is focused mostly on fabricating features in soft materials. Recently, researchers have started focusing their efforts on producing microscale features in hard materials (hardness ≥ 50 HR_c) since they find applications in the manufacture of micro molds and dies. Weule et al. [4] have demonstrated the capability of the micro milling process for fabricating micro injection molds.

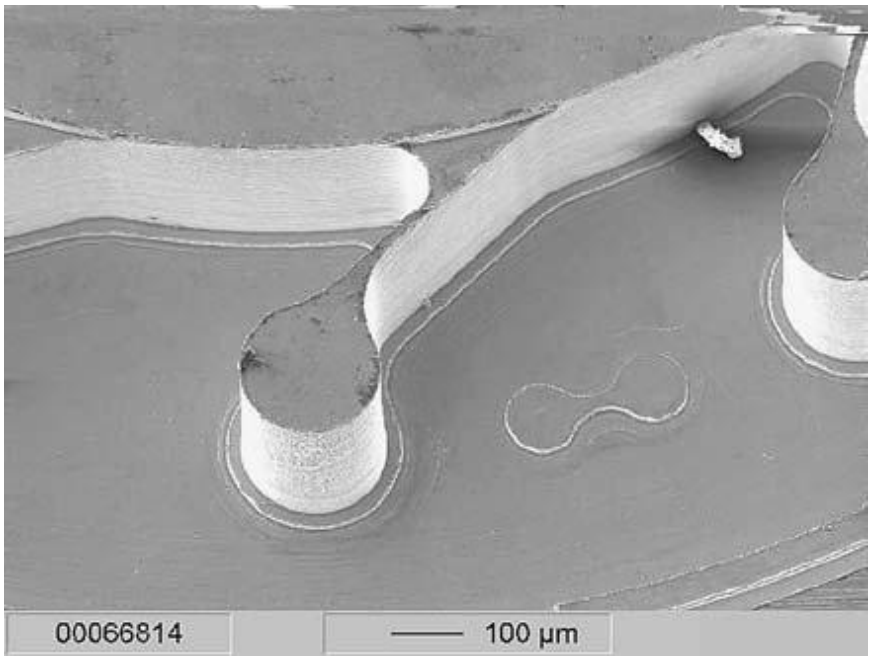

Figure 2.6: Turbine inlet structure in brass [55].

Since micro molds and dies need to withstand repeated thermal and mechanical cycles during the molding process, a material like hardened tool steel is a natural choice for the mold/die. However, the part feature accuracy and material removal rate in micro milling of such difficult-to-machine materials are limited by the machine-tool system stiffness (especially for small foot print machines), and the flexural stiffness, strength, and wear resistance of the micro tools normally used. Fig. 2.7 shows severe accumulation of plastically deformed material when machining 58 HR_c tool steel with a 200 µm end

mill. In addition, rapid tool wear is a problem since it negatively impacts part feature accuracy and finish [8, 9].

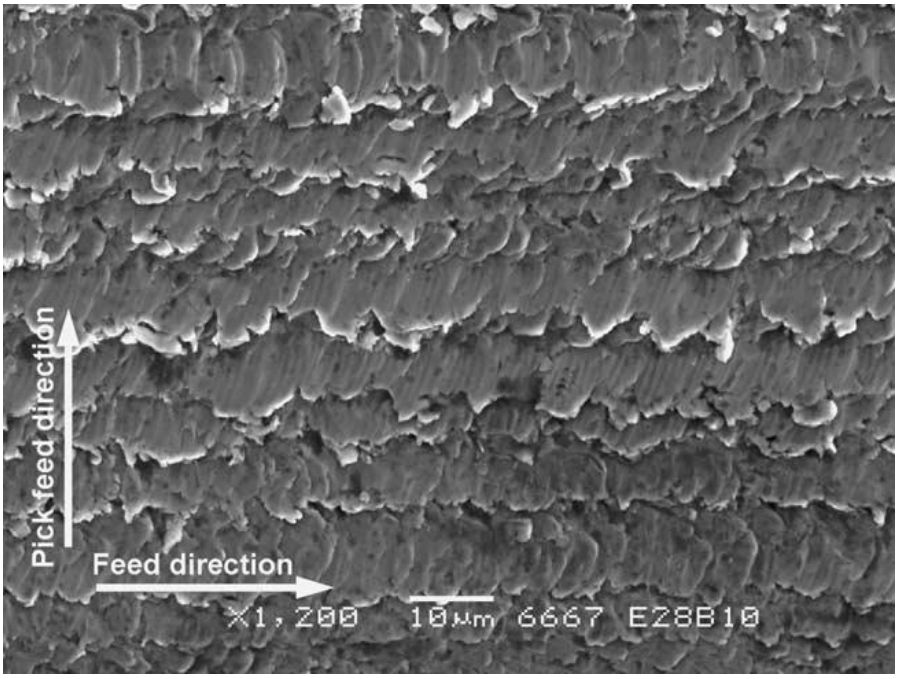

Figure 2.7: Surface of hardened tool steel (58 HR_c) milled with a 200 µm end mill [8].

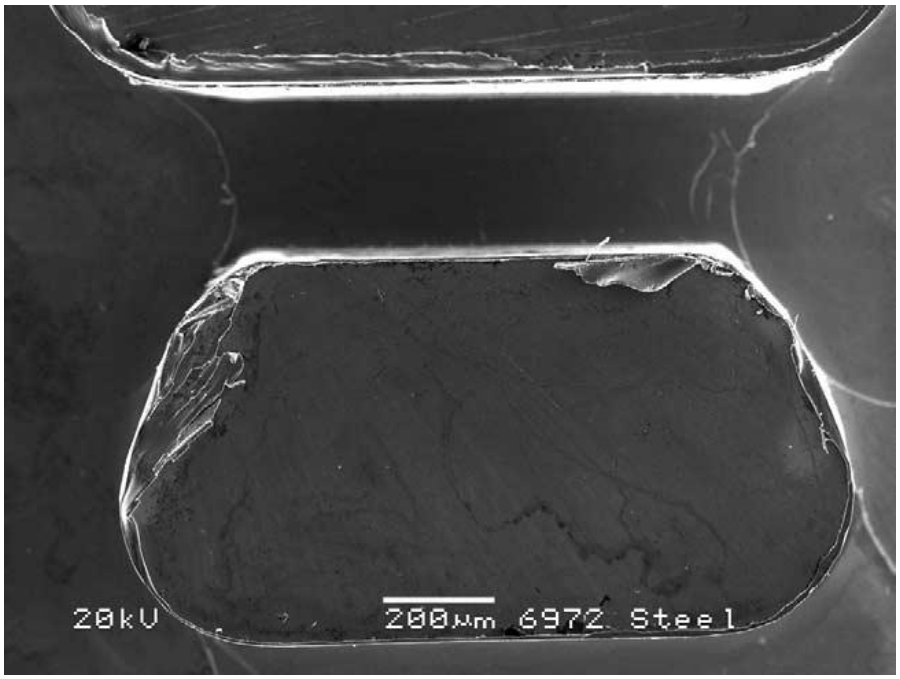

Figure 2.8: Micro milled injection mold insert in tool steel (35 HR_c) [8].

Because of rapid tool wear, burr formation increases significantly as seen in the SEM image of the micro milled mold insert shown in Fig. 2.8. Consequently, subsequent finishing processes are necessary to remove the burrs and improve the surface quality.

Previous work indicates that the low stiffness and limited strength of micro tools limits their tool life, material removal rates and part feature accuracy, especially when cutting hard materials like tool steel. In addition, there is no reported work on micro machining of high strength ceramics. These limitations necessitate the development of hybrid processes to create microscale features in hard materials. The next section will focus on discussing prior work on hybrid process development and characterization.

2.3 Laser Assisted Machining

2.3.1 Macroscale

Laser assisted machining has been investigated extensively for macroscale shaping of hard-to-machine metals and ceramics. The process involves the use of a high power continuous wave (CW) laser beam to soften the material in front of the cutting tool for achieving reductions in cutting forces, and hence an increase in material removal rates. Laser assisted machining of inconel 718 and Ti-6Al-4V was initially investigated by Rajagopal et al. [20]. Konig et al. [21] first successfully applied this technique to ceramic machining. Subsequently, experimental investigation of laser assisted machining of silicon nitride ceramics has been performed extensively by a number of researchers [22, 57, 58]. Deformation mechanisms and constitutive modeling for shear zone stresses in LAM of silicon nitride have been proposed [59]. In addition, laser assisted machining of other ceramics such as sintered mullite and magnesia-partially-stabilized-zirconia have

also been reported [60, 61]. These studies focus on material removal mechanisms, temperature prediction, wear modeling and evaluation of surface integrity. Germain et al. [62] evaluated the machinability and surface integrity of AISI 52100 steel and Ti6Al4V in laser assisted machining. Other related works include laser assisted machining of compacted graphite iron [63], inconel 718 [64, 65], titanium metal matrix composite [66] and high power diode assisted turning of D2 tool steel [67]. Transient thermal analysis using numerical models [68, 69] have been carried out for macroscale laser assisted turning to optimize the laser and cutting variables in order to reduce cutting forces and minimize tool wear. Rozzi, et al. [68, 69] modeled a translating laser beam used to heat a rotating workpiece. The model incorporated the effects of surface emission and convection at the machined and un-machined surfaces. Heat assisted machining, if not optimized, results in sub-surface thermal damage and degradation of the microstructure and mechanical properties [70].

2.3.2 Microscale

Laser assisted machining at the microscale has been investigated by a limited number of researchers. Singh et al. [12, 13] demonstrated the use of laser heating to induce localized thermal softening in a micro grooving process. They developed a two axis laser assisted micro grooving setup as shown in Fig. 2.9. They reported 56% and 46% reductions in the cutting and thrust forces, respectively, with a 35 W fiber laser when cutting H13 tool steel (42 HR_c). Jeon et al. [23] showed that the radial and tangential forces are reduced by 57% and 64%, respectively, when milling 1018 steel with laser assist using the set up shown in Fig. 2.10. In this setup, a conventional milling machine is integrated with a 100

W Nd:YAG laser having a spot size of 5 mm. Also, hard-to-machine materials were not investigated in their work.

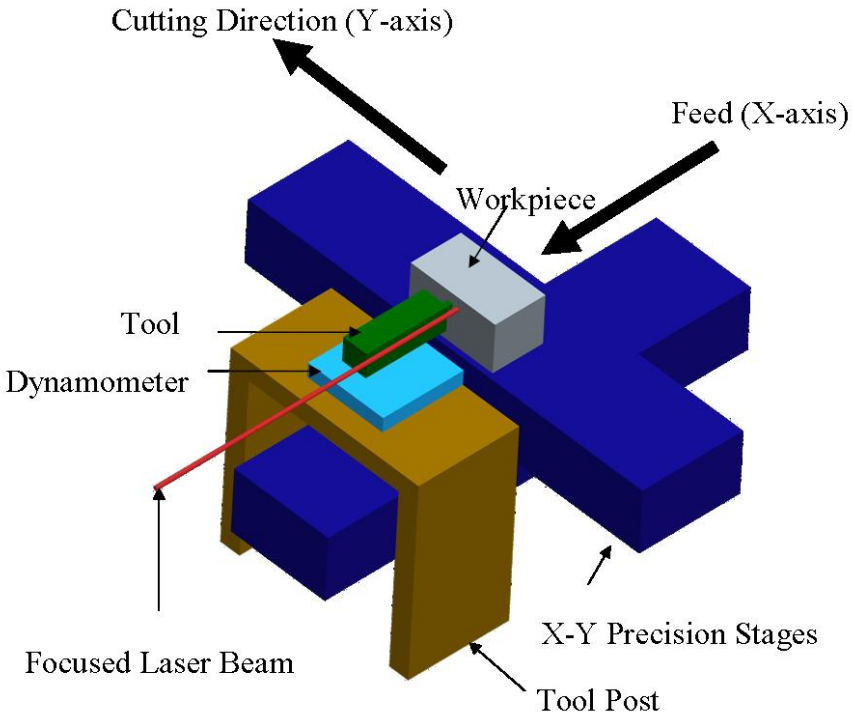

Figure 2.9: Schematic of the laser assisted micro grooving process [12, 13].

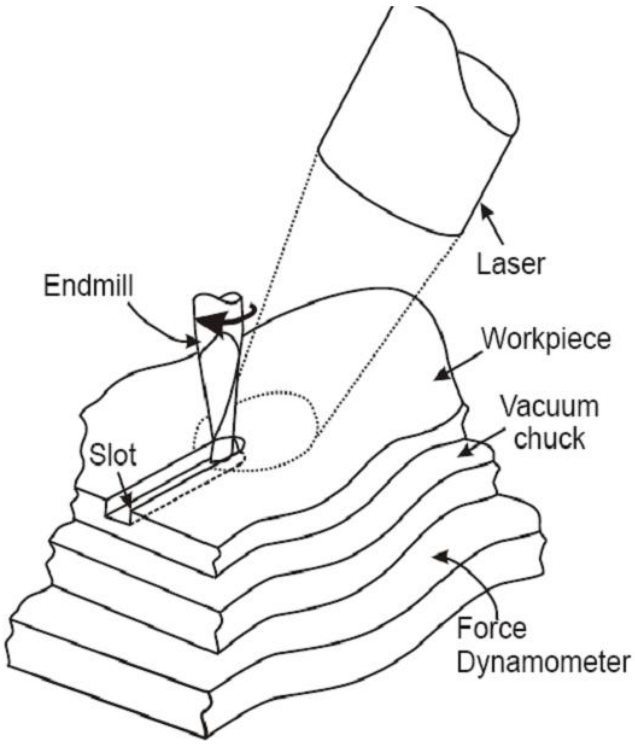

Figure 2.10: Schematic of the laser assisted micro milling process [23].

Shelton and Shin [24] evaluated the effect of laser assist on Ti-6Al-4V and 316 stainless steel and demonstrated a reduction in the rate of increase in the root mean square value of the acoustic emission (AE) signal with laser assist. They attributed this observation to reduced tool wear. With the aid of finite element modeling, they estimated that the thrust forces are reduced by 15% and 48%, respectively, when micro milling Ti-6Al-4V and 316 stainless steel with laser assist.

2.3.3 Modeling of Cutting Forces in LAM at the Macro and Microscale

The prediction of cutting forces in laser assisted milling of metals at the macro and microscales is not reported in the literature. Shin et al. [24] used the Finite Element Method (FEM) to show that the contact pressure between the chip and the tool decreases

in the LAMM process, which results in reduced tool wear and cutting forces. In end milling, the material shears along a curved path, which necessitates the need to account for the temperature distribution along the path, in addition to the change in the uncut chip thickness. Analytical models have been developed for the end milling process without laser assist at the macro as well as the microscale [41, 50, 71-74].

The limited prior work on LAMM indicates that laser assist helps in reducing tool wear and cutting forces. However, a detailed investigation of the LAMM process capability has not been reported. In particular, the limits of the LAMM process as far as material removal rates are concerned have not been investigated. Furthermore, an in-depth study of tool wear and tool life in LAMM versus conventional micro milling and its impact on the cutting forces, surface finish and burr formation are lacking. In addition, a force model to understand the effect of different laser and cutting parameters on the cutting forces produced in the LAMM process is not reported.

2.4 Laser Assisted Machining of Ceramics

Structural ceramics are being increasingly used because of their attractive high temperature wear resistance, chemical inertness and high strength-to-weight ratio properties [75]. Ceramics like silicon nitride, aluminum oxide and silicon carbide are characterized by very high hardness. Hence, shaping these hard ceramics is difficult and is usually accomplished by diamond grinding, which is characterized by low material removal rates and is therefore a slow process [76]. As a result, the grinding cost is very high and ranges from 70 to 90% of the component cost [77, 78]. The principal material removal mechanism in grinding of hard ceramics is brittle fracture, which often results in

the formation of surface micro cracks because of the low fracture toughness of high strength ceramics. Because micro features (e.g. in ceramic bearings) need to withstand repeated thermal and mechanical cycles, micro cracking should be avoided by appropriate selection of the grinding process parameters. In general, high surface cutting speeds and low depths of cut are recommended to minimize subsurface damage in grinding ceramics, which leads to an increase in machining time [79].

Consequently, researchers have proposed a two step grinding strategy for improving productivity when grinding ceramics [79]. The first step is to rough grind the ceramic material leaving a specified amount of stock, which is followed by a series of finish grinding passes to remove the damaged stock left from the first step. This strategy is mostly applicable at the conventional (or macro) scale because the grinding wheels used can withstand higher forces. At the macroscale, laser assisted machining of hard ceramics like silicon nitride has been studied extensively as seen earlier in section 2.3.1. At the microscale, however, the maximum depth of cut allowed in rough microgrinding is often limited by the catastrophic failure of the fragile microgrinding tool due to excessive forces produced in the operation. Furthermore, the availability of tool materials at the microscale make it difficult to use the laser assisted micromachining process directly [80, 81].

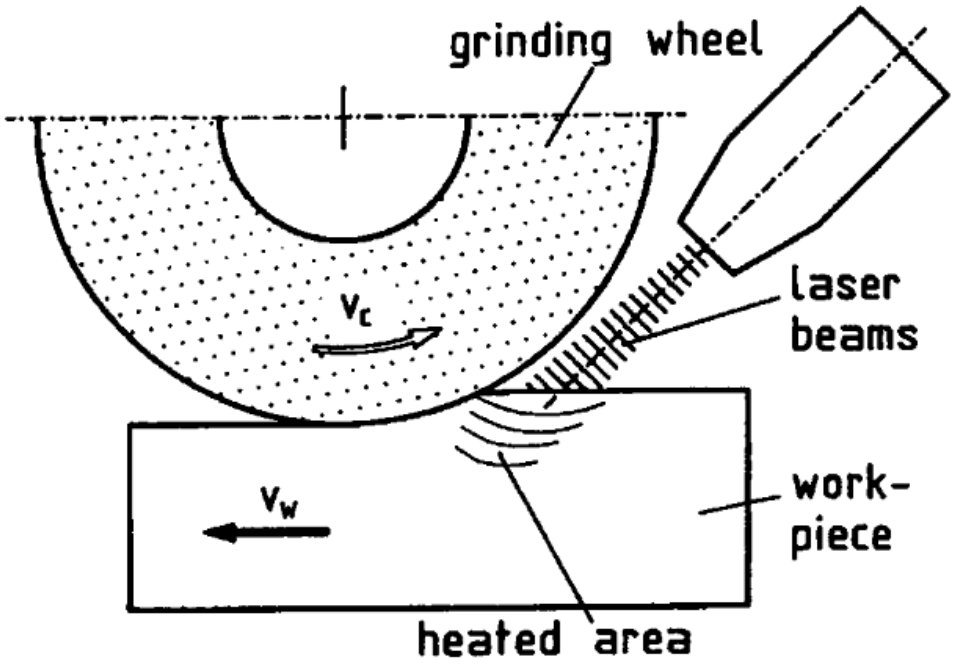

Figure 2.11: Schematic of the laser assisted micro grinding process [82].

A possible approach is to extend the laser-based controlled fracture technique proposed by Tsai et al. [83, 84] for three-dimensional shaping of silicon nitride ceramics. Their approach relies solely on the use of a continuous wave laser to induce and propagate thermal cracks in the ceramic. No mechanical cutting is used. They report a stable separation of the brittle material due to the local tensile stresses at the crack tip developed as a result of rapid laser heating followed by cooling. No work has yet been reported on using this technique at the microscale to machine silicon nitride using laser assist. It should be pointed out that at the macroscale, researchers have employed the thermal softening effect of laser irradiation to achieve ductile regime finish grinding of hard ceramics [79, 82]. This process is shown schematically in Fig. 2.11.

However, their technique of weakening of the work material through thermal softening is different from the thermal cracking mechanism reported in this thesis. The

latter involves the generation of thermal cracks to weaken the work material rather than using the thermal softening effect. This technique is described in greater detail in the thesis.

2.5 Cutting Tool Coatings

Cutting tool wear is known to occur via four *major* wear mechanisms, namely adhesive wear, abrasive wear, delamination wear, and wear due to chemical diffusion [11, 85, 86]. At the macroscale, tool wear modes and mechanisms have been studied extensively in the last few decades. One of the principal tool wear modes is flank wear, which is caused primarily by the abrasion of hard particles on the tool flank face. This wear mode is found to be dominant at low cutting speeds. Another important wear mode is crater wear, which is characterized by the formation of a crater on the tool rake face, and is typically dominant at higher cutting speeds where adhesive wear and thermal diffusion mechanisms are active. Chemical diffusion is another wear mechanism observed at high cutting speeds due to higher cutting temperatures, especially in uncoated tungsten carbide tools used to cut ferrous or titanium alloys [87]. In microscale cutting, however, rubbing and ploughing effects tend to dominate [5]. Depending on the stresses and temperatures generated by these physical processes, the tool wear modes and the dominant tool wear mechanisms in micro cutting could be significantly different from those in macroscale cutting. Very little work has been reported to date on either the tool wear modes or the fundamental wear mechanisms that are active in micro milling and other micromachining processes.

Tool coatings have been applied for decades with the intent of reducing the negative impact of the different tool wear mechanisms mentioned earlier. Specifically, coatings serve to reduce tool-chip friction, reduce adhesion between the tool and workpiece, act as a barrier to chemical diffusion, and reduce abrasive wear [11]. Hard nitride coatings have been applied over the last few decades [88] and have proved to be very successful in improving tool life in conventional scale milling, with up to 10X increases [89]. The useful life of milling tools is greatly improved by the use of TiN and cBN-TiN coatings [90]. Similarly, TiCN coatings have yielded tool life increases of up to 3 times compared to TiN coated tools [91]. Bouzakis et al. [92] studied different types and thicknesses of coatings for machining of 42CrMo4V steel and found that 6 μm thick TiAlN coatings gave the best performance. In addition, multi-layer coatings are currently being developed and preliminary results are encouraging [93, 94].

There is very little scientific work reported on tool coatings for micromachining applications. Recently, the importance of coatings in improving tool life in micromachining has been recognized by a few researchers. Pfefferkorn et al. [95, 96] have studied diamond coatings deposited using Chemical Vapor Deposition (CVD) on tungsten carbide end mills to obtain a 2 μm thick diamond coating. They found that this coating performs well in machining of soft aluminum alloys. They also found that the cutting and thrust forces were reduced significantly when compared to uncoated tools. The performance improvement was attributed to the superior tribological properties of the coating, clearly indicating the potential for coatings to improve tool life in micro milling.

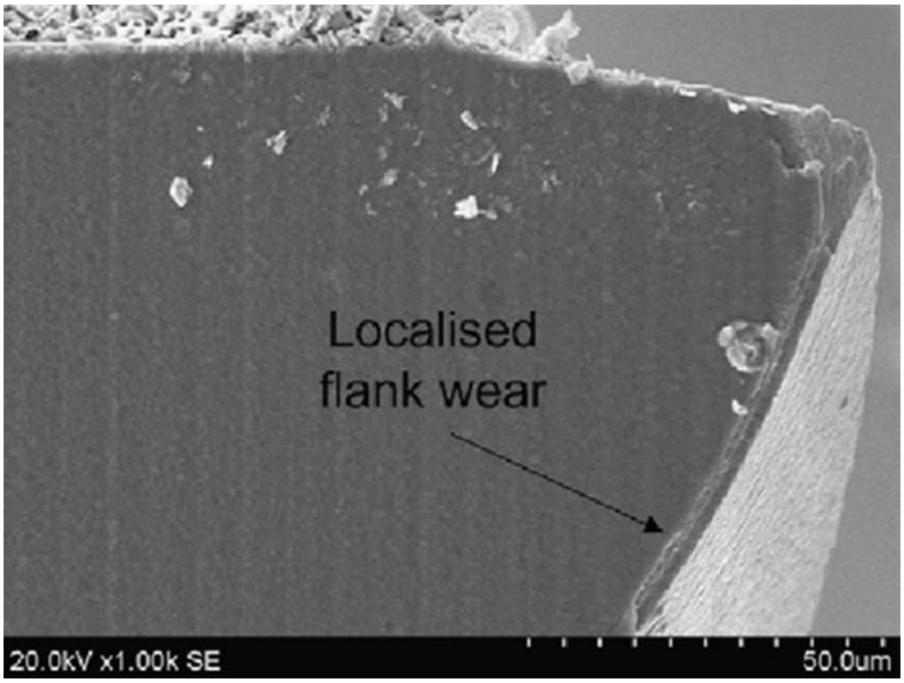

Figure 2.12: Flank wear in a TiAlN coated tool [1].

A simplified analysis of cutting temperatures in micro milling [97] suggests that the temperature rise experienced when cutting 1018 steel and Al6061-T6 is of the order of 100˚-200˚C. Aramcharoen et al. [1] studied different coatings in micro milling of tool steel of hardness up to 45 HR_c. They concluded that coatings help in reducing edge chipping and tool wear. TiN coatings yielded the best performance measured in terms of flank wear. Figure 2.12 shows flank wear in a TiAlN coated tool when micro milling with a 0.5 mm diameter end mill. Although this coating had the lowest hardness, it demonstrated good adhesion and surface quality. Also, the principal wear mechanism for CrN and TiCN coated tools was found to be delamination. Overall, the study suggests that TiN coating is the most effective coating when machining tool steels (45 HR_c). Tool coatings used in conventional macro and micro milling processes [1, 95, 96] may not be

suitable for LAMM, since the heat generated in LAMM is significantly higher than in the micro milling process.

Based on the literature review, there is insufficient understanding of the fundamental wear behavior of micro tools with and without laser assist. In addition, a systematic scientific investigation of the wear behavior of different tool coatings for LAMM is lacking . This knowledge is essential for the selection or development of new coatings for the micro end mills.

2.6 Summary

It is clear from the literature survey that:

- Very little investigation has been carried out to evaluate the process capability of the laser assisted micro milling process.
- No work has yet been reported on the modeling of cutting forces in laser assisted micro milling process.
- No work has yet been reported on the application of lasers to assist machining of high strength ceramics at the microscale.
- There exists insufficient understanding of the wear behavior of coated micro end mills with and without laser assist.

The rest of this thesis describes the development, experimental characterization, and modeling of the laser assisted machining process to create microscale features in hard metals and high strength ceramics.

CHAPTER 3

DESIGN AND FABRICATION OF THE LASER ASSISTED MICRO MILLING SETUP

This chapter is aimed at designing and fabricating a LAMM setup for machining microscale features in hard-to-machine materials. This is the outcome of a need to enhance the material removal rates in micro milling process with laser assist. This chapter describes the design and fabrication of the experimental setup in detail. A technique to detect tool-workpiece contact is developed as part of the experimental setup and is discussed briefly in this chapter. In addition, the chapter discusses preliminary experiments on A2 tool steel to understand and evaluate the effect of laser assist on tool wear and accuracy of the machined groove produced in the LAMM process.

3.1 Approach

The approach used to develop the LAMM setup basically combines a low power continuous wave fiber laser ($\leq$ 35 W) with the conventional micro milling process. The laser beam could be used to soften the work material in a region immediately in front of the cutting tool when machining hard metals, or could be used to generate thermal cracks to weaken the base material when machining high strength ceramics. The two approaches were discussed briefly in Chapter 1. The intensity of the laser beam can be varied via the power and spot size of the laser used. Through suitable modeling and experimentation, the thermally affected region can be confined to the desired volume of material removal, thereby leaving no residual thermally affected zone in the parent material. The design and

fabrication approach and associated evaluation of the setup are reported in the following sections of this chapter.

3.2 Design and Fabrication

A novel laser assisted micro milling machine has been designed and developed to enable the creation of free-form three-dimensional microscale features in hard materials and to study the process characteristics. The schematic of the experimental setup is shown in Fig. 3.1 and the actual setup is shown in Fig 3.2.

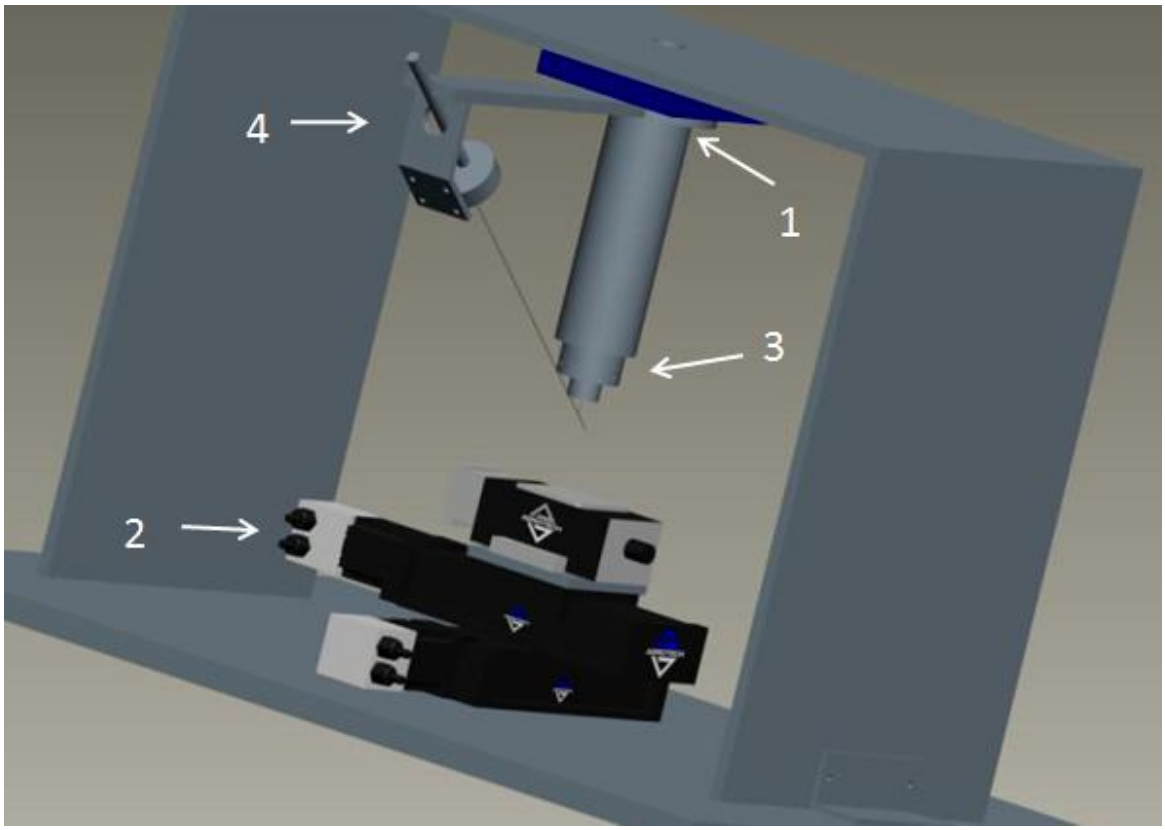

Figure 3.1: Schematic of the experimental setup (1- rotary stage for orienting the laser, 2- stacked linear stages – X,Y and Z, 3- spindle assembly, 4- laser delivery system).

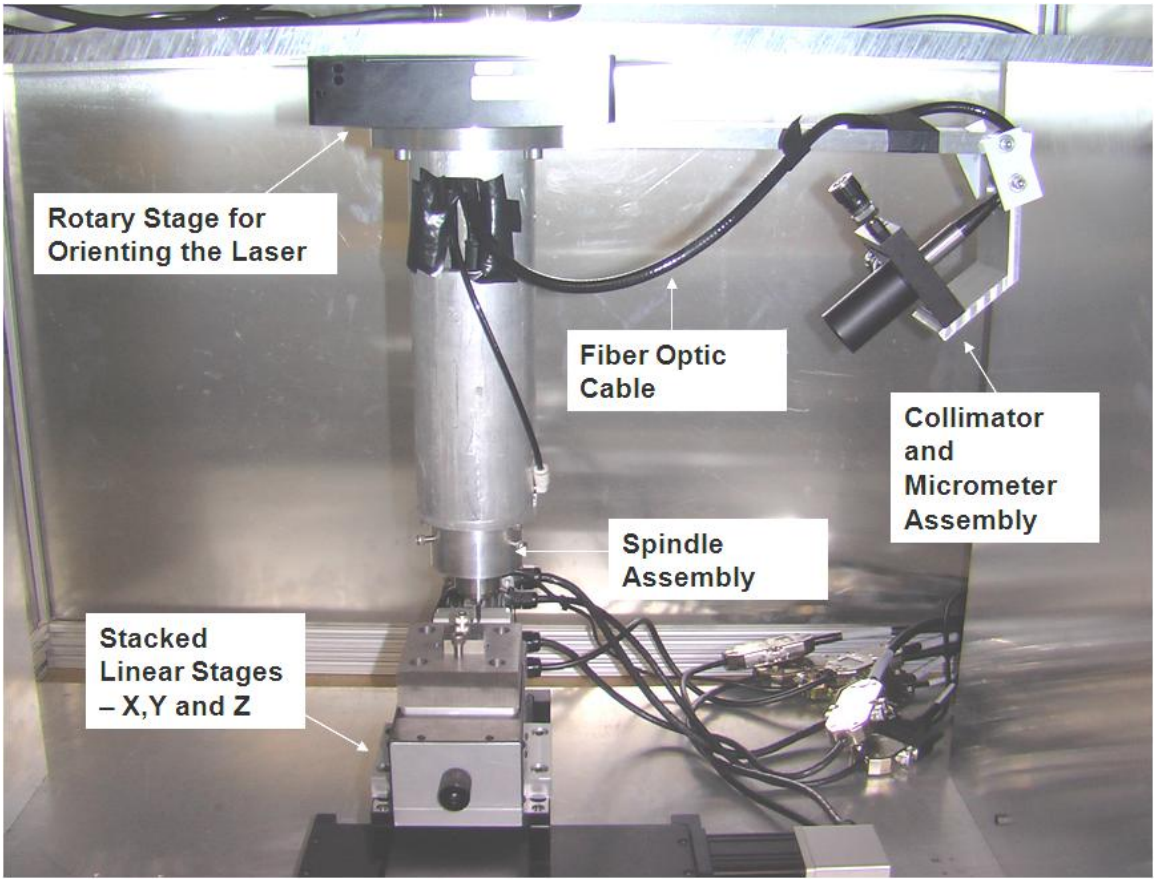

Figure 3.2: Experimental setup.

The machine consists of three stacked linear motion ball screw stages (Aerotech ATS-125 Linear X and Y stages, AVS-105 Z-axis lift stage) and a rotary stage (Newport URS150cc) that enables the positioning of the laser beam at any spot around the micro milling tool. The stages are driven by Aerotech NDrive CP10 motion controllers, which are integrated into a single interface using the Aerotech A3200 motion control software. This configuration of the machine tool enables the creation of three dimensional features in hard materials. The positioning resolution of the ATS-125 linear stage is 0.1 μm with 1 μm accuracy per 25.4 mm of axial travel. The ATS-125 linear stage has 100 mm of travel, can withstand 180 N of axial force, and has a maximum attainable speed of 30

m/min. The AVS-105 Z-axis lift stage has 5 mm of travel along with a maximum load carrying capacity of 50 N, and a maximum travel speed of 0.3 m/min. The URS150cc stage is DC servo motor driven, and has a continuous 360º travel range with a resolution of 0.0005º. The maximum rotary speed of the stage is 80º/sec and has a normal centered load capacity of 300 N.

The design implemented in this work enables the programming of the laser position concurrently with the motion of the linear stages to obtain the desired laser and cutting tool path. This is essential for machining curved features. A schematic is shown in Fig. 3.3, which explains this unique ability of the setup to create curved features. All existing experimental setups reported in literature have a stationary laser beam, which directly limits their ability to create curved features even in 2D [23, 24].

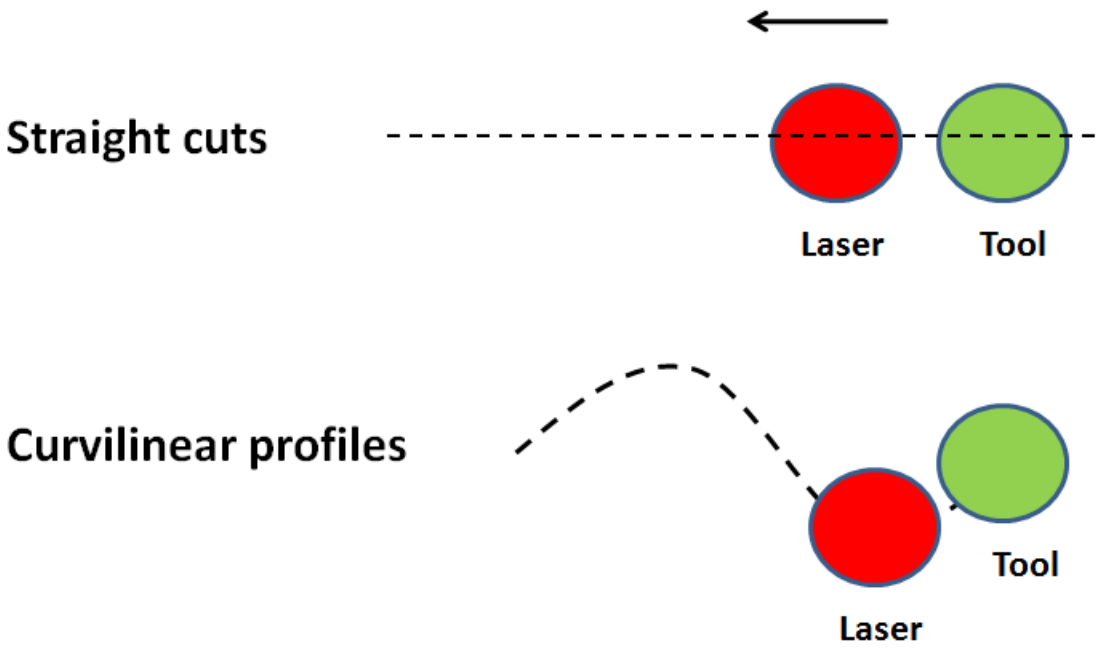

Figure 3.3: Positioning of the tool at any point before the cutting tool enables the creation of 3D features.

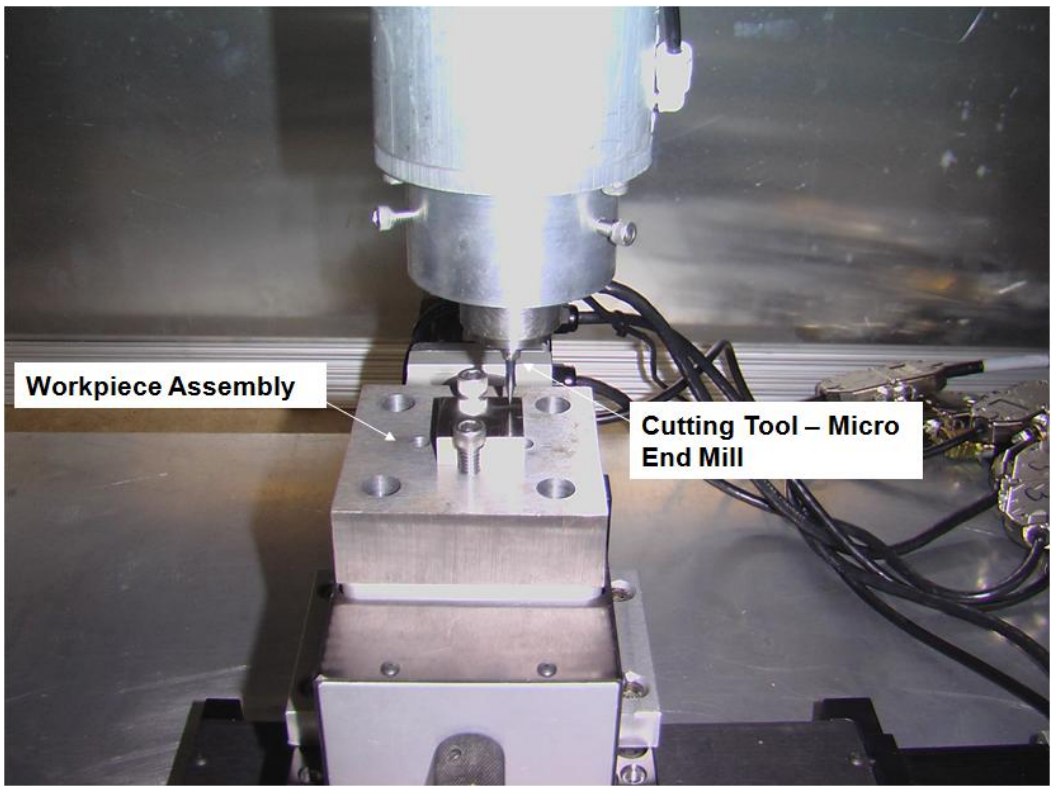

Figure 3.4: Workpiece assembly.

The workpiece assembly is mounted on the AVS-105 Z lift stage as shown in Fig. 3.4. A variable high speed electric spindle with a maximum rotational speed of 80,000 rpm is used to achieve cutting speeds of up to 40 m/min. The spindle is stationary and mounted to the machine tool structure through the large aperture in the rotary stage. A relatively low power (max. 35 W) Ytterbium doped continuous wave near infra-red (IR) (1.06 μm) fiber laser (IPG Photonics - YLM 30) is used to achieve highly localized thermal softening of the material immediately in front of the cutting tool during the micro milling process. The laser beam is emitted from a 7 μm diameter single mode fiber through a collimator. A red aiming beam that is collinear with the laser beam allows the laser to be approximately spotted. The collimated laser beam is focused using a lens to

the required spot size based on the focal length of the lens and the distance between the lens and the workpiece. No assist gas is used in the tests.

The laser spot size used can be adjusted depending on the dimensions of the feature to be machined. The laser power can be controlled in real time using the laser controller which modulates the power of the laser beam. The laser, spindle and the four axes of motion are controlled simultaneously via a common computer interface. The setup is instrumented to measure the cutting forces using a piezoelectric force dynamometer (Kistler Minidyne® 9256C2). The distance between the irradiated spot and the cutting tool can be adjusted using the micrometer stage mounted on the rotary axis that positions the laser beam. The distance is set by repeatedly burning laser marks on the workpiece and measuring the location of the mark relative to the cutting tool. Once the laser-to-tool distance is fixed, it simply needs to be checked at regular intervals to ensure consistency over time. The positioning error of the laser beam with respect to the cutting tool is +/- 10 μm.

Representative features created in A2 tool steel (62 HR_c) using the LAMM setup are shown in Figs. 3.5-3.7. The machining of circular grooves shown in Fig. 3.5 is made possible only because of the unique design of the experimental setup, which enables the positioning of the laser at any point in front of the cutting tool. The feed velocity of the X and Y stages when machining circular features is determined automatically by the A3200 motion controller based on the angular velocity of the rotary stage. This is essential for maintaining the position of the laser beam with respect to the cutting tool. In the experimental setup the maximum rotational speed of the laser beam is 80º/sec for

machining curved features, which limits the feed rates of the X and the Y stages. This can be improved further by using faster rotary stages.

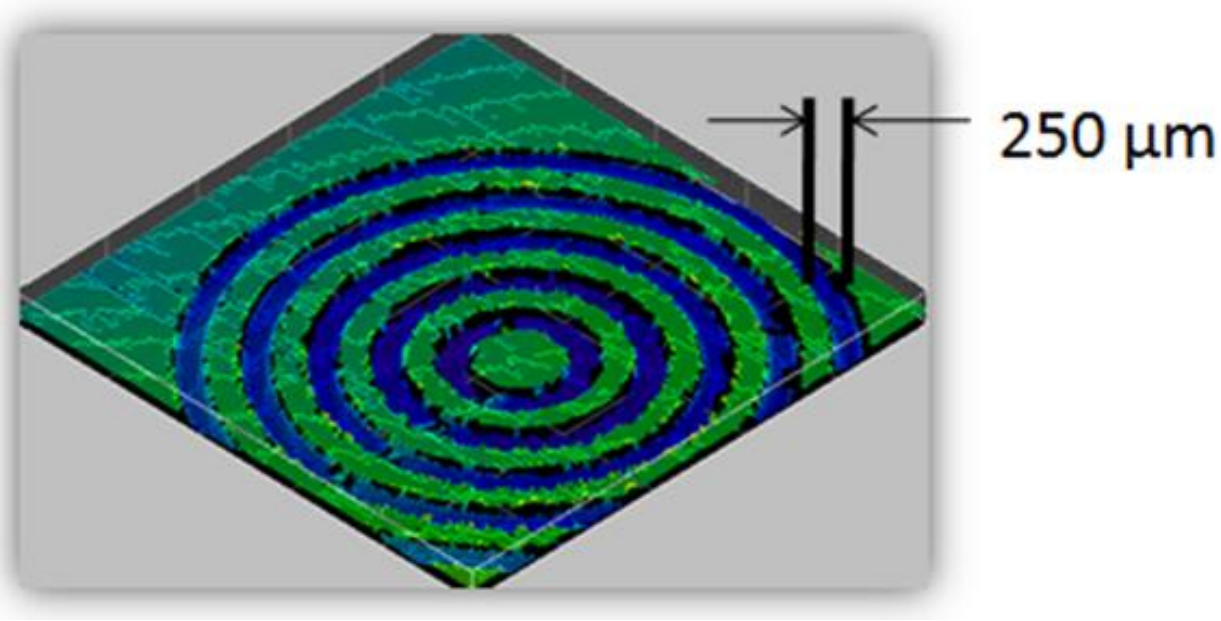

(a)

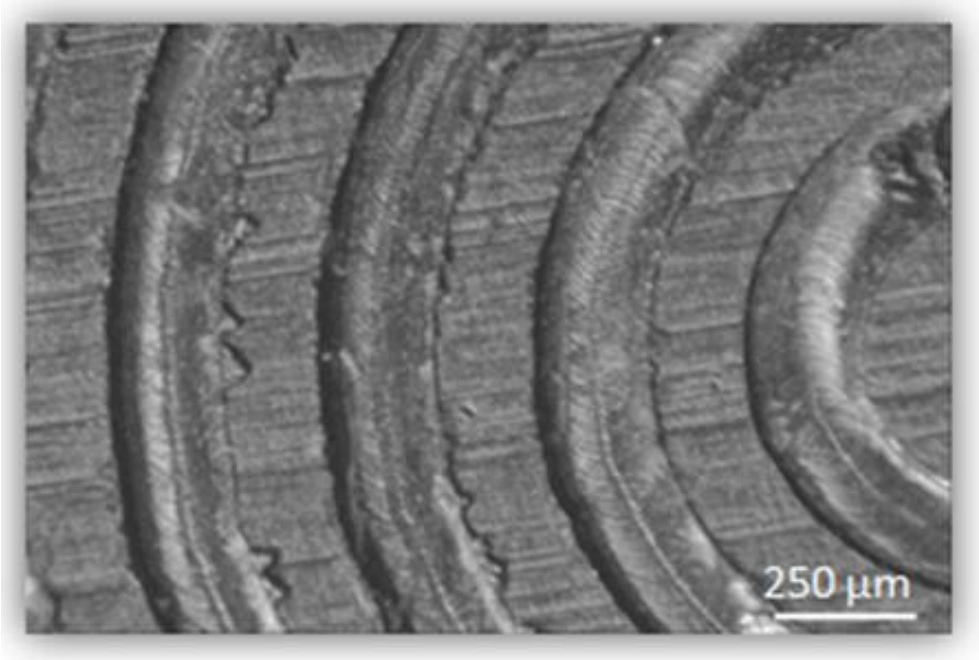

(b)

Figure 3.5: (a) White light interferometer and (b) optical image of a circular groove (20 µm deep) pattern machined in A2 tool steel (62 HR_c).

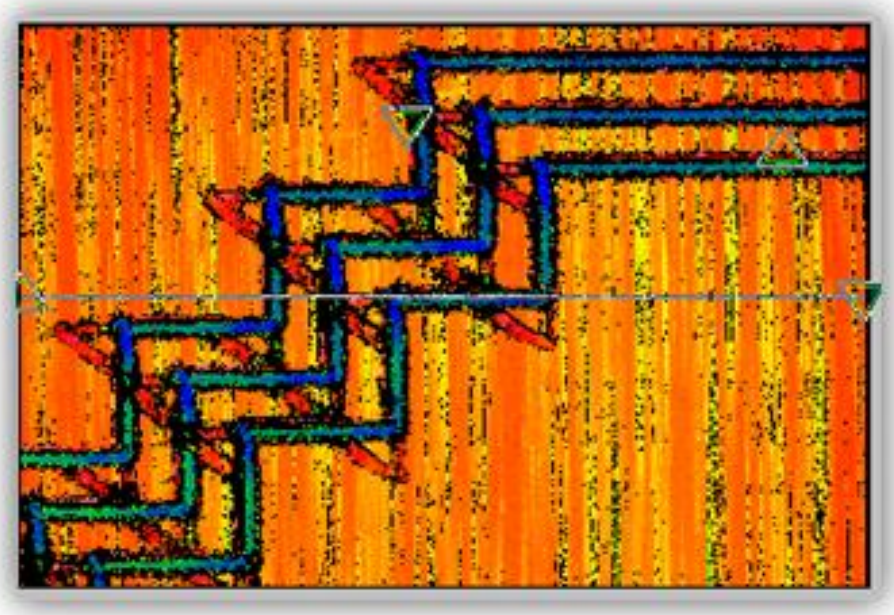

Figure 3.6: White light interferometer image of 250 μm wide, 20 μm deep steps machined in A2 tool steel (62 HR_c).

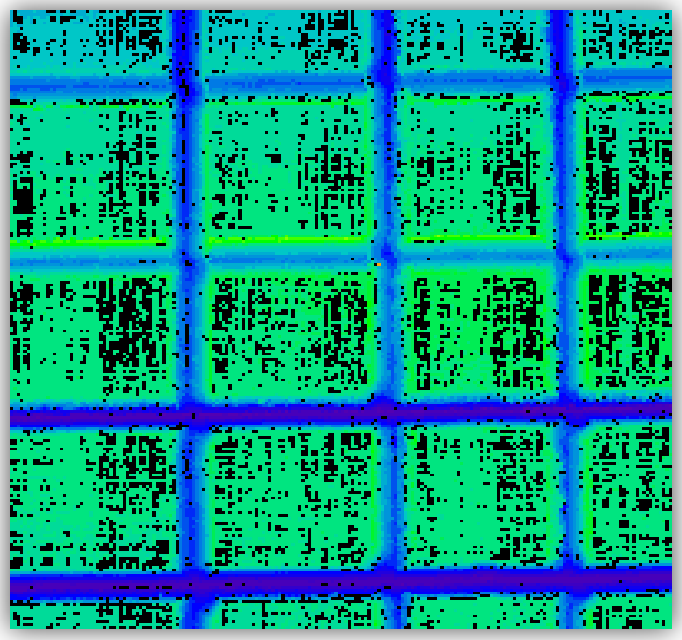

Figure 3.7: White light interferometer image of 250 μm wide, 20 μm deep pattern machined in A2 tool steel (62 HR_c).

3.3 Tool-Workpiece Contact Detection

A key requirement in micro milling is the need for accurate tool setting, which has a direct impact on the dimensional accuracy of the machined feature. Due to the small tool size (25 μm~500 μm dia.), it is difficult to accurately set the program zero for the tool position in the axial (Z) direction relative to the workpiece surface. Traditional methods of setting tool position in conventional milling such as the use of tool pre-setter are generally inadequate for micro milling. At present, different methods are being used or have been proposed to address this issue. One method employs laser based detection of tool position, which has been reported to yield an accuracy of 50 μm [98]. This method involves a two step process and is not sufficiently accurate. Another approach involves the use of machine vision to detect tool position. This technique is expensive since it requires a very high magnification camera along with a direct line-of-sight to the tool at all times. Researchers have also proposed use of the electrical signal generated when the tool contacts the workpiece [99]. However, this approach is limited to conductive workpiece and tool materials.

Yet another reported method consists of using an acoustic emission (AE) sensor to detect tool-workpiece contact by monitoring the root-mean-square (RMS) value of the output voltage signal [6, 98]. Bourne et al. [98] studied this technique for different tool-workpiece combinations and found that the accuracy of contact detection is ~1 μm. They noted that the tool overshoot into the workpiece surface is influenced by tool size, tool geometry, contact detection threshold, workpiece material, surface roughness, etc. However, they did not investigate the accuracy of the technique for different micro tool geometries (e.g. ball nose end mills) and for very hard workpiece materials (>50 HR_c).

Min et al. [6] have reported that the AE method produced an average overshoot of less than 0.1 μm in a stainless steel workpiece.

The tool-workpiece contact detection method developed as a part of the experimental setup is based on analyzing the spectral content of the lateral vibration of the micro milling spindle. The technique, described in the following section, is applicable to all tool-workpiece material combinations, conductive and non-conductive, and is relatively inexpensive and simple. Note that although the spindle vibration signal has been used in prior work for tool condition monitoring at the macroscale [100-102], it has not been used for detecting tool-workpiece contact at the microscale. A detailed investigation was carried out to understand the effects of tool wear, step size, tool geometry, workpiece surface roughness, workpiece material hardness and contact detection threshold on the tool contact detection accuracy of the spindle vibration-based method and is reported elsewhere [103].

3.3.1 Setup

A uniaxial accelerometer (Kistler Model 8636C50, ±50g range, 6KHz frequency range) is affixed to the spindle housing (~125 mm above the tool tip) to monitor the lateral vibrations of the spindle as shown schematically in Fig. 3.8. The accelerometer output is amplified and sampled by a personal computer, which runs the data acquisition software. Note that the exact location of the accelerometer depends on the kinematics and physical configuration of the specific micro milling machine used. In the current setup, the accelerometer is mounted on the spindle assembly and not on the workpiece/fixture since the spindle is stationary and the workpiece translates with the stacked motion stages. This

minimizes the impact of noise generated from stage motion on the accelerometer signal. However, under certain circumstances the accelerometer can be mounted on the workpiece and the following tool contact detection technique is still applicable.

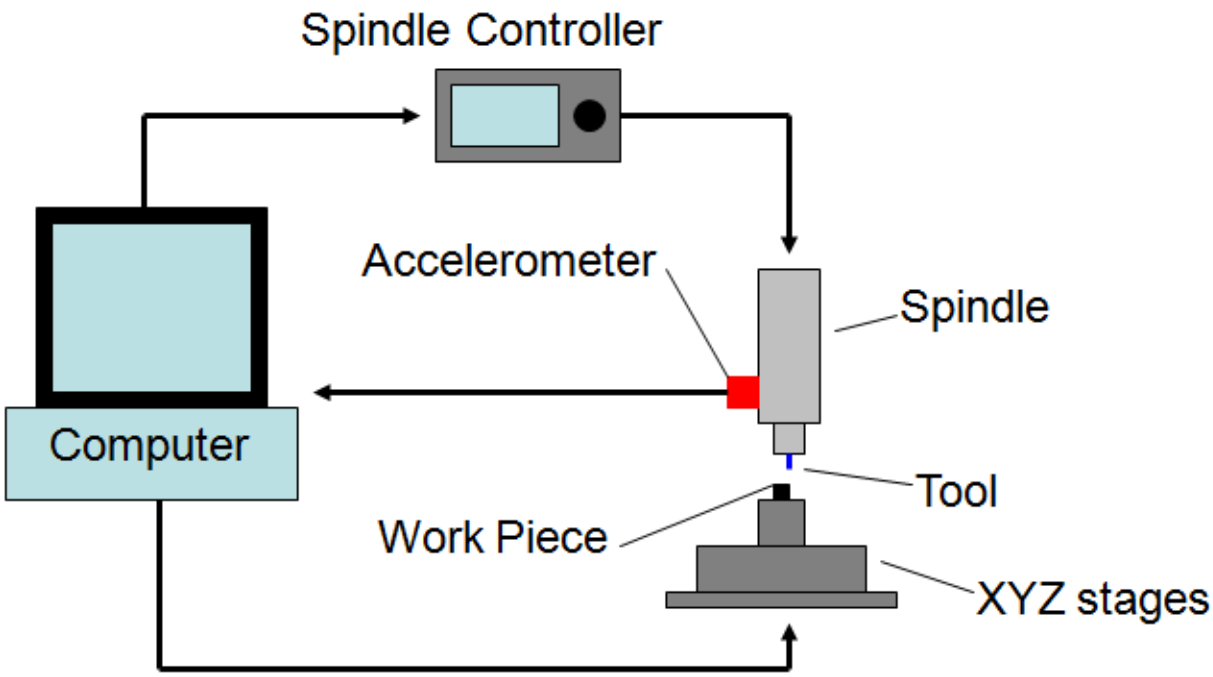

Figure 3.8: Schematic of the spindle vibration monitoring system.

3.3.2 Approach

The tool-workpiece contact detection approach is summarized in Fig. 3.9. The spindle acceleration signal is sampled at 5 KHz as the tool is made to approach the workpiece surface in step increments of 0.1~0.5 μm while the spindle is rotating at 16,000 rpm. There is a programmed 1 second dwell between each step to account for the time needed for data transmission and power spectra calculation. The signal is then digitally filtered with a Butterworth band pass filter (Impulse Infinite Response Mode, 100-1000 Hz band pass). Only the frequency range containing the spindle rotation frequency (266 Hz for the

16,000 rpm spindle speed used in the current machine) is selected and the remaining spectral content is filtered out. Note that the foregoing spindle speed was chosen from initial trials aimed at identifying the speed at which the tool-workpiece contact detection sensitivity is highest for the micro milling machine used in this work.

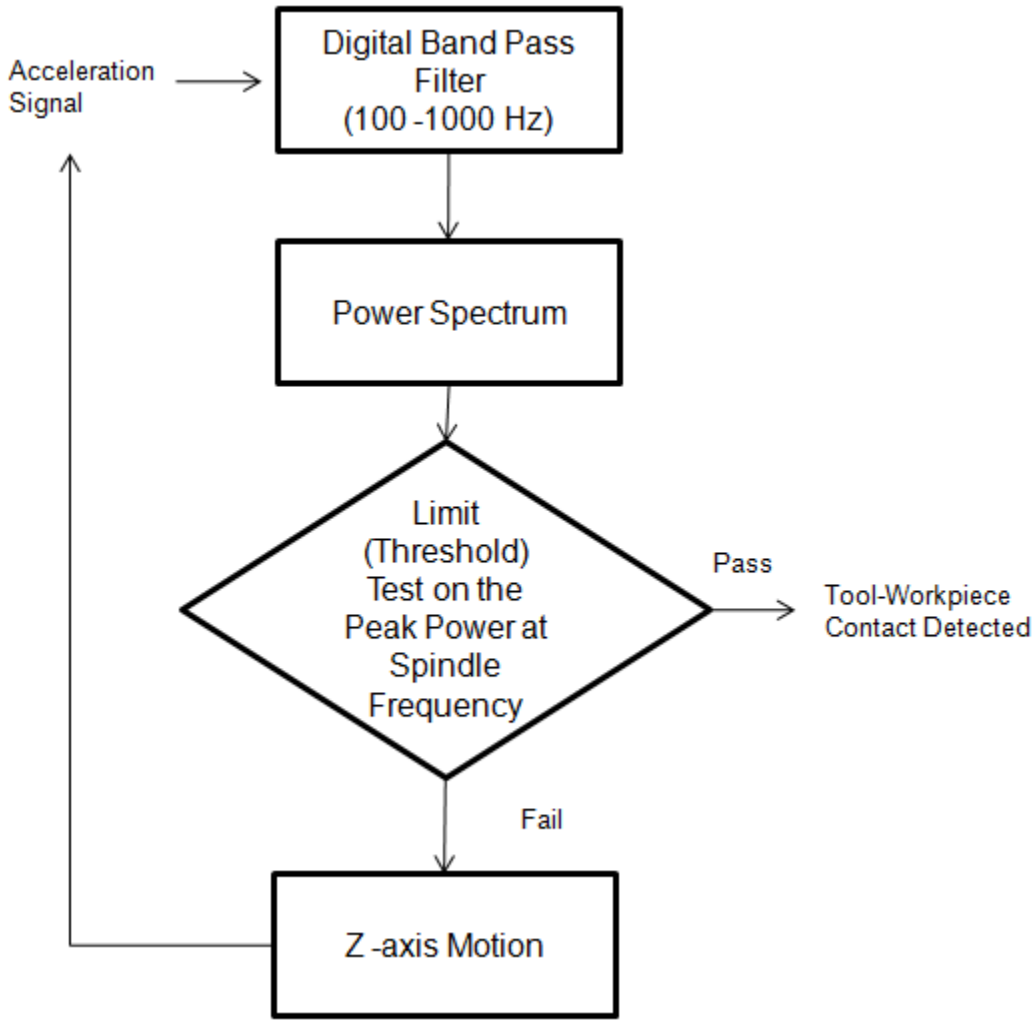

Figure 3.9: Flowchart illustrating the contact-detection approach.

The power spectrum of the band-pass filtered acceleration signal is computed every 1024 consecutive data samples as shown in Fig. 3.10. A limit or threshold test on

the peak power at the spindle rotation frequency is then performed as shown in Fig. 3.11. The threshold band (indicated by the dashed lines in Fig. 3.11) is selected such that it is insensitive to random variations in the peak power. Note that smaller the threshold band, greater the contact detection sensitivity.

During the tool-workpiece contact detection process, after each step increment, the peak power at the spindle rotation frequency is checked to see if it still lies within the preset threshold. Tool-workpiece contact is detected when the peak power at the spindle rotation frequency falls outside the threshold. At this point the current Z-axis position is stored and the Z axis stage motion halted. Note that the contact detection threshold can be optimized to minimize the contact detection time and is dependent on the signal-to-noise ratio for the micro milling machine used.

The rise or fall of the spindle frequency peak power at contact is explained by the effect of tool geometry on the vibration signal. For a square micro end mill, the tool motion is constrained and the amplitude of vibration decreases when the tool contacts the workpiece (see Point 3 in Fig. 3.11). For a ball nose end mill, the spindle frequency peak always increases upon tool contact (see Point 2 in Fig. 3.11). This is attributed to a phenomenon similar to drill wandering, which results in unbalanced forces and negative damping and tends to increase the amplitude of vibration and hence the spindle frequency peak [104]. For the ball nose end mill, the peak power initially rises and then falls below the threshold once cutting is fully established, since the amplitude of vibration then decreases. For a square end mill, this effect is not noticeable since there is less rubbing between the tool and workpiece upon contact and the transition to cutting is rapid.

The depth of indentation on the workpiece surface caused by tool overshoot is taken as a measure of the tool-workpiece contact detection accuracy. A small overshoot signifies high contact detection accuracy. The algorithmic procedure outlined in Fig. 3.9 is automated and controlled via a single software interface.

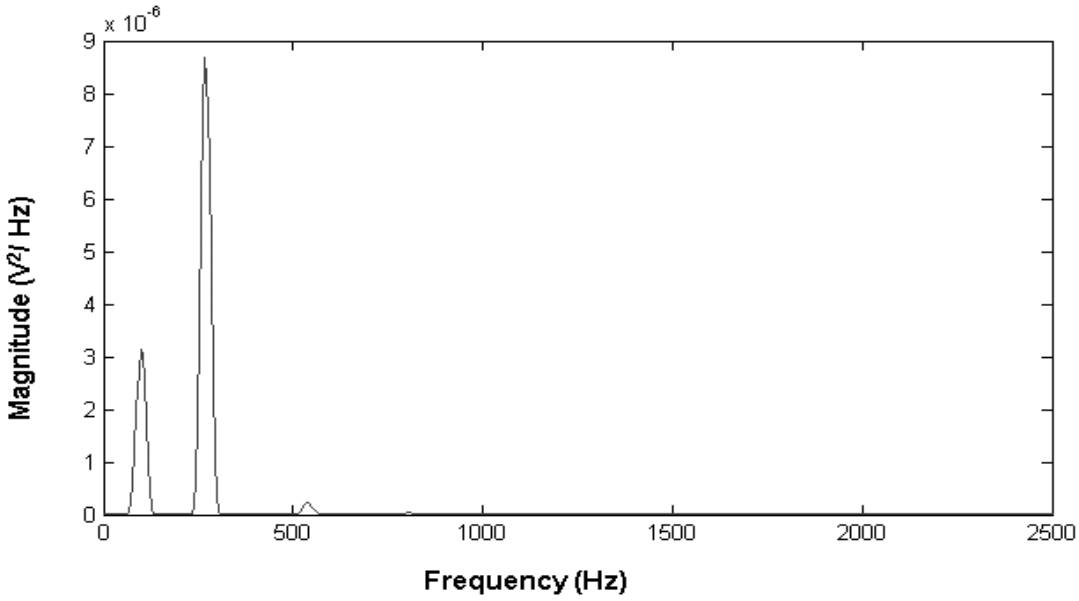

Figure 3.10: Power spectrum of the spindle acceleration signal. The dominant peak is at 266 Hz and corresponds to a spindle rotation speed of 16,000 rpm.

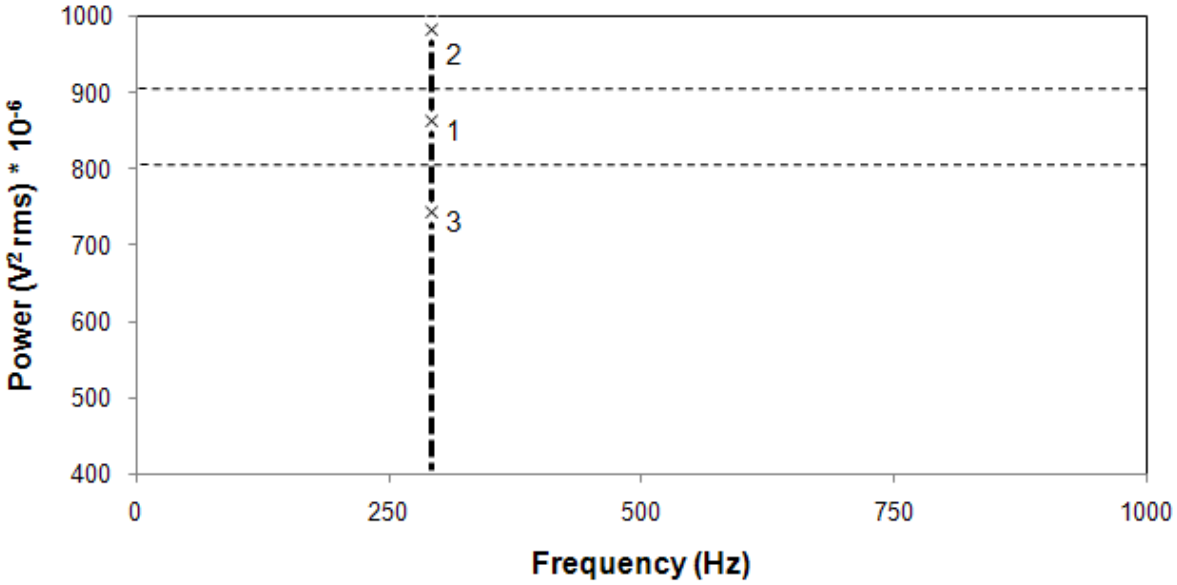

Figure 3.11: Graph showing peak power at the spindle rotation frequency (266 Hz); the dashed lines indicate the preset threshold. Point 1: peak power prior to tool-workpiece contact, Point 2: peak power for a ball nose end mill in contact with the workpiece (above threshold). Point 3: peak power for a square end mill in contact with the workpiece (below threshold).

3.3.3 Some Results

The detailed investigation and results are reported in Kumar et al. [103], and not reproduced here since they are not central to the main focus of this thesis. The results show that the method is capable of sub-micron contact detection accuracy depending on the workpiece hardness, roughness, and contact detection threshold. Figure 3.12 shows the effect of workpiece hardness on the tool overshoot (or tool setting error) for the conditions listed in the figure.

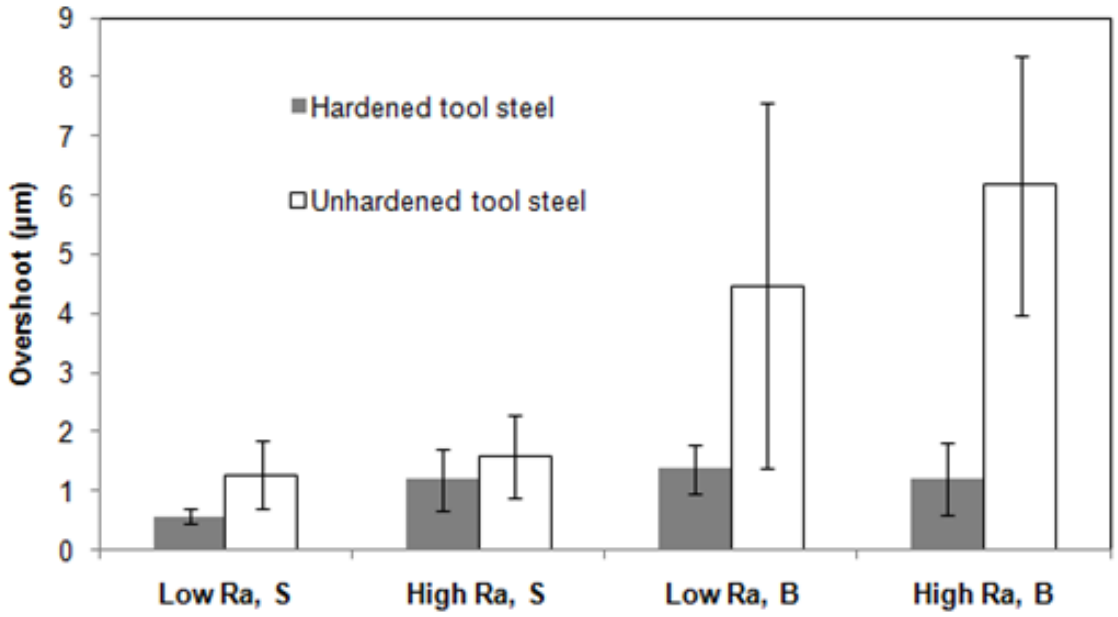

Figure 3.12: Comparison of tool overshoot as a function of material hardness (0.1 µm step size; 'S' indicates square end mill, 'B' indicates ball nose end mill).

3.4 Basic Evaluation of the LAMM Setup

Tests were conducted in A2 tool steel (62 HR_c) to perform a basic evaluation of the LAMM setup. The composition of A2 tool steel is given in Table 3.1. The laser spot size used in this work is approximately 160 µm but can be adjusted depending on the dimensions of the feature to be machined. The laser power is set to 7.5 W and the distance between the center of the laser spot and the cutting tool axis is set to 250 µm for all tests reported here.

Table 3.1: Nominal chemical composition of A2 tool steel.

Element	C	Mn	Si	Cr	Ni	Mo	V	Cu
Weight %	0.95-1.05	1.00	0.5	4.75-5.5	0.3	0.9-1.4	0.15-0.5	0.25

TiAlN-coated Tungsten carbide 4-flute ball end mills of 250 µm diameter were used in the experiments. Six parallel grooves each 25.4 mm in length and spaced 0.4 mm apart were milled from ‘edge 1’ to ‘edge 2’ (as shown in Fig. 3.13).

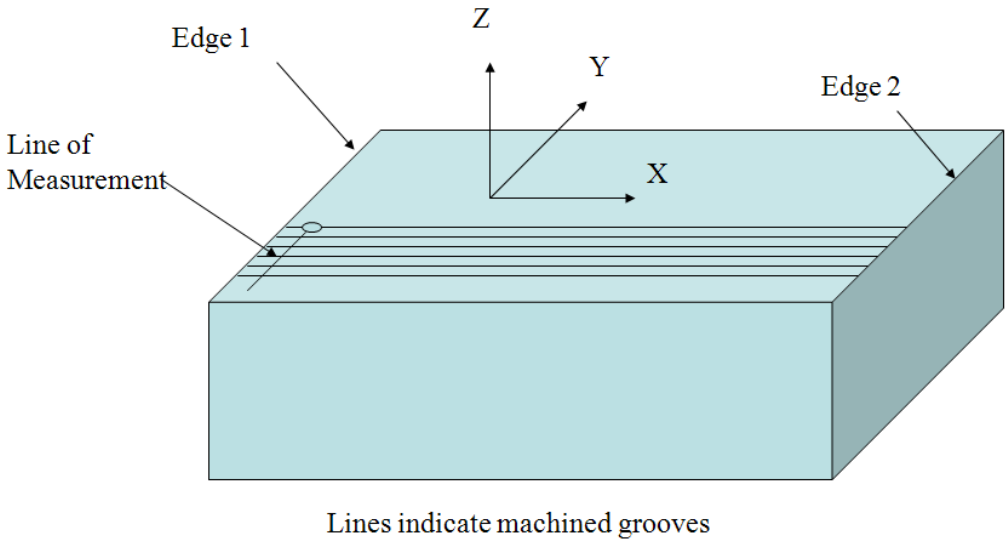

Figure 3.13: Machined grooves and line of dimensional measurement

Dry micro milling tests were carried out at three different cutting speeds (14, 23 and 32 m/min) while keeping the feed rate and axial depth of cut fixed at 1 µm/flute and 25 µm, respectively. These values were chosen from a set of preliminary tests where the axial depth and feed were gradually increased till catastrophic tool failure occurred at an axial depth of 25 µm and a feed of 3 µm/flute. As a result, a conservative value of tool feed (1 µm/flute) was chosen for the experiments. The measured response is the groove depth as a function of the cutting distance. The groove dimensions were measured by a scanning white light interferometer. Note that the groove depth and width were measured at various points along the groove. A number of readings were taken along the groove and averaged.

Figure 3.14 shows the variation in groove depth with cutting distance with and without laser heating for the conditions listed in the figure. It is clear from the plot that the groove depth with laser heating is closer to the set depth of cut than without laser heating. Note that the initial difference in groove depth for the two cases is predominantly due to tool deflection and, to a smaller extent, initial tool wear. The effect of tool deflection is arguably smaller with laser heating [12, 13] and therefore yields a groove depth closer to the set depth of cut. It is also apparent from Fig. 3.14 that the rate of change in groove depth with cutting distance is slightly less in laser assisted micro milling. This is attributed to a lower rate of tool wear in the presence of laser heating. Figure 3.15 shows the optical images of the ball end mill after cutting six grooves with and without laser assist. Figure 3.15 (c) shows the image of the micro ball end mill after cutting without laser assist. It is clear from the figure that the tool tip is severely worn and has lost its round shape. This is thought to be due to tool chipping during initial engagement followed by severe mechanical wear of the exposed uncoated tungsten carbide tool material [10]. Consequently, a small depth of cut is typically used in conventional micro milling. However, as seen in Fig. 3.15 (b), tool wear is less severe with laser assist and also appears to be more gradual. This is clearly desirable from a standpoint of part feature accuracy.

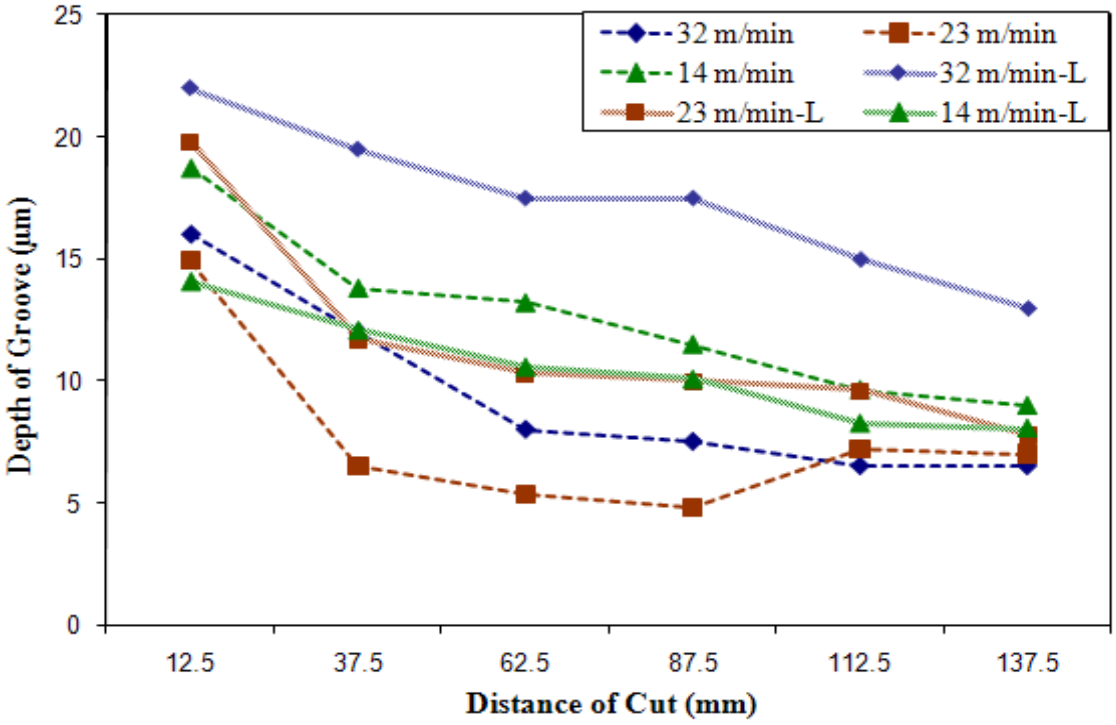

Figure 3.14: Effect of laser assist on groove depth variation along the centerline of the six parallel grooves at different cutting speeds (axial depth of cut: 25 µm, feed: 1 µm/flute, laser power: 7.5 W) ('L' in the legend refers to the laser heating case).

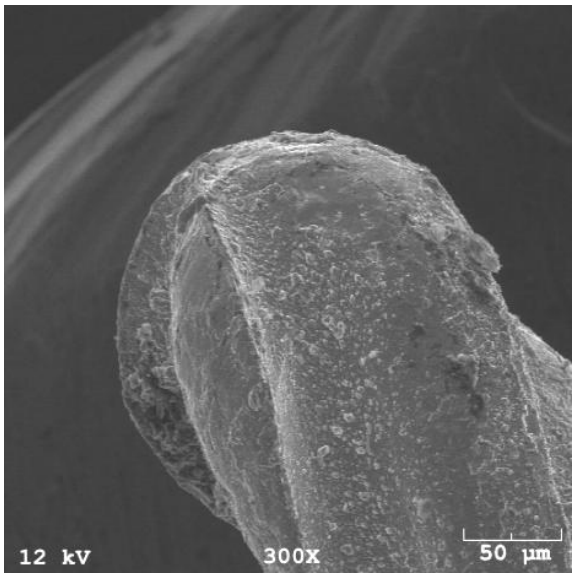

(a)

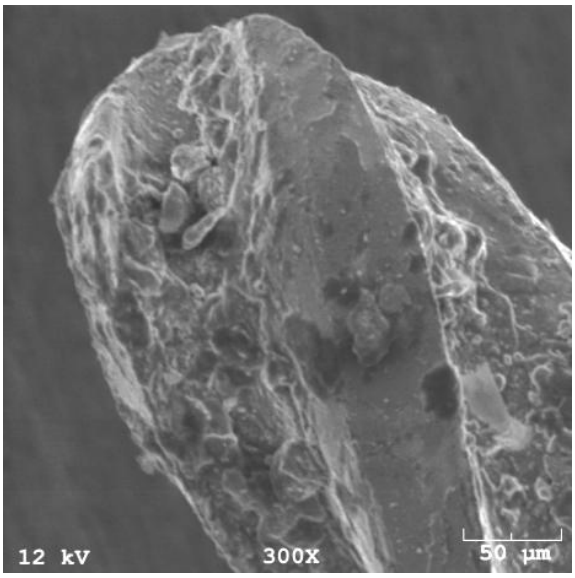

(b)

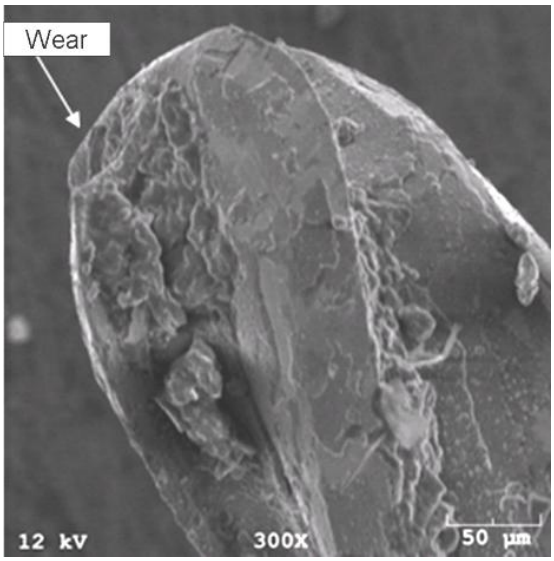

(c)

Figure 3.15: Images of ball end mill (a) new tool ; (b) and (c) after 150 mm cutting distance; (b) is with laser and (c) is without laser (cutting speed: 32 m/min, axial depth of cut: 25 µm, feed: 1 µm/flute, laser power: 7.5 W).

It is evident from Fig. 3.14 that the groove depth accuracy with laser heating is higher over a longer cutting distance than without it. The reduction in groove depth with cutting distance is attributed primarily to end mill wear, albeit the interaction of tool wear, tool deflection and tool-workpiece thermal expansion (in the laser heating case) is complex. Nevertheless, this result clearly illustrates the potential advantage of laser assisted micro milling over conventional micro milling.

3.5 Summary

In this chapter, the design and fabrication of the laser assisted micro milling setup was presented highlighting the unique design which enables the creation of microscale features in hard-to-machine materials. As part of the experimental setup, a new technique for detecting tool-workpiece contact was developed and demonstrated to work with sub-micron accuracy. In addition, initial experiments demonstrated that laser assist helps in improving the accuracy of the machined groove by reducing tool wear. The following chapter presents a detailed experimental investigation of LAMM of A2 tool steel (62 HR_c), to evaluate the effect of laser assist on material removal rates, cutting forces, surface finish, and burr height.

CHAPTER 4

EXPERIMENTAL CHARACTERIZATION OF LASER ASSISTED MICRO MILLING OF METALS

The previous chapter discussed the design and fabrication of the LAMM setup and results of preliminary investigations on the effect of laser assist on micro milling of A2 tool steel. The novel setup enables the creation of three dimensional microscale features in hard materials. The preliminary investigations indicated that using laser assist results in an increase in groove accuracy and leads to a reduction in tool wear. However, the real advantage of laser assist is to enhance micro milling productivity by facilitating an increase in the material removal rates, along with a reduction in cutting forces, when compared to the conventional micro milling process. In addition, this knowledge is essential to understand the economic feasibility of the process. Hence, studying the impact of laser assist on the cutting forces, tool wear, machined feature accuracy, surface finish and burr formation is essential to select/optimize process conditions to achieve the desired improvement in the process response. With this objective, this chapter presents a detailed experimental investigation of the laser assisted micro milling process for creating micro features in hard metals. Specifically, a comparison of the material removal rates in LAMM versus conventional micro milling of hardened A2 tool steel (62 HR_c) is presented along with the resulting tool wear behavior. The effect of laser assist on other process responses such as the resultant cutting force, burr height, surface finish, and the thermally affected zone induced by laser heating is presented.

4.1 Experiments

4.1.1 Experimental Conditions

The workpiece material used in the study was A2 tool steel (62 HR_c, 0.595 μm R_a) with the nominal composition listed in Table 4.1. Two-flute 180 μm diameter, TiAlN coated tungsten carbide square end mills (SECO® JM905) were used in the most of the experiments. A few tests with two-flute, 400 μm diameter, TiAlN coated tungsten carbide tools were also performed for reasons discussed later in the chapter. All cutting tests were performed dry.

Table 4.1: Nominal chemical composition of A2 tool steel.

Element	C	Mn	Si	Cr	Ni	Mo	V	Cu
Weight %	0.95-1.05	1.00	0.5	4.75-5.5	0.3	0.9-1.4	0.15-0.5	0.25

The micro slotting tests with and without laser assist, summarized in Table 4.2, were carried out. Each test consisted of eight 25.4 mm long grooves spaced 0.5 mm apart for a total length of cut of 203.2 mm. Note that although longer duration LAMM tests could have been carried out, they were found to be unnecessary since clear advantages of the LAMM process became evident in the first 203.2 mm length of cut. The spindle speed was fixed at 50,000 rpm in all tests. The baseline test utilized the tool manufacturer's recommended feed (2.2 μm) and axial depth of cut (16 μm) for the material hardness used in the study. Two additional tests at a much higher feed rate and axial depth of cut were performed to demonstrate the possible increase in material removal rate with laser assist. Note that tests 3 and 3-L, which represent the maximum material removal rate condition, were replicated twice to confirm repeatability of the test results.

In addition, extended length machining tests were performed for Exp 3-L till the tool failed catastrophically. This was done to assess the impact of laser assist on tool life. The results of these tests are presented in section 4.2.7. For these extended tests, only the groove profile is measured, which indirectly corresponds to the wear of the micro tool.

Table 4.2: Experimental conditions.

Experiment	Axial depth of cut (μm)	Feed rate (μm/flute)	Laser assist (Y/N)
1	16	2.2	**N**
1-L	16	2.2	**Y**
2	32	2.2	**N**
2-L	32	2.2	**Y**
3	32	6.6	**N**
3-L	32	6.6	**Y**

4.1.2 Selection of Laser Parameters

The selection of laser power was governed by the intended temperature rise in the material removal surface to produce the desired reduction in material flow strength. The target temperature was set to 450-500°C because the carbide tool starts to oxidize above this temperature [11]. For determining the laser and process parameters needed to produce the desired temperature rise, a thermal model is necessary. Since, the LAMM process involves a moving laser heat source relative to the workpiece, Jaeger's [105] moving heat source model was used to determine the temperature rise in the material removal surface.

For continuous wave laser heating, standard macroscale heat conduction models are applicable at the microscale. Only in the case of ultrafast pulsed lasers (pulse duration

~10^{-15} sec) , the response time of heat transport in metals is of the order of 10^{-12} seconds, which necessitates the use of more advanced microscale heat transfer models that take this effect into consideration. In case of ultra fast laser interaction with metals, the free electrons in the metal gain energy quickly to arrive at an excited state whereas the crystalline lattice remains at room temperature. After a time lapse, specified as the electron relaxation time, the energy is transferred to the crystalline structure resulting in temperature rise [106].

The temperature distribution in the material removal surface was determined from the analytical model of a moving point heat source over a semi-infinite medium as given by Eq. 4.1 [105]:

$$T(x,y,z) = \alpha \int\int \frac{q(x',y')}{2\pi K s} e^{\frac{-U}{2\kappa}(s-(x-x'))} dx'\,dy', \qquad s = \sqrt{(x-x')^2 + (y-y')^2 + (z)^2}. \tag{4.1}$$

Where, α is the absorptivity, q is the heat intensity (W/m^2), K is the thermal conductivity (W/m-K), κ *is* the thermal diffusivity (m^2/s), and U is the velocity of the heat source (m/s). The temperature dependence of thermal conductivity and specific heat for A2 tool steel was modeled as a linear function of temperature as follows [107]:

$$K = 26.4 + 0.0011T \qquad C = 394 + 0.332T \tag{4.2}$$

Note that the temperature dependence of thermal conductivity necessitates an iterative method for the solution of Eq. 4.1. The analytical equation given by Eq. 4.1 was solved numerically using Simpson's rule at each point in the workpiece material in order to calculate the temperature rise due to the incident laser beam. The effect of laser

irradiation was modeled as a 280 µm diameter Gaussian heat source, the heat intensity distribution of which is represented as follows [15]:

$$q(x, y) = q_0 \exp(x^2 + y^2) \tag{4.3}$$

where q_0 is the heat intensity at the center at the center of the beam.

Figure 4.1(a) shows the relative position of the cutting tool with respect to the laser beam. The workpiece is translating in the (-)X direction and the line AB indicates the depth of the material removal surface. Since, the laser beam is Gaussian, the maximum temperature rise will be along the line A-B. Figure 4.1 (b) shows the top view of the tool with one of the cutting edges shown in the figure. The tangential and radial forces acting on the workpiece are denoted by F_t and F_r, respectively. As seen from the figure, the instantaneous uncut chip thickness 't' changes from '0' to a maximum value 'f_t' over 90º of rotation, which indicates that the cutting forces are maximum at this location. Hence, the temperature rise due to laser assist needs to be maximum at this location in order to reduce the peak forces during the cutting process.

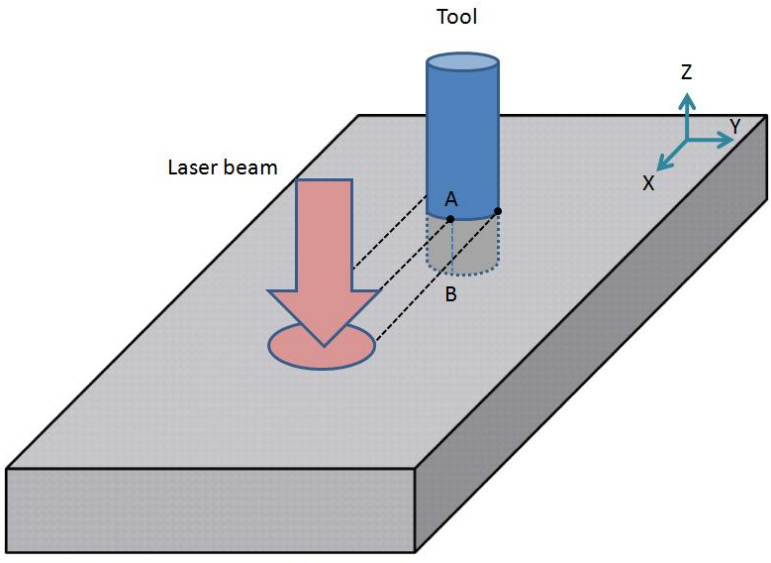

(a)

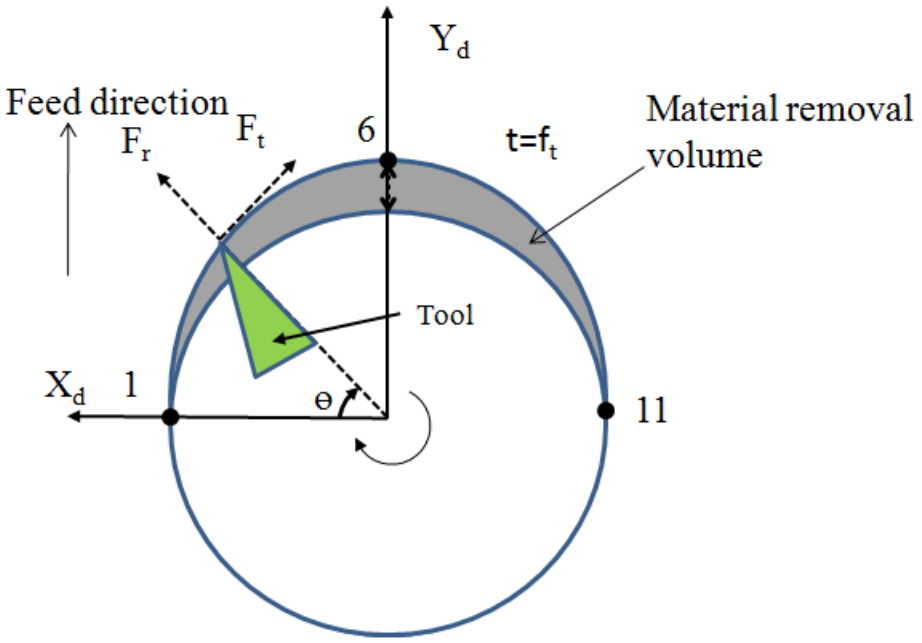

(b)

Figure 4.1: (a) Position of the tool with respect to the laser beam (A-B represents the depth along which the temperature is predicted), **(b)** Top view of the actual path of the cutting tool indicating the cutting forces acting on the workpiece. Temperature rise is predicted at points 1 through 11 along the tool periphery and suffix 'd' refers to the dynamometer coordinate system.

In the experiments, the tool feed rate was varied from 220 mm/min to 660 mm/min, corresponding to tool feeds of 2.2 µm/flute and 6.6 µm/flute, respectively. The distance between the center of the laser spot and the center of the tool was fixed at ~270 µm. The absorptivity of the laser beam was indirectly measured to be ~0.6 for this material using the calibration approach reported in literature [108, 109]. This value compares well with the absorptivity values measured for similar metals [13]. The

calculated average temperature rise along A-B in the material removal surface (see Fig. 4.1) for the laser scanning conditions listed in the figure, and for different laser scan speeds, is shown in Fig. 4.2. It can be seen from the figure that the effect of scan speed on the temperature rise along A-B is found to be insignificant for the range of scan speeds investigated. Therefore, the laser power and spot size were fixed at 18 W and 280 µm, respectively, for all experiments.

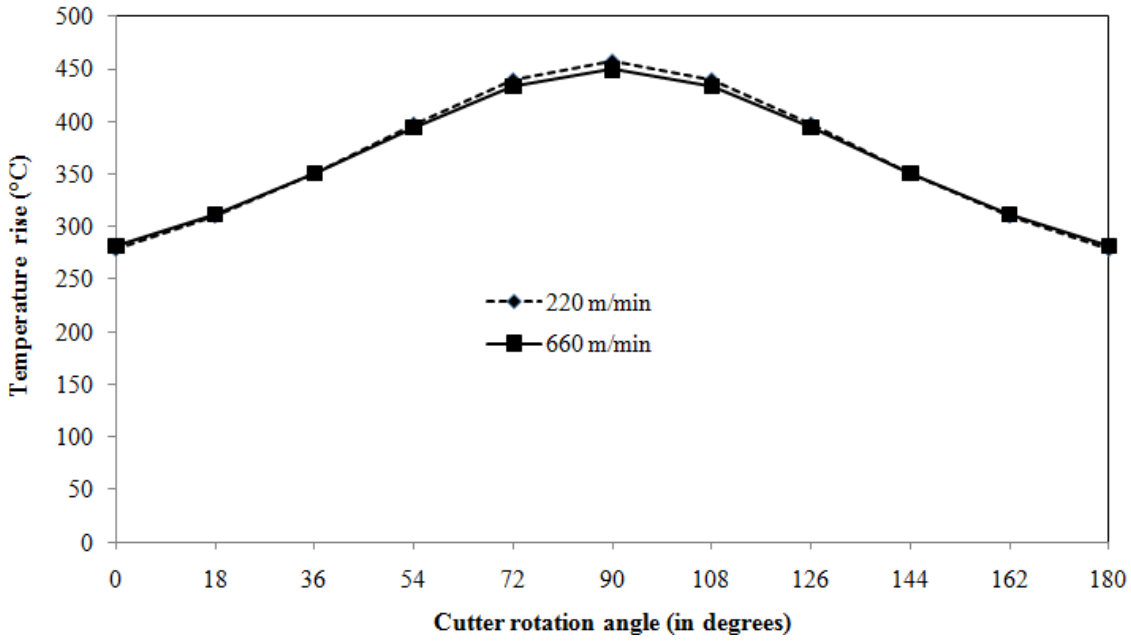

Figure 4.2: Calculated temperature rise along A-B (32 µm) in the material removal surface at points along the periphery of the tool shown in Fig. 4.1 (b) (laser power: 18 W, spot size: 280 µm).

Depending on the softening characteristics of the workpiece material, the laser power, spot size, scanning speed and the cutting tool-laser beam distance have to selected/optimized to obtain the desired temperature rise in the material removal surface.

4.1.3 Measured Responses

The measured responses include the cutting forces, tool wear, machined groove geometry, burr height, and surface roughness, all as a function of the cutting distance. The cutting forces along the X and the Y directions were measured using a 3-axis piezoelectric platform dynamometer (Kistler Minidyn 9256C2). Note that the natural frequency of the dynamometer is 4.8 kHz, which is higher than the maximum tooth passing frequency of 1.66 kHz, and therefore the effect of the measuring instrument dynamics on the force measurements is considered to be negligible. This was also confirmed from the power spectrum plot, which shows that most of the power is concentrated at the spindle rotational frequency and the tooth passing frequency. Tool wear was characterized optically using the Keyence VHX digital microscope after every 50.8 mm of cutting distance and was quantified by the change in the tool corner radius (shown in Fig. 4.3).

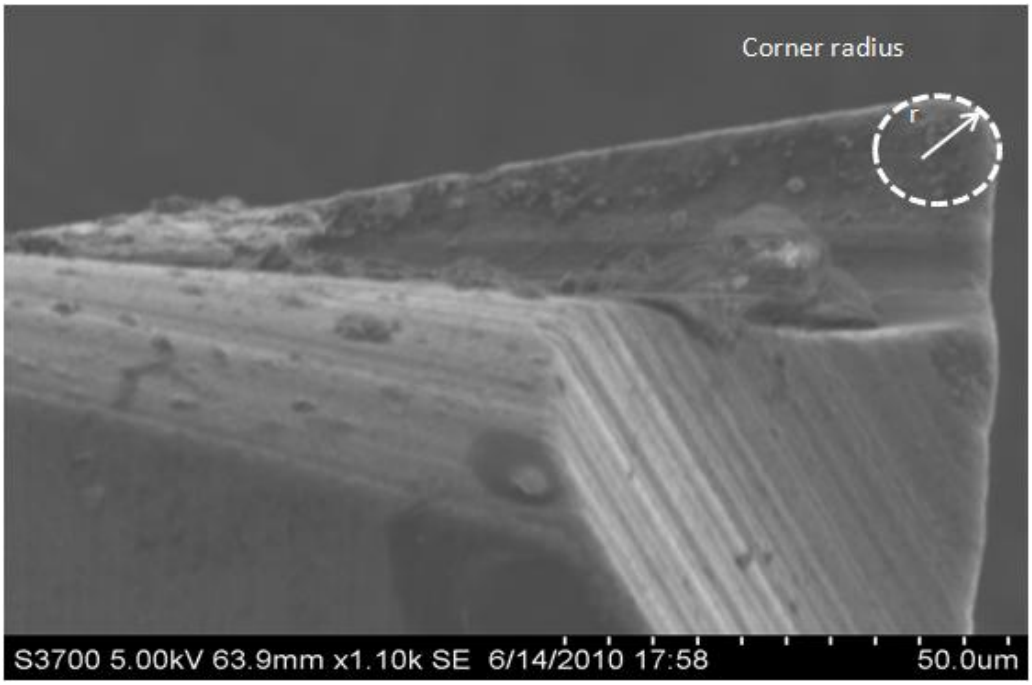

Figure 4.3: SEM Micrograph showing the corner radius of the micro milling tool.

The change in geometry of the machined groove with cutting distance (primarily due to tool wear) was measured using a confocal laser scanning microscope (Olympus LEXT). The burr height was determined from the measured groove geometry and represents the average of ten measurements for each groove. The three dimensional surface roughness height (S_a) was measured over an area of 270 x 70 μm^2 and is also reported in this chapter. The following section discusses the findings of this experimental study in detail.

4.2 Results and Discussion

4.2.1 Cutting Forces

Changes in the maximum resultant force per tool revolution with groove number (or cutting distance) are shown in Figs. 4.4(a) and 4.4(b). .The resultant cutting force at each time instant was calculated as,

$$R = \sqrt{F_x^2 + F_y^2 + F_z^2} \tag{4.4}$$

The average of the 100 maximum peaks over a cutting distance of 25.4 mm is reported as the maximum resultant force. For all cases without laser assist, the resultant force increases with increasing groove number/cutting distance mainly because of tool wear. Tool wear is discussed in detail in section 4.2.2. In contrast, no significant increase in the resultant force with cutting distance is observed in the tests carried out with laser assist. In addition, the resultant force magnitudes with laser assist are much lower than the corresponding cases without laser assist, especially in the higher feed and depth of cut tests. Specifically, it can be seen in Fig. 4.4(a) that, with the exception of Exp 1, the more aggressive non-laser assist tests (Exp 2 and 3) result in rapid increase in the resultant force, with Exp 3 resulting in early catastrophic failure of the tool. The tools can be analyzed for defects to further understand its role in tool failure. Repeatability of the results for the most aggressive test cases (Exp 3 and 3-L) are shown in Fig. 4.4(b).

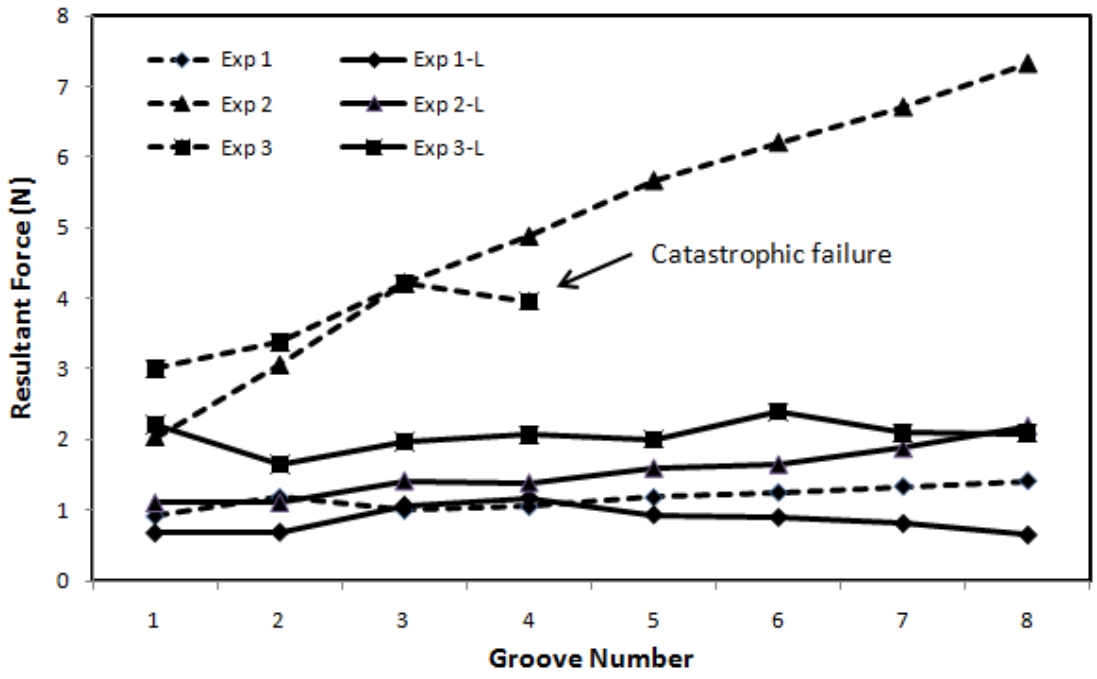

Figure 4.4(a): Changes in the maximum resultant force (averaged over each groove) with groove number for tests listed in Table 4.2.

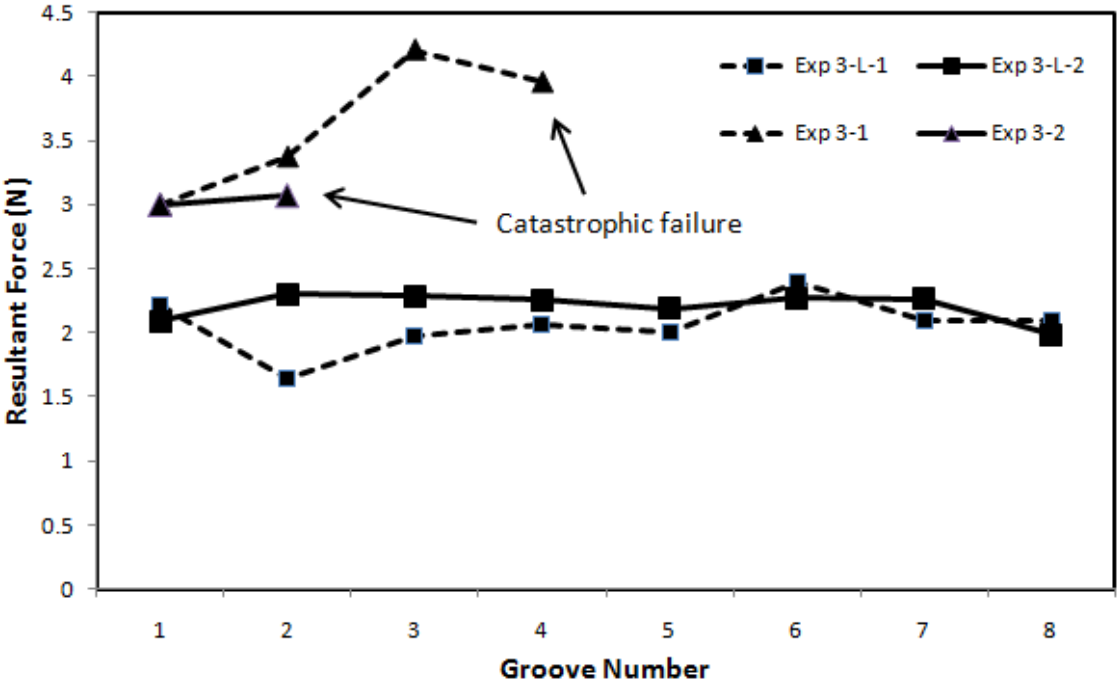

Figure 4.4(b): Changes in maximum resultant force (averaged over each groove) with groove number (extensions '1' and '2' in the legend indicate test repetitions).

It can be seen from Table 4.3 that the average % reduction in the resultant force due to laser assist is higher for Exp 2-L and Exp 3-L than Exp 1-L. The higher % reduction in Exp 2-L is due to the fact that the resultant force in Exp 2 (no laser assist) is much greater because of tool wear, as shown later in section 4.2.2.

Table 4.3: Reduction in the maximum resultant force averaged over all the machined grooves.

Experiment	**Average % reduction in the resultant force**
1-L	26
2-L	69
3-L	43

The variation in specific cutting energy (averaged over each groove) with groove number is shown in Fig. 6. The specific cutting energy for each groove was calculated by dividing the peak resultant force by the product of the tool feed and the *measured* axial depth of cut. It can be seen that the specific cutting energy with laser assist is lower than the corresponding value obtained without laser assist. In addition, for all cases without laser assist, the specific cutting energy increases with groove number whereas the increase is significantly less for the laser assisted cases. The observed increase in the specific cutting energy for the non-laser assist cases is attributed to increased tool wear as shown later in the chapter. Also, note that the specific cutting energy is lowest for tests with the highest feed of 6.6 μm/flute for both with and without laser assist cases. This is consistent with the well-known size effect in machining.

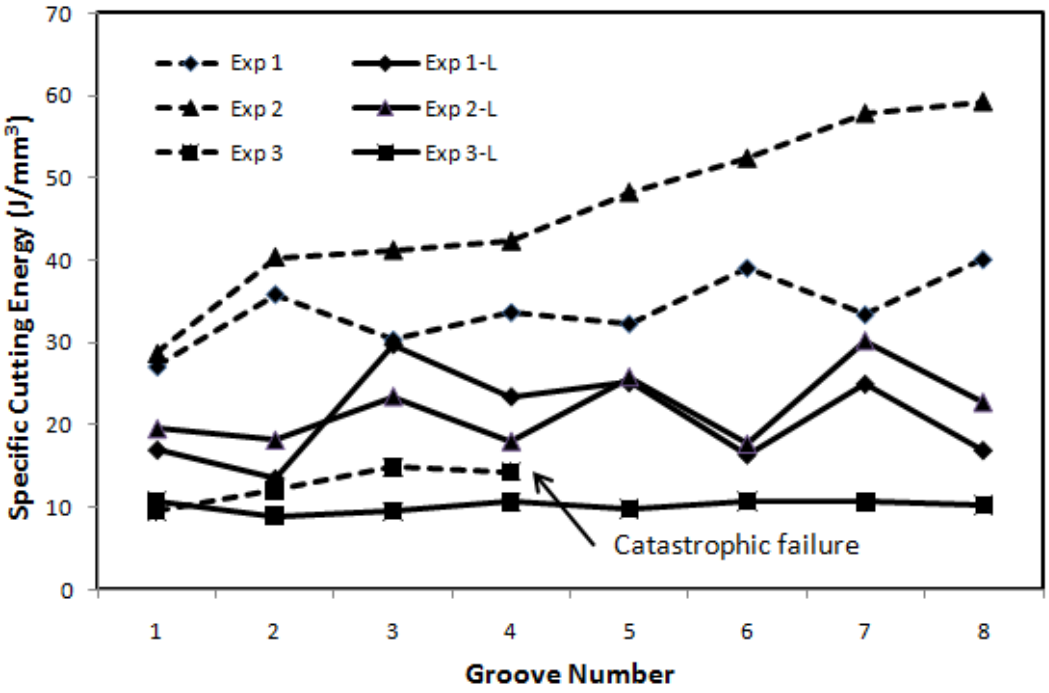

Figure 4.5: Variation in the average specific cutting energy with groove number.

As seen in Figs. 4.4 and 4.5, tool life in the conventional micro milling process is limited by catastrophic tool failure at the highest feed rate and axial depth of cut. On the other hand, the corresponding LAMM tests show negligible increase in the resultant force or the specific cutting energy. It is precisely under such conditions that the LAMM process becomes a viable alternative to conventional micro milling. Specifically, the LAMM test at 6.6 µm/flute and 32 µm axial depth of cut represents a six fold increase in material removal rate (11.9 mm^3/min) over the tool manufacturer recommended cutting conditions (1.99 mm^3/min).

4.2.2 Tool Wear

The change in corner radius of the micro tool as a function of the cutting distance is shown in Fig. 4.6. The increase in corner radius for the LAMM tests is found to be much smaller than the corresponding non-laser assist cases. For instance, the corner radius in Exp. 2-L increases from 1.8 µm to 6 µm and from 1.8 µm to 34.2 µm in Exp 2. The change in corner radius is very gradual for all cases with laser assist while the only non-laser assist case exhibiting a similar trend is Exp. 1. For the remaining two cases (Exp 2 and 3), severe tool chipping and breakage is observed, thereby preventing a comparison over the entire cutting distance of 203.2 mm.

The SEM images of the tool before and after cutting under different conditions are shown in Figs. 4.7 through 4.12. Figure 4.7 clearly indicates rounding of the tool corner due to abrasive wear in Exp 1. This is the only non-laser assist case where gradual wear of the tool was observed.

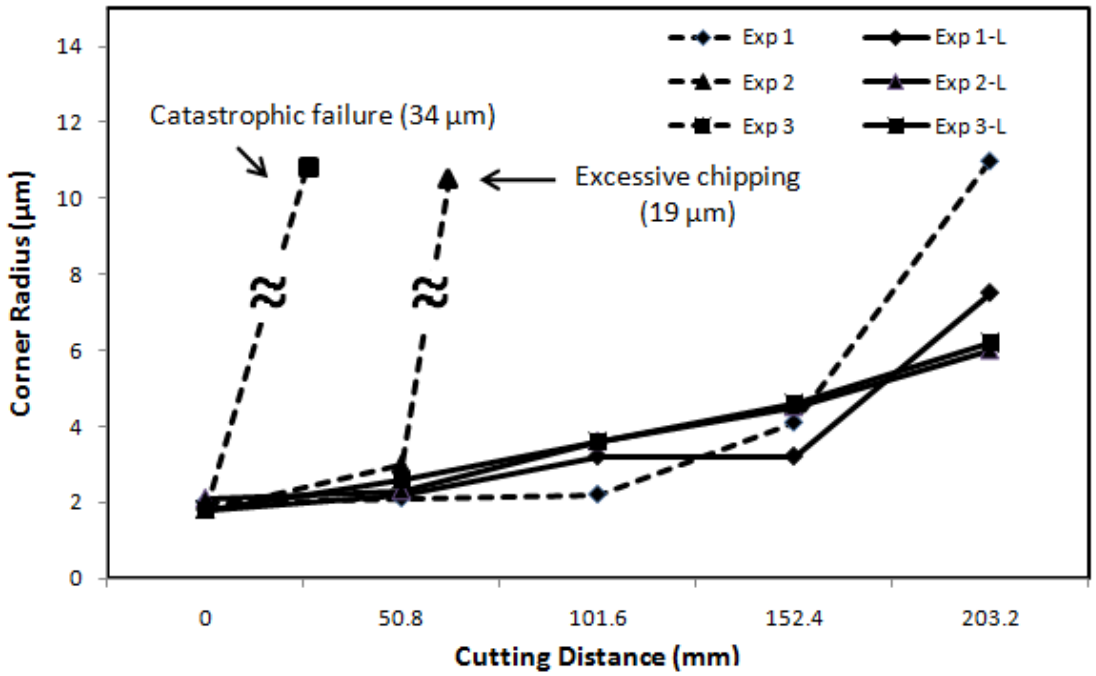

Figure 4.6: Change in tool corner radius with cutting distance.

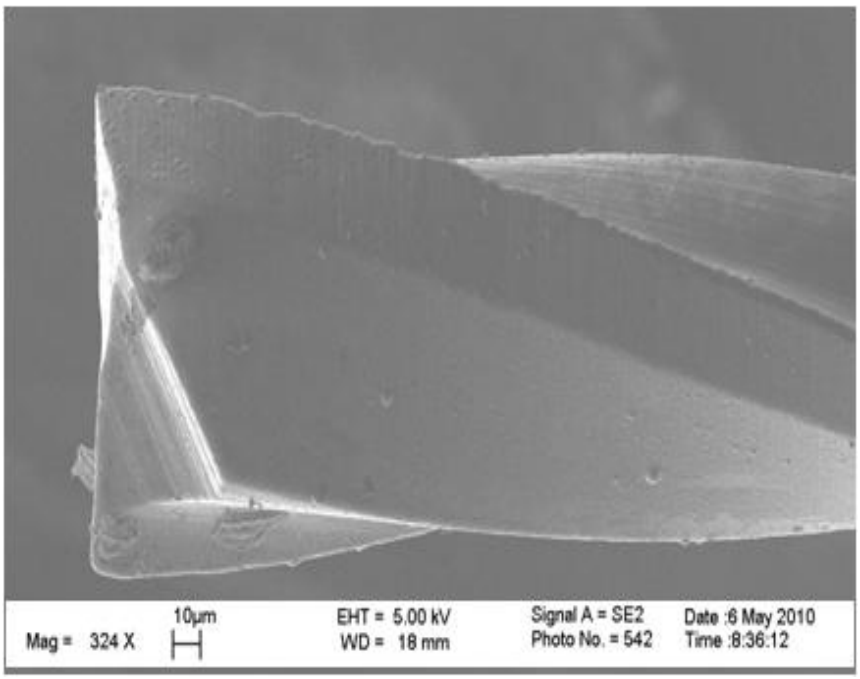

Before cutting

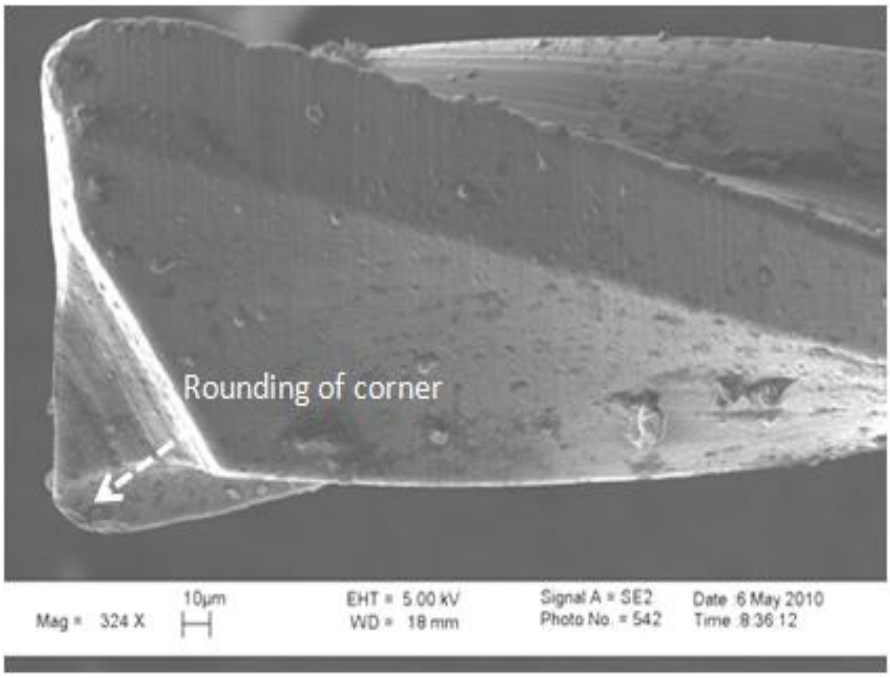

After cutting 203.2 mm

Figure 4.7: SEM micrographs of tool before (top) and after cutting (bottom) (feed: 2.2 µm/flute, axial depth: 16 µm, no laser assist).

The SEM micrograph in Fig. 4.8 shows rounding of the corner after 203.2 mm of LAMM (Exp 1-L). Small amounts of softened work material are found to be adhering to the tool. For identical cutting conditions, the tool wear with laser assist is less than the non-laser assist case (see Fig. 4.7). Also, as seen in Fig. 4.6, the tool corner radius at the end of cut is highest among all the LAMM tests.

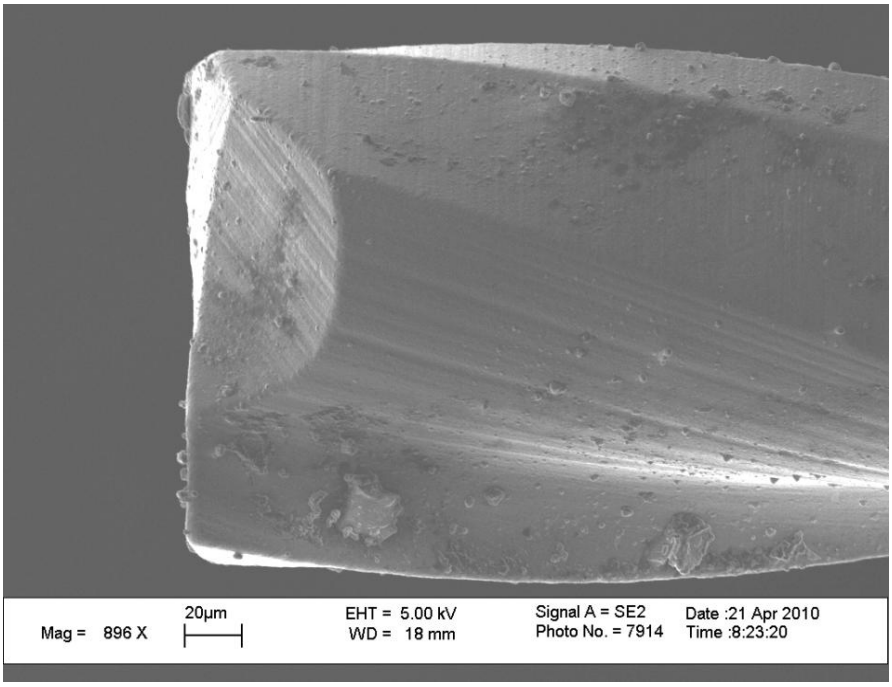

Before cutting

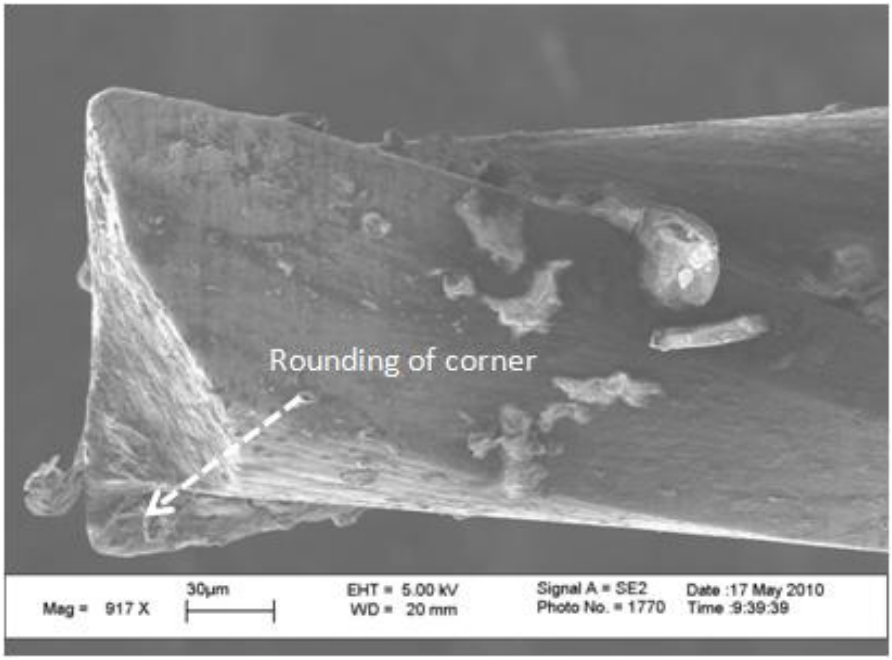

After cutting 203.2 mm

Figure 4.8: SEM micrographs of the tool before (top) and after machining (bottom) (feed: 2.2 µm/flute, axial depth: 16 µm, with laser assist).

Figure 4.9 clearly shows significant evidence of tool wear. In addition to gradual abrasive wear, some chipping due to micro fracture (see inset) is also observed. Note that the feed for this test is 2.2 µm/flute but the axial depth of cut is twice that in Exp 1. This suggests that the tool performs poorly at higher than the recommended axial depth of cut and feed rate. Contrary to expectations, laser heating has a beneficial effect on tool wear as seen in Fig. 4.10 compared to Fig. 4.9. Under these conditions, tool wear is less, even though adhesion of work material to the tool surfaces is observed.

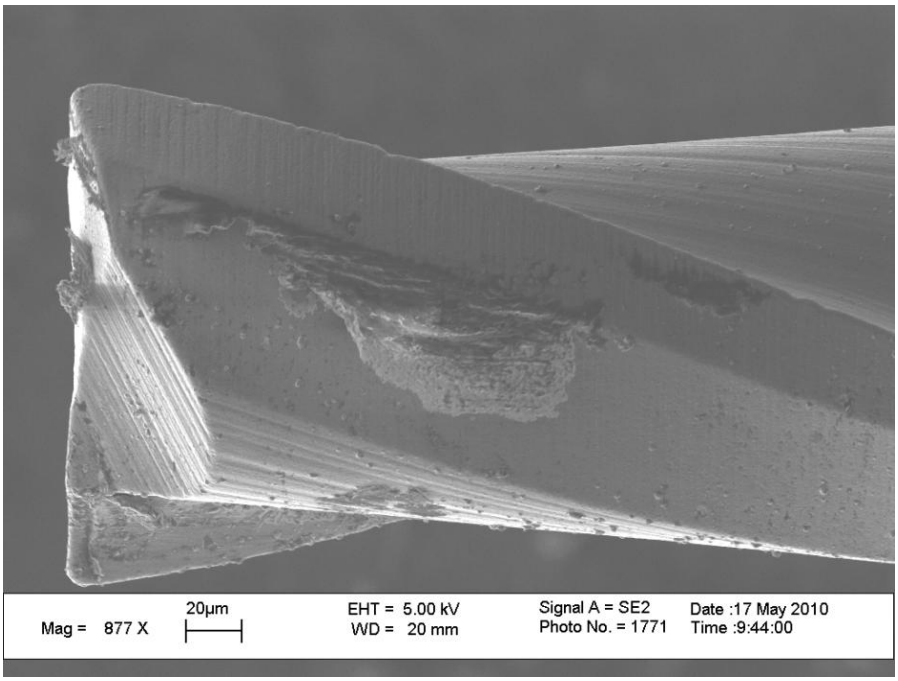

Before cutting

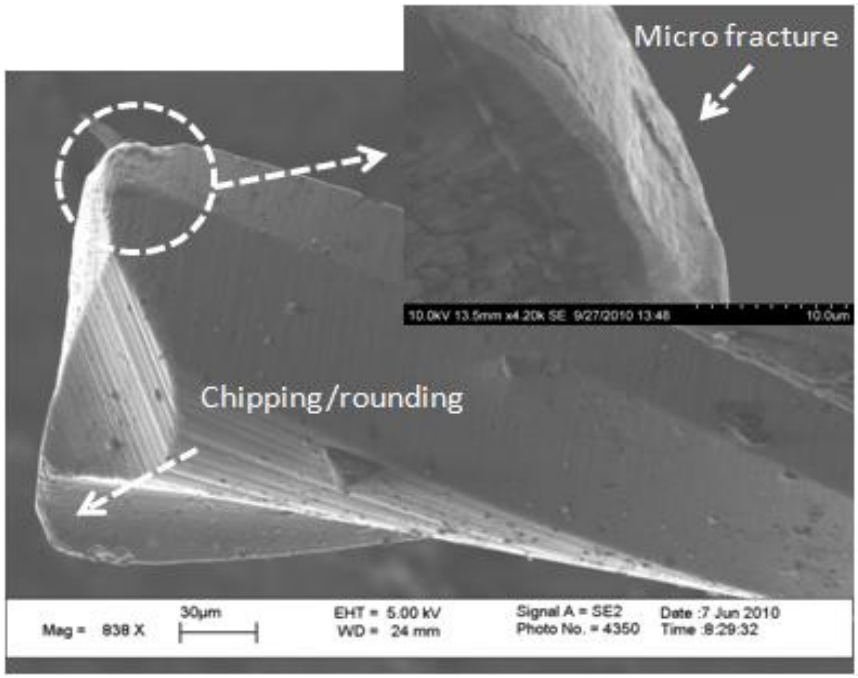

After cutting 101.6 mm

Figure 4.9: SEM micrographs of the tool before (top) and after cutting (bottom) (feed: 2.2 µm/flute, axial depth: 32 µm, no laser assist).

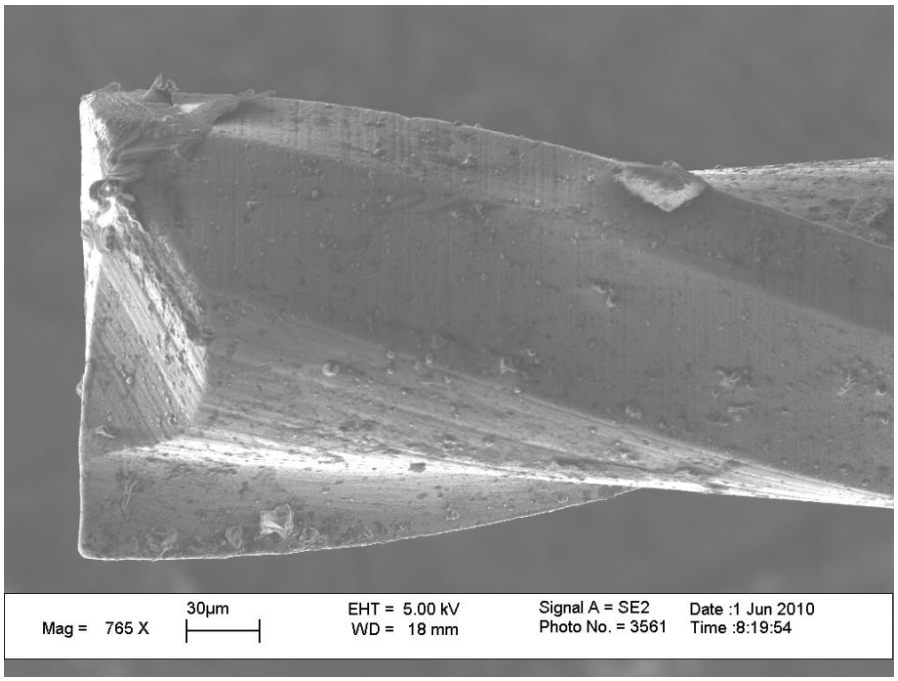

Before cutting

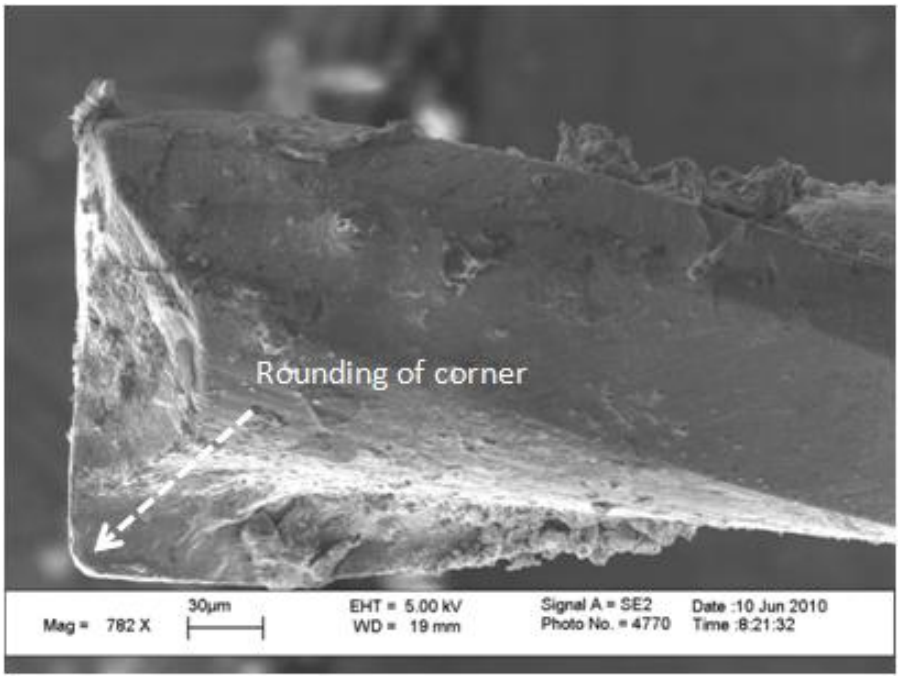

After cutting 203.2 mm

Figure 4.10: SEM micrographs of the tool before (top) and after cutting (bottom) (feed: 2.2 µm/flute, axial depth: 32 µm, with laser assist).

The SEM micrograph in Fig. 4.11 shows substantial rounding of the tool corner after just 50.8 mm length of cut, indicating rapid wear. The tool shattered after 76.2 mm length of cut due to excessive cutting forces. Under the cutting conditions noted in the figure (feed rate: 6.6 µm/flute, depth of cut: 32 µm), LAMM yields superior tool wear results as seen in Fig. 4.12. This is due to less rubbing and more cutting at the highest tool feed rate compared to the 2.2 µm/flute case. This is the best case among all experiments conducted.

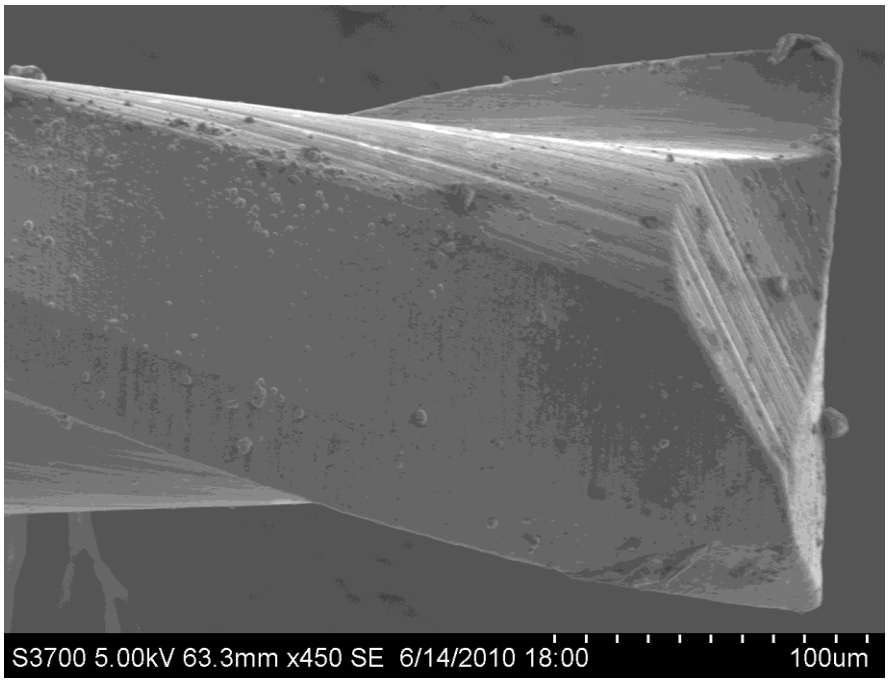

Before cutting

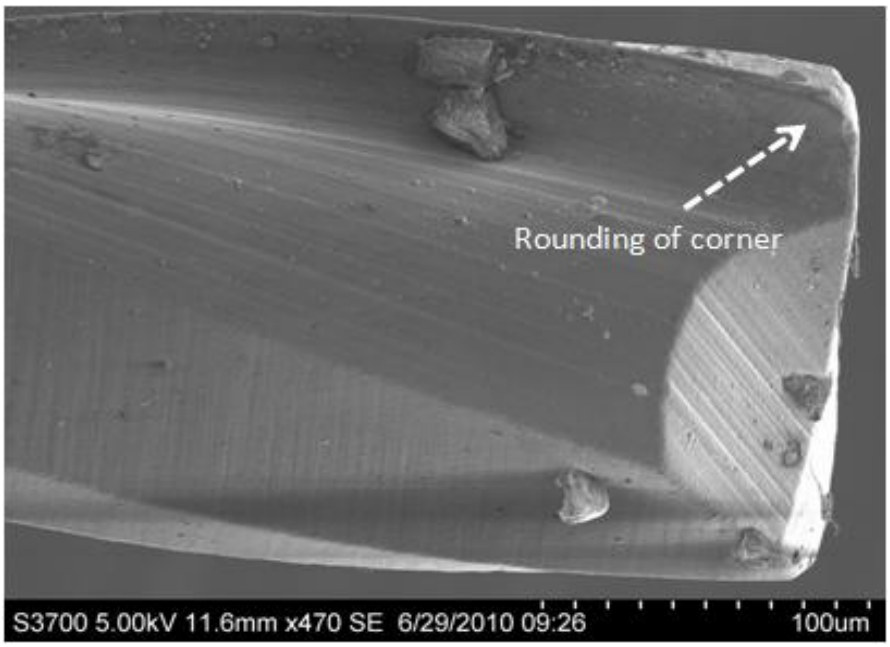

After cutting 50.8 mm

Figure 4.11: SEM micrographs of the tool before (top) and after cutting (bottom) (feed: 6.6 µm/flute, axial depth: 32 µm, no laser assist).

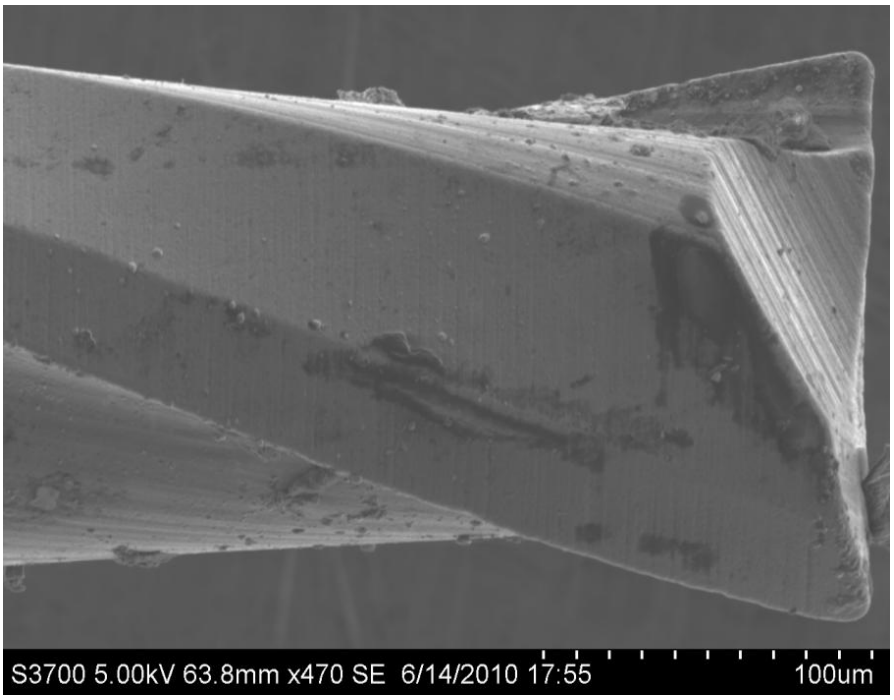

Before cutting

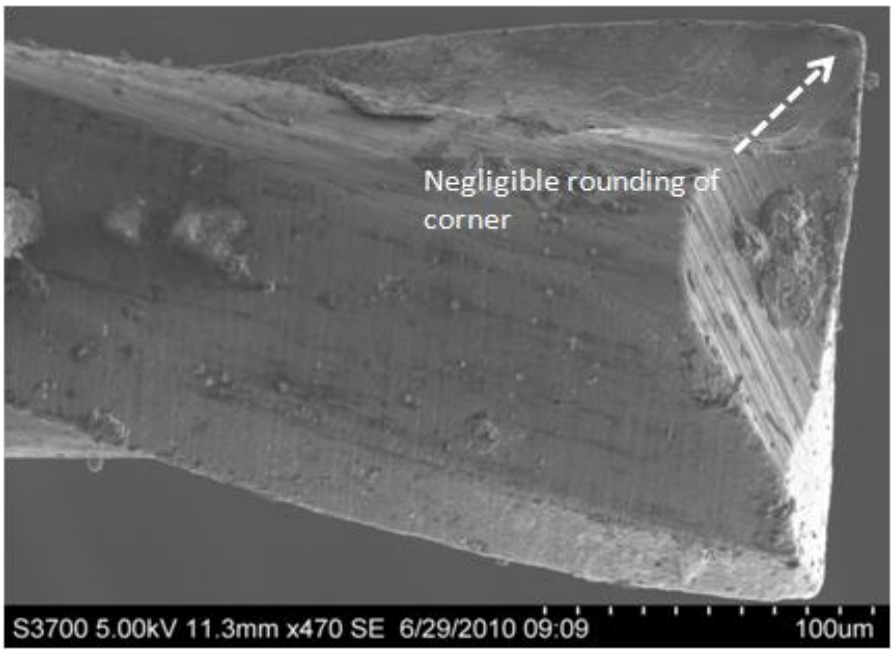

After cutting 203.2 mm

Figure 4.12: SEM micrographs of the tool before (top) and after cutting (bottom) (feed: 6.6 µm/flute, axial depth: 32 µm, with laser).

In addition to the change in corner radius, the change in cutting edge radius was measured for two representative test cases (Exp 3 and 3-L) at a location 15 µm away from the end face of the tool towards the tool shank and is shown in Fig. 4.13. While the tool in the non-laser assist test failed catastrophically after 50.8 mm of cutting, it can be seen that the edge radius in the laser assist case increases with cutting distance and is quite large. This implies that higher tool feed rates should be used to minimize the impact of tool edge radius on ploughing of the material. However, the maximum feed rate is limited by the tool strength.

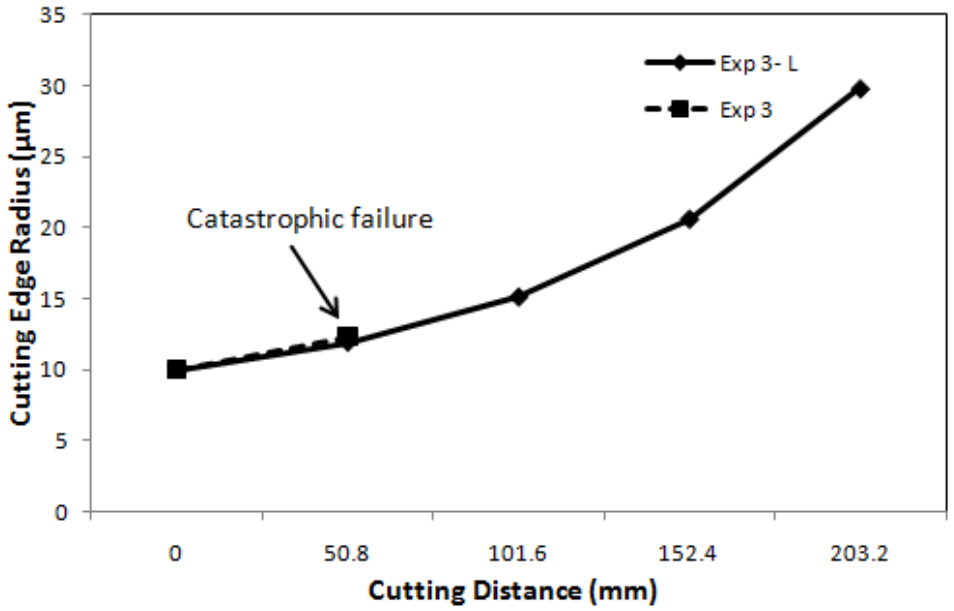

Figure 4.13: Change in cutting edge radius with cutting distance (feed: 6.6 µm/flute, axial depth: 32 µm, with laser assist).

4.2.3 Groove Geometry

The groove cross-sectional geometries at the start and end of the cut for the different test cases are shown in Figs. 4.14 through 4.16. In every case, the groove profile matches the tool profile shown in the previous section. Figures 4.14(a) and (b) compare the groove profiles with and without laser assist after 5 mm and 203.2 mm of cutting, respectively. In the absence of laser heating the groove profile changes significantly due to rapid tool wear. The profile in Fig. 4.14(a) clearly indicates an increase in the tool corner radius. It can be also discerned that the axial depth of cut is higher than the set depth of cut for all cases with laser assist. This effect is attributed to tool and workpiece thermal expansion, which effectively results in a higher depth of cut. Since the actual depth of cut is higher than the set depth of cut, the actual improvement in the material removal rate with laser

assist is more than six times the recommended cutting conditions suggested by the tool manufacturer.

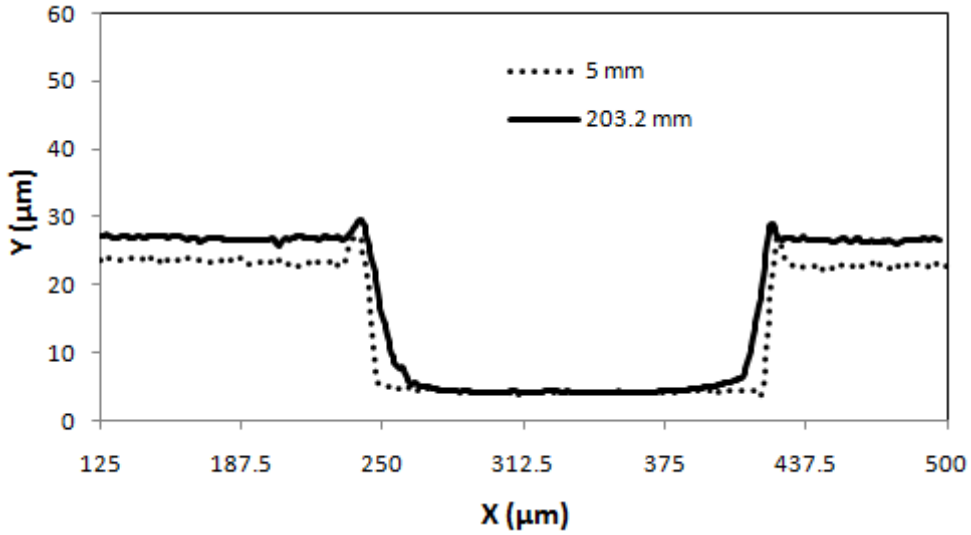

(a) Without laser assist

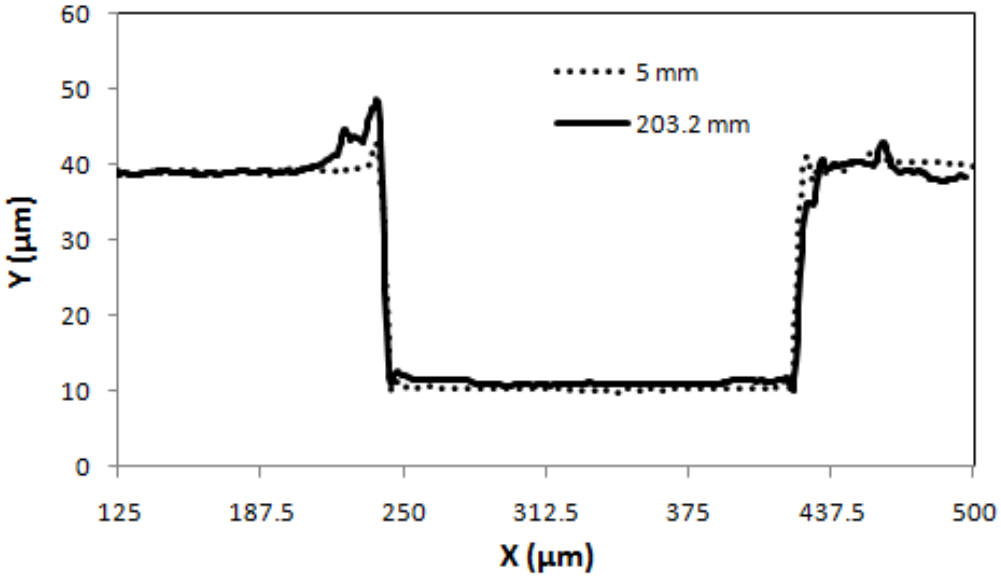

(b) With laser assist

Figure 4.14: Groove cross section at the start (5 mm) and end (203.2 mm) of cut (feed: 2.2 µm/flute, axial depth: 16 µm).

Figures 4.15(a) and (b) compare the groove profiles with and without laser assist. Figure 4.15(a) clearly shows that the impact of tool wear is significant and results in increased ploughing of the work material, as seen from the larger burrs at the groove sides. In contrast, in LAMM, the change in groove profile with cutting distance is minimal, indicating reduced tool wear and improved groove dimensional accuracy.

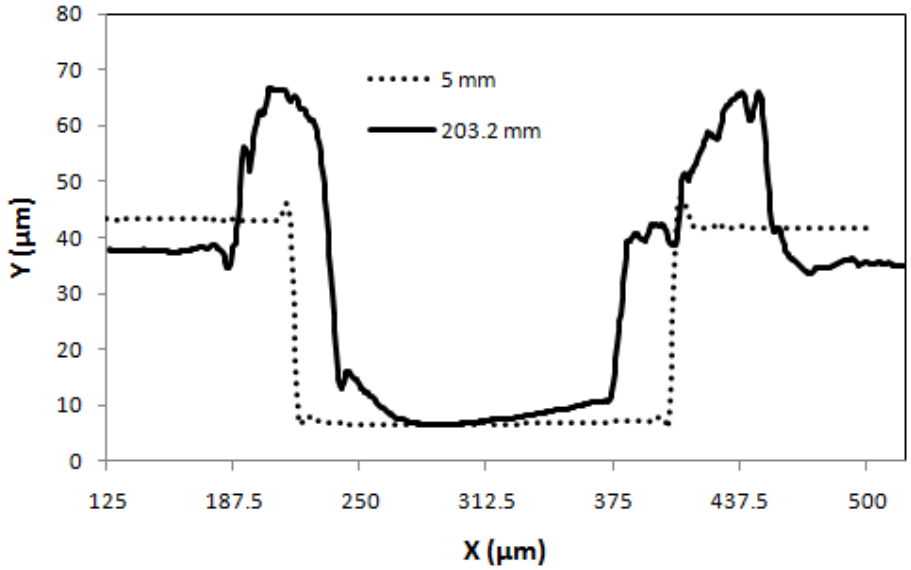

(a) Without laser assist

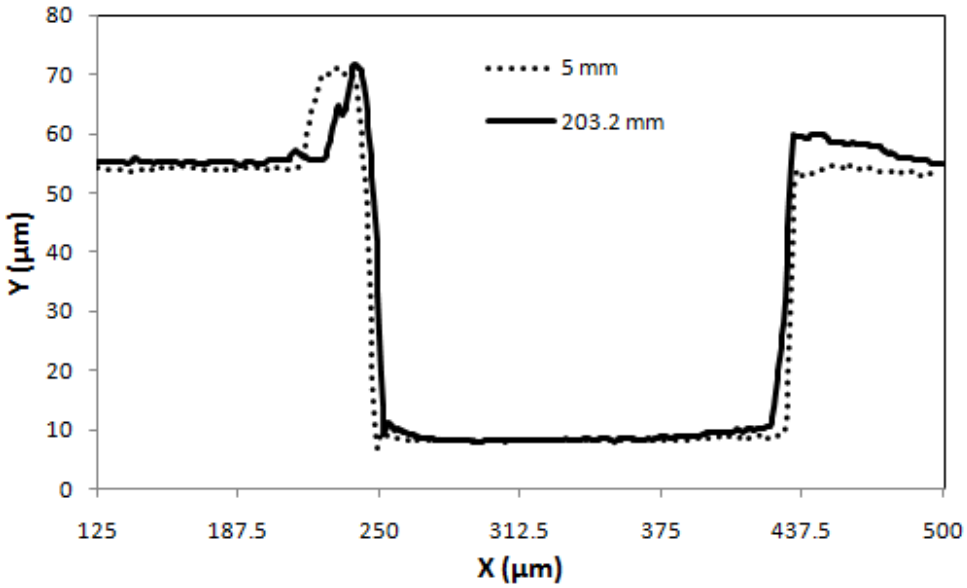

(b) With laser assist

Figure 4.15: Groove cross section at the start (5 mm) and end (203.2 mm) of cut (feed: 2.2 µm/flute, depth of cut: 32 µm).

Figure 4.16 shows the groove profile after 76.2 mm length of cut, at which point the tool broke catastrophically. The figure indicates rapid tool wear progression at a feed of 6.6 µm/flute and axial depth of 32 µm. Even after a cutting distance of 203.2 mm, the change in groove shape (especially the depth) is small indicating the potential of the LAMM process to extend tool life while providing significantly higher material removal rates and improve accuracy of the feature.

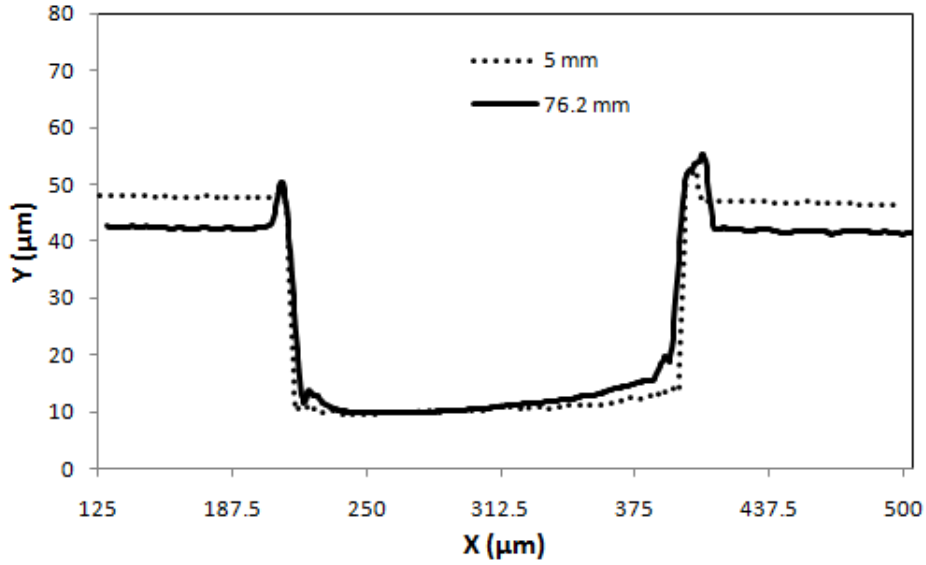

(a) Without laser assist

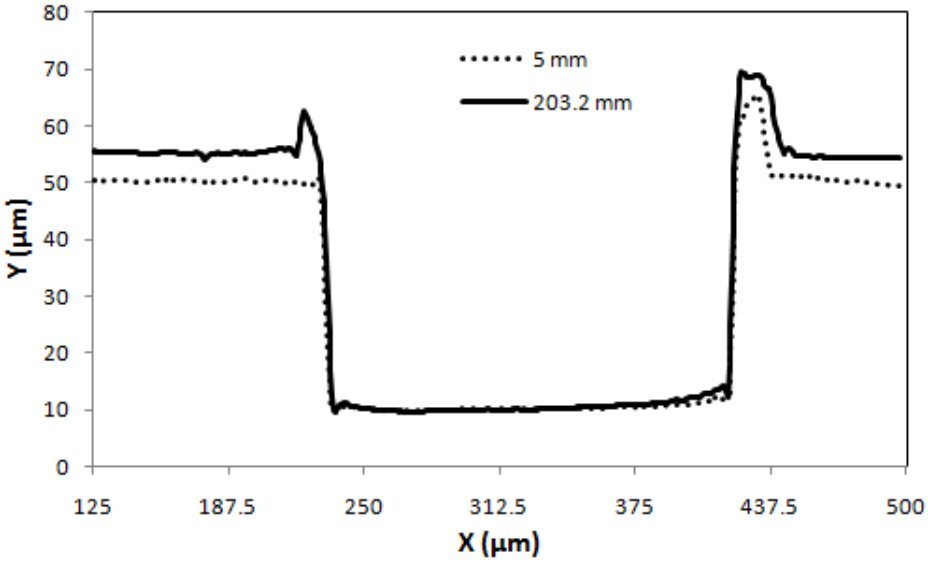

(b) With laser assist

Figure 4.16: Groove cross section at the start and end of cut (feed: 6.6 µm/flute, axial depth: 32 µm).

4.2.4 Burr Height

The average burr heights with cutting distance are shown in Fig. 4.17. It can be seen that, in general, the burr heights in the presence of laser assist are larger than without laser assist. Specifically, the average burr height increases from 5.25 µm in Exp 1 to 10.68 µm in 1-L. This increase is attributed to the higher ductility of the softened workpiece material, which tends to be pushed out at the groove edges due to the very small ratio of uncut chip thickness to tool edge radius in the groove entrance and exit regions. These burrs have to be removed subsequently using finishing processes. The burr height at the end of cut (203.2 mm) in Exp 2 is the highest because of excessive tool wear (see Fig. 4.9). Excessive tool wear and edge chipping, as seen in Fig. 4.9, increases the ploughing of the tool into the work material, resulting in higher burrs.

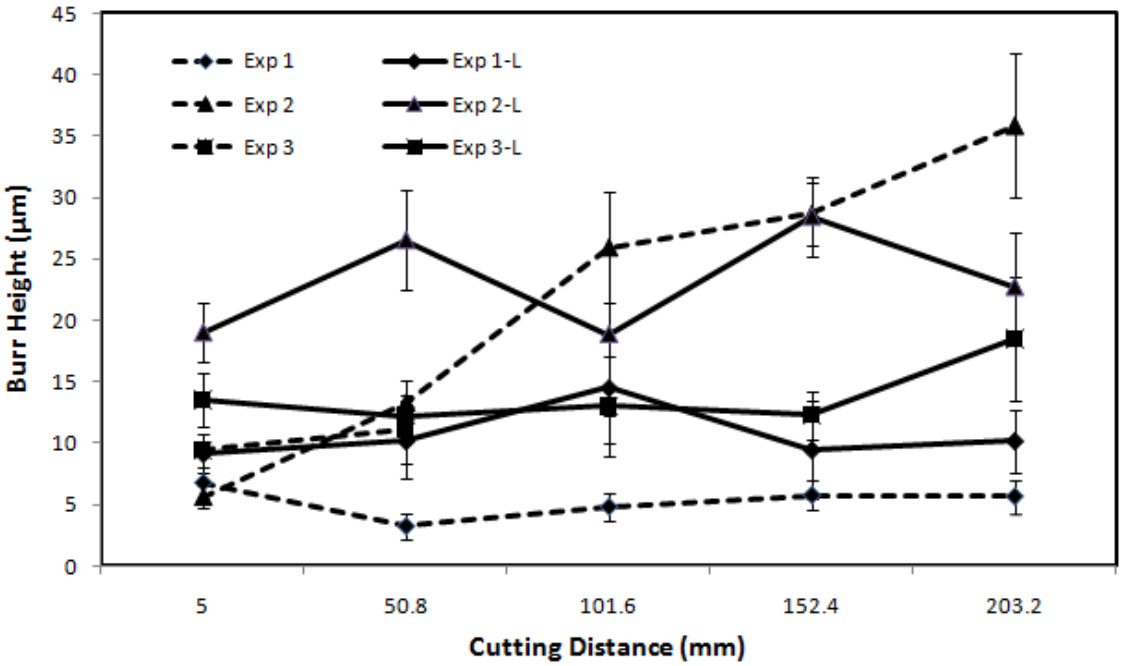

Figure 4.17: Burr height versus cutting distance (error bars represent ± 1σ variation).

4.2.5 Surface Roughness

The variation in groove floor surface roughness with cutting distance is shown in Fig. 4.18. The roughness is seen to generally decrease with cutting distance in both the laser assist and non-laser assist cases due to the burnishing action of the rounded tool corner. The graph also shows that the surface roughness obtained with laser assist is higher than the corresponding non-laser assist case. This is consistent with the results for laser assisted micro grooving reported earlier by Singh et al. [4]. The increase in surface roughness with laser assist is attributed to the higher ductility of the material due to thermal softening.

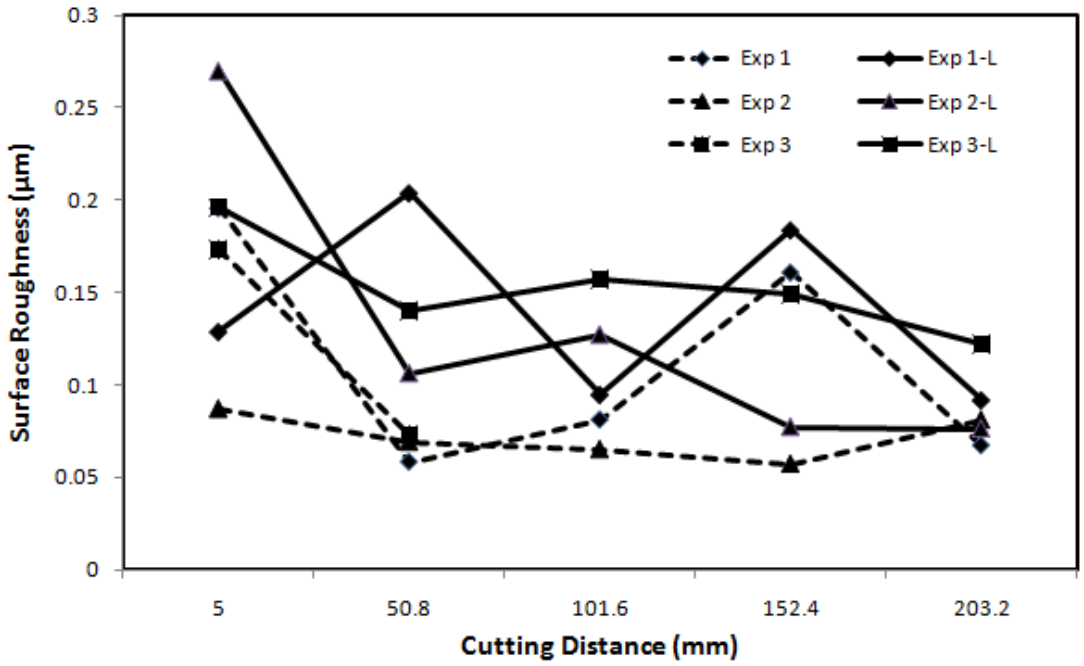

Figure 4.18: Variation of surface roughness (S_a) of the groove floor with cutting distance.

4.2.6 Thermally Affected Zone

The size of the thermally affected zone produced by the laser spot size used in the previous experiments is shown in Fig. 4.19. It should be noted that the thermally affected region is not removed entirely by the tool in Exp 1-L, 2-L and 3-L. This is because the width of the thermally affected zone (phase transformed region) is wider than the tool diameter. However, if a larger diameter tool is used, the entire thermally affected region can be removed. Figure 4.20 shows a metallurgically polished and etched cross-section of the groove produced in LAMM with a 400 μm diameter tool for the same laser parameters used in the earlier experiments. It can be seen that the thermally affected zone is completely removed.

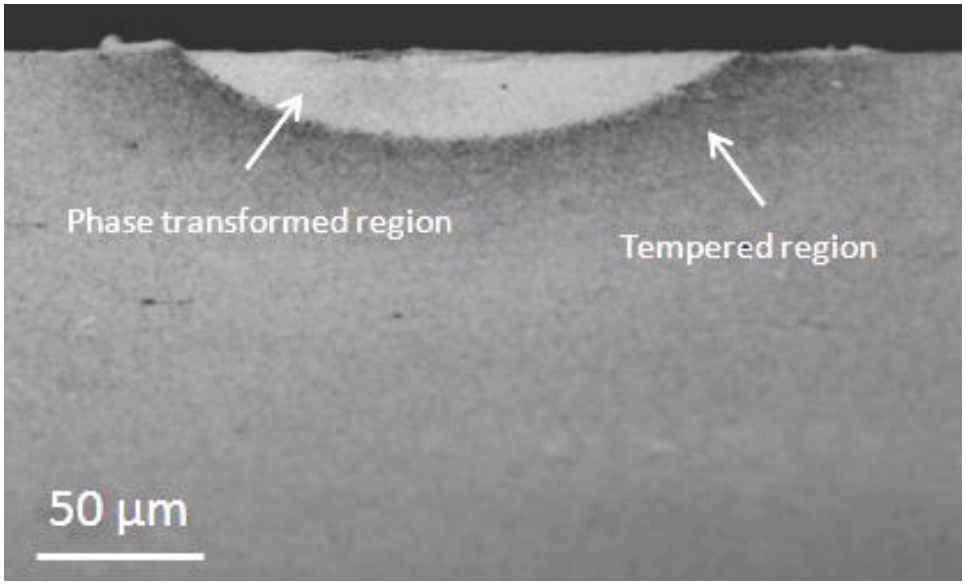

Figure 4.19: Optical micrograph of the cross section of the laser scanned path (laser power: 18 W, spot size: 280 μm, scan speed: 440 mm/min).

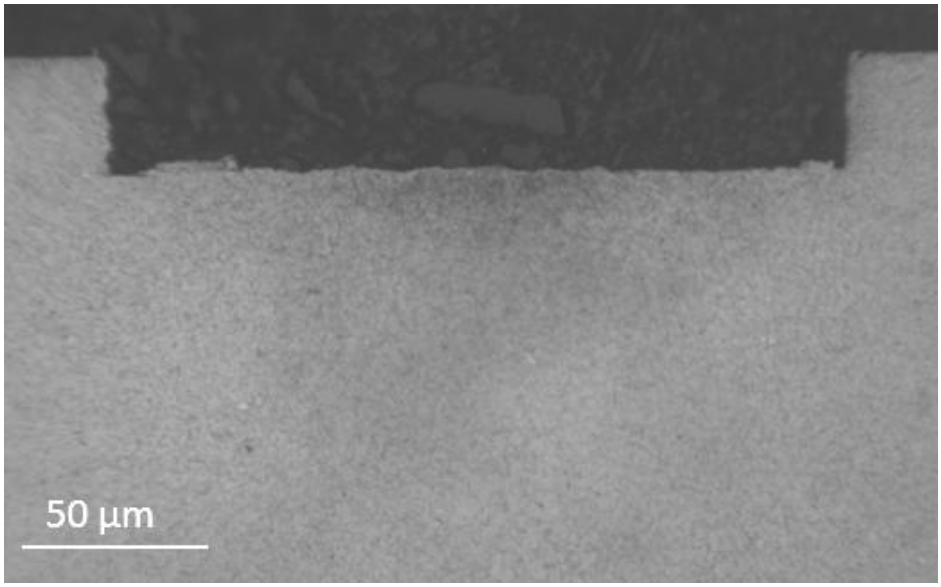

Figure 4.20: Optical micrograph of the cross section of the machined groove (400 µm tool, feed: 4.4 µm/flute, axial depth: 55 µm, laser power: 18 W, spot size: 280 µm, scan speed: 440 mm/min).

The peak resultant force values for the 400 µm diameter tool with and without laser assist are shown in Fig. 4.21. It can be seen that even though the tool diameter is somewhat larger than the width of the thermally affected zone, and hence the tool is cutting through harder material near the groove edges, there is still significant reduction in the resultant force obtained in LAMM. In contrast, without laser assist, the force increases significantly with groove number because of tool wear.

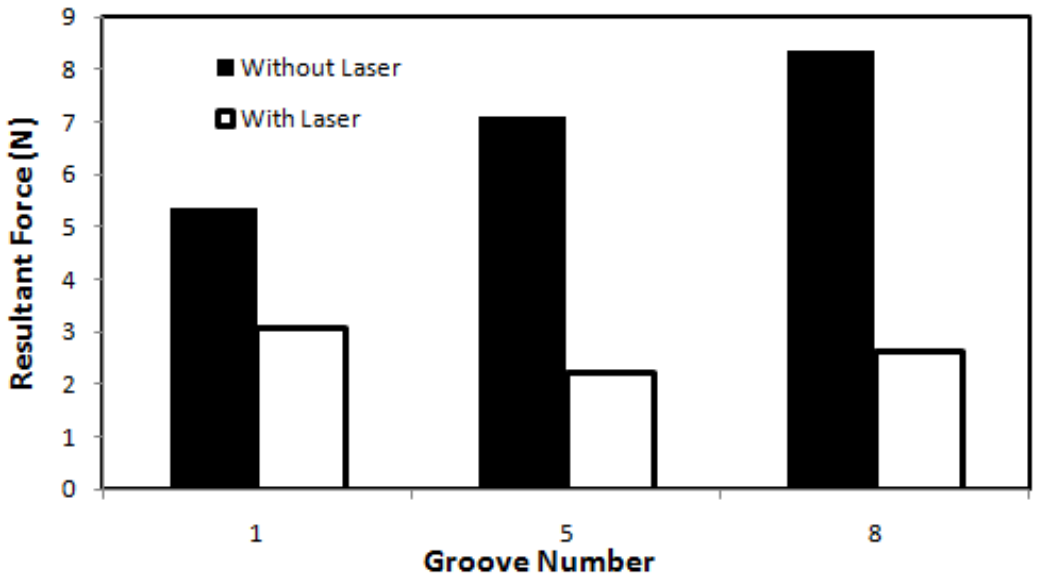

Figure 4.21: Change in the average peak resultant force with groove number (400 µm tool, feed: 4.4 µm/flute, axial depth: 55 µm).

Figure 4.22 shows a comparison of the burr heights obtained with the 400 µm tool with and without laser assist. It can be seen that even though the burr heights with laser assist are larger than without laser assist, their magnitudes are generally much smaller than in the earlier experiments with the 180 µm diameter tool (see Fig. 4.17). Note that it is also possible to limit the width of the thermally affected region to the tool diameter by carefully adjusting the spot size. However, since the spot size in the earlier experiments is slightly larger than the groove width, the material near the groove edges softens and causes the material to flow plastically, which results in larger burr heights.

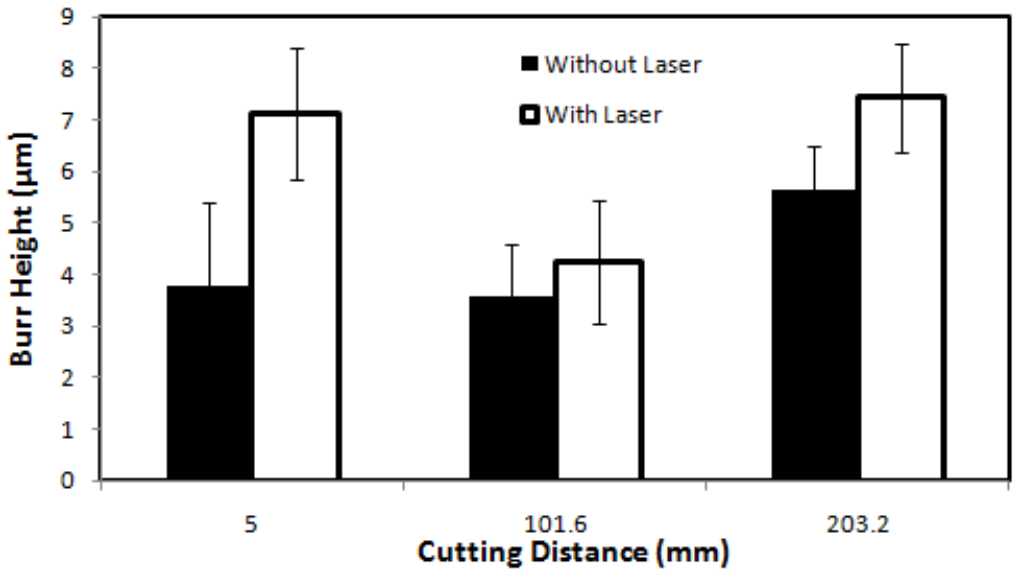

Figure 4.22: Burr height versus cutting distance with and without laser heating (400 µm tool, feed: 4.4 µm/flute, axial depth: 55 µm).

Figure 4.23 shows a comparison of the surface roughness obtained with and without laser assist when using the larger tool diameter. It is clear from this figure that comparable surface roughness can be obtained with laser assist while still lowering the cutting forces significantly. SEM micrographs of the tool shown in Fig. 4.24 clearly reveal significant wear after 203.2 mm of cutting without laser assist. This observation correlates well with the increase in resultant force with cutting distance shown in Fig. 4.21. In contrast, tool wear with laser assist is seen to be negligible and is consistent with that seen in the earlier tests.

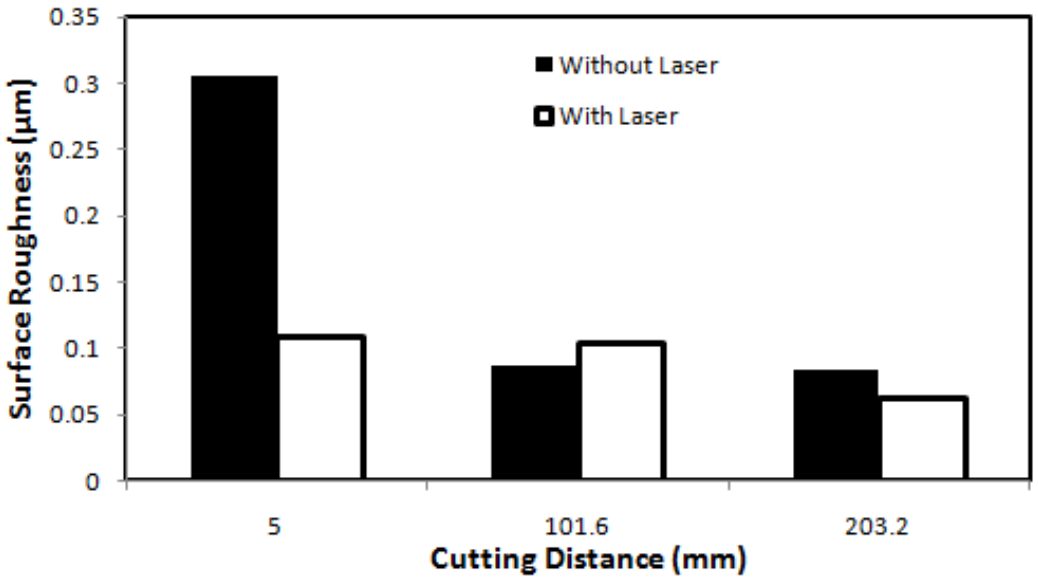

Figure 4.23: Surface roughness (S_a) versus cutting distance with and without laser heating (400 µm tool, feed: 4.4 µm/flute, axial depth: 55 µm).

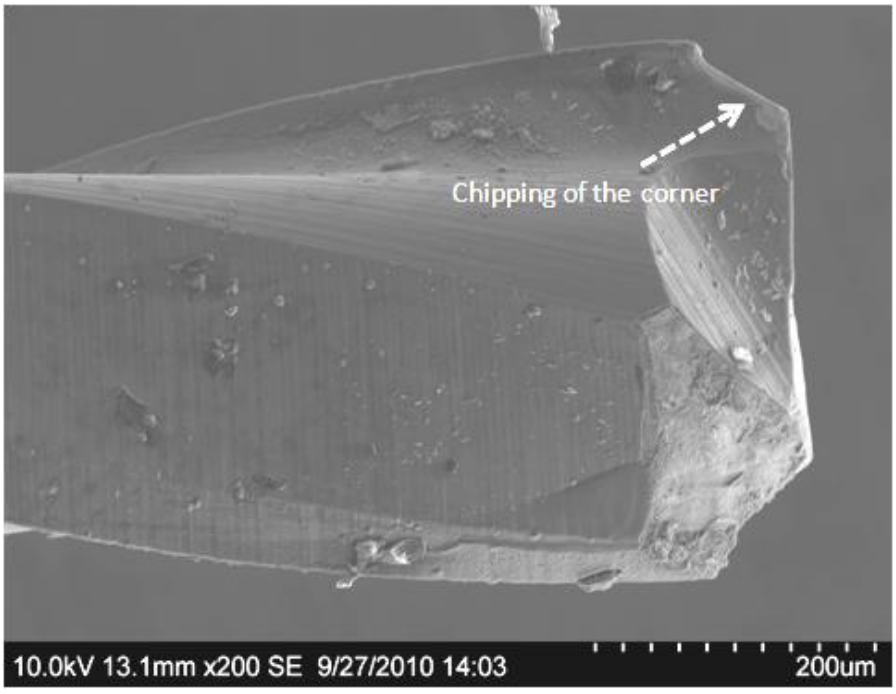

(a) Without laser assist

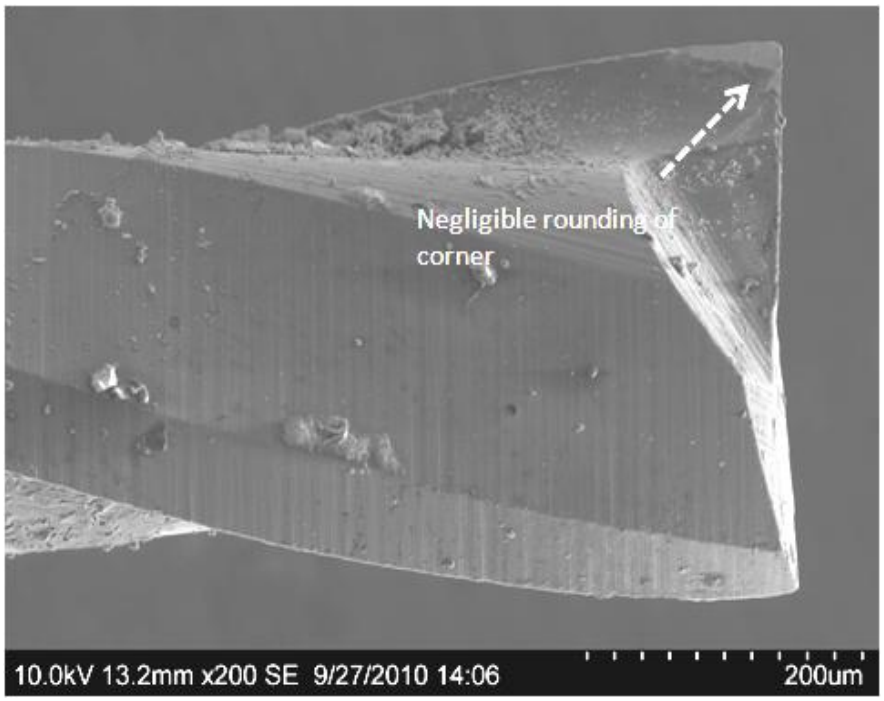

(b) With laser assist

Figure 4.24: SEM micrographs of the 400 µm tool after cutting 203.2 mm (a) without (top) and (b) with laser assist (bottom) (feed: 4.4 µm/flute, axial depth: 55 µm).

4.2.7 Extended Running Tests

As indicated earlier in section 4.1.1, a few more experiments were conducted using 180 µm diameter end mills under conditions or identical to Exp 3-L, till the cutting tool fails catastrophically in order to assess the impact of laser assist on tool life. Figure 4.25 compares the initial profile of the machined groove with the groove profile obtained after 406.4 mm of machining. The width of the groove reduces after a cutting distance of 406.4 mm indicating wear of the cutting tool. The experiments were repeated twice and the tool failed after cutting 431.8 mm and 457.2 mm respectively, which is significantly nine times higher than the no laser assist case shown in Fig. 4.4(b).

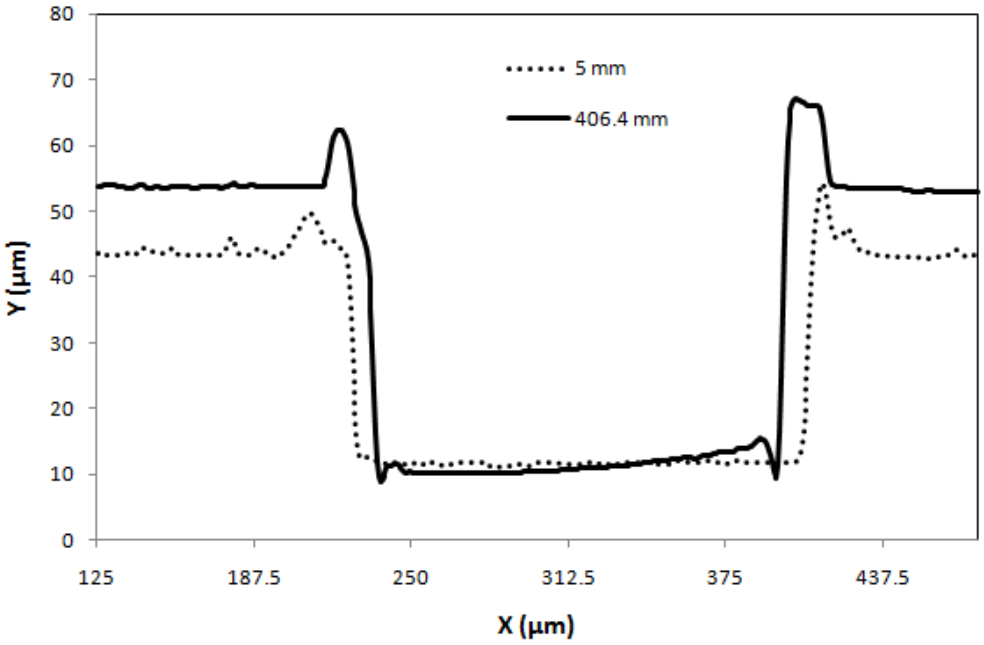

Figure 4.25: Groove cross section at the start (5 mm) and end (406.4 mm) of cut (feed: 6.6 µm/flute, axial depth: 32 µm).

4.3 Summary

This chapter presented a detailed evaluation of the process capability of LAMM for a hard-to-machine metal. Micro end milling experiments carried out on hardened A2 tool steel (62 HR_c) with and without laser assist yielded the following key conclusions:

1. The peak resultant force decreases with laser assist under all the conditions with a maximum reduction of 69% between Exp II and Exp II-L. In addition, there is a drop in the average specific cutting energy with laser assist indicating the dominance of cutting through shearing rather than ploughing.
2. The amount and rate of tool wear as measured by the rounding of the tool corner are significantly lower with laser assist even at material removal rates that are at

least six times higher than the tool manufacturer's recommendations. Under such conditions, and without laser assist, the carbide tool either wears rapidly or fails catastrophically.

3. When the laser spot size is larger than the tool diameter, the burr height is found to increase with laser assist. This is attributed to thermal softening of the work material. When a tool diameter larger than the laser spot size is used, the increase in burr height is much smaller.
4. When the laser spot size is larger than the tool diameter, the surface roughness is found to increase with laser assist due to increased thermal softening of the material. When a tool diameter larger than the laser spot size is used, comparable surface roughness is obtained.
5. The tool life increases by up to nine times with laser assist under the assumption that the catastrophic tool failure is the tool wear criterion.

The next chapter will focus on the modeling of cutting forces in laser assisted micro milling.

CHAPTER 5

FORCE MODELING IN LASER ASSISTED MICRO MILLING

The previous chapter focused on experimentally characterizing the LAMM process. The results indicated that laser assist yields increased material removal rates along with reduced tool wear and cutting forces when machining a hard metal (A2 tool steel, 62 HR_c). However, laser assist leads to increased burr formation and poor surface finish due to thermal softening of the workpiece material. This presents an interesting optimization problem of trying to increase the material removal rates by reducing the cutting forces, while reducing the burr formation and improving surface finish by confining the thermally affected zone to the region of material removal. To accomplish this, a mathematical model to understand the influence of the different laser and machining parameters on the cutting forces, in addition to the estimation of temperature distribution in LAMM, is required. Consequently, a physics based force model is developed to predict cutting forces when machining a hard metal with laser assist. LAMM experiments are carried out on 52100 bearing steel (62 HR_c), over a range of feed rates and laser powers to validate the force model. In addition, the influence of laser assist on the force distribution and burr formation is discussed, which will enable better understanding and optimization of the process.

5.1 Force Modeling

The basis for the development of the LAMM cutting force model is the unified mechanics of cutting approach by Armarego et al. [50]. This approach mathematically

relates the developed cutting analysis for conventional machining processes such as turning and milling to the fundamental oblique cutting mechanics together with the values of basic quantities (shear yield strength k_0, shear angle ϕ_0 and friction angle β) obtained from orthogonal tests. However, in the proposed cutting force model for LAMM, the basic quantities are derived from models reported in literature in combination with experimental data. The effect of laser assist is incorporated into this model by accounting for the variation in shear stress with temperature along the curved material removal surface. In this work, the approach commonly used for modeling conventional machining processes is assumed to be valid at the micro scale and some of the differences in the process physics like the size effect due to the finite tool edge radius are captured through the calibration parameters used in the model. The overall methodology for the prediction of forces in LAMM is shown in Fig. 5.1.

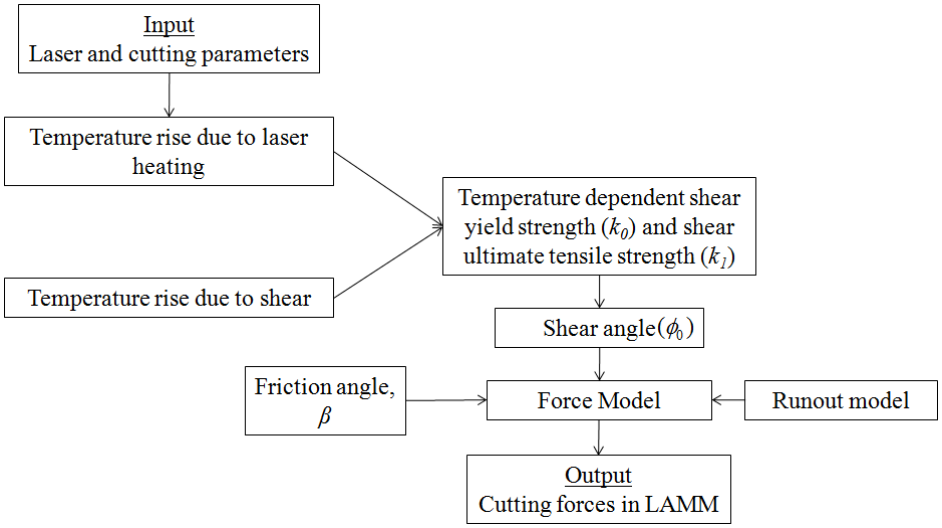

Figure 5.1: Overall methodology of the LAMM force model.

The key elements include a thermal model for laser heating [105], a thermal model for the prediction of temperature rise due to the cutting process [110], a shear

angle model for chip formation [111], a material model for flow strength [112], a mechanistic model for the milling process [50] and a runout model [113]. Each of these individual elements of the force model is discussed in the subsequent sections. The force model has three basic quantities to be estimated: shear yield strength k_0, shear angle ϕ_0 and friction angle β.

The inputs to the LAMM force model are the laser parameters (power, spot size and the laser-cutting tool distance) and the machining parameters (diameter of the cutting tool, feed, spindle speed, depth of cut and runout parameters) (see Fig. 5.1). In the first step, the temperature rise due to laser heating in addition to the temperature rise due to plastic deformation in the cutting process is estimated at discrete points along the curved material removal surface. Second, the temperature-dependent shear yield (k_0) and shear ultimate tensile strengths (k_1) are estimated at each of these points along the periphery of cut. In the third step, the shear angle (ϕ_0) is calculated along the curved material removal surface using a model which depends on k_0 and k_1. The effect of spindle and cutting tool axis offset runout is incorporated into the force model by computing the actual instantaneous uncut chip thickness at various points along the periphery of cut. The friction angle (β) is used as a calibration parameter which is estimated from a limited number of actual experiments. The outputs of the force model are the radial and tangential forces produced in the laser assisted micro milling process. The radial and tangential forces are appropriately transformed to the desired dynamometer coordinate system to validate the predicted forces against the measured cutting forces. The flowchart of the force prediction methodology along with the equations are summarized in Fig. 5.2.

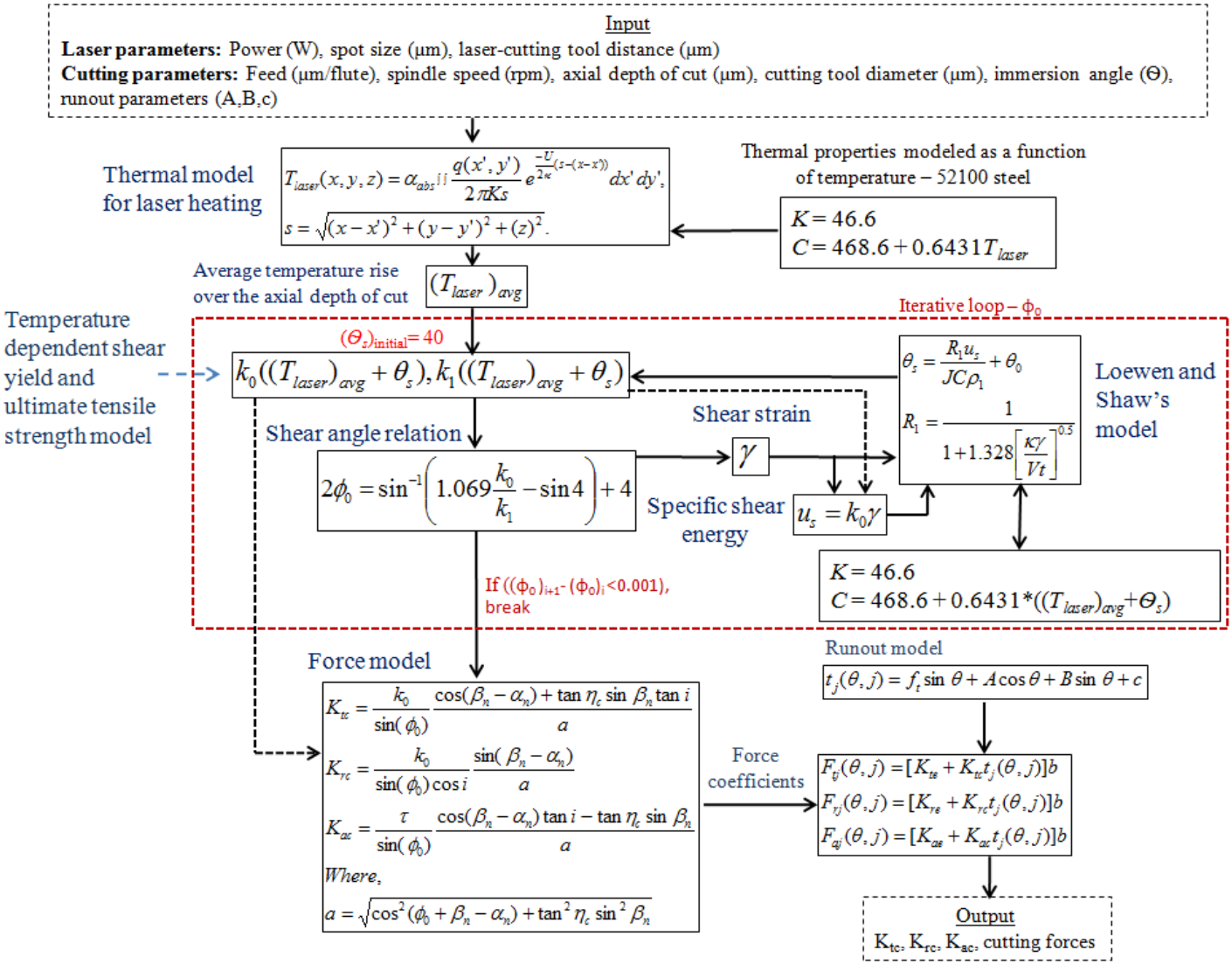

Figure 5.2: Flowchart of force prediction methodology.

5.2 Mechanistic Model for Cutting Force Prediction

In this work, the mechanistic model developed by Armarego et al. [50] will be adapted to model the cutting forces in laser assisted micro milling. The generalized elemental tangential (dF_t), radial, (dF_r), and axial (dF_a) cutting forces acting on the workpiece of an ideal system (with a rigid cutter and zero eccentricity in the cutter axis of rotation) in the dynamometer coordinate system as shown in Figs. 5.3(a) and (b) are given by,

$$\begin{aligned} dF_{tj}(\theta, j) &= [K_{te} + K_{tc} t_j(\theta, j)]dz \\ dF_{rj}(\theta, j) &= [K_{re} + K_{rc} t_j(\theta, j)]dz \\ dF_{aj}(\theta, j) &= [K_{ae} + K_{ac} t_j(\theta, j)]dz \end{aligned} \tag{5.1}$$

Where $t_j \cong f_t \sin\theta_j(z)$ is the instantaneous uncut chip thickness with no runout, j refers to the flute, f_t is the feed per tooth, dz is the thickness of the element along the tool axis and θ is the tool immersion angle. Since the depths of cut used in the micro milling experiments in this study are small, the differential elemental thickness dz in Eq. 5.1 is assumed to be equal to the depth of cut, b, and hence Eq. 5.1 simplifies to,

$$\begin{aligned} F_{tj}(\theta, j) &= [K_{te} + K_{tc} t_j(\theta, j)]b \\ F_{rj}(\theta, j) &= [K_{re} + K_{rc} t_j(\theta, j)]b \\ F_{aj}(\theta, j) &= [K_{ae} + K_{ac} t_j(\theta, j)]b \end{aligned} \tag{5.2}$$

Note that the model does not explicitly account for the finite cutting edge radius of the micro end mill. This effect is indirectly captured through the calibration parameter β, which accounts for tool-workpiece frictional contact conditions around the tool edge.

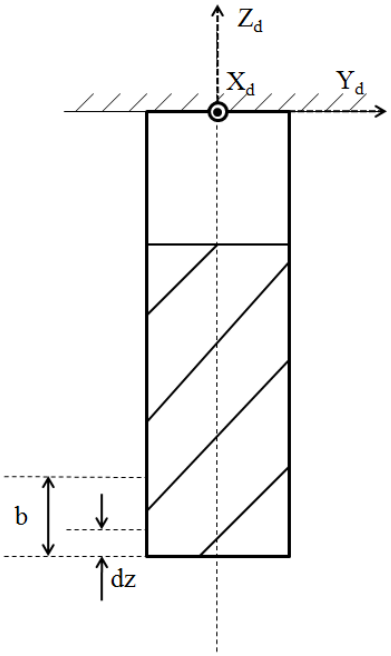

(a)

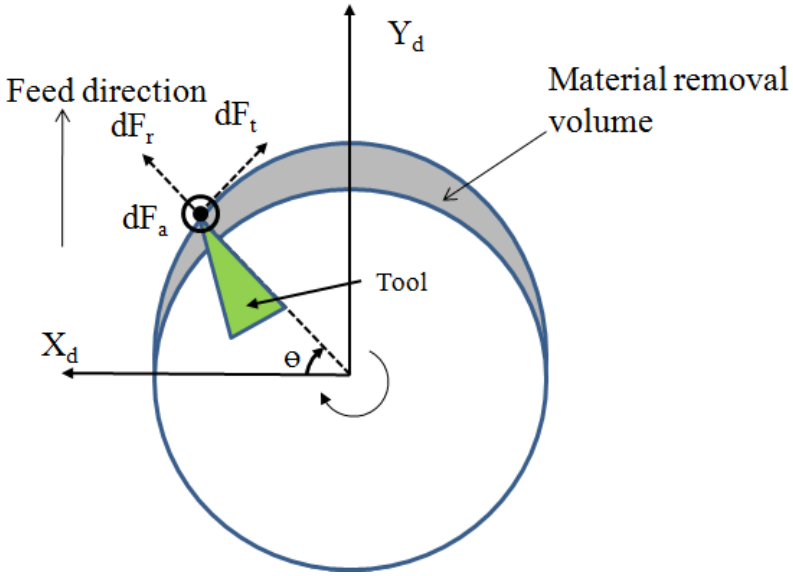

(b)

Figure 5.3: Geometry of a helical end mill **(a)** front view, and **(b)** end view showing the elemental forces (suffix 'd' refers to dynamometer coordinate system).

The cutting forces in Eq. 5.2 are modeled in terms of two fundamental phenomena, a constant edge component in the tangential, radial and axial directions due to rubbing or ploughing at the cutting edge represented by the edge force coefficients K_{te}, K_{re}, and K_{ae} respectively, and a cutting component due to shearing at the shear zone and friction at the rake face, represented by the cutting force coefficients K_{tc}, K_{rc}, and K_{ac} respectively. Each force component is assumed to be proportional to the uncut chip area. The edge force components are assumed to be zero for all the cases discussed below since it is difficult to isolate the edge force component from the experimentally measured forces. This is due to the very low magnitudes of cutting forces in the micro milling process when compared to conventional milling. In addition, it will be shown that even with the above assumptions, the model is in reasonable agreement with the experimentally measured forces. The cutting force coefficients are calculated using Eq. 5.3, which is determined from the mechanics of oblique cutting as presented by Altintas [114],

$$
\begin{aligned}
K_{tc} &= \frac{k_0}{\sin(\phi_0)} \frac{\cos(\beta_n - \alpha_n) + \tan\eta_c \sin\beta_n \tan i}{a} \\
K_{rc} &= \frac{k_0}{\sin(\phi_0)\cos i} \frac{\sin(\beta_n - \alpha_n)}{a} \\
K_{ac} &= \frac{k_0}{\sin(\phi_0)} \frac{\cos(\beta_n - \alpha_n)\tan i - \tan\eta_c \sin\beta_n}{a} \\
&\textit{Where,} \\
a &= \sqrt{\cos^2(\phi_0 + \beta_n - \alpha_n) + \tan^2\eta_c \sin^2\beta_n}
\end{aligned}
\tag{5.3}
$$

Where,

k_0 - shear yield stress modeled as a function of temperature,

β_n - normal friction angle,

η_c - chip flow angle,

α_n - normal rake angle, and

i - inclination (or) helix angle.

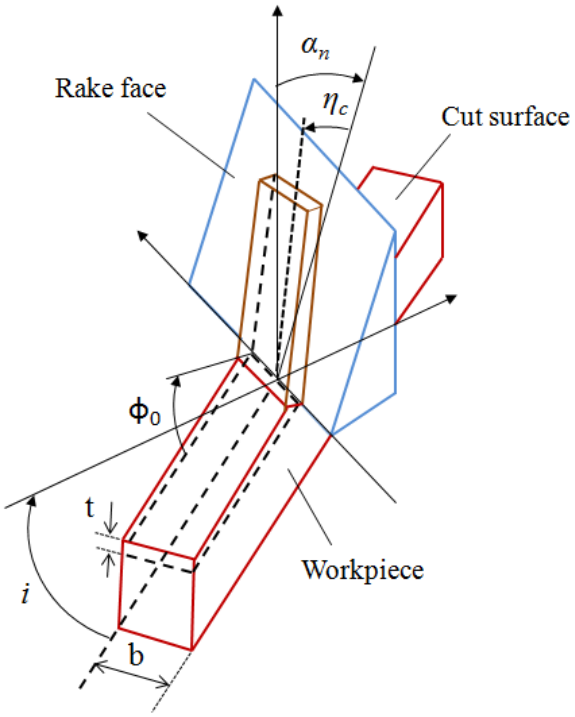

Figure 5.4: Geometry of oblique cutting process (adapted from [114]).

The schematic of the oblique cutting process along with the different angles is shown in Fig. 5.4. The normal rake (α_n) and normal friction (β_n) angles are related to the radial rake (α_r) and the friction (β) angles through Eq. 5.4. The radial rake and the helix angles are obtained from the specified tool geometry.

$$\begin{aligned} \tan\alpha_n &= \tan\alpha_r \cos i \\ \tan\beta_n &= \tan\beta \cos\eta_c \end{aligned} \tag{5.4}$$

The chip flow angle (η_c) is obtained by the application of Stabler's rule, which assumes that η_c and the inclination angle (i) are equal [114]. This rule has been

successfully applied by Biscacco et al. [41] to predict cutting forces in micro milling with minimum error. The Stabler's rule was originally developed for the milling process with negligible side flow. This assumption is reasonable since the width of cut is much larger than the uncut chip thickness in the milling process. In addition, this rule has been shown to work with high accuracy over a wide range of rake angles, -10º to 30º, which justifies its use in micro milling where the rake angle is negative over some portion of the tool due to the finite edge radius [115, 116]. The friction angle (β) cannot be measured directly and is therefore calibrated to match the experimentally measured cutting force data for each distinct tool used.

Figure 5.5 compares the peak tangential (F_t), radial (F_r) and axial (F_a) forces for various helix angles computed using Eq. 5.2 for the conditions listed in the figure. It can be clearly seen that the axial forces are negligible at low helix angles. The micro end mills used in this study has a helix angle of 20°. Hence, the axial force (F_a) is neglected in the calibration and validation experiments reported in this chapter.

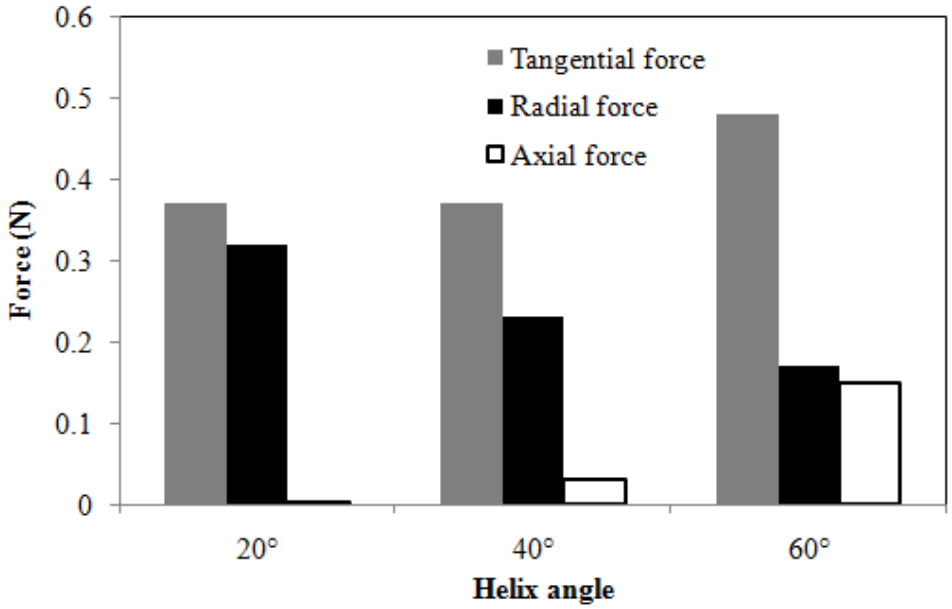

Figure 5.5: Comparison of peak tangential (F_t), radial (F_r) and axial (F_a) forces for various helix angles (AISI 52100 steel, laser power: 18 W, feed rate: 660 mm/min, distance between the center of the laser beam and the edge of the cutting tool: 200 µm, spindle speed: 50,000 rpm, feed: 6.6 µm/flute, no. of flutes: 2, depth of cut: 16 µm, radial rake, α_r : 4°, friction angle, β: 57°, no runout).

The radial and tangential forces are transformed into the dynamometer coordinate system, using the following equations to compare the model predicted forces with the measured forces.

$$\begin{aligned} F_{X_d} &= -F_t \sin(\theta) + F_r \cos(\theta) \\ F_{Y_d} &= F_t \cos(\theta) + F_r \sin(\theta) \end{aligned} \tag{5.5}$$

The basic quantities to be determined in Eq. 5.3 are the shear yield strength (k_0), shear angle (ϕ_0) and friction angle (β) as a function of the immersion angle (θ). These parameters are determined using existing models reported in the literature. First, the

temperature rise at discrete points along the curved material removal surface due to laser heating and the cutting process is calculated as discussed in sections 5.2.1 and 5.2.2. Second, this temperature distribution is used to estimate the shear yield strength (k_0) and shear ultimate tensile strength (k_1) at each point using the material model described in section 5.2.3. In the third step, the shear angle (ϕ_0) is estimated using the model explained in section 5.2.4. The effect of runout is incorporated by altering the uncut chip thickness (t_j) in Eq. 5.2, the details of which are given in section 5.2.5.

Experiments are then performed to measure the cutting forces in 52100 steel (62 HR_c) as given in section 5.3. The LAMM force model is calibrated using the friction angle (β) and the runout parameter (c), to match the experimental data for one of the cases (section 5.4). The calibrated values are then used to estimate the cutting forces for the remaining process conditions with varying feed rates and laser powers to evaluate the predictive capability of the model (section 5.5).

5.2.1 Temperature Rise Due to Laser Heating

The thermal model described in chapter 4 takes into consideration the effects of laser parameters such as laser power, spot size, scan speed and the cutting tool-laser beam distance. The output of the thermal model is the temperature rise, $T(x,y,z)$, at each point in the workpiece material. The thermal properties are modeled as a linear function of temperature and are given in Fig. 5.2. Figure 5.6 shows the top view of the cutting tool along with the radial cutting force, F_r, and the tangential cutting force, F_t, acting on a end mill tooth. The schematic clearly indicates that the undeformed chip thickness increases gradually from zero ($t=0$) to the maximum at the center ($t=f_t$), which is a characteristic of

the end milling process in the absence of runout. Figure 5.7 shows the temperature distribution in the material removal surface along different points in the periphery indicated in Fig. 5.6, for the conditions listed in the figure.

Figure 5.7 shows that the temperature rise is around 275 ºC at the point of maximum chip thickness, where the maximum thermal softening effect is desired. The temperature varies from a minimum value of 165 ºC to maximum of 275 ºC in the material removal surface. This temperature rise is only due to laser heating. The temperature rise associated with plastic deformation during cutting is calculated using Loewen and Shaw's model [110] and is explained in the following section.

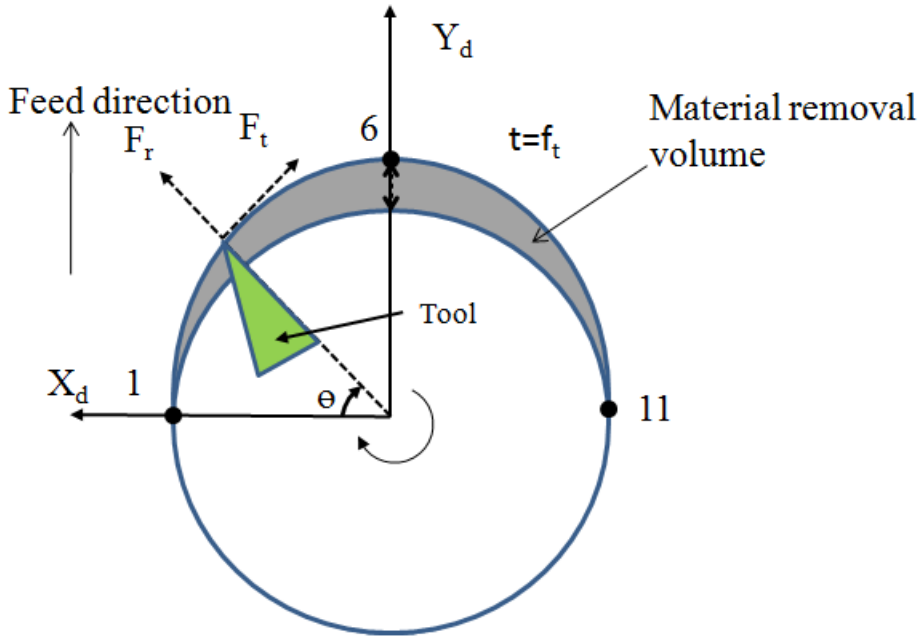

Figure 5.6: Actual path of the cutting tool indicating the cutting forces; temperature rise is predicted at equi-spaced points 1 through 11, 18º apart along the periphery.

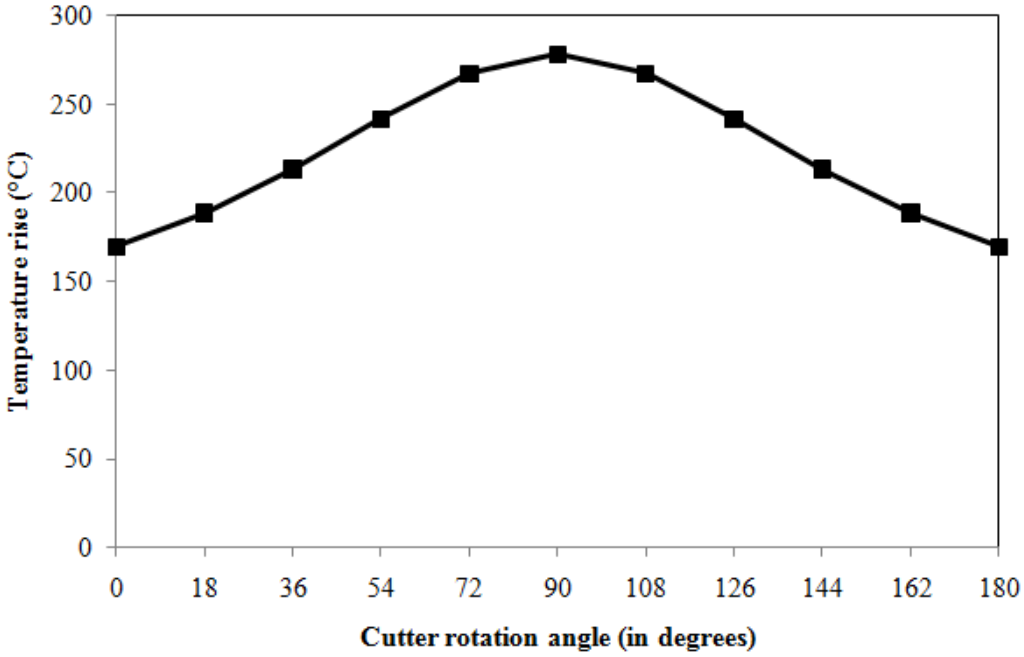

Figure 5.7: Calculated temperature rise due to laser heating along the depth (20 μm) in the material removal surface along the periphery of a 180 μm diameter tool (see Fig. 5.6) (AISI 52100 steel, laser power: 18 W, scan speed: 660 mm/min, distance between the center of the laser beam and the edge of the cutting tool: 200 μm).

5.2.2 Temperature Rise Due to Plastic Deformation

Loewen and Shaw's model is employed to predict the temperature rise due to plastic deformation in the cutting process [110]. The cutting process is assumed to be orthogonal at each point in the periphery of the cut. This assumption is reasonable since the temperature rise due to laser heating is much higher than the temperature rise due to plastic deformation in the cutting process as shown below. The temperature rise due to shear at each point along the periphery of cut is calculated using,

$$\theta_s = \frac{R_1 u_s}{C\rho J} + \theta_0 \tag{5.6}$$

Where,

$$R_1 = \frac{1}{1 + 1.328\left[\frac{\kappa\gamma}{Vt}\right]^{0.5}} \tag{5.7}$$

$$u_s = k_0\gamma \tag{5.8}$$

$$\gamma = \cot(\phi_0) + \tan(\phi_0 - \alpha_r) \tag{5.9}$$

Where

ϕ_0 - shear angle,

α_r - radial rake angle,

k_0 - shear yield stress,

t - instantaneous uncut chip thickness,

κ - thermal diffusivity,

J - mechanical equivalent of heat,

u_s - specific cutting energy,

V - cutting speed,

and γ - shear strain.

The parameter 'R_1' refers to the fraction of heat conducted into the chip. The expression for shear strain γ is based on the geometry of the fundamental orthogonal cutting process. An example calculation for the temperature rise due to the cutting process without laser assist when using a 180 μm diameter tool, at a feed of 6.6 μm/flute, axial depth of cut of 20 μm and a spindle speed of 50,000 rpm is presented in Fig. 5.8.

The maximum temperature rise due to the cutting process is around 120 ºC at the center of the cut (under conditions listed in Fig. 5.8), where the uncut chip thickness is maximum.

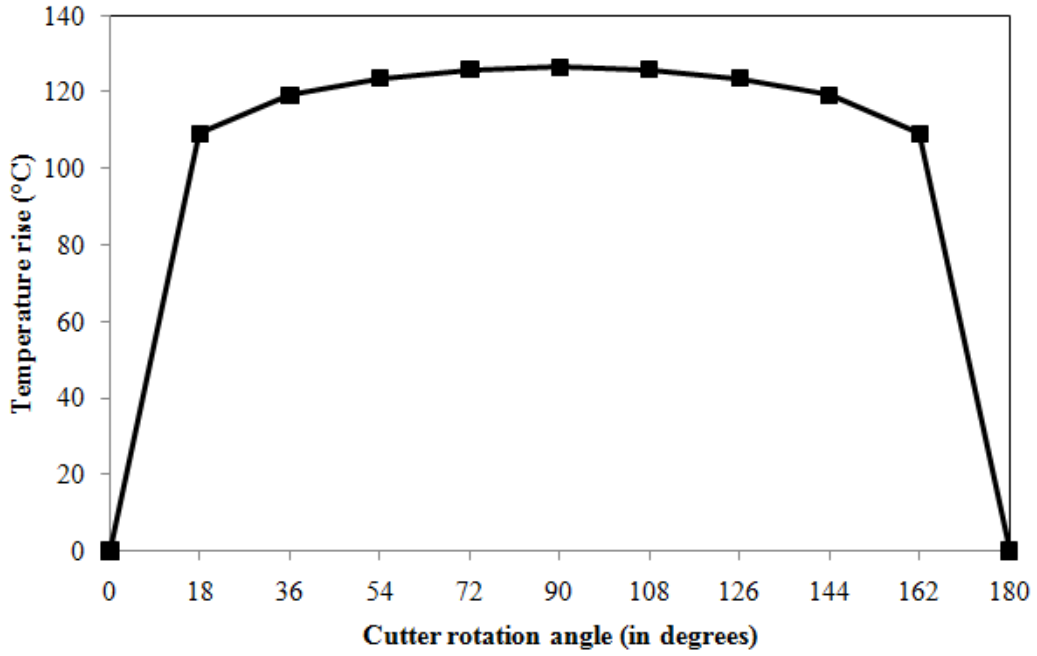

Figure 5.8: Calculated temperature rise due to cutting along the periphery (see Fig. 5.6) (feed: 6.6 µm/flute, axial depth of cut: 20 µm, spindle speed: 50,000 rpm, no laser assist).

However, under the same cutting conditions but with laser assist, the temperature rise due to plastic deformation in the cutting process is considerably lower due to the reduced shear yield strength of the material, as seen in Fig. 5.9. It is interesting to note that the maximum temperature rise only due to the cutting process is no longer at the center due to thermal softening of the material arising from laser heating at the point of maximum uncut chip thickness.

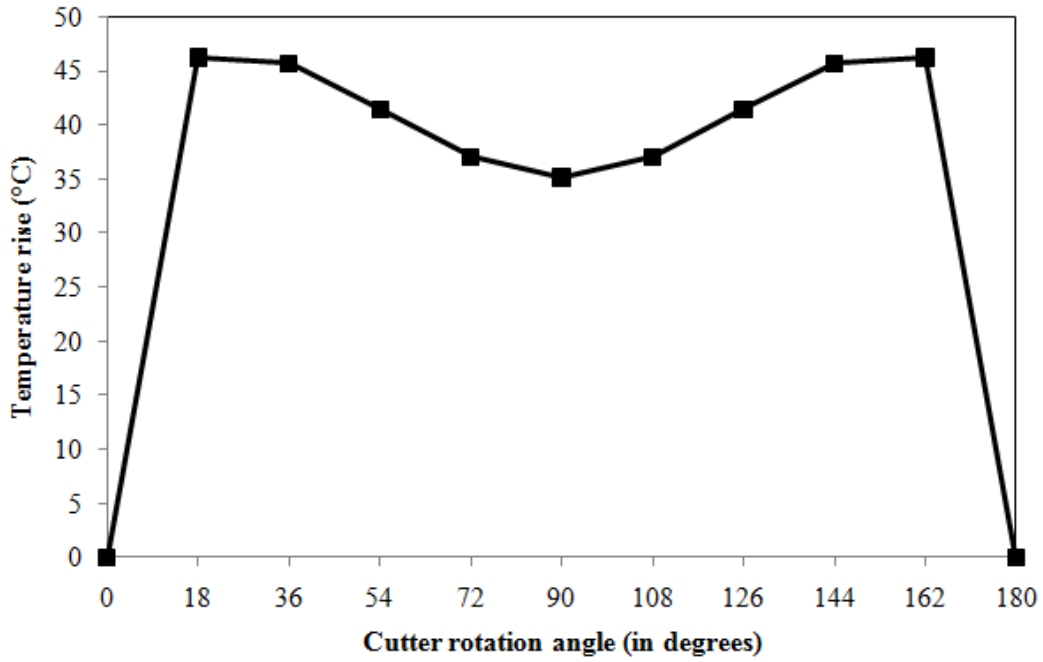

Figure 5.9: Calculated temperature rise only due to the cutting process along the periphery in LAMM (see Fig. 5.6) (feed: 6.6 µm/flute, axial depth of cut: 20 µm, spindle speed: 50,000 rpm, laser power: 18 W, scan speed: 660 mm/min, distance between the center of the laser beam and the edge of the cutting tool: 200 µm).

In addition, the temperature rise due to cutting is small compared to the temperature rise due to laser heating. Therefore, the inclusion of temperature rise due to cutting will not significantly change the prediction of cutting forces in LAMM. Nevertheless, for all calculations discussed in the subsequent sections, this effect is included.

5.2.3 Material Model

The yield strength and the ultimate tensile strength of 52100 steel as a function of temperature are plotted in Fig. 5.10 [112]. This data is obtained from tensile testing and accounts for the effect of strain rate through the velocity modified temperature approach and compares well with data obtained from actual cutting experiments. In addition, Guo et al. [112] have shown that 52100 steel is insensitive to strain rates typically encountered in the machining process (~10^4-10^5/s). The effect of strain hardening varies with each material and appropriate models have to be incorporated to account for this effect. A fourth order least squares polynomial is fit to the data points for 52100 steel and the resulting fits are also shown in Fig. 5.10. The R^2 values for both fits are 0.99, indicating a very good fit. Knowledge of the variation of yield and tensile strengths with temperature is essential to calculate the shear angle described in section 5.2.4.

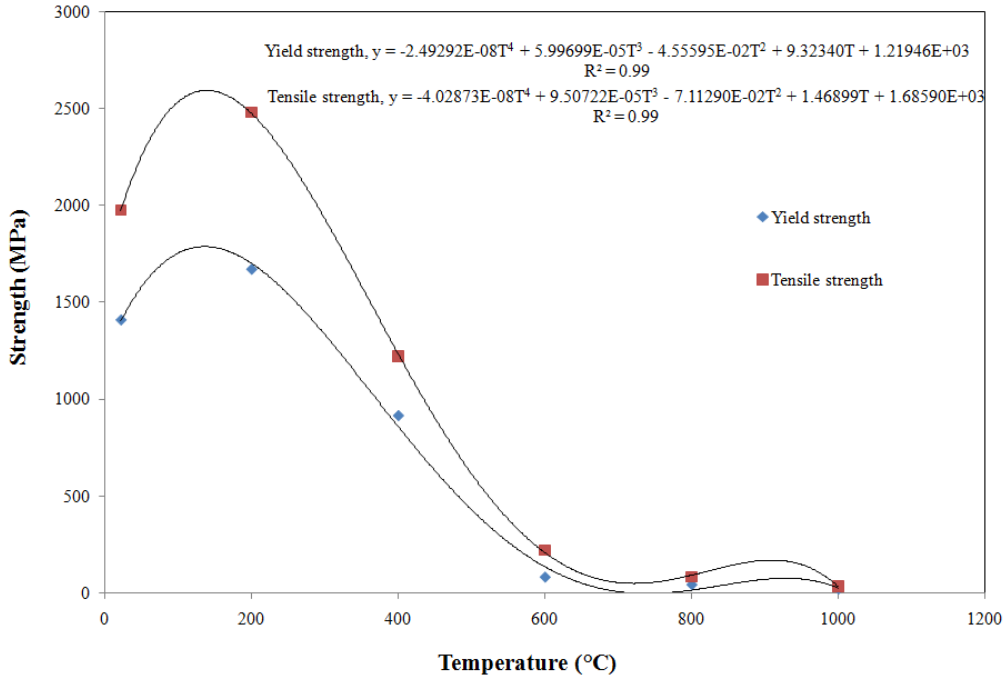

Figure 5.10: Temperature dependence of the yield and ultimate tensile strengths of 52100 steel (62 HR_c) [112].

5.2.4 Prediction of Shear Angle in LAMM

The model developed by Wright [111] is used to estimate the shear angle during the laser assisted micro milling process. At each point in the periphery of the milling cutter, the shear angle is estimated using this model, which is based on work material strain hardening characteristics. The model has been shown to accurately predict the shear angle for a wide range of workpiece/tool material combinations [111]. This model was selected since most of the models reported in literature require the use of experimental data like chip thickness from cutting experiments to calculate the shear angle [11]. Specifically, at the microscale, the measurement of chip thickness is difficult and time consuming. In addition, the calculation of shear angle from measured cutting forces is complex because of other unknown parameters like friction angle (β) and runout parameters, which significantly impact the cutting forces and also need to be simultaneously estimated in Eq. 5.2.

Wright's model for shear angle assumes that the chip begins to form when plastic instability initiates. Hence, it is necessary to calculate the minimum amount of plastic work needed to cause shear instability in a severely work-hardened material. The onset of plastic collapse is calculated using the upper bound method and is found to occur at a shear plane angle $\phi = 45 + \frac{\alpha}{2}$ [111]. However, due to work-hardening, the deformation zone geometry is non-unique and the shear plane can rotate into the softer material ahead of this initial instability. By calculating this additional rotation of the shear plane, the shear angle can be estimated.

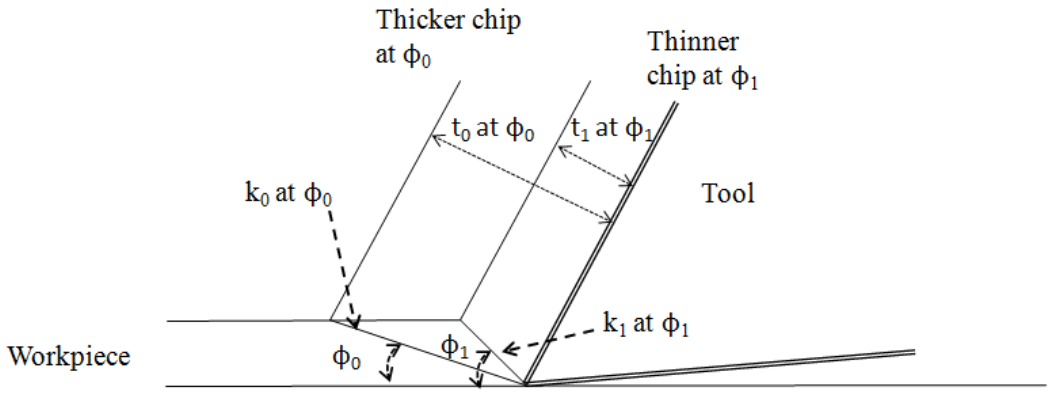

Figure 5.11: Schematic showing the rotation of the shear plane from ϕ_0 to ϕ_1 as a result of strain hardening [111].

The rotation of shear plane is shown schematically in Fig. 5.11. By equating the minimum plastic work rate required for initiating shear instability in a severely work hardened material, to the work rate of shearing a soft material along a longer shear plane, the shear angle 'ϕ_0' is estimated using Eq. 5.10,

$$k_1\left[\frac{\cos\alpha}{\cos(\phi_1-\alpha)}\frac{wt_0}{\sin\phi_1}\right]=k_0\left[\frac{\cos\alpha}{\cos(\phi_0-\alpha)}\frac{wt_0}{\sin\phi_0}\right] \tag{5.10}$$

Using the analysis involving the calculation of the lowest upper bound of plastic work, the shear angle for plastic collapse was estimated to be [111],

$$\phi_1=45+\frac{\alpha}{2} \tag{5.11}$$

For a 4 degree rake angle tool used in the experiments in this chapter, Eq. 5.10 simplifies to

$$2\phi_0=\sin^{-1}\left(1.069\frac{k_0}{k_1}-\sin 4\right)+4 \tag{5.12}$$

where, k_0 and k_1 are the shear yield and shear ultimate tensile strengths of the material.

There are a few basic assumptions behind this model. First, the model ignores the effect of friction at the tool-workpiece interface on the shear angle. Second, the effects of strain rate and temperature rise due to the cutting process are also neglected. However, by using the knowledge of variation in yield and ultimate tensile strengths of the material with temperature, it is possible to use the model to estimate the shear angle at higher temperatures. This approach has been used here to estimate the shear angle at the higher temperatures generated in LAMM.

When micro milling 52100 steel using a 180 μm diameter tool (4º rake), at a feed of 6.6 μm/flute, axial depth of cut of 20 μm, spindle speed of 50,000 rpm, the shear angle at the point of maximum uncut chip thickness is predicted using Eq. 5.12 to be 23.8 degrees, which is comparable to the reported shear angle values calculated in the literature (23 to 30 degrees) for orthogonal cutting of 52100 steel [112].

5.2.5 Runout Model

The effect of spindle runout and cutting tool axis offset runout on the uncut chip thickness in micro milling is taken into consideration using the three parameter model given in Eq. 5.13 [113],

$$t_j(\theta, j) = f_t \sin\theta + A\cos\theta + B\sin\theta + c \tag{5.13}$$

Where, f_t is the feed per tooth, Θ is the immersion angle of the flute, A and B are the spindle runout parameters assuming a two lobe runout model, and c is the actual axis offset runout of the cutting tool due to center offset and tool geometric errors. The change in runout parameters of the spindle due to the cutting process is not considered in this

study. In addition, only a two lobe runout model is considered because of the difficulty in measuring the runout parameters for a higher lobe model for the micro end mills. The two lobe run-out parameters *A* and *B* are determined experimentally using two laser interferometers as shown schematically in Fig. 5.12. The laser interferometers are mounted orthogonal to each other and are aimed at the tool shank. The parameters *A* and *B* are calculated from these measurements. Direct measurement of runout at the tool tip is very challenging at the microscale since the spot size of the laser interferometer (0.8 mm) is much greater than the diameter of the tool. Hence, in this work the runout is measured on the shank of the tool in order to estimate the runout parameters *A* and *B*.

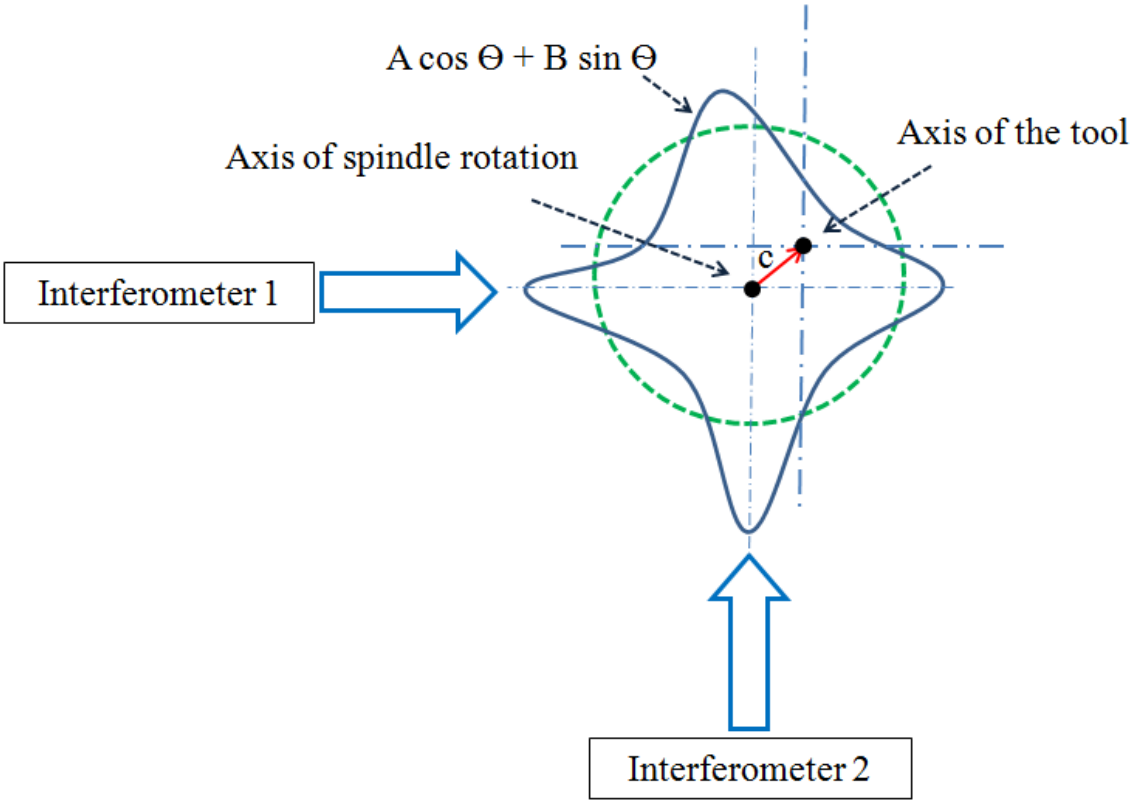

Figure 5.12: Schematic of the runout parameters and its measurement.

The third parameter *c* is the actual shift of the tool axis with respect to the spindle axis as indicated in Fig. 5.12. This error might be due to a number of factors such as the difference in the radii of the flutes, center offset, etc. This parameter is calibrated to match the predicted forces with the experimental force data. For example, a cutting force calculation using the model is shown in Fig. 5.13 along with the measured values. In this calculation, the parameters *A* and *B* in Eq. 5.13 are assumed to be zero and the *c* value is varied to match the peak forces as shown in Fig. 5.13.

It can be seen that although this simple one parameter model is able to capture the troughs in the measured force signal, it cannot capture the peaks, which are indicated using dotted circles in the figure. Hence, the parameters *A* and *B* are important to capture the positive peaks in the force profile, which occur at flute entry and exit as seen in Fig. 5.13. The positive peaks are attributed to the multilobe runout of the spindle, which can be modeled using the sine and cosine terms in Eq. 5.13. The three parameter model in Eq. 5.13 assumes a two lobe runout with axis offset. To obtain better accuracy, more interferometers can be used to measure the multilobe runout parameters [113]. Note that the runout model does not explicitly account for any dynamic effects. The results presented in the subsequent sections indicate that the model prediction is good even with the two lobe assumption.

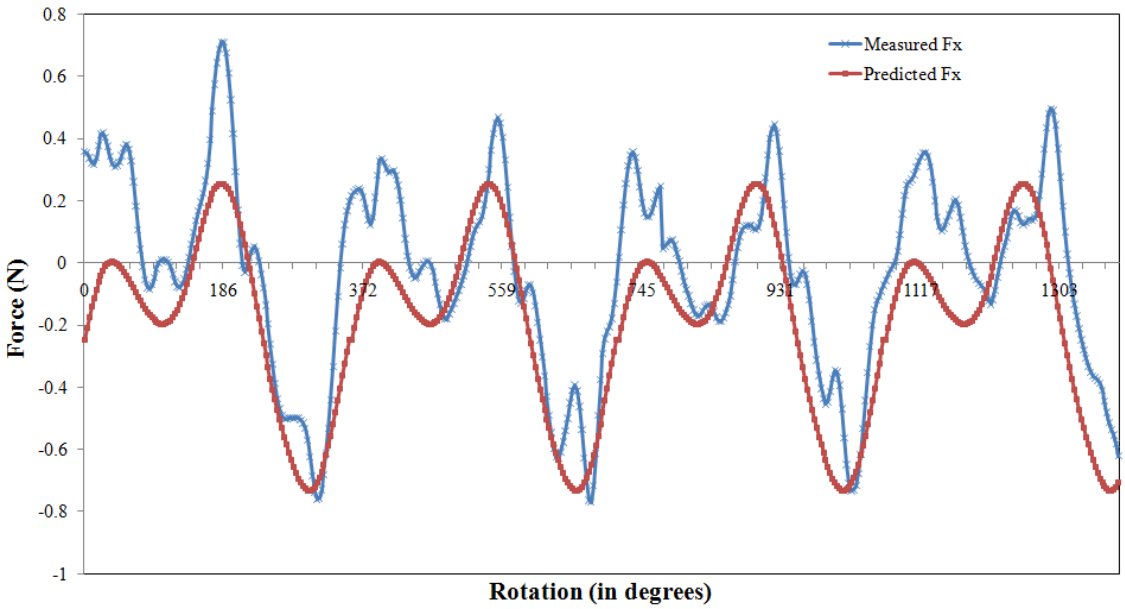

Figure 5.13: Model prediction of F_x over four cutter rotation cycles along with the experimental data (feed: 6.6 µm/flute, depth: 20 µm, spindle speed: 50,000 rpm, laser power: 19 W, scan speed: 660 mm/min, tool diameter: 180 µm, no. of flutes: 2, distance between the center of the laser beam and the edge of the cutting tool: 200 µm).

5.3 Micro Milling Experiments

The workpiece material used in the study was 52100 bearing steel (62 HR_c) with the nominal composition listed in Table 5.1. The hardness of this material is same as that of A2 tool steel used earlier in the experiments discussed in chapter 4. This material was selected because of the availability of well documented thermal and mechanical properties over the range of temperatures experienced in the LAMM process. Two-flute 180µm diameter, TiAlN coated tungsten carbide square end mills (SECO® JM905) were used in the experiments.

Table 5.1: Nominal chemical composition of 52100 steel.

Element	C	Mn	Si	Cr
Weight %	1.04	0.35	0.25	1.45

A series of slot milling experiments, summarized in Table 5.2, were performed. The total length of cut in each experiment was 25.4 mm. The spindle speed was fixed at 50,000 rpm. The feeds and laser powers were varied in the experiments to analyze the effects of these variables on the predictive ability of the model. The tool manufacturer's recommended feed and depth of cut for the material hardness used in the study are 2.2 µm per flute and 16 µm, respectively. The laser spot size was fixed at 280 µm in all experiments. The cutting force was measured using a 3-axis piezoelectric platform dynamometer (Kistler Minidyn 9256C2). The tool number is also shown in the table to account for the change in the runout parameters each time a new tool is mounted in the spindle.

The power spectrum of the sampled signal obtained in Exp I-3 is shown in Fig. 5.14. It clearly indicates that the dominant frequencies are the spindle and tooth passing frequencies. Additionally, the maximum measurement error specified by the manufacturer of the force dynamometer is 10 % at the operating frequency (Kistler® 9256C2 manual). At a spindle speed of 50,000 rpm, the resonant frequencies of the dynamometer ($f_n(x)$=4 kHz, $f_n(y)$=4.8 kHz, $f_n(z)$=4.6 kHz) are not excited as seen in Fig. 5.14. Hence, the measured data is not affected significantly by the dynamics of the dynamometer.

Table 5.2: Experimental conditions.

Experiment	Tool Number	Feed (µm/flute)	Laser power (W)	Axial depth of cut (µm)
I-1	1	2.2	18	16
I-2	1	4.4	18	16
I-3	1	6.6	18	16
II-1	2	2.2	12	16
II-2	2	6.6	12	16
II-3	2	2.2	24	16
II-4	2	6.6	24	16

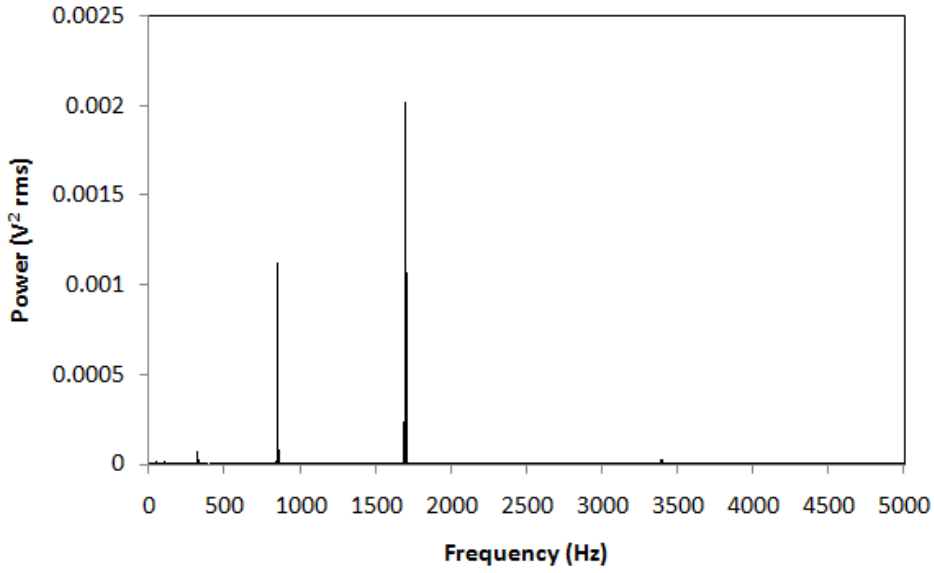

Figure 5.14: Power spectrum of the measured force signal for Exp I-1 (tool number: 1, feed: 2.2 µm/flute, depth of cut: 16 µm, and laser power: 18 W).

5.4 Model Calibration and Results

The model described previously in section 5.1 was used to predict the cutting forces for each of the cases listed in Table 5.2. The model has two calibration parameters, β and c, along with the measured runout parameters, A and B. These parameters were varied to match the experimental data for one of the test cases (for each new tool), and then compared with the remaining test results to evaluate the predictive capability of the model. Figures 5.15 (a) and (b) compare the predicted and measured F_x and F_y forces for Exp I-3 (tool #1) over four cutter rotation cycles. The calibrated values of β and c are 48º and 3.6 µm, respectively, and the measured values of A and B are 1.8 µm and -0.5 µm, respectively. Similarly, 5.16 (a) and (b) show a comparison of the predicted and measured F_x and F_y forces for Exp II-4 (tool #2) over four cycles. The calibrated values of β and c are 57º and 1 µm, respectively, and the measured values of A and B are 1.8 µm and -0.5 µm, respectively. The β value changes from 48º to 57º for the two calibration cases. This is thought to be due to the dependence of β on the runout parameter c since a change in its value will affect the tool-workpiece contact conditions. The contact conditions are very complex and are not well understood even at the macroscale. At the microscale, even a small change in the tool edge radius can have a significant impact on the value of β. Even for new tools, the edge radius typically varies by a micron or less due to the lower repeatability of the manufacturing processes used to make these tools. In addition, the tools used were coated with TiAlN with a coating thickness of around 2 µm, which indicates that even a small amount of chipping of the coating will lead to significant changes in the c and β values.

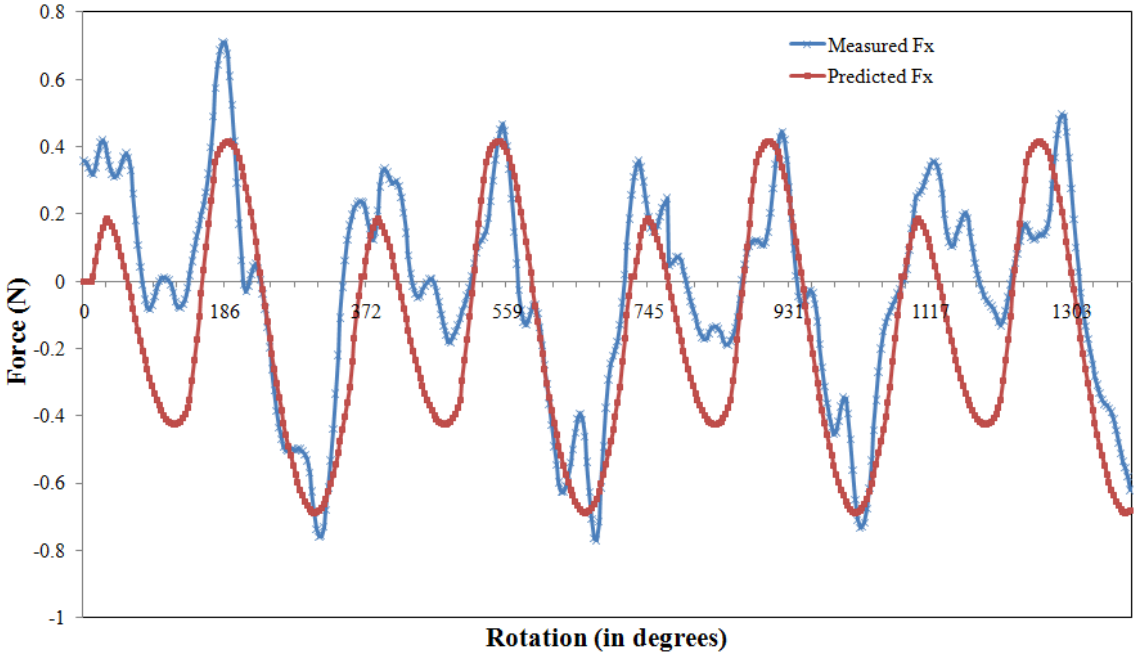

(a)

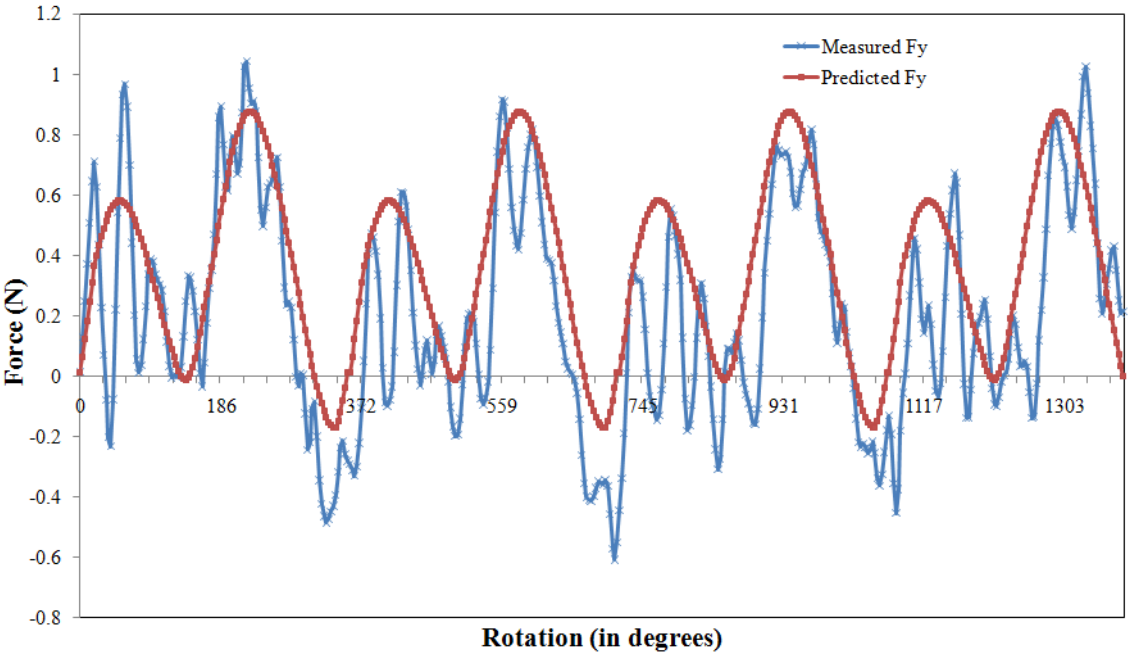

(b)

Figure 5.15: Comparison of predicted and measured (a) F_x and (b) F_y over four cycles under conditions listed in Table 5.2 for Exp I-3 (tool number: 1, feed: 6.6 µm/flute, depth of cut: 16 µm, and laser power: 18 W).

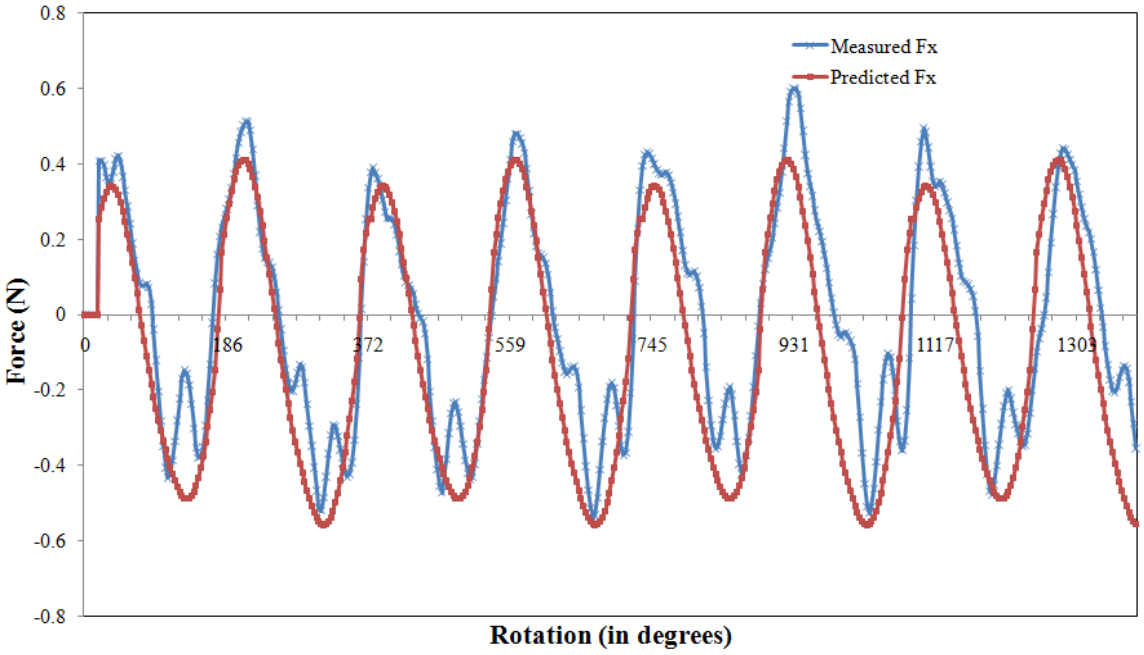

(a)

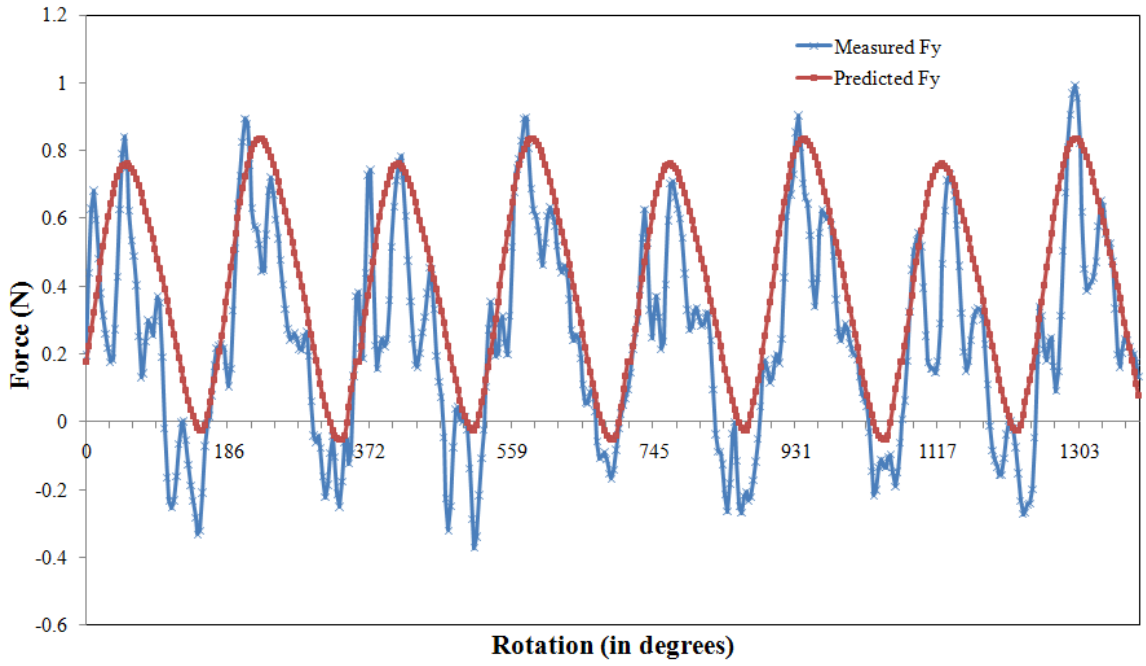

(b)

Figure 5.16: Comparison of predicted and measured (a) F_x and (b) F_y over four cycles under conditions listed in Table 5.2 for Exp II-4 (tool number: 2, feed: 6.6 µm/flute, depth of cut: 16 µm, and laser power: 24 W).

It can be seen that the predicted force profile agrees well with the measured force profile for Exp I-3 and Exp II-4. There is still some error in capturing the positive peaks in F_x as seen in Figure 5.15(a). This error might be due to the complex entry and exit contact conditions of the tool with the workpiece. This is more evident from the F_y force profile for both cases, as shown in Figs. 5.15(b) and 5.16(b). In addition, the dynamics of the process is not modeled, which is clearly evident from the noisy peaks, especially in the measured F_y force profile as shown in Fig. 5.16(b).

5.5 Model Validation

The calibrated values of β and c reported in the previous section are used to predict the cutting forces for the remaining test cases and are compared against the measured values. The predicted and measured forces for Exp I-2 and Exp II-2 are shown in Figs. 5.17 and 5.18. As seen clearly from the figures, the model is able to predict cutting forces with good accuracy. As mentioned earlier, the experimentally measured force profiles in the Y direction are noisy due to the dynamics and complex cutting conditions that exist at the tool-workpiece interface during tool entry and exit.

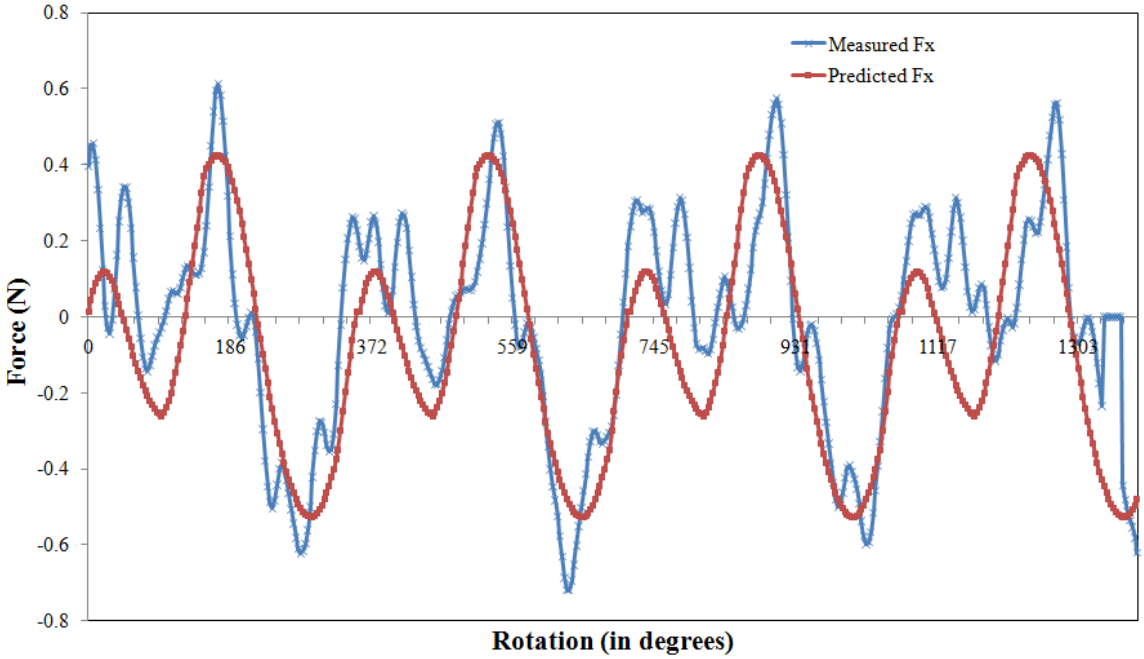

(a)

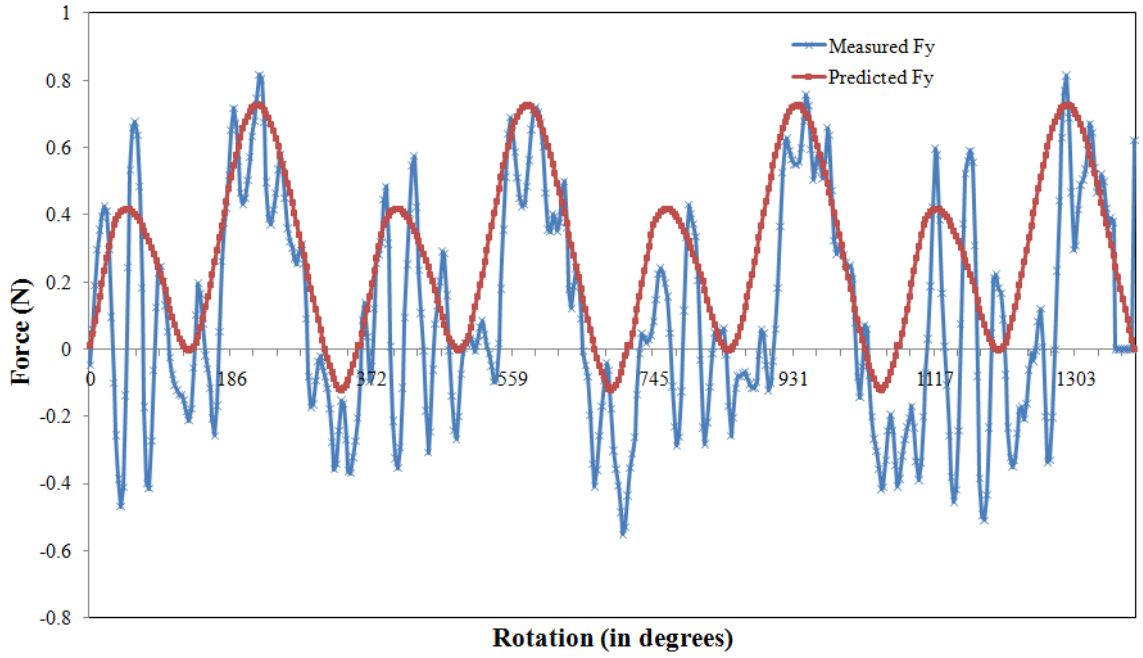

(b)

Figure 5.17: Comparison of predicted and measured (a) F_x and (b) F_y over four cycles under conditions listed in Table 5.2 for Exp I-2 (tool number: 1, feed: 4.4 µm/flute, depth of cut: 16 µm, and laser power: 18 W).

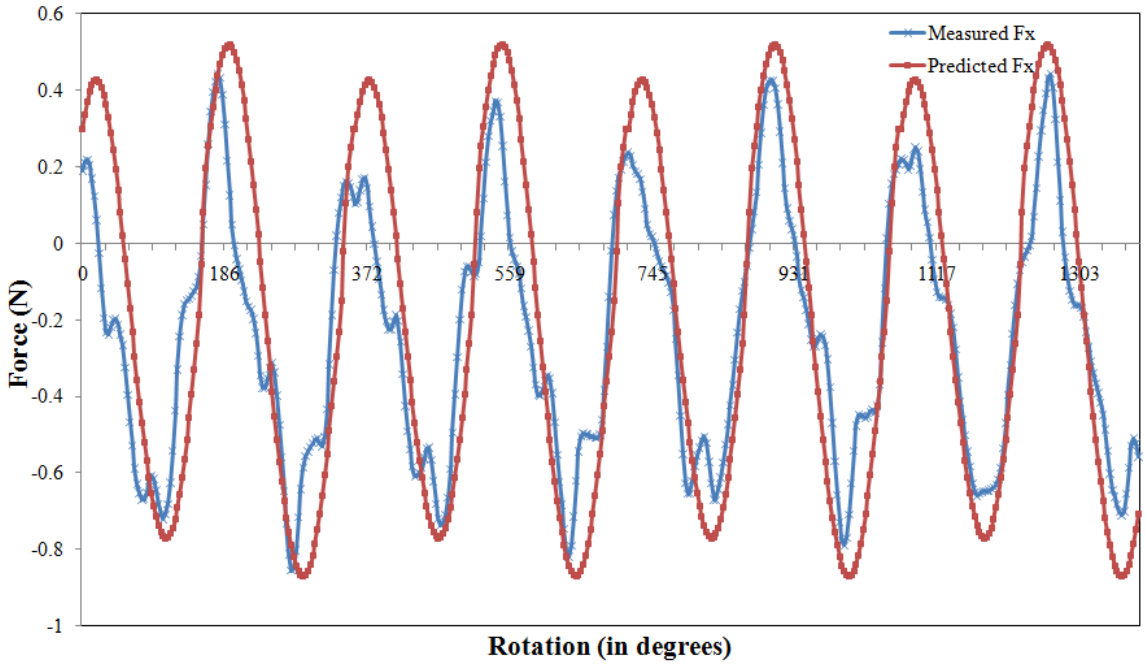

(a)

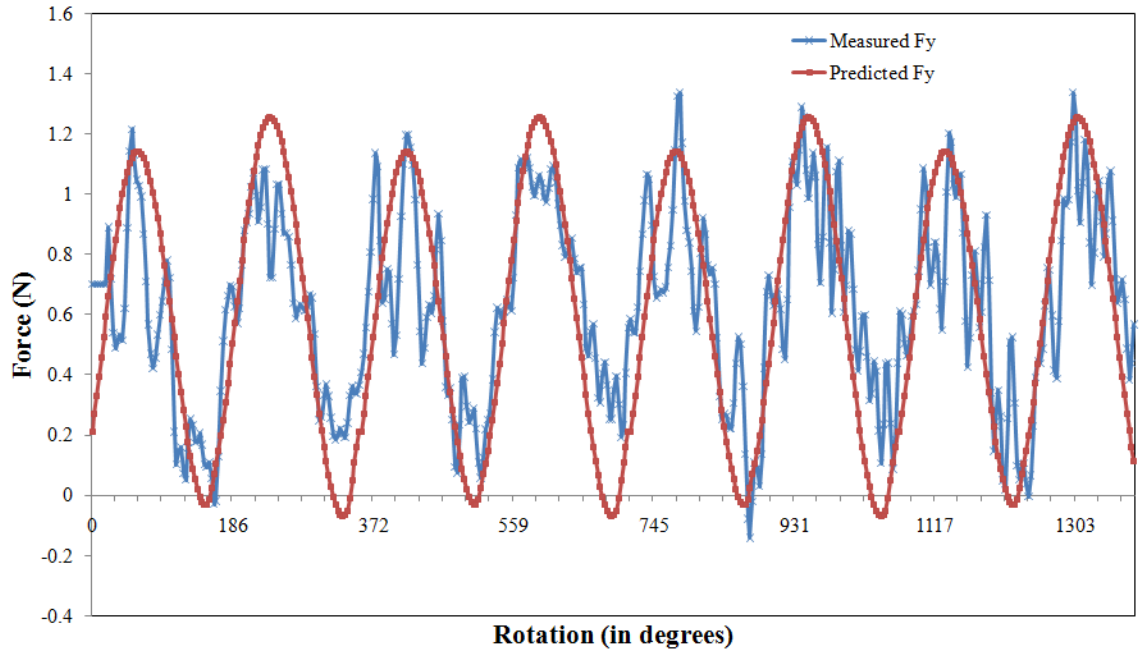

(b)

Figure 5.18: Comparison of predicted and measured (a) F_x and (b) F_y over four cycles under conditions listed in Table 5.2 for Exp II-2 (tool number: 2, feed: 6.6 µm/flute, depth of cut: 16 µm, and laser power: 12 W).

To reiterate, the main objective of the model presented in this chapter is to aid in the selection of laser parameters to reduce the peak cutting forces. Hence, a comparison of the absolute values of the peak predicted cutting forces with the experimentally measured values is essential and is shown in Figs. 5.19 and 5.20 for all the experiments. The minimum and maximum mean errors in the predicted values of F_x and F_y when compared with experiments is between 2% and 15% respectively, clearly confirming the predictive capability of the model. The values of β and c are insensitive to the feed as seen from Exp I-1 through Exp I-3. In addition, the calibration parameters β and c are also found to be relatively insensitive to different laser powers, which are varied between Exp II-1 and II-3, and between Exp II-2 and Exp II-4.

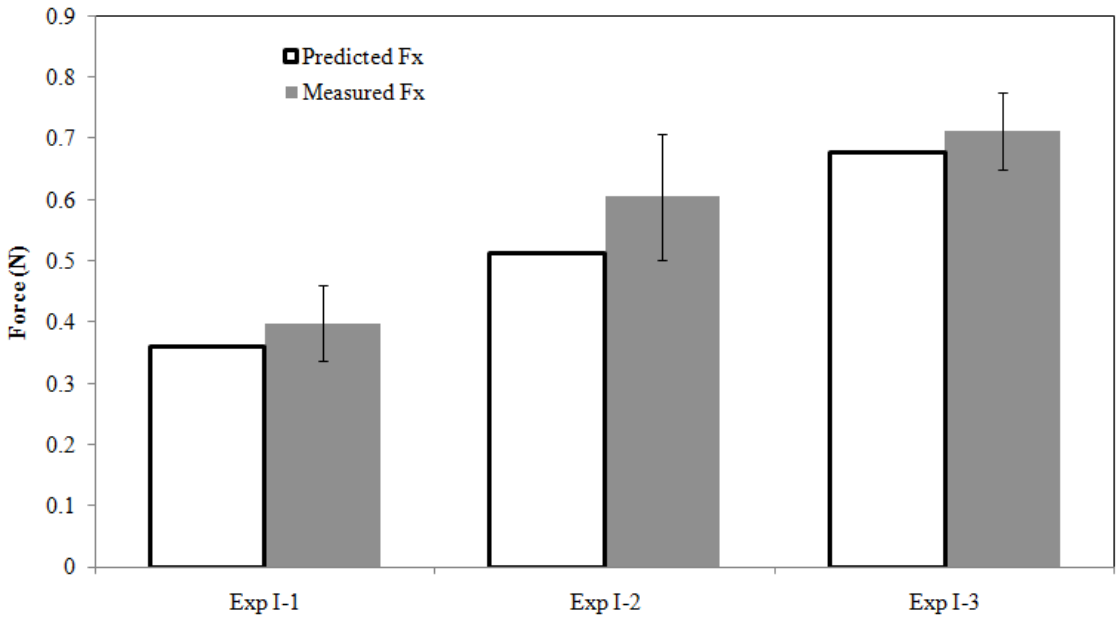

(a)

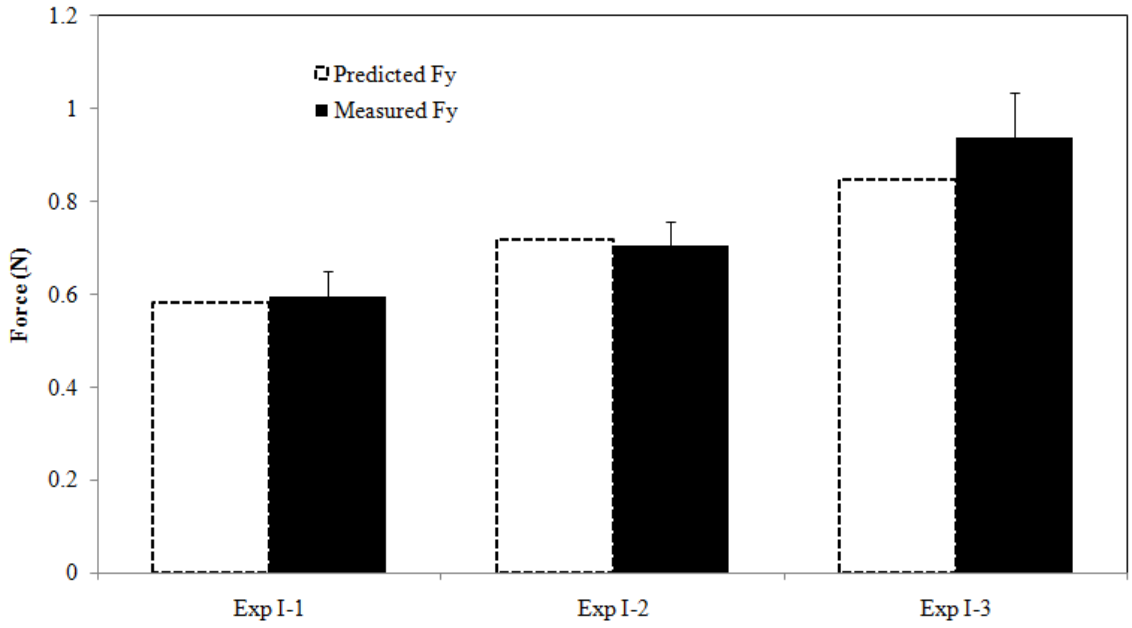

(b)

Figure 5.19: Comparison of predicted and measured absolute peak cutting forces, **(a)** F_x and **(b)** F_y using laser assist under different conditions for Exp I (Table 5.2).

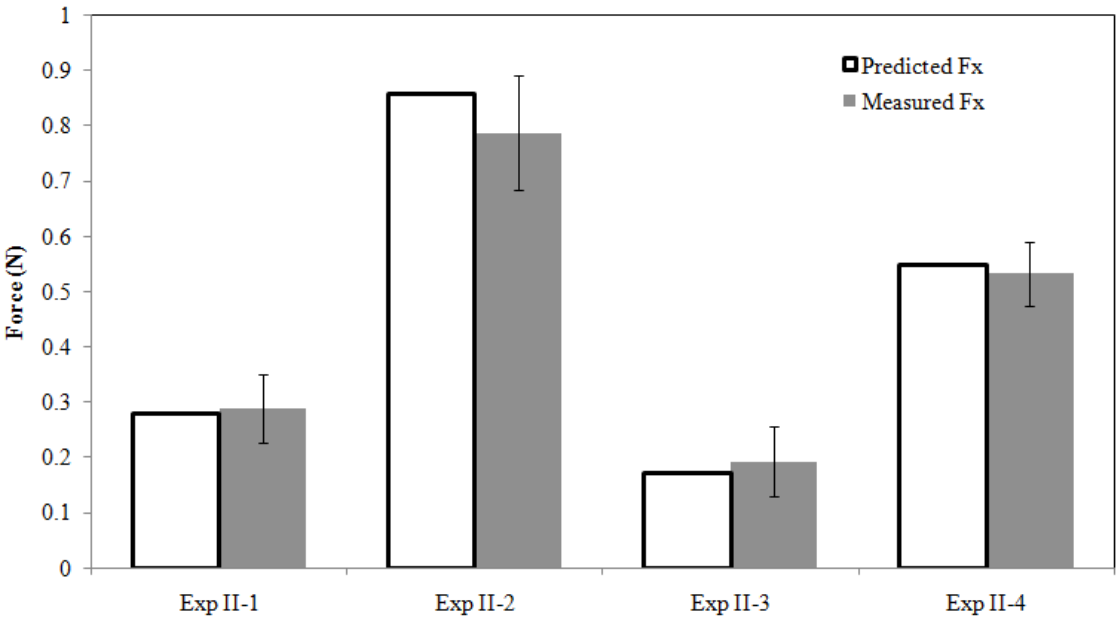

(a)

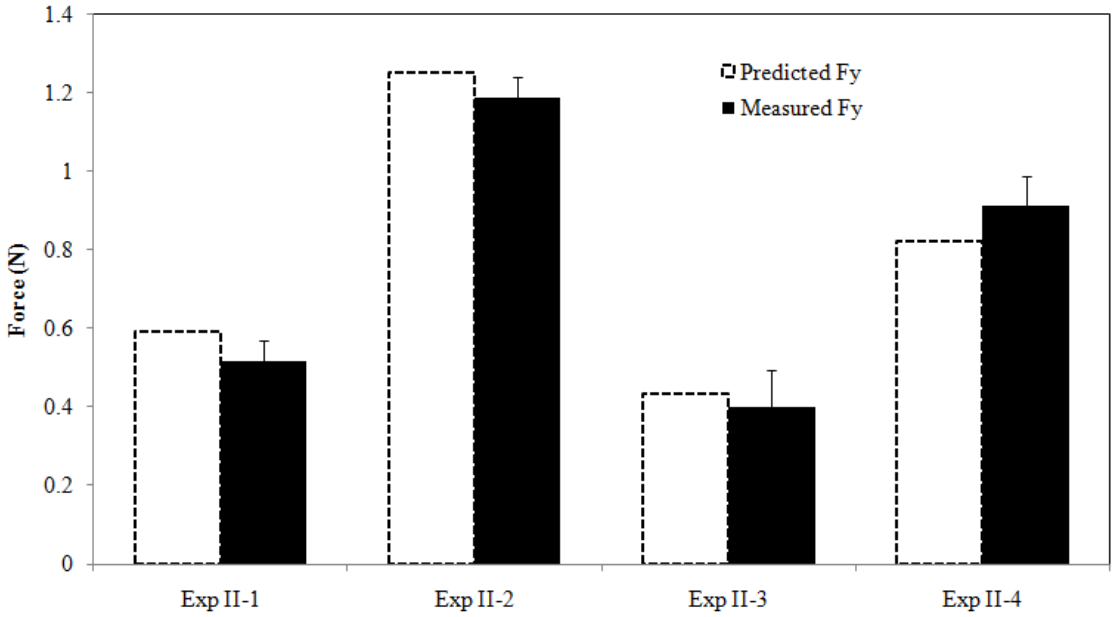

(b)

Figure 5.20: Comparison of predicted and measured absolute peak cutting forces, **(a)** F_x and **(b)** F_y using laser assist under different conditions for Exp II (Table 5.2).

5.6 Discussion

Figure 5.21 presents a comparison of the predicted radial and tangential forces acting on one of the flutes over a cycle of cutting for the conditions listed in the figure. The initial flat portion indicates that the cutting flute is not engaged with the workpiece in that region. The flute starts to engage with the workpiece exactly at 180º, which is due to the assumption of zero cutter runout. As the uncut chip thickness increases, the radial and the tangential forces start to increase gradually from zero to a maximum at the center of cut. The peak radial and tangential forces are lower with laser assist than without laser assist as seen from Fig. 5.21. In addition, there is clear evidence of a near 'flat hat' type force profile with laser assist due to the Gaussian nature of the laser beam, which produces a

maximum temperature rise in the work material at the center of cut. Consequently, there is a drop in the magnitude of the shear yield strength of the material at the point of maximum uncut chip thickness, which causes a reduction in the cutting forces.

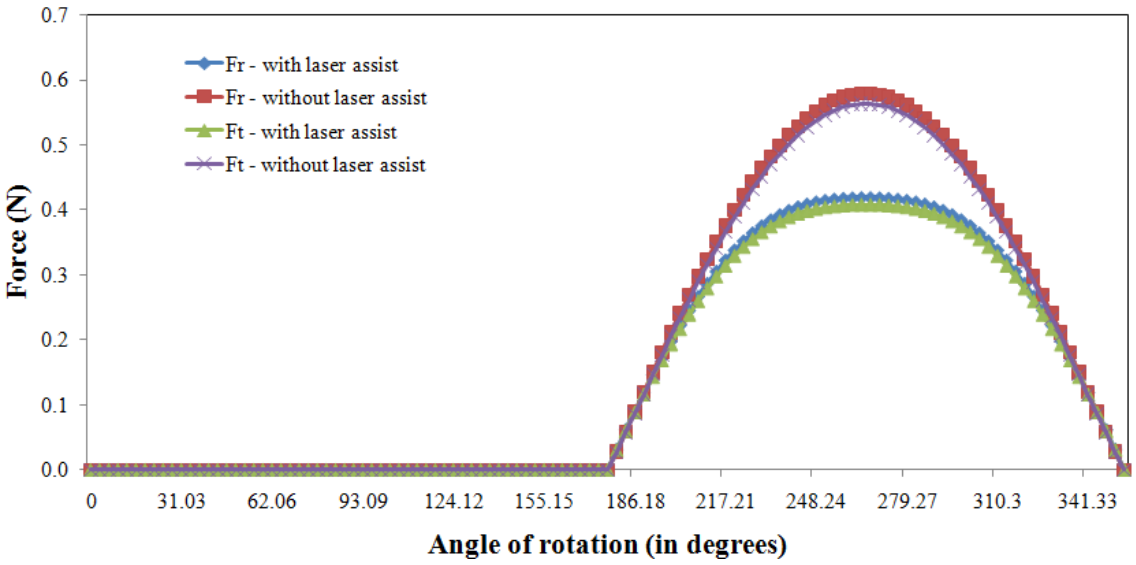

Figure 5.21: Comparison of predicted radial (F_r) and tangential (F_t) cutting forces for one of the flutes with and without laser assist over one full cycle (tool number: 1, feed: 6.6 µm/flute, depth of cut: 16 µm, and laser power: 18 W, no runout, β: 48°).

Figure 5.22 shows the variation of shear yield strength with temperature rise and uncut chip thickness for one of the flutes over a full cycle of cutting. Because of the Gaussian nature of the laser beam, the peak temperature increases, and consequently the shear yield strength decreases at the point of maximum uncut chip thickness. Additionally, as shown in Fig. 5.21, the forces are found to be similar with laser assist (for the conditions shown in the figure) at cutter entry and exit, compared to the without laser case, which is beneficial from the standpoint of burr formation. When the work material becomes soft, it generally leads to an increase in burr formation, which is not

desirable because of additional finishing steps required to remove the burrs. The laser parameters like power, spot size, scanning speed and the distance between the cutting tool and the laser beam can be varied to obtain the desired drop in the shear yield strength while minimizing thermal softening of the work material at cutter entry and exit. This in turn will minimize the burrs at entry and exit.

The combination of laser and cutting parameters (feed: 6.6 µm/flute, depth of cut: 16 µm, and laser power: 18 W, no runout, β: 48º) shown in Fig. 5.21 presents a case which yields the desired effect of reduction in the peak cutting forces at the point of maximum uncut chip thickness, while keeping material strength (and hence the forces) comparable to the without laser assist case at the entry and exit of cut.

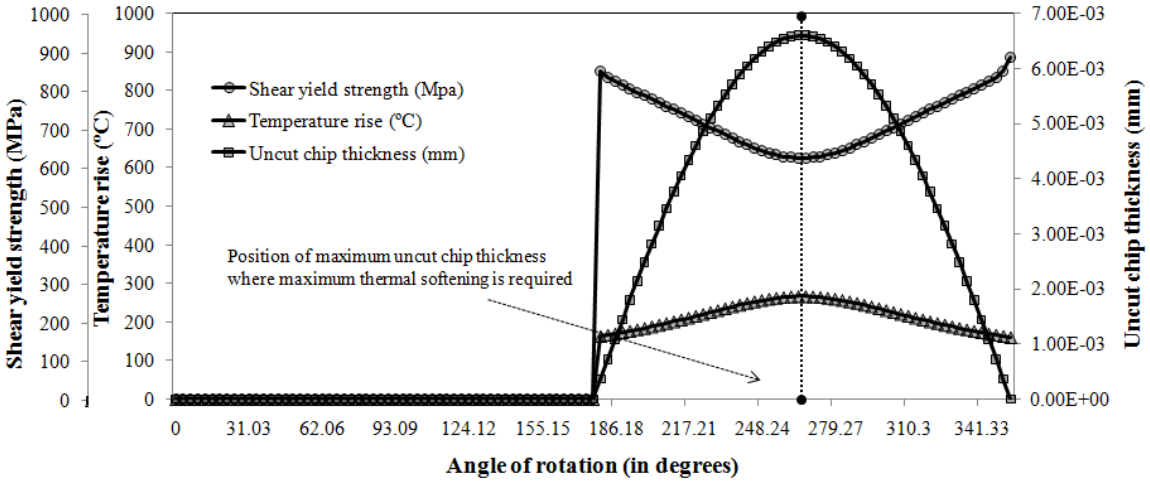

Figure 5.22: Variation of shear yield strength (MPa), temperature rise (ºC) and uncut chip thickness (mm) for one of the flutes over one full cycle (tool number: 1, feed: 6.6 µm/flute, depth of cut: 16 µm, and laser power: 18 W, no runout, β: 48º).

Furthermore, when the laser power is increased to 35 W, as shown in Fig. 5.23, the predicted forces drop significantly at the center of cut, which translates directly into

the possibility of higher material removal rates in LAMM because higher feed rates can be used without causing tool failure. However, the additional force drop at tooth entry and exit as the cutter rotates through the material often results in an increase in burr formation due to greater thermal softening. It is interesting to observe the shift in the peak cutting force from the center of cut due to the competing effects of thermal softening and the increase in uncut chip thickness. Without this model, it would have been impossible to visualize and quantify this shift in the peak cutting forces in LAMM. The shift can have a direct impact on the deflection of the micro tools, because the amount of deflection is proportional to the cutting force. By obtaining a near 'flat hat' type force profile, the variation in deflection with the immersion angle of the end mill can be minimized. In addition, laser assist leads to a reduction in the peak-to-peak value of the cutting forces, which might enhance the fatigue life of the micro tools. This can also have a direct positive impact on the life of the coatings these tools.

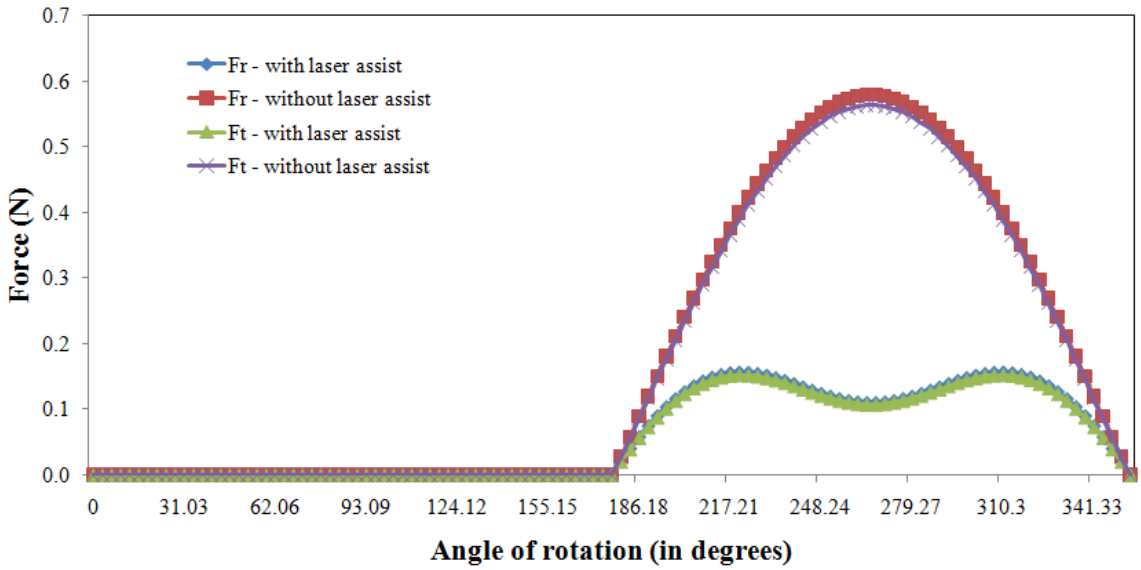

Figure 5.23: Comparison of predicted radial (F_r) and tangential (F_t) cutting forces for one of the flutes with and without laser assist over one full cycle (tool number: 1, feed: 6.6 µm/flute, depth of cut: 16 µm, and laser power: 35 W, no runout, β: 48º).

The variation of radial force, F_r, and tangential force, F_t with the inclusion of the runout effect is shown in Fig. 5.24. Depending on the runout characteristics, there is a shift in the peak cutting force with laser assist. In addition, the peak forces for one of the flutes are higher with runout due to an increase in the effective uncut chip thickness. The symmetric peak distribution shown in Fig. 5.23 is no longer present due to runout, although a peak shift is observed. Hence, runout has a significant effect on the cutting forces obtained in this process, and an accurate knowledge of the parameters will help the end user design the process so as to obtain the desired reduction in cutting forces while minimizing burr formation.

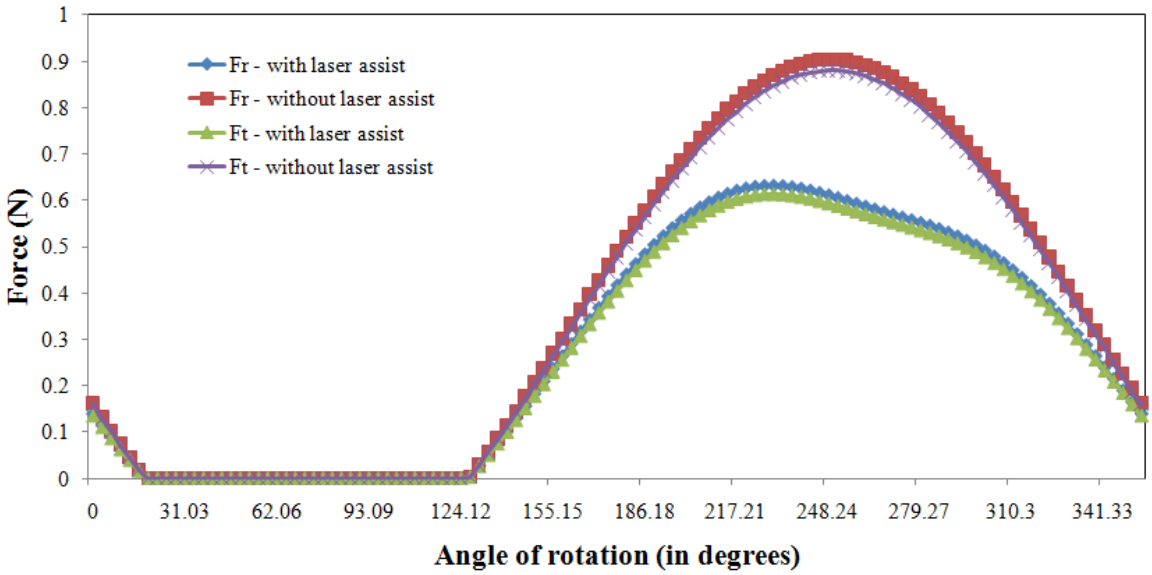

Figure 5.24: Comparison of predicted radial (F_r) and tangential (F_t) cutting forces for one of the flutes with and without laser assist over one full cycle (tool number: 1, feed: 6.6 µm/flute, depth of cut: 16 µm, and laser power: 18 W, runout parameters: A:1.8 µm, B:-0.5 µm, β: 48°).

5.7 Summary

This chapter presented a physics-based force model for LAMM, that captures the effect of thermal softening due to laser heating. The unknown parameters in the model are the friction angle (β) and the runout parameter (c) which are used as calibration parameters. In spite of the assumptions made in the model, the model presented in this chapter predicts the peak-to-peak cutting forces to within 2-15% of the measured values. The following specific conclusions can be drawn from this modeling effort:

- The model predicts the cutting forces with a maximum error of 15% when compared to the measured values, clearly validating the predictive capability of the model.
- The model is insensitive to β over a range of feeds (in this case, between 2.2 μm and 6.6 μm/flute) and also over a range of laser powers (in this case, between 12 and 24 W), which indicates that the model can be used for optimization over a range of feed rates and laser powers.
- The runout plays an important role in determining the profile of the cutting forces and is captured with minimum error using the two lobe runout model.
- The model predicts the shear angle over a range of temperatures by accounting for the variation in shear yield and tensile strength of the workpiece material with temperature.
- The model provides valuable insight into the mechanics of the process. Specifically, knowledge of the shift in the peak cutting forces with the increase in laser power is insightful. Also, the decrease in shear strength at the edge of the cut

is captured, thereby accounting for the observed increase in burr formation with laser assist.

The force model developed and verified in this chapter can be used to select optimum laser parameters that yield the maximum reduction in cutting forces without causing a significant increase in burr formation at the edges due to thermal softening.

CHAPTER 6

CHARACTERIZATION OF LASER ASSISTED MICRO GRINDING OF CERAMICS

The previous two chapters discussed the effect of laser assist on micro milling of A2 tool steel and 52100 bearing steel. The results indicated that the peak resultant force decreases with laser assist. In addition, the amount and rate of tool wear is significantly lower with laser assist. This chapter investigates the effect of laser assist on micro grinding of high strength ceramics. Micro grinding process is employed instead of the micro milling process because of the brittleness of the ceramic material and the superior surface quality requirements of ceramic parts. At the microscale, the maximum depth of cut allowed in rough micro grinding is often limited by the catastrophic failure of the fragile micro grinding tool due to excessive forces produced in the operation. This limitation is addressed in the present thesis by adopting a two-step strategy to reduce the grinding forces by first locally weakening the ceramic material through the introduction of thermal cracks and subsequently removing it mechanically by a micro grinding tool. In the first step, analytical and Finite Element (FE) models are used to predict the size of the thermally cracked region induced by the laser beam in the ceramic. Experiments have been carried out on reaction sinter bonded silicon nitride (1450 HV) to evaluate the effect of laser pre-heating on the micro grinding forces, tool wear, surface morphology and finish.

6.1 Approach

The approach utilized for laser-assisted micro grinding of ceramics is shown schematically in Fig. 6.1. The distance '*d*' indicates the distance between the laser spot and the micro grinding tool. When '*d*' is greater than a critical limit 'd_{crit}', the thermal effects of the laser are not experienced by the grinding tool. Instead, thermal cracks are produced in the irradiated region due to tensile stresses generated during rapid cooling of the ceramic material after the laser has passed over it. Hence, the purpose of laser irradiation is to induce thermal cracks in the region of interest thereby locally weakening the ceramic. By controlling the laser parameters, it is possible to confine these cracks to the material removal volume.

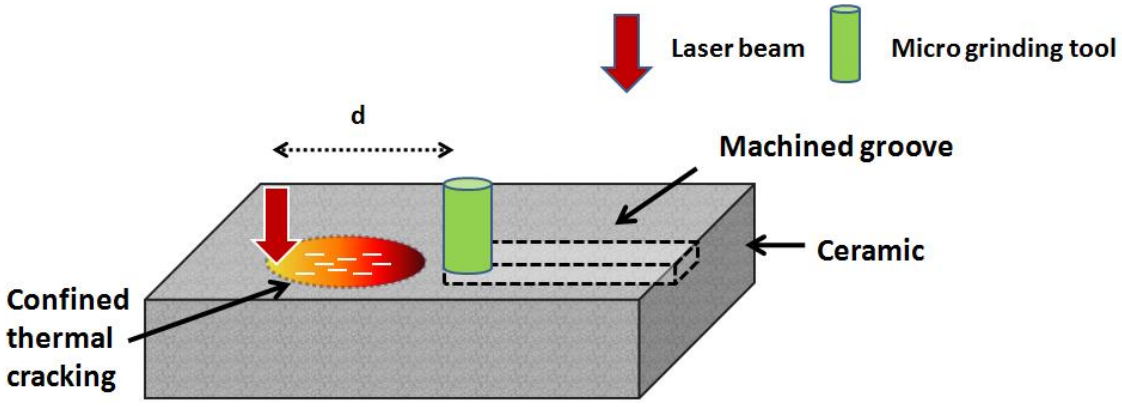

Figure 6.1: Schematic of the proposed mechanism for material removal ($d>d_{crit}$).

The proposed laser-assisted micro grinding process is carried out in the following two steps:

1. Scan the ceramic with the laser to induce localized tensile thermal stresses in the material. When this stress exceeds the fracture stress, cracks form on the surface.

2. Use a micro grinding tool to mechanically remove the laser affected (weakened) region at higher material removal rates than possible in conventional micro grinding.

The last step can be followed by a series of conventional finish grinding steps to improve the surface finish. This two-step strategy is particularly advantageous since coolants can be used without occlusion of the laser beam (unlike in prior laser-assisted grinding work [8, 9]). The following section focuses on the details of the workpiece material used to evaluate the proposed two step approach. Also presented are analytical and finite element models of the laser scanning process to determine the laser parameters necessary to induce thermal cracks in a specific volume of the ceramic.

6.2 Workpiece Material

The workpiece material used in the micro grinding experiments was a 25 mm (L) x 25 mm (W) x 3.75 mm (D) reaction bonded silicon nitride (CERALLOY®) sample. This material is known for its high temperature strength, excellent fracture toughness, high hardness and tribological properties. Some of the physical and mechanical properties of this ceramic are listed in Table 6.1. Consequently, this material is used in bearings where minimum wear with minimal lubrication is required.

Table 6.1: Properties of CERALLOY® (Ceradyne, Inc.).

Property	
Theoretical density (%)	>99.5
Flexural strength (MPa)	700-800
Elastic modulus (GPa)	310
Hardness (HV)	1450
Thermal conductivity (W/mK)	26
Thermal expansion coefficient (/ºC)	3.1×10^{-6}

6.3 Step 1: Laser Scanning

This section will focus on the details of the first of the two step process proposed earlier in section 6.1. The main purpose of the laser scanning step is to induce cracks in the work material and confine them to the desired region of material removal. Figure 6.2 shows a typical cross-section of the laser scanned specimen for the conditions listed in the figure. The depth of the heat-affected region is ~30 μm as indicated in Fig. 6.2. A thin layer of material (5-7 μm) close to the centerline of the laser scan becomes amorphous and is easily removed mechanically. This is due to the Gaussian nature of the laser beam, which produces temperatures above the dissociation temperature of the ceramic at the center of the laser spot.

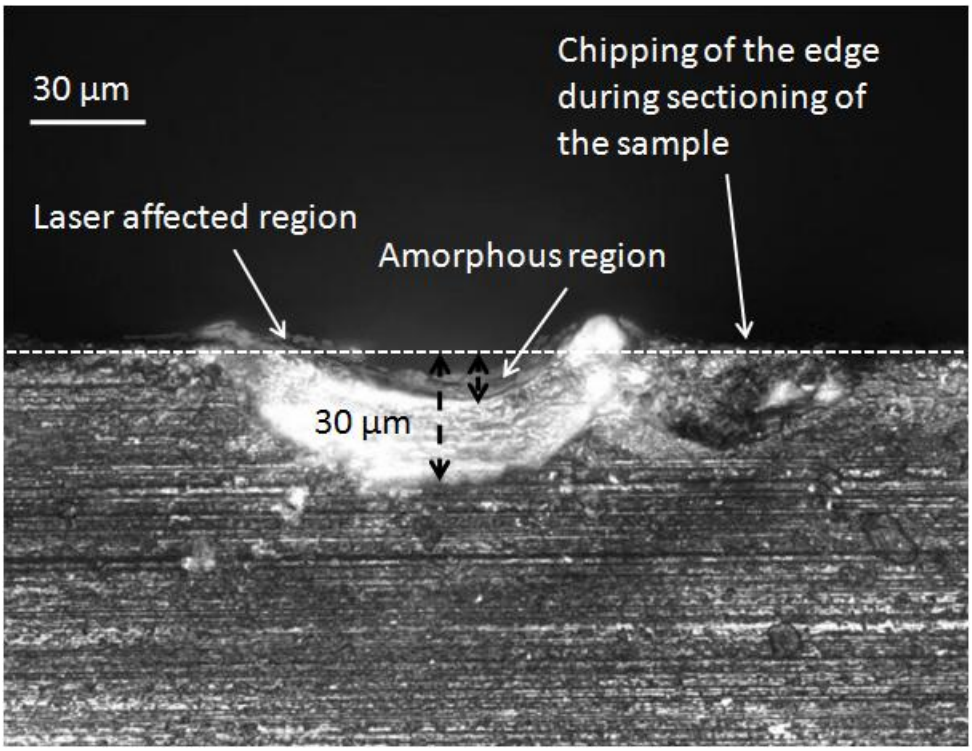

Figure 6.2: Optical micrograph of the cross-section of the laser scanned surface showing the thermally affected region (white color) (laser power: 18 W, scan speed: 100 mm/min, spot size: 280 µm).

The calculation of depth and width of the thermally affected region is essential to confine the thermally affected volume to the region of material removal. Additionally, this information will be useful in optimizing the process parameters to induce cracks in the desired region of interest. The following section describes the use of analytical and Finite Element (FE) models to predict the size of the region with thermal cracks. The finite element model is also developed since it will be shown that the analytical model fails to accurately predict the size of the thermally affected region when the stress state deviates from a state of plane stress. The predicted values are compared with measured values to evaluate the adequacy of the two models.

6.3.1 Analytical Model

Laser scanning generates a thermal gradient in the ceramic material, which results in rapid thermal expansion during laser heating and rapid thermal contraction during subsequent cooling. During the heating stage, thermal expansion is prevented by the surrounding rigid material resulting in compressive stresses. In the subsequent cooling stage, tensile stresses are generated when the ceramic material tries to contract under steep thermal gradients and is prevented from doing so by the rigid surrounding material. These tensile stresses cause fracture of the ceramic material, if they are greater than the critical thermal fracture stress. This is the physical basis for the application of the following model.

As a first approximation, the thermally affected region is modeled as a circular disc with radial temperature variation, *T(r)*, which is induced by the laser beam as shown in Fig. 6.3. The thickness of the disc '*h*' and the diameter '*2a*' indicate the depth and width of the thermally affected region, respectively. Since preliminary experiments indicate that '*h*' is much smaller than the diameter '*2a*' of the disc, the stresses in the material are assumed to be in a state of plane stress ($h/2a << 1$) [117]. In addition, the end and side faces of the disc are assumed to be traction free. This is a reasonable assumption since the cracks generated due to the thermal gradients will cause separation of the affected material from the unaffected base material, thus making the faces traction free during the cooling stage.

The radial and tangential stresses at a distance '*r*' from the center of a solid disc of radius '*a*' subjected to a temperature distribution, *T(r)*, is given by [117] ,

$$\sigma_{rr} = E\left[\frac{1}{a^2}\int_0^a \alpha T(r) r dr - \frac{1}{r^2}\int_0^r \alpha T(r) r dr\right]$$
$$\sigma_{\theta\theta} = E\left[-\alpha T + \frac{1}{a^2}\int_0^a \alpha T(r) r dr + \frac{1}{r^2}\int_0^r \alpha T(r) r dr\right] \quad (6.1)$$

Where, E is the young's modulus, and α is the thermal expansion coefficient. The temperature distribution is estimated using the moving heat source model discussed earlier in chapter 4.

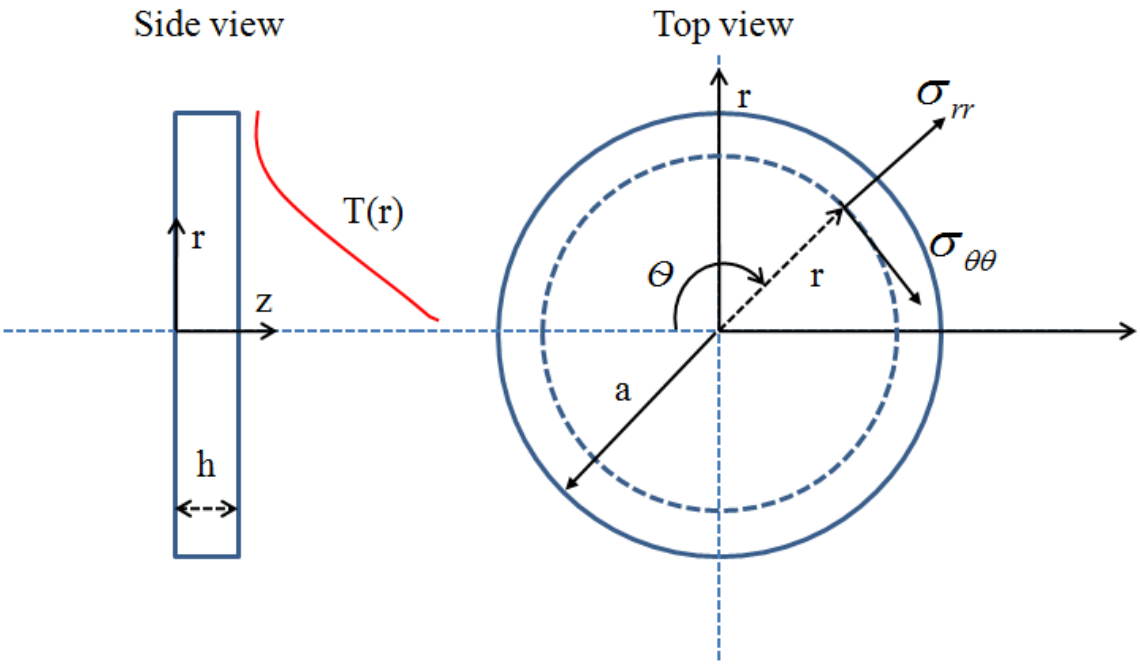

Figure 6.3: Model of a circular disc of diameter '*2a*' and thickness '*h*' subjected to a temperature distribution *T(r)*, showing radial and tangential stresses.

When the heat source is removed, the material starts to contract (coefficient of thermal contraction = -α). This thermal contraction generates tensile stresses in the material, which are estimated using Eq. 6.1. When the tensile stresses exceed the thermal

fracture stress of the ceramic material (σ_f), cracks nucleate resulting in a weak base material. The width of the affected region is estimated from the in-plane stress distribution ($z=h$) calculated using Eq. 6.1. From the stress distribution, the location at which the tensile stresses exceed the critical thermal fracture stress is identified to determine the width of the cracked region.

To determine the depth of the cracked region, the in-plane stresses are estimated in different planes along the depth of the ceramic material. By identifying the maximum depth at which the in-plane stresses exceed the critical thermal fracture stress of the ceramic, the cracked depth is determined. In determining the in-plane stresses at various depths, the stresses in the different planes are assumed to not interact with each other. This is a reasonable assumption for thin discs ($h<<2a$), but when the thickness of the disc approaches the diameter ($h \sim 2a$), the stresses in the different planes will interact to reduce the net displacement in order to satisfy the compatibility condition. As a first approximation, the interaction between stresses in the different planes in the depth direction is neglected. The validity of this assumption is later tested by comparing the calculated depth and width of the cracked region with actual measurements obtained from laser scanning experiments. The calculated depth value provides an upper bound on the depth of the affected region.

As an example, the variation of stresses on the surface of a silicon nitride specimen (E = 320 GPa, and α = 2.2e-6 / °C [118]) laser scanned at a speed of 100 mm/min, and a laser power of 25 W and spot size of 280 μm, is shown in Fig. 6.4 (a) and (b). The calculated radial stress is found to be more than the critical thermal fracture stress of 350 MPa in a circular region of radius 195 μm, indicating the half-width of the

affected region (see Fig. 6.4(a)). The critical thermal fracture stress data is obtained from actual laser shock experiments reported in the literature [118]. The calculated tangential stress is found to be above the critical thermal fracture stress up to a radial distance of 91 μm (see Fig. 6.4(b)). This indicates that the width of affected region is determined by the radial stresses, which cause the cracks to nucleate predominantly in the laser scanning direction.

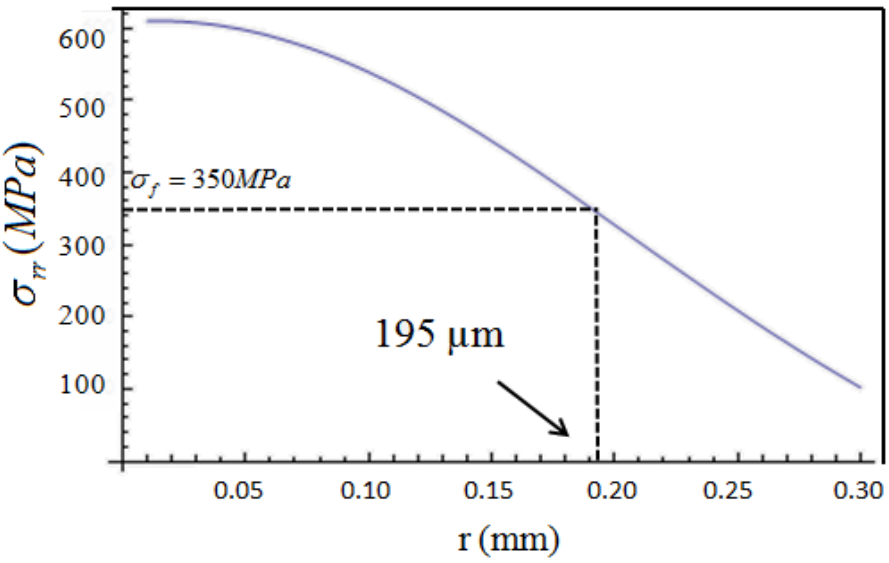

(a)

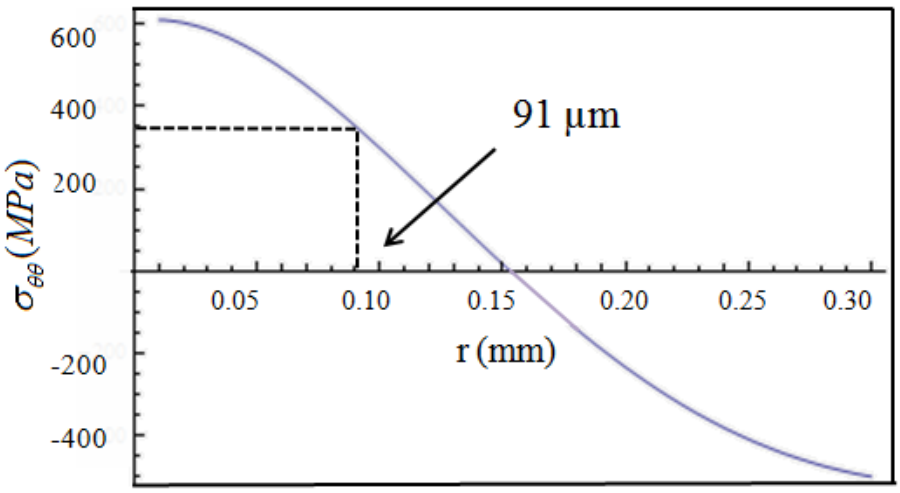

(b)

Figure 6.4: Variation of (a) radial, and (b) tangential surface stresses along the radius of a circular disc, subjected to a temperature field produced by a Gaussian 1.06 µm laser beam of power: 25 W, scanning speed: 100 mm/min, and spot size: 280 µm.

The SEM image in Fig. 6.5 shows the presence of longitudinal cracks in the laser scanning direction confirming that the radial stresses are predominant at the edge of the laser scanned region, causing the cracks to propagate. In Fig. 6.6, the variation of radial stresses 70 µm beneath the surface calculated using equation 6.1 is shown. At this depth, the radial stress in the center drops below the critical fracture stress of 350 MPa. Hence, 70 µm is the predicted depth of the thermally cracked region. The experimental validation of the model is discussed in detail in section 6.3.3.

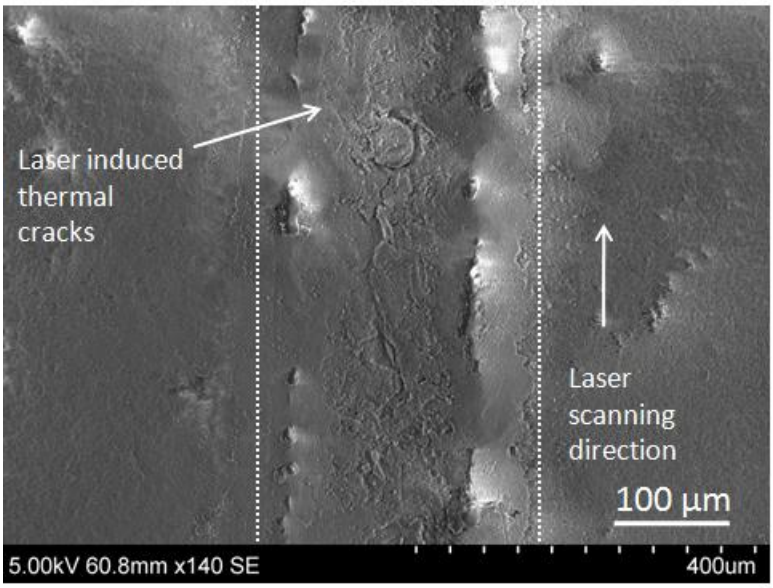

Figure 6.5: SEM micrograph of laser scanned silicon nitride surface showing thermal cracks induced by laser irradiation (laser power: 15 W, scan speed: 100 mm/min, spot size: 280 µm).

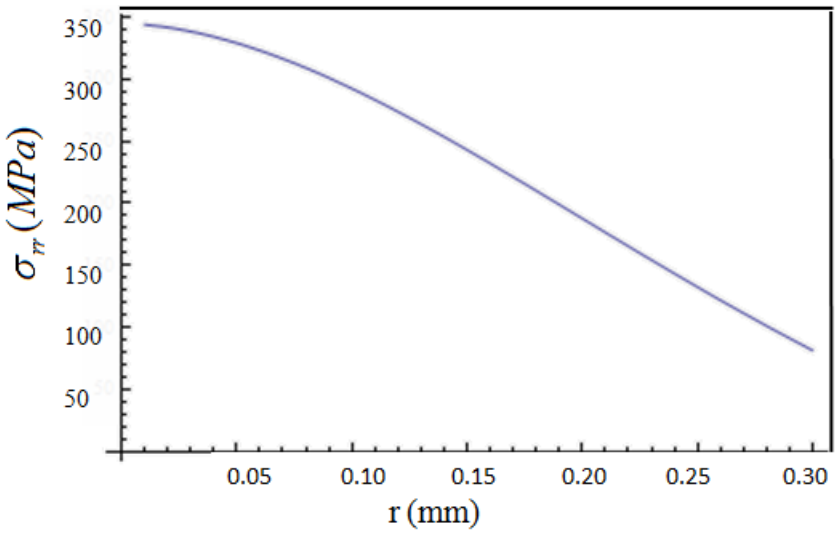

Figure 6.6: Variation of radial stress with the radius of a circular disc, 70 µm beneath the surface, subjected to a temperature field generated by a 1.06 µm Gaussian laser beam of power: 25 W, scanning speed: 100 mm/min, and spot size: 280 µm.

6.3.2 Finite Element Model

In the analytical model described in section 6.3.1, a state of plane stress is assumed. In addition, the stresses in the planes at different depths are assumed to not interact with each other. In the FE method, the size of the thermally affected region is predicted by relaxing the foregoing assumptions and considering a full three-dimensional stress state. In addition, it gives the depth of the thermally cracked region directly by identifying the location where a particular stress component has exceeded the critical thermal fracture limit.

This section will focus on developing a FE model to predict the width and depth of the thermally cracked region. Based on the temperature distribution calculated using the moving heat source model discussed in Chapter 4, the thermal stress distribution is obtained by solving the following set of thermo-mechanical equations using the FE method. The equilibrium equations in three dimensions are given by [117],

$$\begin{aligned} \frac{\partial \sigma_{xx}}{\partial x} + \frac{\partial \tau_{xy}}{\partial y} + \frac{\partial \tau_{xz}}{\partial z} &= 0 \\ \frac{\partial \tau_{xy}}{\partial x} + \frac{\partial \sigma_{yy}}{\partial y} + \frac{\partial \tau_{yz}}{\partial z} &= 0 \\ \frac{\partial \tau_{xz}}{\partial x} + \frac{\partial \tau_{yz}}{\partial y} + \frac{\partial \sigma_{zz}}{\partial z} &= 0 \end{aligned} \tag{6.2}$$

The constitutive equations relating the stresses and strains for the thermo-mechanical problem, are given by,

$$
\begin{aligned}
\sigma_{xx} &= \lambda e + 2\mu\varepsilon_{xx} - (3\lambda + 2\mu)\alpha T \\
\sigma_{yy} &= \lambda e + 2\mu\varepsilon_{yy} - (3\lambda + 2\mu)\alpha T \\
\sigma_{zz} &= \lambda e + 2\mu\varepsilon_{zz} - (3\lambda + 2\mu)\alpha T \\
\sigma_{xy} &= 2\mu\varepsilon_{xy} \\
\sigma_{xy} &= 2\mu\varepsilon_{xy} \\
\sigma_{xy} &= 2\mu\varepsilon_{xy}
\end{aligned}
\tag{6.3}
$$

where μ and λ are Lame's elastic constants. The analytical model discussed earlier in section 6.3.1 is a special case solution of Eqs. 6.2 and 6.3. These equations can be solved analytically only for a few cases reported in literature [117]. Otherwise, numerical techniques have to be employed to solve these equations, one such technique being the FE method. The FE method is implemented in this work using the commercially available ANSYS code.

The geometry of the FE model is shown in Fig. 6.7 along with the imposed temperature boundary condition. The temperature distribution is estimated at each of the nodes using the moving heat source model discussed in chapter 4. The element selected for meshing the model is SOLID185, which is an eight node element used for 3-D modeling of solid structures subject to stress and temperature loads. The model geometry consists of 213,282 nodes. The temperature rise is applied as a boundary condition to each of these nodes. One of the nodes (x=0,y=0,z=0) is fixed to prevent rigid body motion and the block is free to expand in all directions.

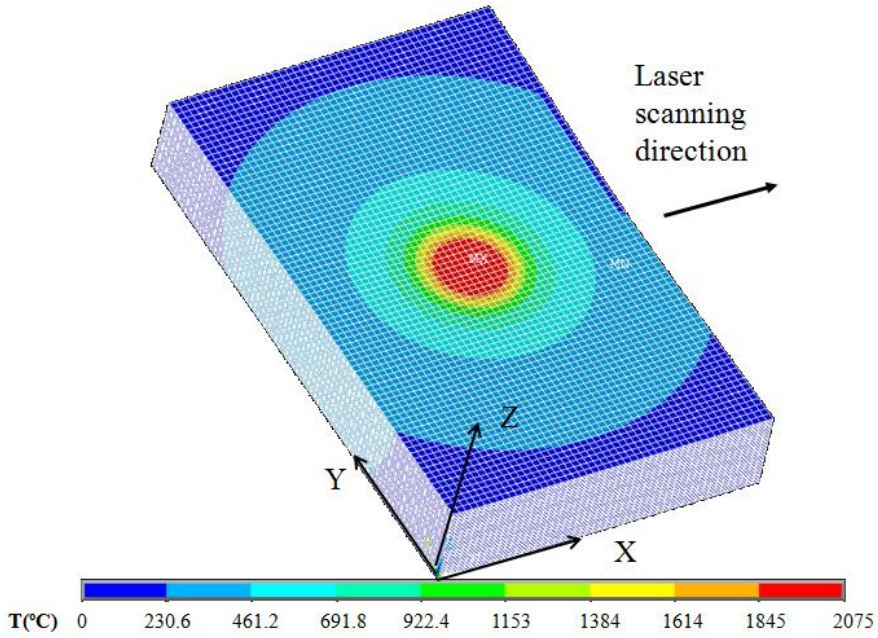

Figure 6.7: FE model of a slab of thickness '*t*', subjected to a temperature distribution *T(x,y,z)* at every node (model dimensions: 1.6 mm x 1 mm x 0.25 mm).

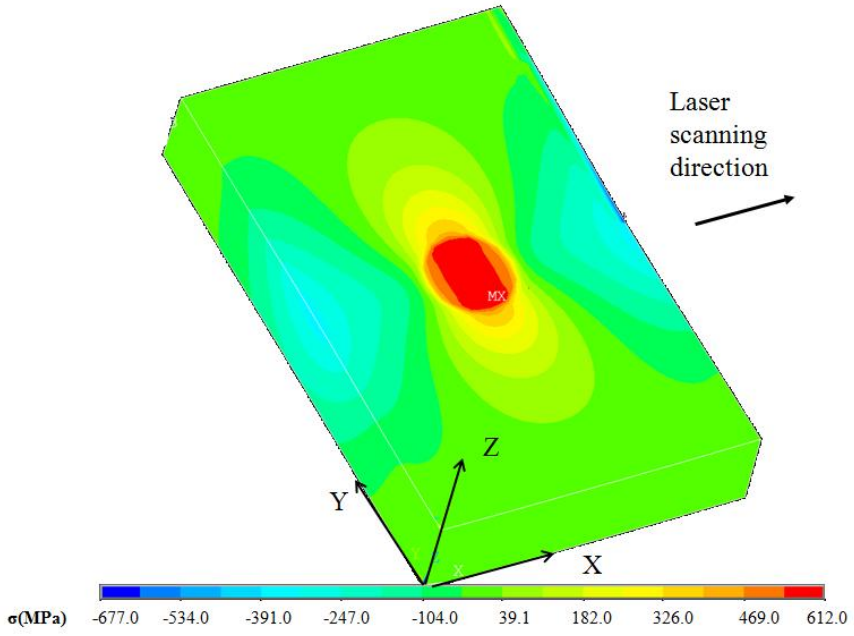

Figure 6.8: Variation of σ_{yy} on the surface of the laser scanned specimen (laser power: 25 W, scanning speed: 100 mm/min, and spot size: 280 μm).

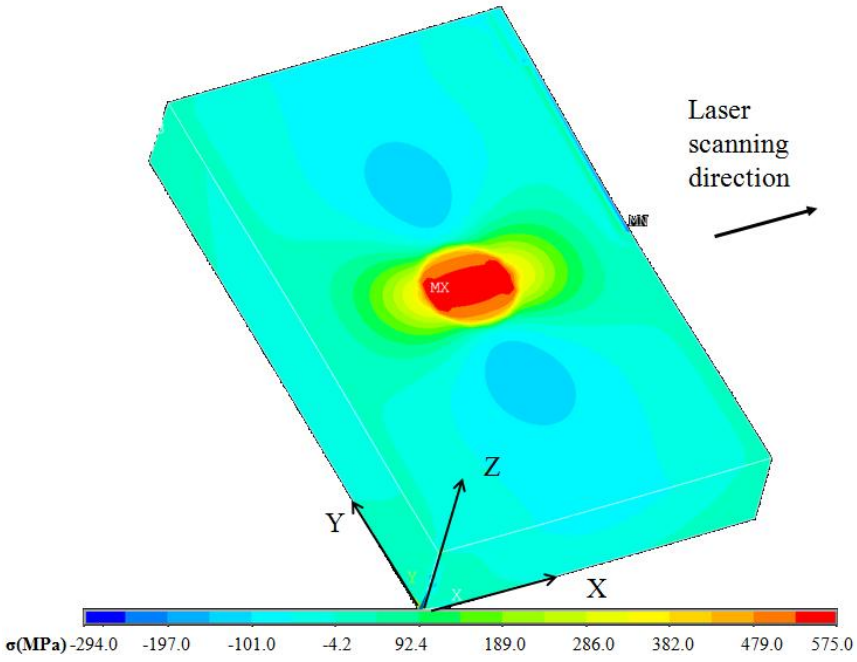

Figure 6.9: Variation of σ_{xx} on the surface of the laser scanned specimen (laser power: 25 W, scanning speed: 100 mm/min, and spot size: 280 μm).

Figures 6.8 and 6.9 show the stress distributions during thermal contraction in the laser scanned material. It can be seen that the stress in the Y direction (σ_{yy}) governs the width of the thermally cracked region, which is similar to the results obtained using the analytical model discussed in section 6.3.1. The width of the cracked region for the laser scanning conditions listed in the figure is found from the FE model to be 340 μm. The comparison of the model with the experiments is discussed later in section 6.3.3. Figure 6.10 shows the stress distribution along the center plane (x=0.8 mm) in the depth (Z) direction. The depth of the cracked region is found to be 70 μm, which is the depth to which the stresses exceed the fracture strength of the ceramic material.

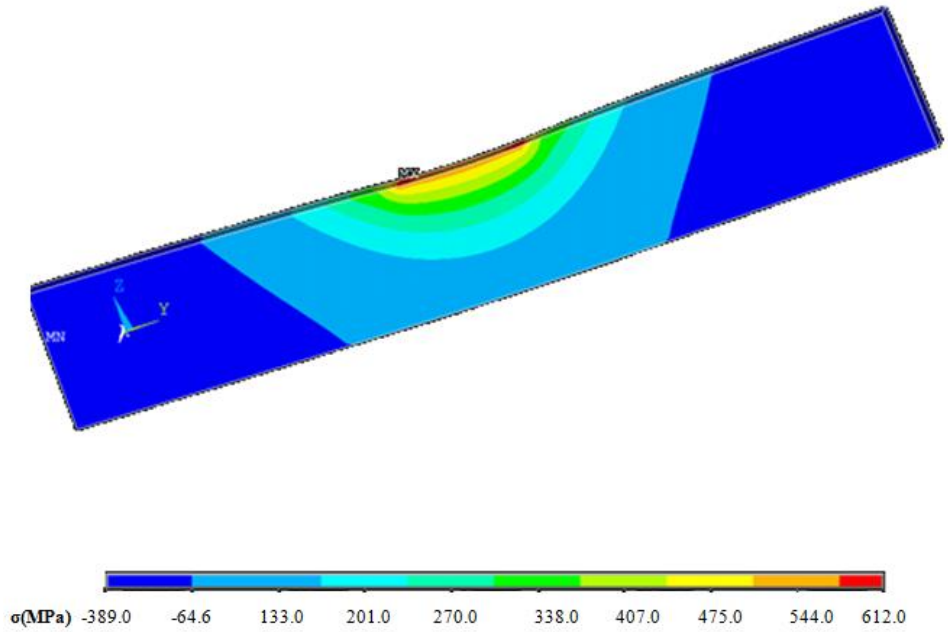

Figure 6.10: Variation of σ_{yy} (x=0.8 mm plane in Fig. 6.7) along the depth of the laser scanned specimen (laser power: 25 W, scanning speed: 100 mm/min, and spot size: 280 μm).

6.3.3 Laser Scanning Experiments and Model Validation

Laser scanning experiments for the different laser parameters listed in Table 6.2 were performed to determine the width and depth of the thermally affected region in silicon nitride. The width and depth of the affected region were measured using an optical microscope as shown earlier in Fig. 6.2. The three dimensional view of a typical laser scanned specimen with all the fractured particles removed is shown in Fig. 6.11. Comparisons of the measured values and predicted values using the analytical model discussed in section 6.3.1, and the FE model discussed in section 6.3.2, are presented in Figs. 6.12 and 6.13.

Table 6.2: Experimental plan.

Experiment	Laser power (W)	Scan speed (mm/min)	Spot size (µm)
I	15	100	280
II	20	100	280
III	25	100	280
IV	15	600	280
V	20	600	280
VI	25	600	280

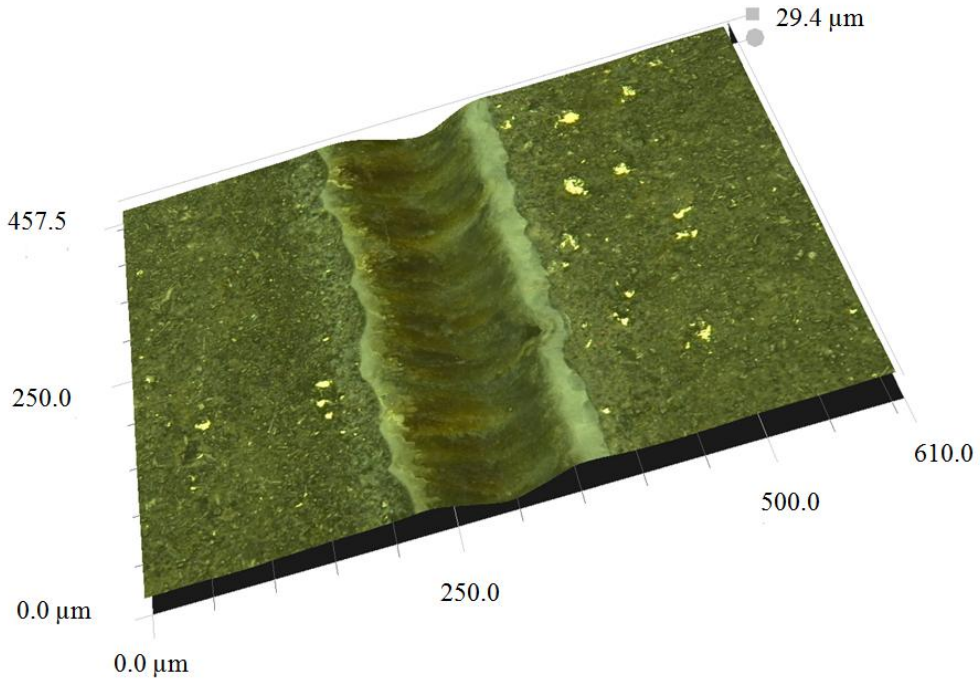

Figure 6.11: Optical micrograph of the laser scanned specimen (laser power: 15 W, scan speed: 100 mm/min, spot size: 280 µm). Note that the thermally cracked material has been removed by light polishing.

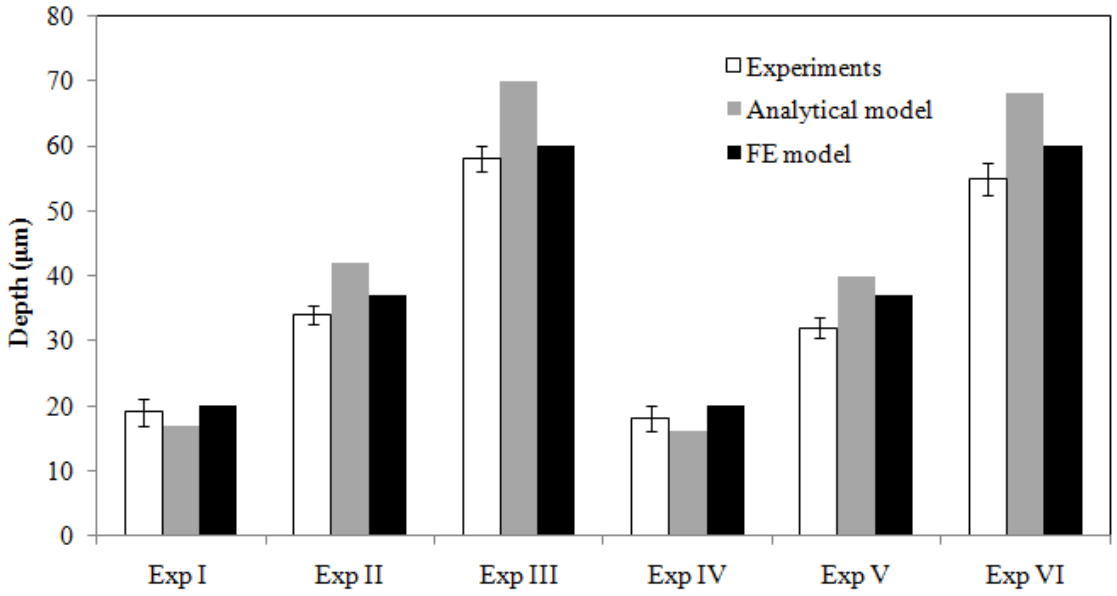

Figure 6.12: Comparison of the measured depth of affected region with the predicted values obtained using the analytical and FE models.

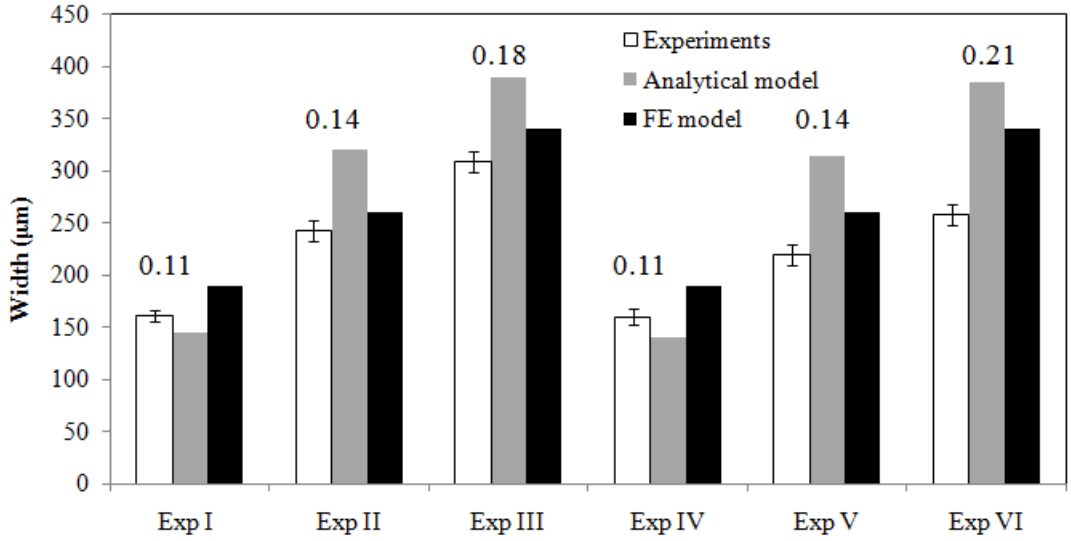

Figure 6.13: Comparison of the measured width of affected region with the predicted values obtained using the analytical and the FE models (Measured '*h/2a*' ratios are shown above each experiment).

Figures 6.12 and 6.13 clearly indicate that the width and depth of thermally cracked region increases with increase in laser power while the scanning speed has an insignificant effect on the size of the affected region. The analytical model tends to over predict the depth and width of the cracked region. This is primarily due to the assumption that stresses in different axial planes do not interact with each other. In addition, as seen from the figures, the error in the prediction of the depth and width of the affected region depends on the (*h/2a*) ratio of the circular plate. At lower laser powers, the '*h/2a*' ratio is <<1, i.e., it approaches a state of plane stress. When this ratio decreases, the errors in the predicted depth and width of the affected region decrease as is evident from Figs. 6.12 and 6.13. Hence, the analytical model can predict the depth and width with reasonable accuracy when the volume of the cracked region is small. The difference between the measured and the predicted values of the depth of cracked region decreases from 25% to less than 10% when the laser power decreases from 25 W (Exp III) to 15 W (Exp I). Similarly, the difference between the predicted and measured values of the width of the cracked region decreases from 30% to less than 12% when the laser power decreases from 25 W to 15 W. The average difference between the FE model prediction and the measured depths is ~9%, and is ~15% for the width of the cracked region, which is reasonable considering the approximations made in the model.

For all the micro grinding experiments discussed later, a 0.8 mm diameter micro grinding tool is used, which is greater than the spot size of the laser (280 μm). Hence, multiple overlapping passes are needed to scan the full width of the slot to be ground in the specimen. The specimen is scanned using a laser beam power of 18 W (spot size: 280 μm) with a scanning speed of 100 mm/min. Under these laser scanning conditions, the

depth of the affected region is predicted to be 30 μm by the FE model, which agrees favorably with the measured value as seen from Fig. 6.2. The SEM micrograph of the surface of the scanned specimen is shown in Fig. 6.14, which indicates significant weakening of the ceramic due to cracking. The overlap of the laser scans can be changed depending upon the spot size of the laser, but is kept constant at 0.1 mm for all the experiments discussed in section 6.4.

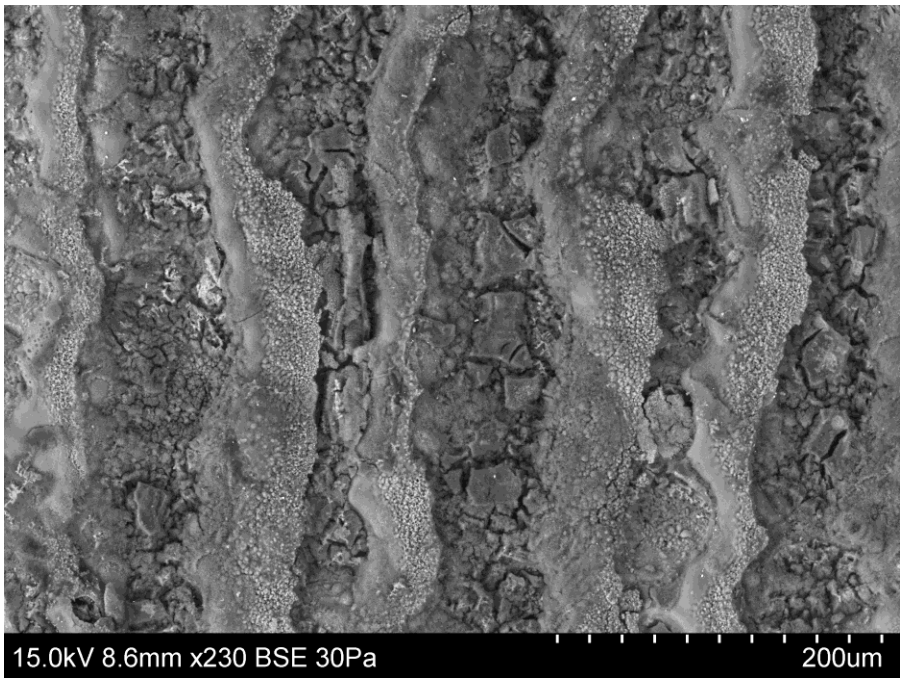

Figure 6.14: SEM Micrograph of laser scanned silicon nitride surface showing thermal cracks induced by laser irradiation (laser power: 18 W, scan speed: 100 mm/min, spot size: 280 μm, overlap: 0.1 mm).

6.3.4 Possible Applications of the Model

The FE model and the analytical model (for lower laser powers) can be reformulated to determine the laser scanning conditions necessary to induce cracks in a known volume of the ceramic material. Consequently, these models can serve as process parameter design

tools that can be used by the process planner to determine the process parameters in step 1 of the proposed two step approach. The following section describes step 2 of the proposed approach.

6.4 Step II: Micro Grinding

6.4.1 Experimental Plan

Most of the tests reported in this step were performed with metallic bond (180-200 grit size) 800 µm diameter abrasive diamond grinding pencils. Figure 6.15 shows a metallic bonded abrasive grinding pencil. In addition, tests were conducted with electroplated diamond tools of the same diameter but with a grit size of 220 µm (see Fig. 6.16). Note that the electroplated tools have a higher number of abrasive grits than the metallic bonded micro grinding pencils. However, the electroplated tools have a single layer of diamond abrasive that is bonded to the tool shank using a nickel substrate, while the metallic bonded tools have more than one layer of abrasive distributed uniformly in the matrix and bonded to the base material using a high temperature bond. Hence, metallic bonded tools can be dressed to expose unused grains, while electroplated tools cannot be dressed.

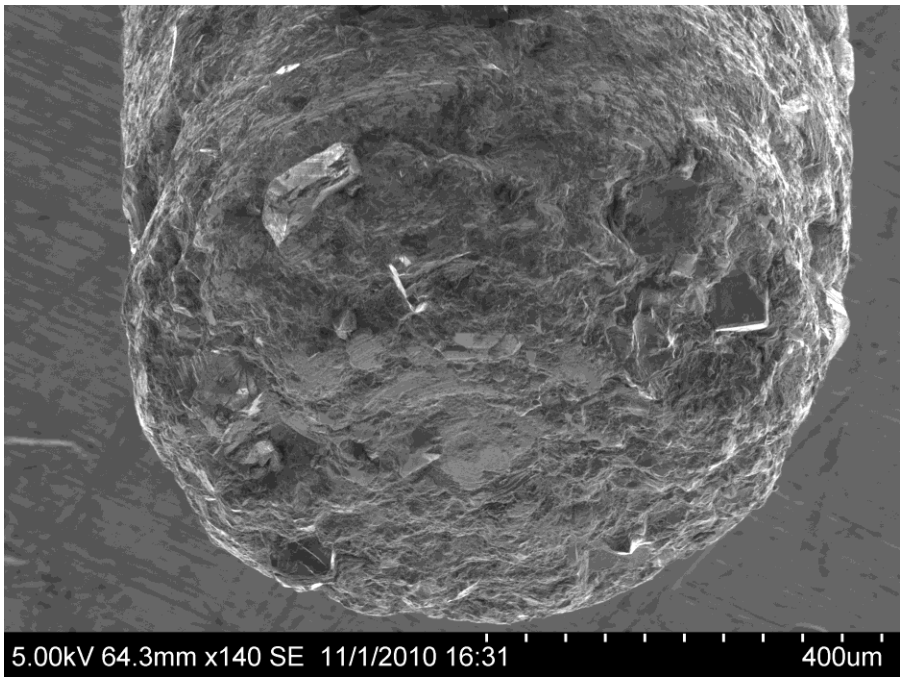

Figure 6.15: Metallic bonded micro abrasive pencil.

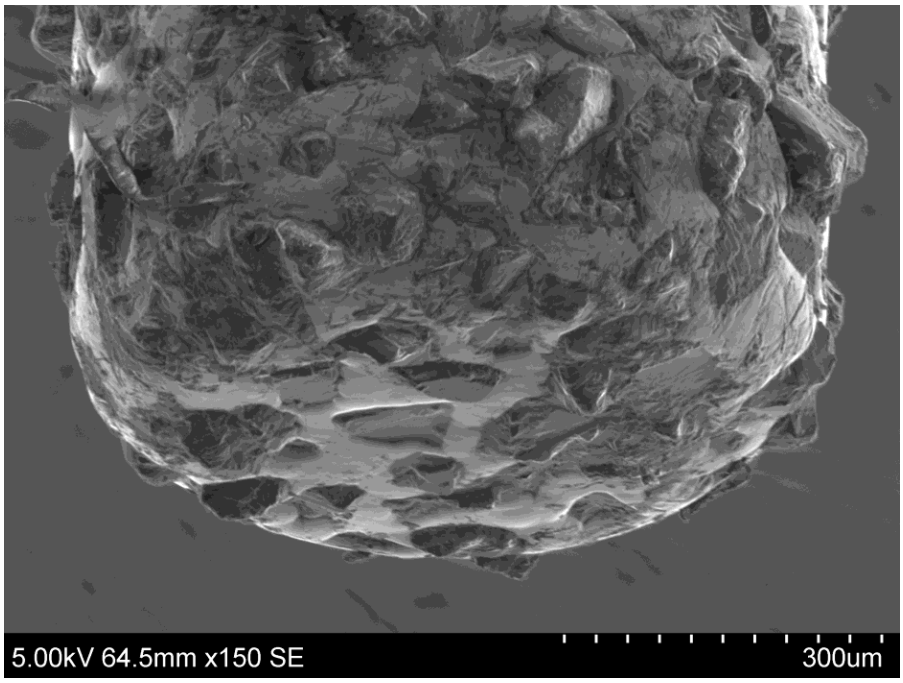

Figure 6.16: Electroplated micro abrasive pencil.

Dry micro grinding tests were carried out with metallic bonded and electroplated abrasive diamond grit pencils of 0.8 mm diameter at different depths of cut as listed in Table 6.3. The objective was to grind a feature of dimensions 8 mm (L) x 0.8 mm (W) x 50 μm (D). The entire specimen was first laser scanned under conditions given in Fig. 6.14. Ten micro grinding passes were then made in Exp I and I-L while five passes were made in Exp II and Exp II-L. The length of each pass is 8 mm. Note that the depth of cut per pass is different in Exp I and II. The suffix 'E' in Table 6.3 denotes electroplated tools.

Table 6.3: Experimental plan.

Experiment	Wheel speed (rpm)	Feed rate (mm/min)	Depth of cut (μm/pass)	Laser (Y/N)
I	80,000	50	5	N
II	80,000	50	10	N
I-L	80,000	50	5	Y
II-L	80,000	50	10	Y
I-E	80,000	50	5	N
I-E-L	80,000	50	5	Y
II-E-L	80,000	50	10	Y

The feed rate was kept constant at 50 mm/min in all tests. These grinding conditions were chosen from a set of preliminary tests where the maximum grinding force allowed was limited to 25 N. This force limit is the typical fracture limit of 0.8 mm diameter abrasive pencils as reported by Hoffmeister et al. [80]. The depth of cut/pass

was limited to 5 μm/pass for electroplated tools without laser assist because of higher grinding forces observed with these tools.

6.4.2 Measured Responses

The measured responses include the maximum and average resultant grinding force, surface roughness, tool wear and dimensions of the machined groove. The grinding forces were measured using a 3-axis piezoelectric platform dynamometer (Kistler Minidyn 9256C2) at a sampling rate of 10 kHz. The resultant grinding force at each sampling instant was calculated as $R=\sqrt{F_x^2+F_y^2+F_z^2}$ and the average value for each groove is reported here. The groove geometry was measured using a confocal laser scanning microscope (Olympus LEXT). In addition, the three dimensional surface roughness parameters (S_a, S_q) reported in the chapter were measured over a 400 x 200 μm^2 area. The tool condition before and after grinding was observed in a SEM.

6.5 Results and Discussion

6.5.1 Grinding Force

The average and maximum resultant grinding forces versus the groove number (or grinding pass number) for all experiments is shown in Figs. 6.17 through 6.20. It can be seen that the magnitudes of the resultant force with laser assist are lower than without laser assist. The average (and maximum) force generally increases with increasing grinding distance primarily because of tool wear, which is discussed in section 6.2.3. It

can also be clearly seen from Fig. 6.20 that the reduction in resultant grinding force with laser assist is higher for the initial passes with a axial depth of cut of 10 μm/pass when using electroplated tools. This is attributed to the reduction in strength of the ceramic near the surface due to the thermally affected zone produced by laser irradiation in the first step of the process. The depth of the laser affected region is ~30 μm for the laser scanning conditions used in Step I (see Fig. 6.2). The harder base material present below the thermally affected region is responsible for the higher grinding forces (and therefore smaller force reduction) in subsequent passes over the same area. This reduction in force is not noticeable for the other cases since the actual depth of the groove is ~30 μm for the metallic bonded tools and ~55 μm for the electroplated tools (see section 6.5.4). When considered over all grinding passes, the average (maximum) resultant forces in Exp I-L are 43.2% (28.6%) lower than in Exp-I. Similarly, the forces in Exp II-L are 28.6% (35.7%) lower than those in Exp II. It is noteworthy that even though the depth of cut in Exp II-L is twice the depth of cut in Exp I, the forces in Exp II-L are only slightly higher than in Exp I, thereby indicating the possibility of higher material removal rates in the laser-assisted process.

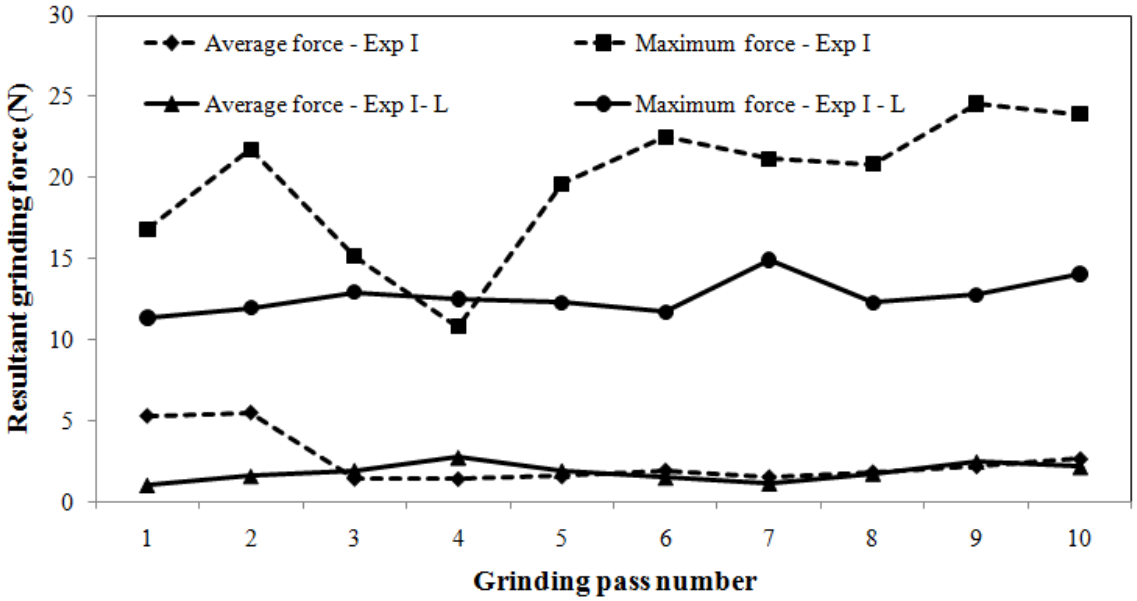

Figure 6.17: Average and maximum resultant forces (averaged over each groove) versus grinding pass number (spindle speed: 80,000 rpm, feed: 50 mm/min, axial depth/pass: 5 µm, length/pass: 8 mm).

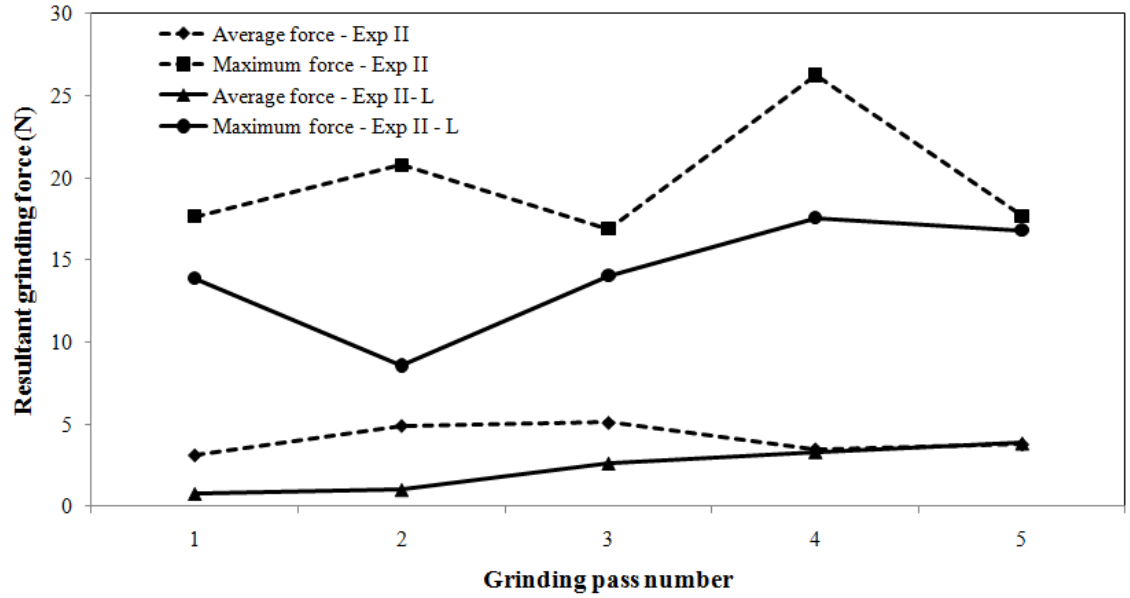

Figure 6.18: Average and maximum resultant forces (averaged over each groove) versus grinding pass number (spindle speed: 80,000 rpm, feed: 50 mm/min, axial depth/pass: 10 µm, length/pass: 8 mm).

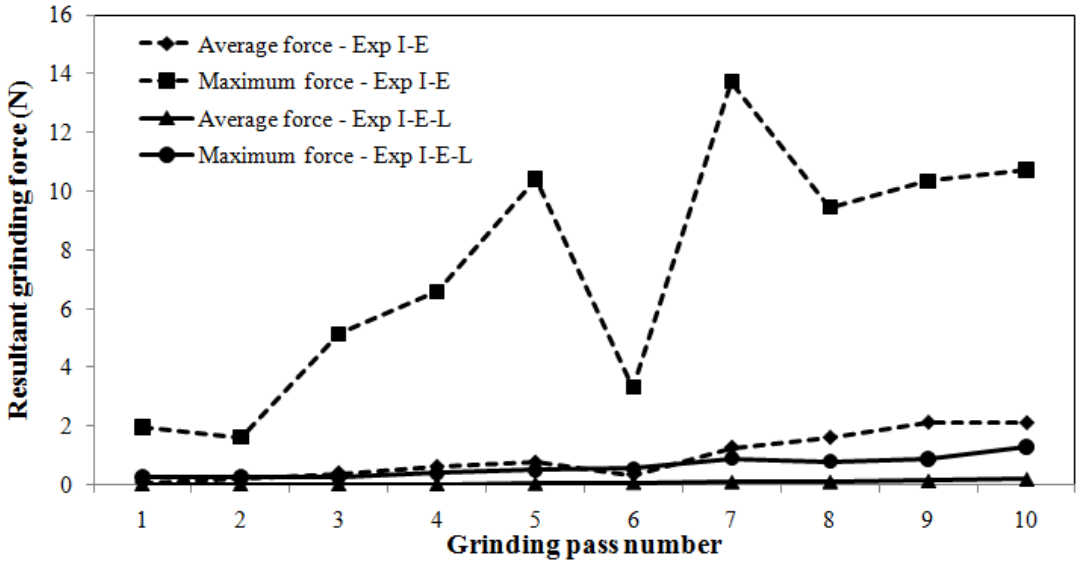

Figure 6.19: Average and maximum resultant forces (averaged over each groove) versus grinding pass number (spindle speed: 80,000 rpm, feed: 50 mm/min, axial depth/pass: 5 µm, length/pass: 8 mm).

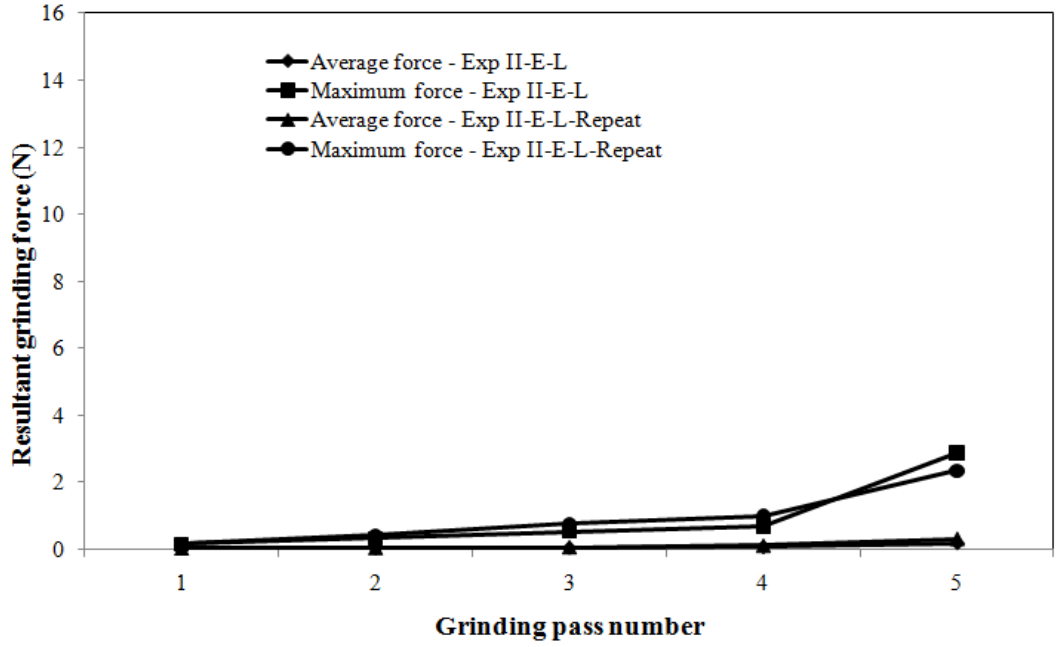

Figure 6.20: Average and maximum resultant forces (averaged over each groove) versus grinding pass number (spindle speed: 80,000 rpm, feed: 50 mm/min, axial depth/pass: 10 µm, length/pass: 8 mm).

Figures 6.19 and 6.20 show the variation of grinding forces with electroplated tools. The maximum force drops significantly with laser assist with a depth of cut of 5 μm/pass as seen in Fig. 6.19. Note that the experiments at a depth of 10 μm/pass are not conducted without laser assist, since the forces are high and can damage the spindle. The force values reported in Fig. 6.20 for the laser assist case are significantly lower than the force values reported for the without laser case shown in Fig. 6.19. These conditions represent a two fold increase in the material removal rate with laser assist while lowering the grinding forces significantly. Consequently, this demonstrates a clear potential of the two step approach to further increase material removal rates with laser assist.

6.5.2 Surface Roughness

The resulting groove floor surface roughness height after micro grinding using metallic bonded and electroplated tools is shown in Figs. 6.21 and 6.22, respectively. It is clear from the figures that comparable surface roughness values can be obtained with the two-step laser assisted micro grinding process, while still achieving reduced grinding forces. This is attributed to the final grinding pass through the unaffected parent material, which produces comparable surface roughness in both cases. Additionally, tool wear plays a significant role in the observed surface roughness, and will be explained in the subsequent section. The standard deviation of the laser assist cases is higher because of the residual thermally affected region in the surface, which causes the variability. This can be removed with additional finish grinding passes. The higher surface roughness obtained with the electroplated tools might be due to the reduced wear of these tools resulting in more cutting than rubbing of the tool with the work material.

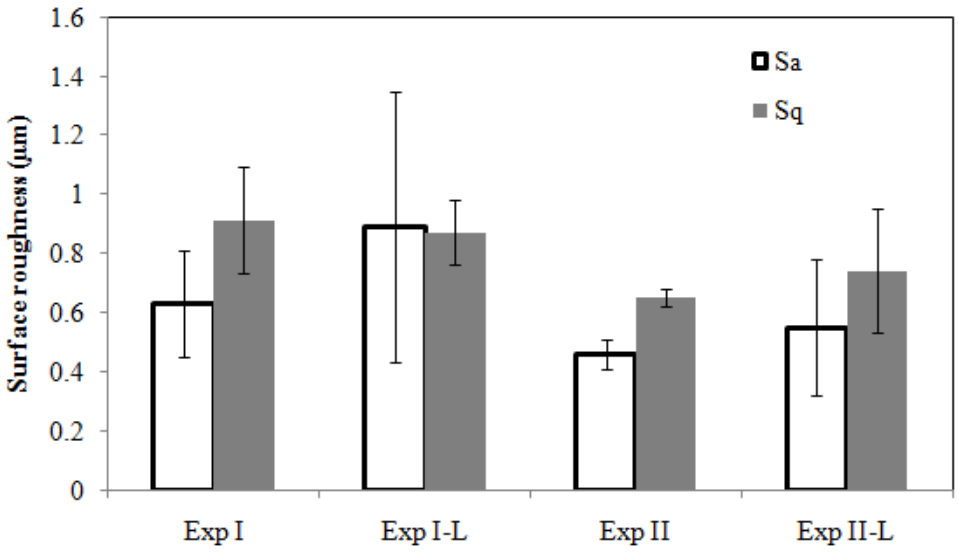

Figure 6.21: Surface roughness (S_a and S_q) of the groove floor (metallic bonded tools). The error bars represent one standard deviation of ten measurements per surface.

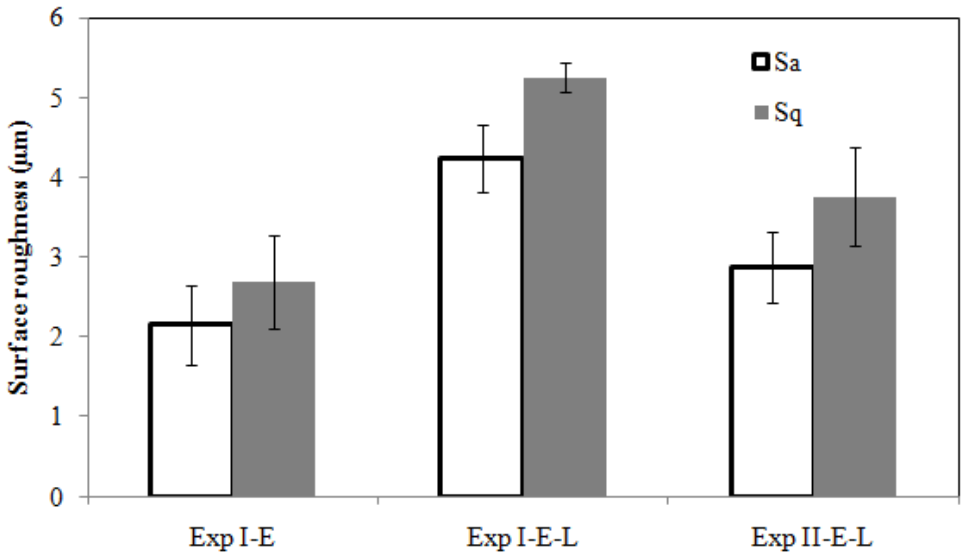

Figure 6.22: Surface roughness (S_a and S_q) of the groove floor (electroplated tools). The error bars represent one standard deviation of ten measurements per surface.

6.5.3 Tool Wear

The SEM images of the micro grinding tool before and after Exp I and Exp I-L are shown in Figs. 6.23 and 6.24, respectively. Figure 6.23 shows evidence of significant rubbing of the tool end face without laser assist. The grits and the bonding material on the bottom face of the micro grinding tool have been completely removed resulting in the higher forces seen earlier in Figs. 6.17 and 6.18. Some rubbing is also observed with laser assist, as seen in Fig. 6.24, but is found to be much less than without laser assist. Similar trends are observed in experiments Exp II and Exp II-L as seen in Figs. 6.25 and 6.26, respectively. It is interesting to note that the rubbing on the bottom face of the electroplated tools is reduced compared to the metallic bonded tools shown in Fig. 6.27.

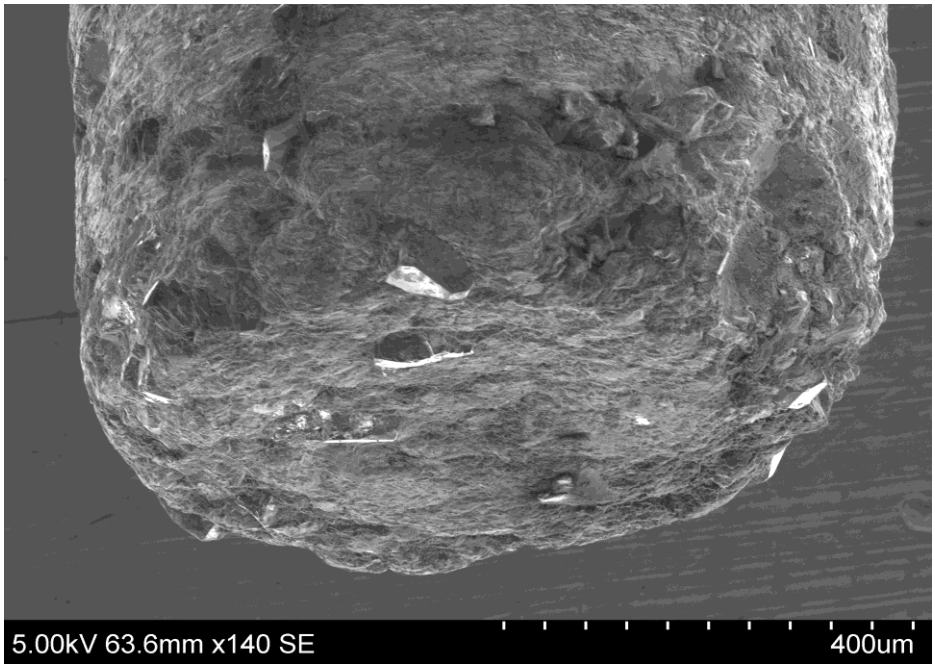

Exp I- Before grinding

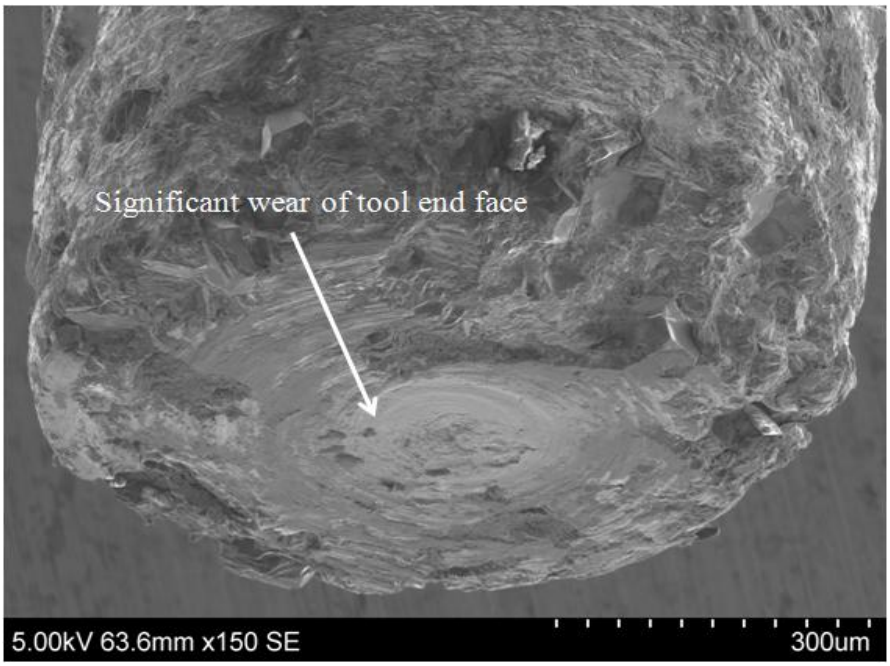

Exp I - After grinding

Figure 6.23: SEM micrographs of tool before (top) and after grinding (bottom) without laser assist (spindle speed: 80,000 rpm, feed: 50 mm/min, axial depth/pass: 10 µm).

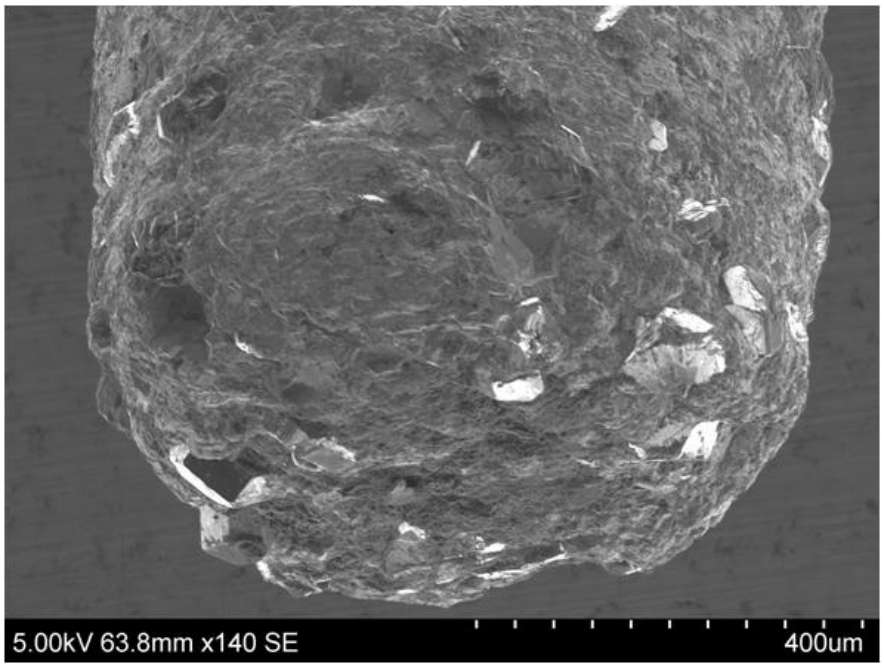

Exp I-L - Before grinding

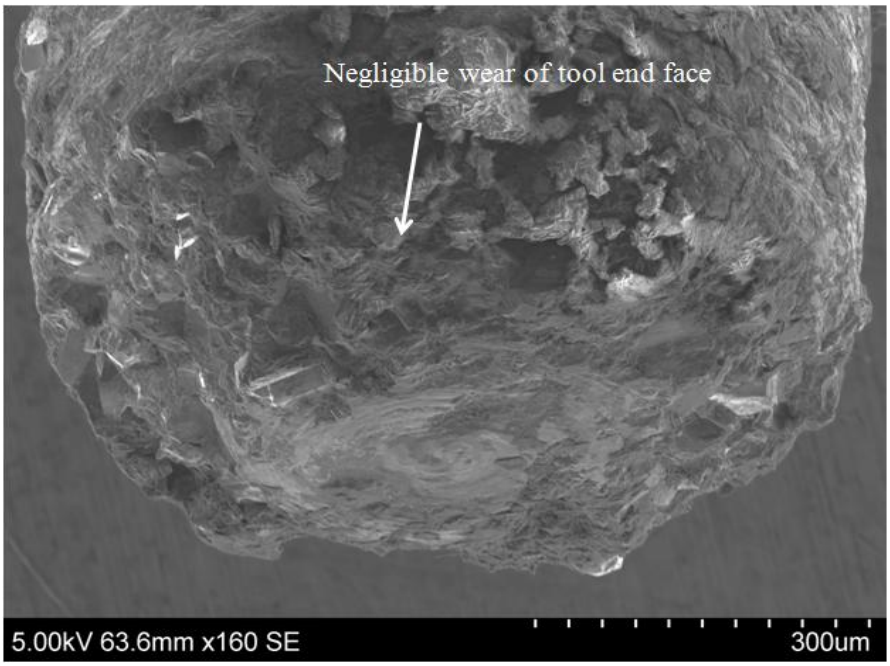

Exp I-L - After grinding

Figure 6.24: SEM micrographs of tool before (top) and after grinding (bottom) with laser assist (spindle speed: 80,000 rpm, feed: 50 mm/min, axial depth/pass: 10 µm).

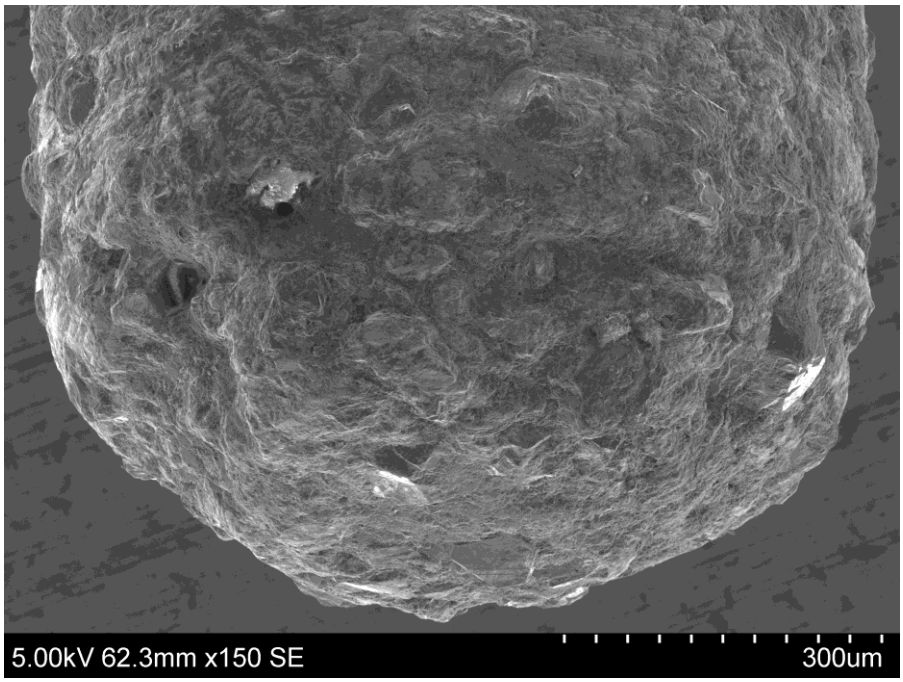

Exp II - Before grinding

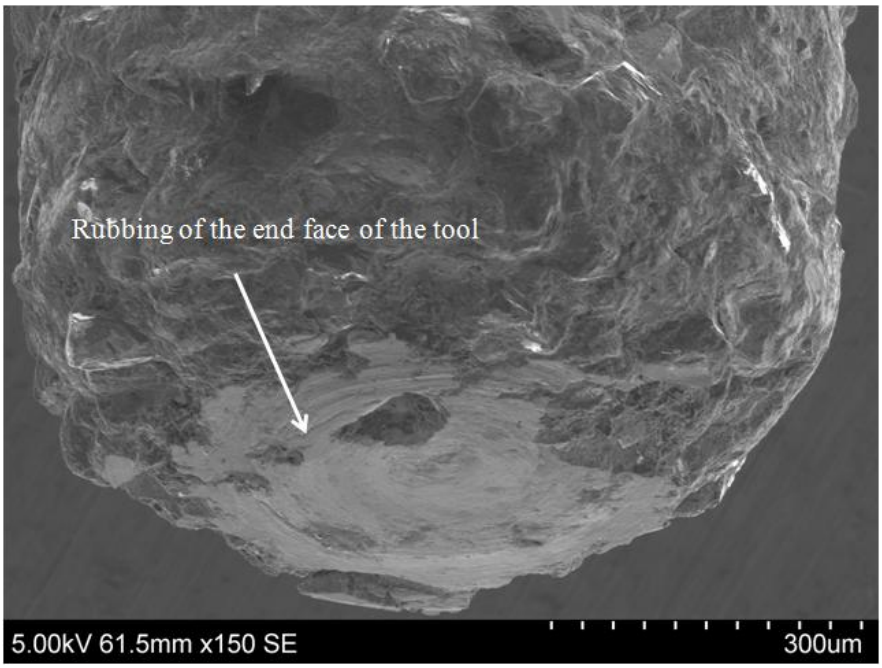

Exp II - After grinding

Figure 6.25: SEM micrographs of tool before (top) and after grinding (bottom) without laser assist (spindle speed: 80,000 rpm, feed: 50 mm/min, axial depth/pass: 5 µm).

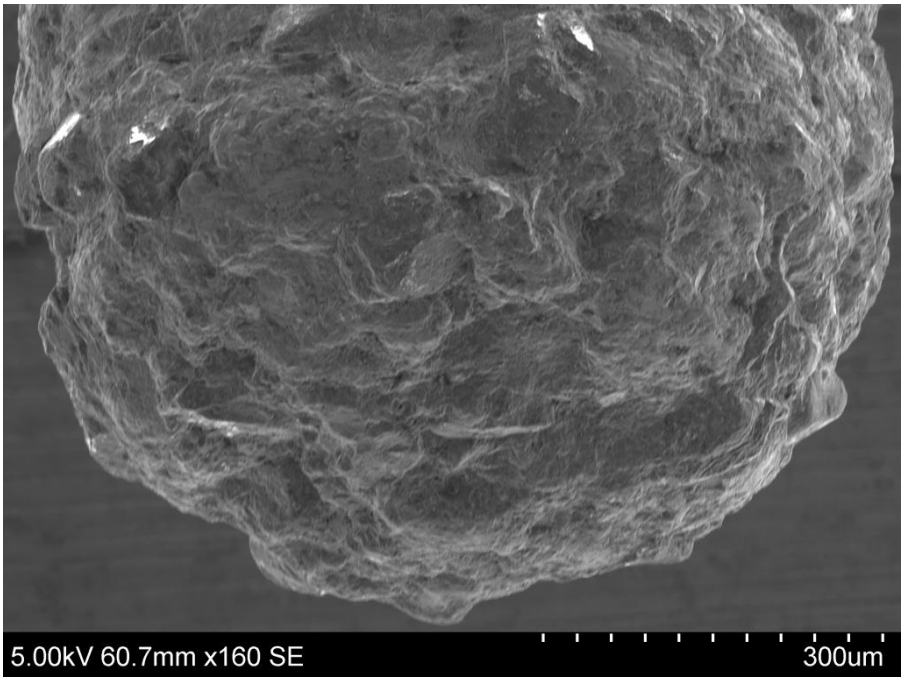

Exp II-L - Before grinding

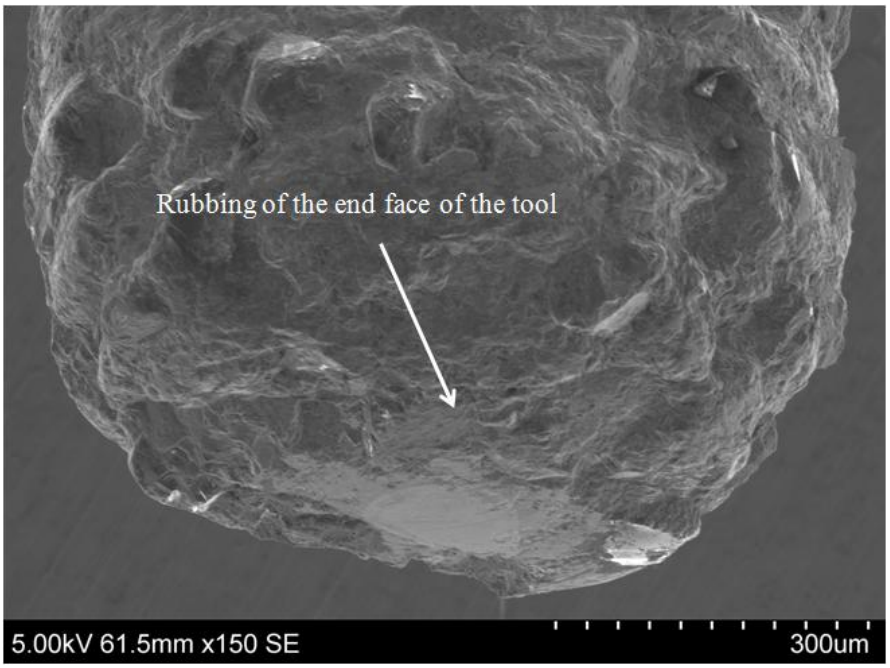

Exp II-L - After grinding

Figure 6.26: SEM micrographs of tool before (top) and after grinding (bottom) with laser assist (spindle speed: 80,000 rpm, feed: 50 mm/min, axial depth/pass: 5 µm).

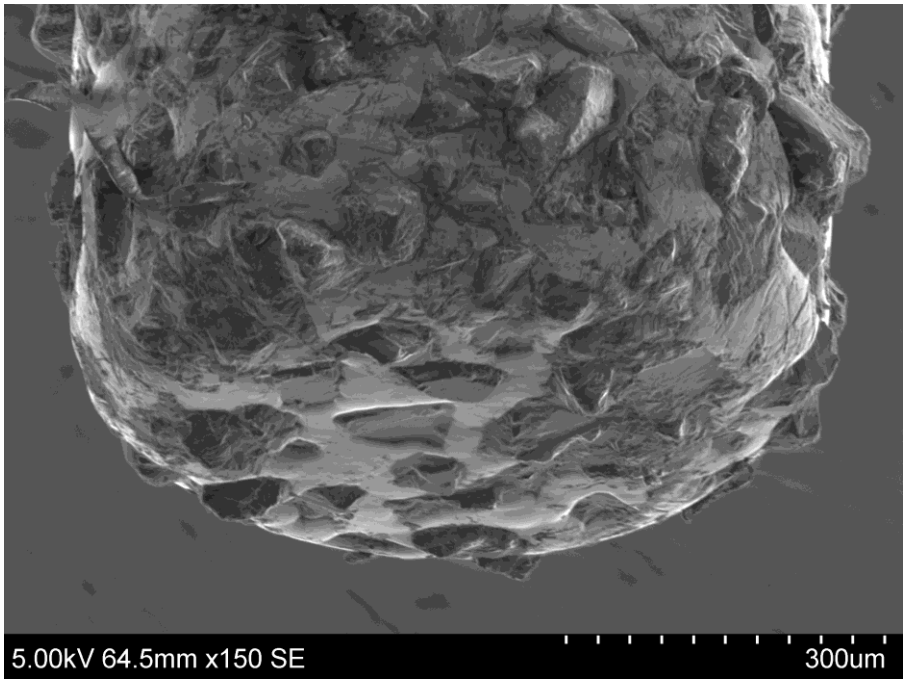

Exp I-E-L - Before grinding

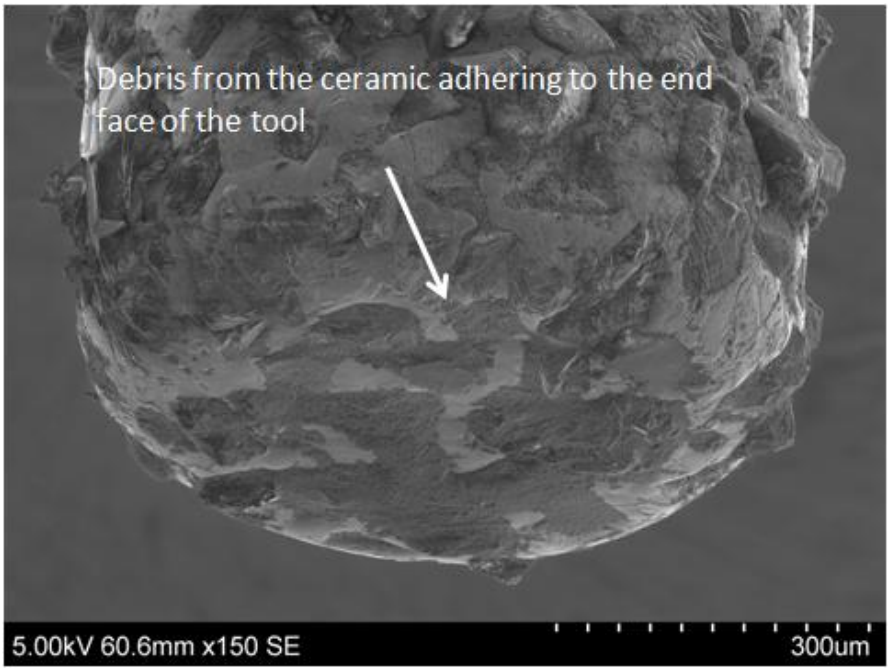

Exp I-E-L - After grinding

Figure 6.27: SEM micrographs of tool before (top) and after grinding (bottom) with laser assist (spindle speed: 80,000 rpm, feed: 50 mm/min, axial depth/pass: 5 µm).

6.5.4 Groove Geometry

The depth of the groove after micro grinding is shown in Fig. 6.28. In most cases the groove depth is found to be lower than the set depth of 50 µm. This is attributed to the wear of the micro grinding tool as seen in the previous section. However, the groove depths with laser assist are higher than without laser assist case, indicating reduced tool wear, which is consistent with the tool condition observed earlier. Figure 6.29 shows the bottom face of the machined groove using laser assist. In addition, a significant difference in groove depth is observed between Exp I-E and I-E-L when using electroplated diamond micro grinding tools. This is attributed to lower tool wear when using electroplated tools as shown in Figs. 6.26 and 6.27.

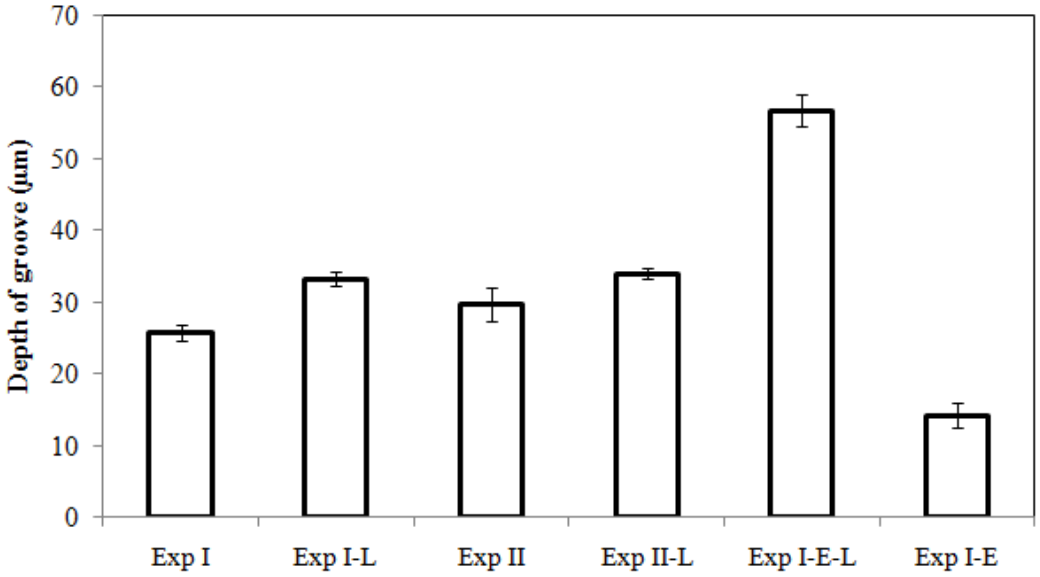

Figure 6.28: Groove depth results. The error bars represent one standard deviation of ten measurements.

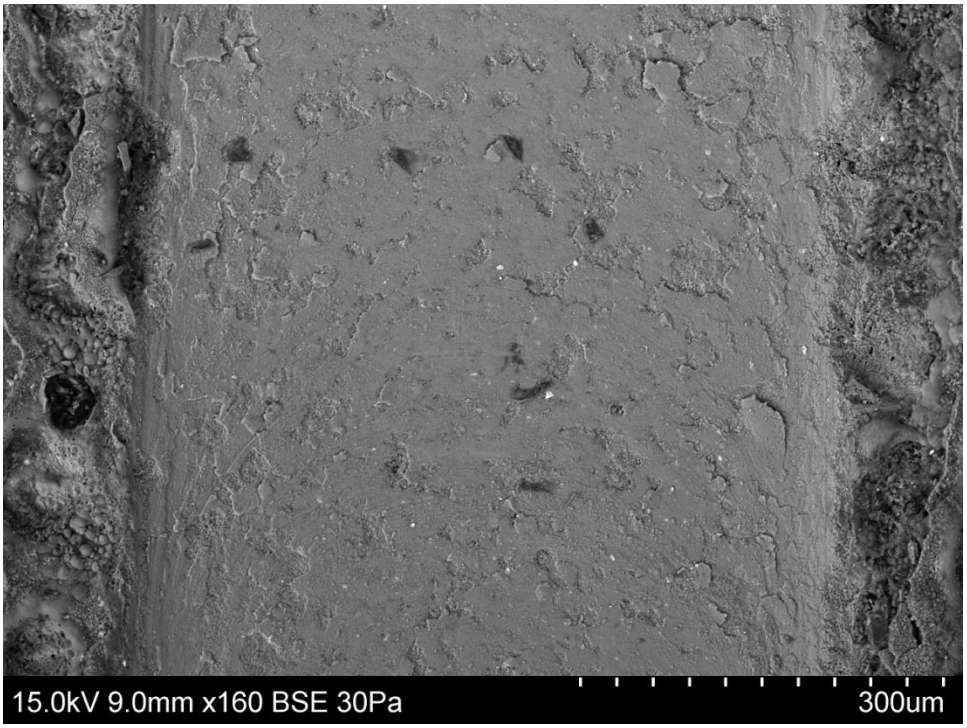

Figure 6.29: SEM micrograph of the machined groove (Exp II-L) (spindle speed: 80,000 rpm, feed: 50 mm/min, axial depth/pass: 10 µm, length/pass: 8 mm).

6.6 Summary

This chapter presented a modeling and experimental study of a laser-assisted micro grinding process for a high strength silicon nitride ceramic. The proposed two-step strategy was found to yield an efficient approach to create a microscale feature in the hard ceramic. The following specific conclusions are derived from this study:

1. In the laser scanning step, the analytical model predicts the depth and width of the thermally cracked zone to within 25% of the measured values. The difference decreases to less than 10% as the '*h/2a*' ratio decreases, i.e., as it approaches a state of plane stress.
2. The FE technique is also used to predict the thermally cracked region due to laser scanning. The results indicate that the average errors in prediction of the depth and width of the cracked region compared to measured values are found to be 10-15%, which indicates that the FE model predictions are in good agreement with measurements.
3. The resultant grinding forces are lower with laser assist under all conditions with a maximum reduction of 43.2% for metallic bonded tools compared to the without laser assist cases.
4. The resulting groove surface roughness values are comparable for both with and without laser assist cases.
5. Tool wear is less with laser assist. The micro grinding tool tends to lose its shape rapidly in the absence of laser irradiation and negatively impacts the dimensional accuracy of the micro groove.

6. Higher depths of cut and therefore higher material removal rates are possible with laser assist while maintaining low grinding forces and tool wear.

CHAPTER 7

WEAR BEHAVIOR OF CUTTING TOOL COATINGS IN LAMM

This chapter presents an experimental study on the performance of different cutting tool coatings for the LAMM process. Tool coatings have been used extensively at the macroscale to increase tool life by enhancing its wear resistance. This chapter deals with empirical performance evaluation of coated tools in LAMM in order to identify the key wear mechanisms. This information will be helpful for the end users of LAMM to select suitable coated cutting tools. In addition, the study will be useful for tool manufacturers in their efforts to improve the quality of coatings for micro tools. The workpiece material used in this study is A2 tool steel (62 HRc). The temperature rise in the material removal surface due to laser heating is determined using the moving heat source model described in Chapter 4. The thermal model permits analysis of the severity of the thermal conditions experienced by the cutting tool in LAMM. Machining experiments are then carried out with laser assist, under manufacturer recommended cutting conditions to evaluate the wear behavior of commercially available (TiAlN, TiCN) and customized coatings (TiSiN, Al2O3, Al2O3 + ZrN). The principal wear mechanism of each coating is identified and discussed.

7.1 Experiments

7.1.1 Experimental Conditions

Laser assisted micro milling experiments were conducted on A2 tool steel (62 HR_c) using the experimental cutting conditions given in Table. 7.1. The tools used were 200 and 250

μm diameter end mills obtained from different tool manufacturers. The slotting experiments were conducted at manufacturer recommended feed rates and depths of cut. A few tests were conducted without laser assist to compare with the laser assist cases.

Table 7.1: Experimental conditions.

Cutting tool	200 μm dia. WC-Co, 2 flute end mills, and 250 μm dia. WC-Co 2 and 4 flute end mills.
Spindle speed	50,000 rpm
Feed rate	200 μm dia. tools - 220 mm/min 250 μm dia. tools - 100 mm/min
Depth of cut	25 μm
Workpiece material	A2 Tool Steel (62 HR_c)
Laser power and spot size	18 W, 280 μm
Distance between the center of the laser spot and the leading edge of the tool	200 μm

7.1.2 Temperature Distribution

The thermal model described in Chapter 4 is used to determine the temperature variation in the material removal surface at the leading edge of the tool. This model permits analysis of the severity of the thermal conditions experienced by the cutting tool in LAMM. The relative positions of the laser spot and the tool used in the LAMM experiments are shown in Fig. 7.1(a). Under these conditions, the temperature distribution is determined at the front edge of the tool along the lines A-B and E-F in Fig. 7.1(a). The temperature is determined along these lines since the incident laser beam has a Gaussian distribution and hence, the temperature rise is maximum at A-B and minimum

at E-F. The temperature rise is found to vary between 300 ºC and 450 ºC (for conditions listed in the figure) on the curved material removal surface, as seen in Fig. 7.1(b). However, this temperature rise is only due to laser heating. In addition, there will be a temperature rise due to plastic deformation associated with the cutting process. Hence, the total temperature rise experienced by the tool will be slightly higher than the values shown in Fig. 7.1 as discussed in Chapter 5.

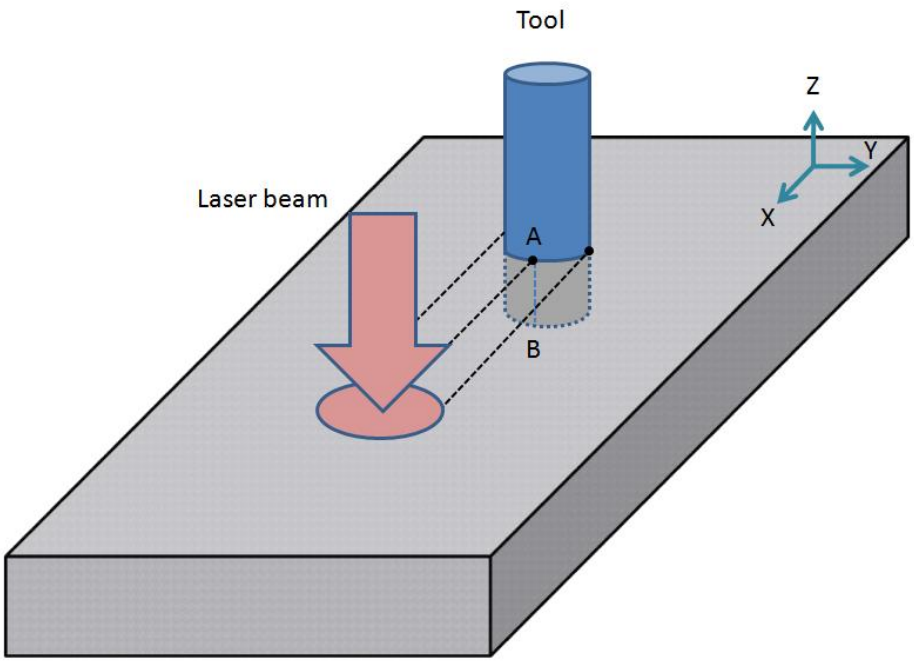

(a)

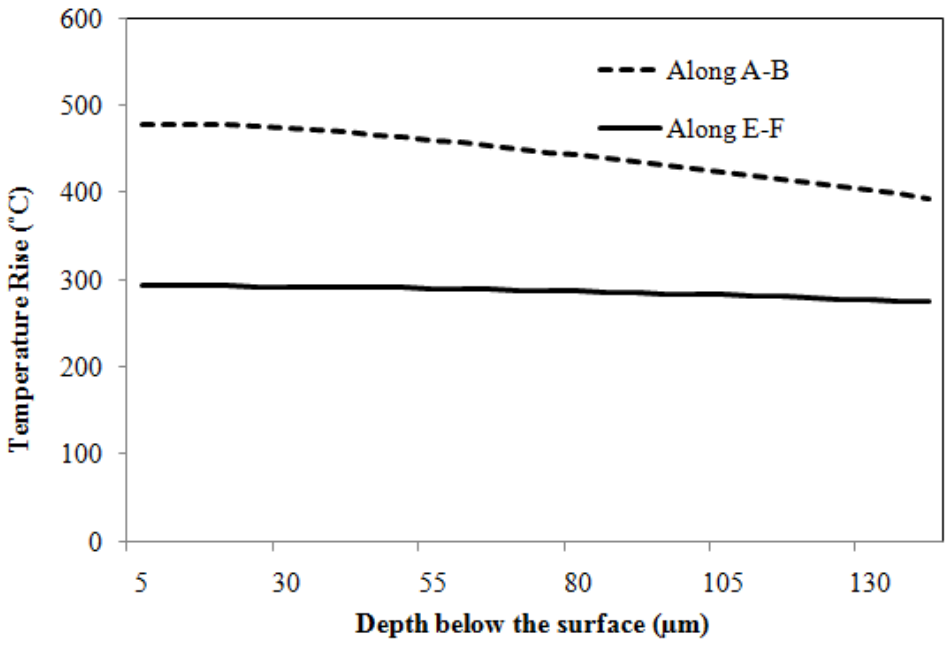

(b)

Figure 7.1: (a): Position of tool with respect to the laser beam (A-B and E-F indicate the lines along which the temperature is calculated), and **(b):** Calculated temperature variation in the workpiece along A-B and E-F (laser power: 18 W, spot size: 280 µm, scan speed: 100 mm/min, laser- tool distance: 100 µm).

It is evident from Fig. 7.1(b) that the temperature rise of 300-450 ºC in LAMM is significant compared to the reported temperature rise of only 100-200 ºC in micro milling of 1018 steel and Al6061-T6 without any laser heating [97]. Consequently, micro milling tools need to be able to withstand higher temperatures for the LAMM process to be viable.

7.1.3 Cutting Tool Coatings and Characterization

The tool coatings evaluated in this study are listed in Table. 7.2.

Table 7.2: Cutting tool coatings**.**

Commercially available	TiAlN, TiCN
Custom coated	TiSiN, Al_2O_3, Al_2O_3 + ZrN

The commercially coatings, TiAlN and TiCN, are available from select cutting tool manufacturers. Tools were also custom coated with TiSiN, alumina (Al_2O_3), and Al_2O_3 + ZrN with collaboration with SECO® tools and Entegris® coatings. The TiSiN coating has been recently shown to outperform TiAlN and TiN in terms of better abrasive wear resistance and fatigue behavior [119]. The Al_2O_3 coating was selected because of its proven ability to resist oxidation at higher temperatures [89]. The thickness of TiSiN and Al_2O_3 coatings ranged from 2.5 to 3 μm. The thickness of the ZrN interlayer, which is used to promote adhesion of the alumina coating to the carbide substrate, is around 0.5 μm. The worn tools were characterized by Scanning Electron Microscopy (SEM) and Energy Dispersive Spectroscopy (EDS) to understand the dominant wear mechanisms.

7.2 Wear Behavior of Coatings

7.2.1 Uncoated Tools

Figure 7.2 shows the SEM micrograph of an uncoated carbide micro end mill after 25 mm of machining. The micrograph reveals extensive rubbing on the flank face of the uncoated tool (indicated by the arrows). Edge rounding without edge chipping is also observed, which indicates gradual abrasive wear of the cutting tool. Discoloration of the

tool due to the reflected laser beam impinging on the tool is also observed (as shown in Fig. 7.2(a)). This is due to oxidation of the uncoated tungsten carbide tool.

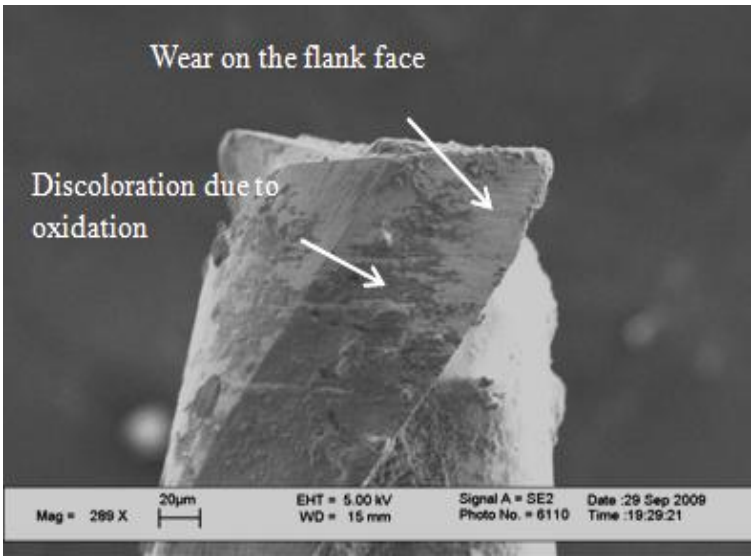

(a)

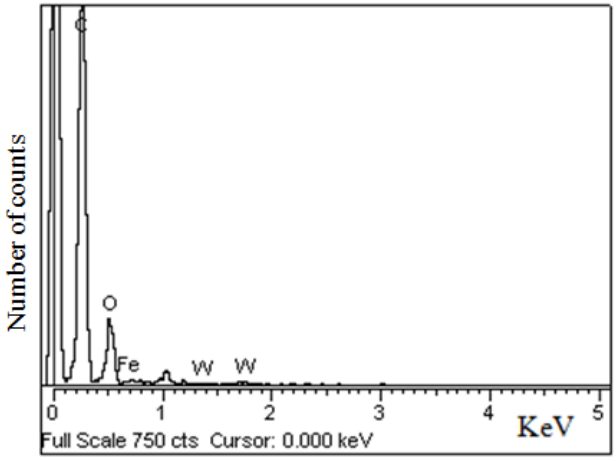

(b)

Figure 7.2: (a) SEM micrograph of uncoated tool after 25 mm of micro milling, **(b)** EDS of the uncoated tool (feed rate: 100 mm/min, depth of cut: 25 µm, laser power: 18 W, spot size: 280 µm).

The EDS spectra obtained from this region (see Fig. 7.2(b)) confirms the presence of oxygen (O). Tungsten carbide begins to oxidize at temperatures above 500 ˚C [11]. The workpiece is heated to a temperature of 450 ˚C, as predicted by the thermal model. In addition, there will be temperature rise due to shear and frictional heat produced by the cutting process. Hence, the total temperature rise is expected to be closer to 500–600 ˚C in LAMM. The ability of the tool to resist wear at these high temperatures will directly determine tool life.

7.2.2 TiCN Coated Tools

The SEM micrograph of a TiCN coated tool before and after machining 25 mm with laser assist is shown in Figs. 7.3(a) and (b), respectively. Figure 7.3(b) shows clear evidence of coating delamination near the cutting tool edge. The coating has been completely removed but the cutting edge is still intact. In addition, there is rounding of the cutting edges indicating gradual tool wear. Improvement in wear performance will be obtained if the coating's surface roughness and adhesion to the WC-Co substrate can be enhanced. Delamination of the coating is confirmed by the EDS spectra (Fig. 7.3(c) and (d)) corresponding to the two regions marked in Fig. 7.3(b). The spectra shown in Fig. 7.3(c) reveals the presence of only tungsten (W) and carbon (C), which indicate that the TiCN coating has been removed from this region.

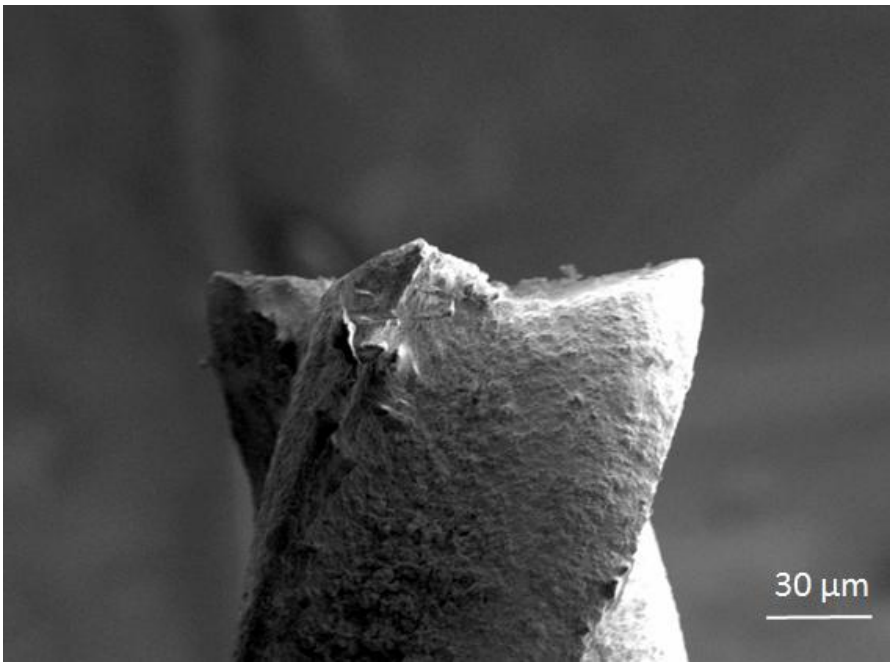
30 µm

(a)

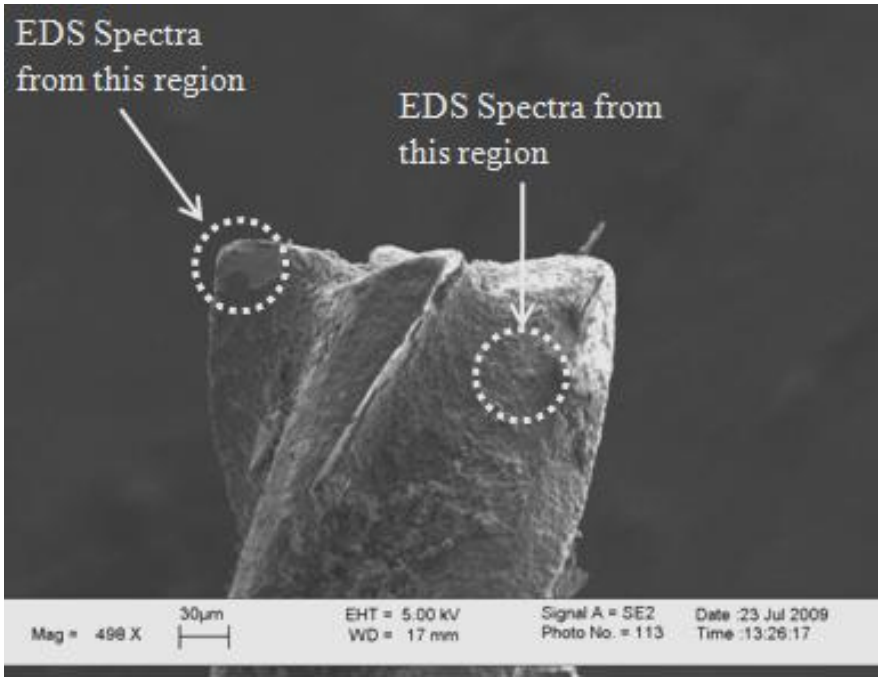
EDS Spectra
from this region
EDS Spectra from
this region
Mag = 498 X
30µm
EHT = 5.00 kV
WD = 17 mm
Signal A = SE2
Photo No. = 113
Date :23 Jul 2009
Time :13:26:17

(b)

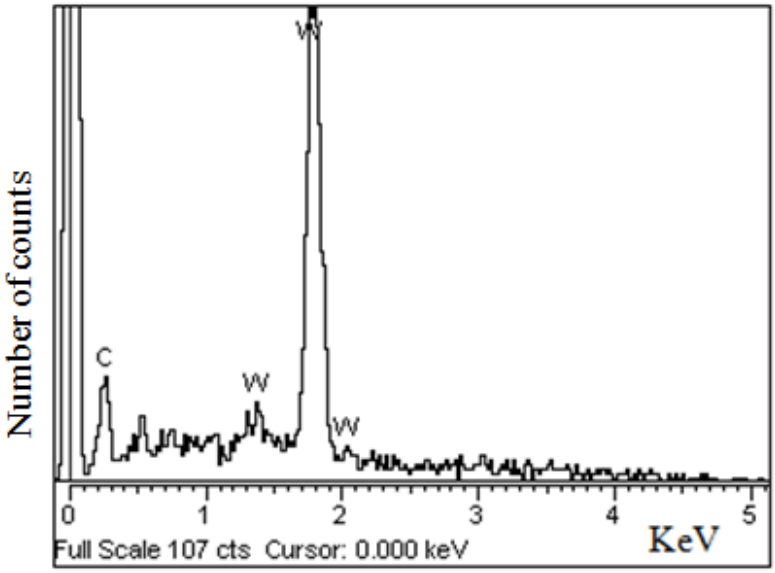

(c)

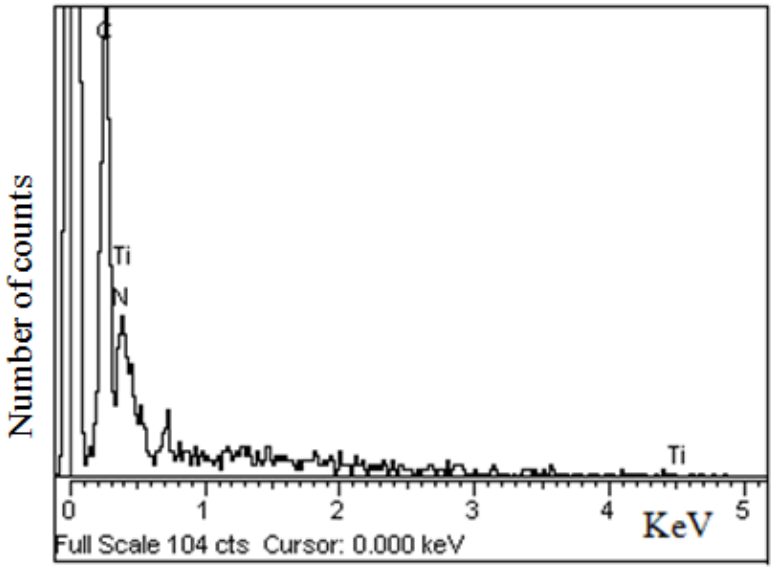

(d)

Figure 7.3: (a) SEM micrograph of a new TiCN coated tool, **(b)** SEM micrograph of a TiCN coated tool after a 25 mm length of cut, **(c)** EDS Spectra of TiCN coated tool (from the top left region near the cutting edge indicated in Fig. 7.3(b)), **(d)** EDS Spectra of TiCN coated tool (from the flank face as indicated in Fig. 7.3(b)) (feed rate: 100 mm/min, depth of cut: 25 µm, laser power: 18 W, spot size: 280 µm).

Figure 7.3(d) indicates the overwhelming presence of titanium (Ti), carbon (C) and nitrogen (N), which confirms the composition of the coating material applied on the carbide substrate. Based on these findings, delamination wear is found to be the dominant mechanism that controls the wear behavior of TiCN coated micro tools.

7.2.3 TiAlN Coated Tools

The SEM micrograph of the TiAlN coated tool (SECO® Mega-T) after 25.4 mm of machining with laser assist is shown in Fig. 7.4 (a). This is the same tool used for all the experiments reported in Chapter 4. The principal wear mechanism of this coating is gradual abrasive wear, which is confirmed by the edge rounding observed in the SEM image. The EDS spectra from the cutting edge (shown in Fig. 7.4(b)) indicates the presence of TiAlN coating. No delamination of the coating is observed, which indicates good adhesion of the coating to the substrate. In addition, significant adhesion of the softened work material to the cutting tool surfaces is also observed. This is confirmed by the Iron (Fe) and (O) peaks in the EDS spectra shown in Fig. 7.4(b).

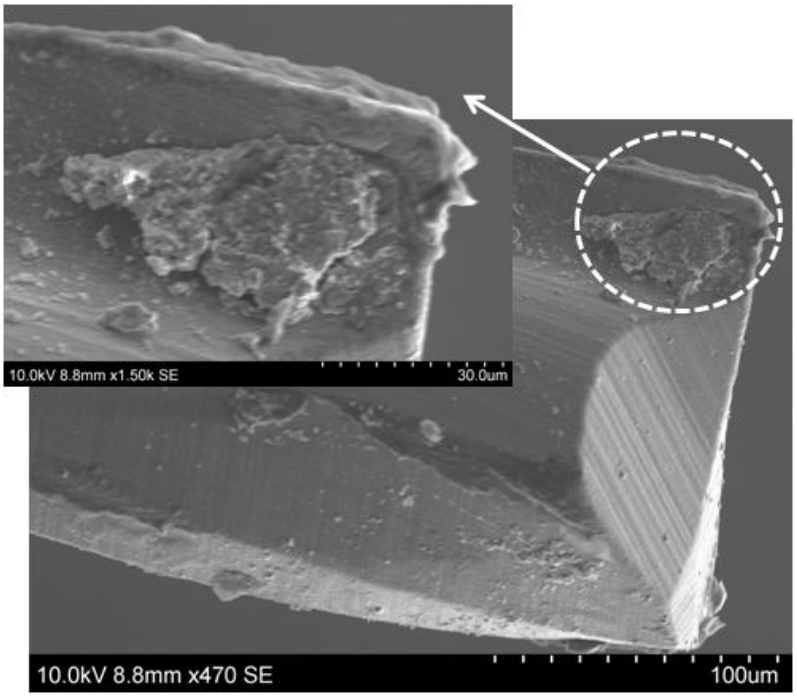

(a)

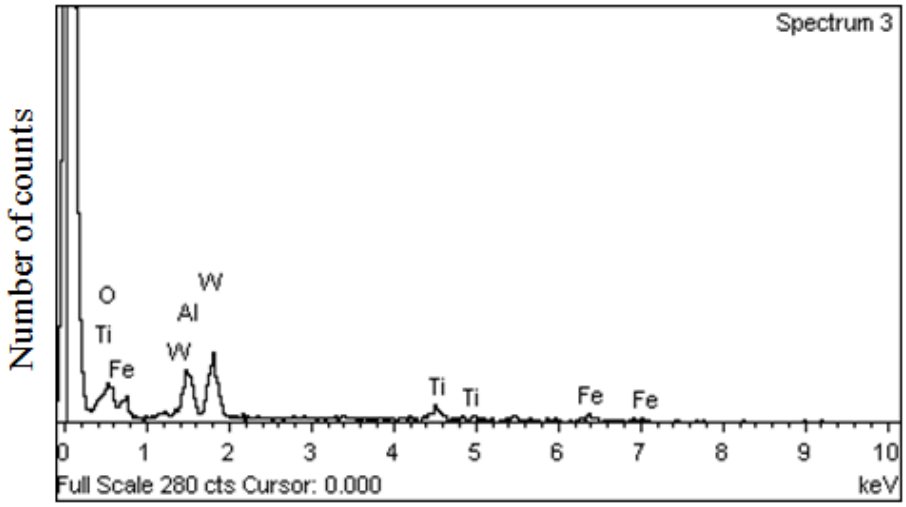

(b)

Figure 7.4: (a) SEM micrograph of the TiAlN (SECO® Mega-T) coated tool after a 25 mm length of cut with laser assist, **(b)** EDS Spectra of TiAlN coated tool (from around the cutting edge) (feed rate: 220 mm/min, depth of cut: 25 µm, laser power: 18 W, spot size: 280 µm).

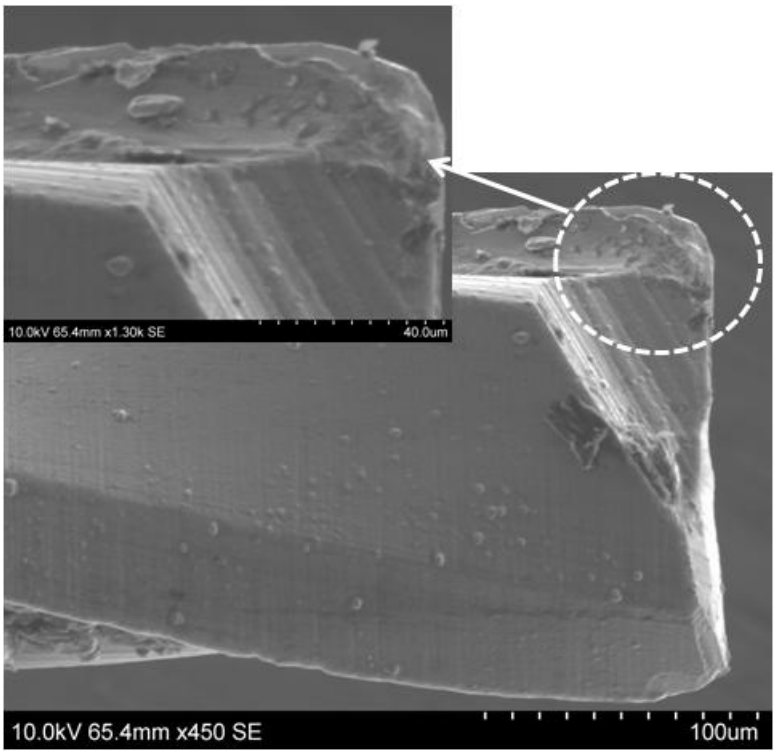

Figure 7.5: SEM micrograph of the TiAlN (Mega-T) coated tool after a 25 mm length of cut without laser assist (feed rate: 220 mm/min, depth of cut: 25 µm).

Figure 7.5 shows the SEM micrograph of a TiAlN coated tool after 25.4 mm length of cut without laser assist. It is evident that the coating is not able to withstand the machining stresses and hence delaminates, which demonstrates that tool wear is higher without laser assist. In contrast, as seen in Fig. 7.5(a), the coating is able to withstand the higher temperatures and lower interfacial stresses experienced by the cutting tool in LAMM.

7.2.4 TiSiN Coated Tools

Figure 7.6(a) shows the SEM micrograph of the TiSiN coated tool after 25.4 mm of machining with laser assist. The coating delaminates under the influence of machining

stresses, which is clearly evident from the micrograph. Additionally, the EDS spectra obtained from near the cutting edge is shown in Fig. 7.6(b) and indicates that the coating has peeled off. Therefore, delamination is the principal wear mechanism of this coating. Adhesion of the TiSiN coating with the WC-Co substrate has to be further improved for the coating to perform better.

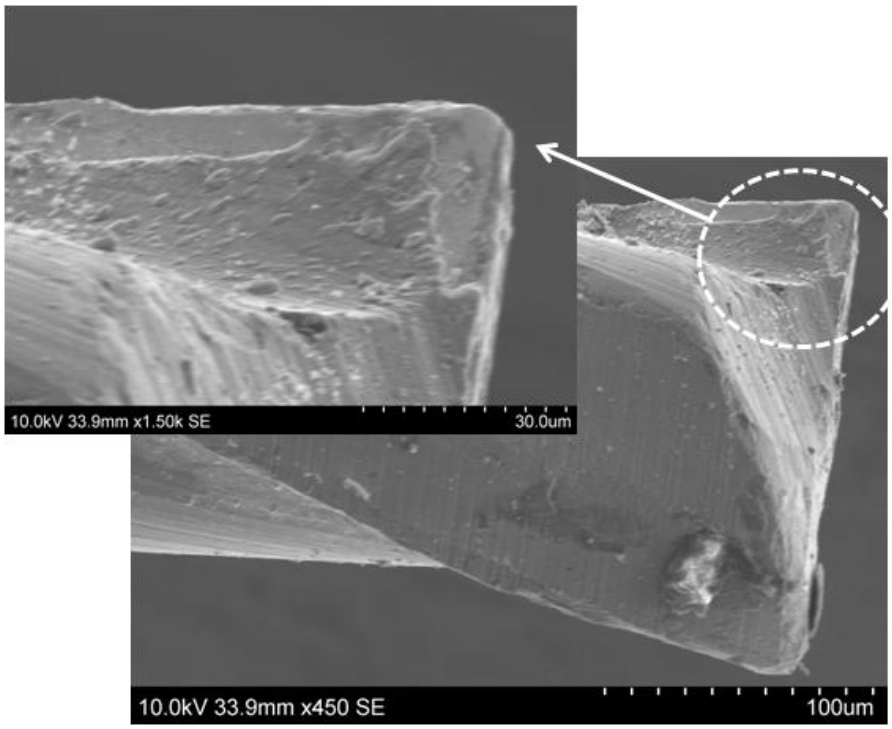

(a)

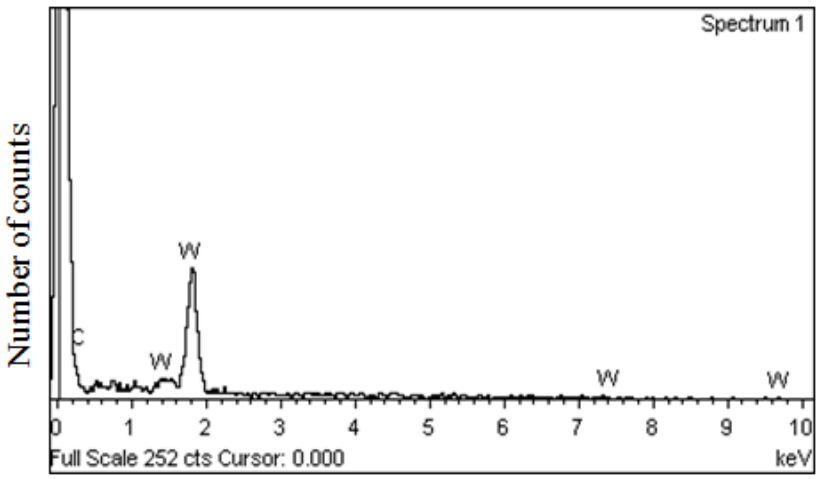

(b)

Figure 7.6: (a) SEM micrograph of a TiSiN coated tool after a 25 mm length of cut with laser assist, **(b)** EDS Spectra of TiSiN coated tool (from the region near the cutting edge) (feed rate: 220 mm/min, depth of cut: 25 µm, laser power: 18 W, spot size: 280 µm).

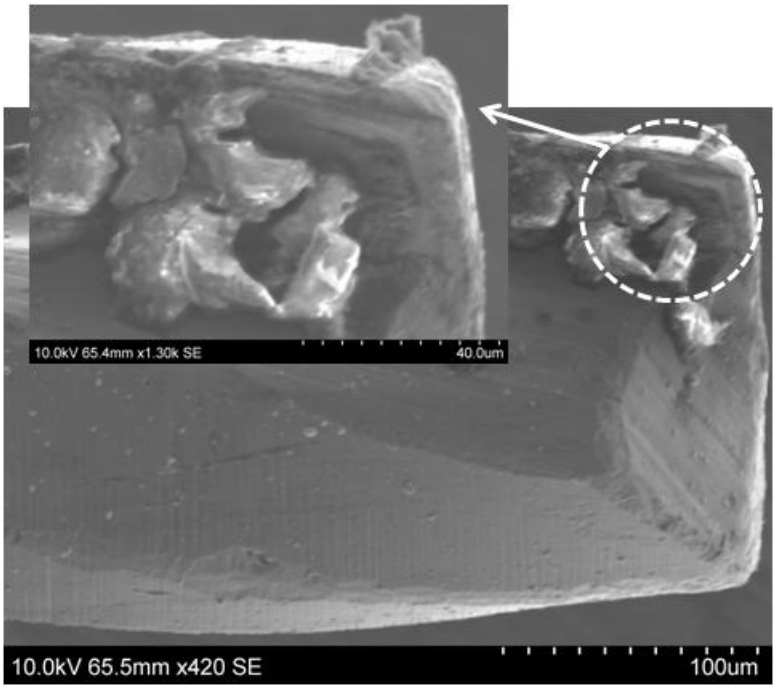

(a)

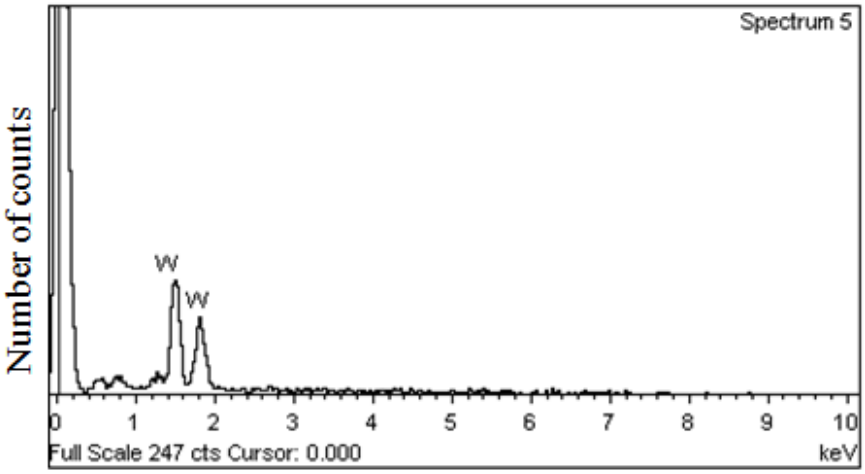

(b)

Figure 7.7: (a) SEM micrograph of a TiSiN coated tool after a 25 mm length of cut without laser assist, **(b)** EDS Spectra of TiSiN coated tool (from the region near the cutting edge) (feed rate: 220 mm/min, depth of cut: 25 µm, no laser).

Figure 7.7(a) shows the SEM micrograph of a TiSiN coated tool after 25.4 mm of machining without laser assist. The coating near the cutting edge has peeled off which is confirmed from the EDS spectra shown in Fig. 7.7(b). Extensive adhesion of the work material with the cutting tool is also observed. The wear mechanism of the coatings with and without laser assist is delamination.

7.2.5 Alumina (Al_2O_3) Coated Tools

Alumina (Al_2O_3) coating of thickness 2.5-3 µm was deposited on a 2 flute WC-Co micro end mill using the Physical Vapor Deposition (PVD) process The coated tool before machining is shown in Fig. 7.8. The coating appears to be relatively smooth when compared to the other coatings. The coating thickness is between 2.5-3 µm. Figure 7.9(a)

shows the SEM micrograph of the worn tool after machining a slot of length 25 mm. The micrograph clearly indicates the peeling of the Al_2O_3 coating. This is thought to be due to a combination of excessive rubbing at the micro-scale combined with poor adhesion of the alumina coating to the tungsten carbide substrate.

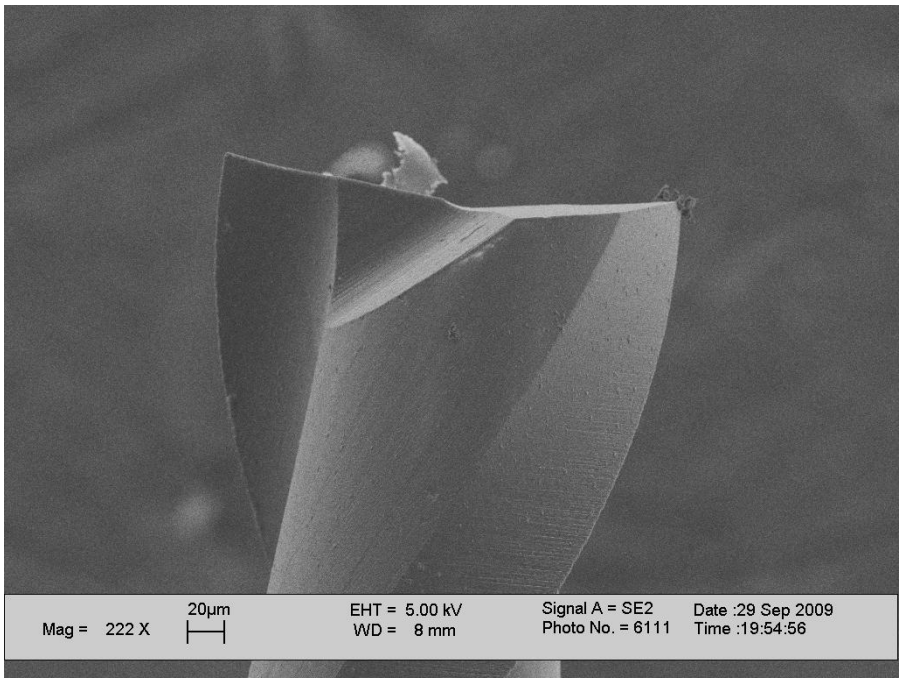

Figure 7.8: SEM micrograph of a new alumina (Al_2O_3) coated end mill (2 flute 250 µm dia.).

The EDS spectra (see Fig. 7.9(b)) from region A close to the cutting edge (marked in Fig. 7.9(a)) clearly indicates complete loss of the alumina coating. The EDS spectra from region B indicated in Fig. 7.9(a) is shown in Fig. 7.9(c) and reveals the presence of elements which make up the composition of the coating (specifically, Al and O). The maximum depth below the substrate surface from which the compositional information is obtained using EDS is around 2 µm. The absence of tungsten and carbon in Fig. 7.9(c) confirms that the thickness of coating remaining in this region is more than 2 µm. The

cutting edge is still intact after 25 mm of machining under the cutting conditions listed in Table. 7.2. Delamination due to inadequate adhesion of the coating to the substrate appears to be the principal wear mechanism for alumina coated tools in micro milling.

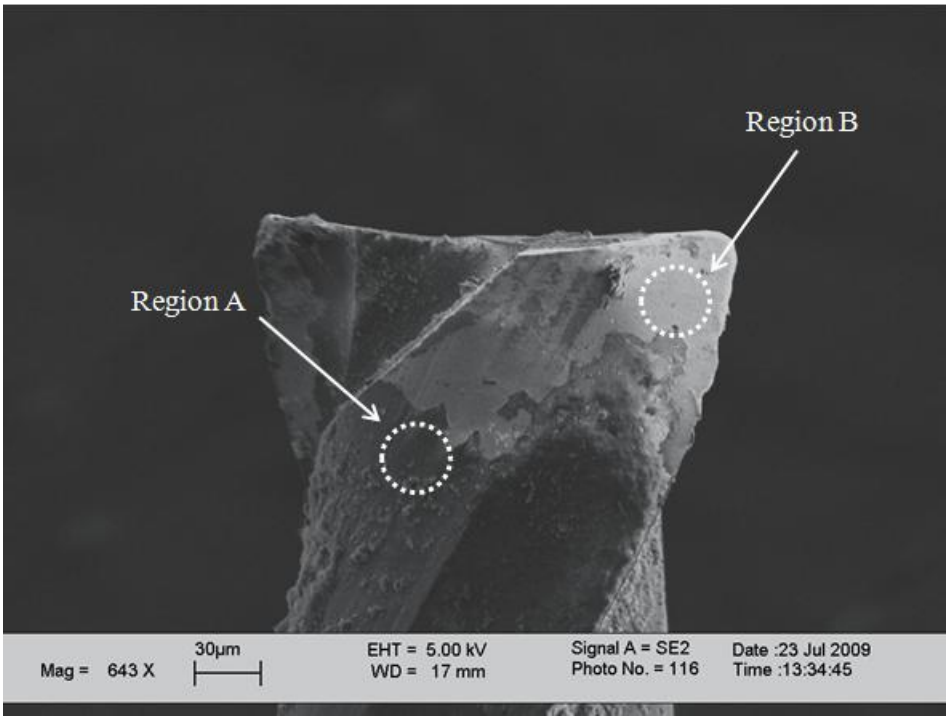

(a)

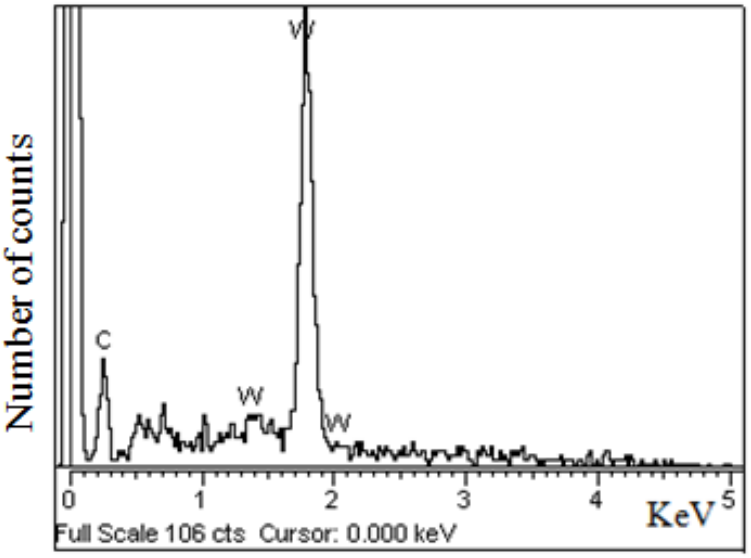

(b)

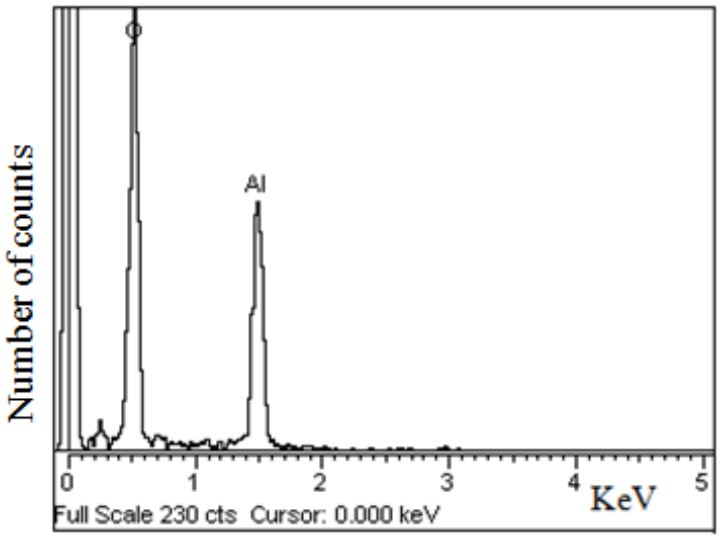

(c)

Figure 7.9: (a) SEM micrograph of alumina (Al_2O_3) coated tool after 25 mm of micro milling, **(b)** EDS Spectra of alumina (Al_2O_3) coated tool (from region A indicated in Fig. 7.9(a)), **(c)** EDS Spectra of alumina (Al_2O_3) coated tool (from region B indicated in Fig. 7.9(a)) after 25 mm of micro milling (feed rate: 100 mm/min, depth of cut: 25 µm, laser power: 18 W, spot size: 280 µm).

7.2.6 Alumina (Al_2O_3) + ZrN Coated Tools

To improve the adhesion of the alumina coating to the carbide substrate, a thin layer of ZrN (600 nm) was deposited on the tool before applying a layer of alumina. Note that ZrN coating has been studied by researchers to promote adhesion between alumina and WC [120]. The micrograph in Fig. 7.10(a) shows that wear is reduced with the Al_2O_3+ZrN coating but some delamination of the coating still occurs near the cutting edge. The EDS spectra from the region indicated in Fig. 7.10(a) is shown in Fig. 7.10(b).

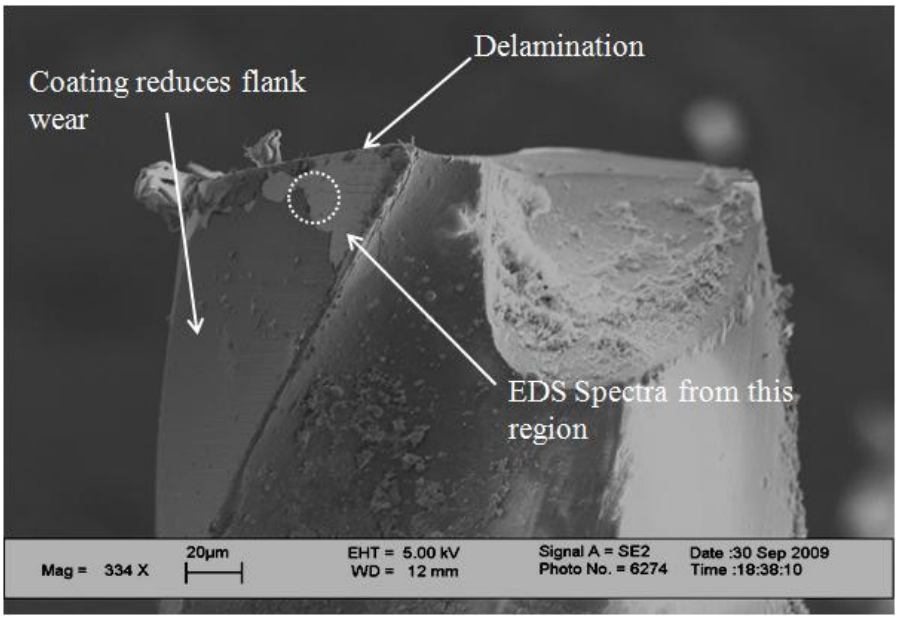

(a)

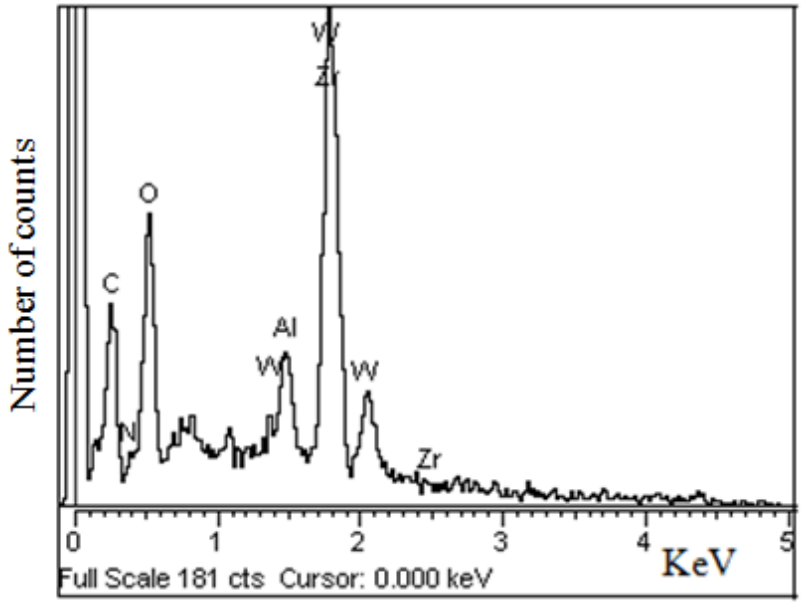

(b)

Figure 7.10: (a) SEM micrograph of alumina Al_2O_3 + ZrN coated tool after 25 mm of micro milling, **(b)** EDS spectra of alumina Al_2O_3 + ZrN coated tool (from the region closer to the cutting edge indicated in Fig. 7.10(a)) after 25 mm of micro milling (feed rate: 100 mm/min, depth of cut: 25 µm, laser power: 18 W, spot size: 280 µm).

The EDS spectra indicate that the ZrN layer is present even after 25 mm of cutting although the alumina coating has been removed by delamination. Hence, the presence of the ZrN interlayer enhances tool life and the wear of the cutting edge appears to be lower than most of the other coatings investigated in this study. The adhesion characteristics of the ZrN interlayer with the alumina coating should be improved to further reduce the wear of this coating.

7.3 Summary

This chapter presented an experimental study on the wear behavior of coated tools in LAMM. Micro milling experiments were carried out on A2 tool steel (62 HR_c) using a wide range of coated tools to evaluate their wear behavior. The following specific conclusions can be drawn from this work:

- Commercially available coatings like TiCN perform poorly due to their inferior adhesive characteristics with the base material. Delamination is found to be the principal wear mechanism of TiCN, TiSiN, and Alumina (Al_2O_3) coated tools under the conditions investigated in this study.
- Wear of the tool coatings without laser assist is higher than with laser assist. This clearly indicates that the coated micro tools are able to withstand the higher temperatures and experience lower interfacial stresses with laser assist.
- The principal wear mechanism of commercially available TiAlN coated tools is gradual abrasive wear with laser assist and delamination wear without laser assist.

- Alumina Al_2O_3 + ZrN tools performed better than most of other coated tools in terms of flank wear, but there is still some delamination of the alumina layer. Hence, improvement in the adhesion characteristics of the coating is needed to further enhance tool life in LAMM.

CHAPTER 8

CONCLUSIONS AND RECOMMENDATIONS

This chapter summarizes the main conclusions of this thesis and suggests related areas for further investigation.

8.1 Main Conclusions

The main conclusions of this thesis are as follows:

8.1.1 Experimental Characterization of LAMM of Hard Metals

A detailed evaluation of the process capability of LAMM for a hard-to-machine metal was performed. Micro end milling experiments carried out on hardened A2 tool steel (62 HR_c) with and without laser assist yielded the following key conclusions:

- The peak resultant force decreases with laser assist under all the conditions with a maximum reduction of 69%. In addition, there is a drop in the average specific cutting energy with laser assist indicating improved cutting through shearing rather than ploughing.
- The amount and rate of tool wear as measured by the rounding of the tool corner are significantly lower with laser assist even at material removal rates that are at least six times higher than the tool manufacturer's recommendations. Under such conditions, and without laser assist, the carbide tool either wears rapidly or fails catastrophically.

- When the laser spot size is larger than the tool diameter, the burr height is found to increase with laser assist. This is attributed to thermal softening of the work material. When a tool diameter larger than the laser spot size is used, the increase in burr height is much smaller.
- When the laser spot size is larger than the tool diameter, the surface roughness is found to increase with laser assist due to increased thermal softening of the material. When a tool diameter larger than the laser spot size is used, comparable surface roughness is obtained.
- The tool life is found to increase by up to nine times with laser assist when micro milling A2 tool steel (62 HR_c) using catastrophic tool failure as the tool life criterion.

8.1.2 Force Modeling in LAMM

A physics-based force model for laser assisted micro milling was developed, which captures the effects of thermal softening due to laser heating and tool runout. The model has found to predict the cutting forces in LAMM with reasonable accuracy. The following significant conclusions were derived from this modeling study:

- The model predicts the peak-to-peak cutting forces with a maximum error of 15% when compared with measured forces, thus indicating that the model is in reasonable agreement with experiments.
- The model is insensitive to the friction angle, β, over a range of feeds (in this case, between 2.2 μm and 6.6 μm/flute) and also over a range of laser powers (in

this case, between 12 and 24 W), which indicates that the model can be used for optimization over a range of feed rates and laser powers.

- The runout plays an important role in determining the profile of the cutting forces and is captured with minimum error using the assumption of a two lobe runout model.
- The model provides valuable insight into the mechanics of the process. Specifically, the knowledge of a shift in the peak cutting forces with increase in laser power is insightful. Also, a decrease in shear strength at the edges of the milled slot is predicted thereby explaining for the observed increase in burr formation with laser assist.

8.1.3 Characterization of Laser Assisted Micro Grinding of Ceramics

A two step laser-assisted micro grinding process was developed to machine high strength ceramics such as reaction-sintered silicon nitride. The proposed two-step strategy was found to yield an efficient approach to create microscale features in the hard material. The following specific conclusions were derived from this study:

- The analytical model of laser heating of the ceramic predicts the depth and width of the thermally cracked zone to within 25% of the measured values. This error decreases to less than 10% as the depth-to-width ratio of the thermally cracked region decreases, i.e., as it approaches a state of plane stress.

- The finite element model used to solve the full three-dimensional thermal stress problem is found to yield 10-15% average errors in the prediction of depth and width of the thermally cracked region when compared with measured values.
- The resultant grinding forces are lower with laser assist under all conditions with a maximum reduction of 43.2% for metallic bonded tools compared to without laser assist cases.
- The resulting groove surface roughness values are comparable for both with and without laser assist cases.
- Tool wear is less with laser assist. The micro grinding tool tends to lose its shape rapidly in the absence of laser irradiation and negatively impacts the dimensional accuracy of the micro groove.
- Higher depths of cut and therefore higher material removal rates are possible with laser assist while maintaining low grinding forces and tool wear.

8.1.4 Wear Behavior of Cutting Tool Coatings in LAMM

LAMM experiments were carried out on A2 tool steel (62 HRc) using a wide range of coated tools to evaluate their wear behavior. The following specific conclusions can be drawn from this work:

- Commercially available coatings like TiCN perform poorly due to their inferior adhesion to the base carbide material. Delamination is found to be the principal wear mechanism of TiCN, TiSiN, and Alumina (Al_2O_3) coated tools under the conditions investigated in this study.

- Wear of the tool coatings without laser assist is higher than with laser assist. This clearly indicates that the coated micro tools are able to withstand higher temperatures and experience lower interfacial stresses with laser assist.
- The principal wear mechanism of commercially available TiAlN coated tools is gradual abrasive wear with laser assist and delamination wear without laser assist.
- Al_2O_3 + ZrN coated tools performed better than most of other coated tools in terms of flank wear.

8.2 Recommendations for Future Work

Related areas for further research include the following:

- The developed force model can be used for optimization of the laser and cutting parameters to achieve maximum reduction in cutting forces while minimizing the residual thermally affected zone.
- The force model can be improved by explicitly accounting for the finite cutting edge radius of the micro end mill.
- The LAMM setup can be used to explore other processes like laser hardening of micro components, which can be performed on the same setup developed for LAMM.
- The limits on geometries that can be machined without occlusion of the incident laser beam should be evaluated. This will aid in further improving the design of the LAMM setup developed in this thesis.
- The effect of laser assist on the machinability characteristics of hard metals like titanium alloys and ceramics like silicon carbide should be investigated.

APPENDIX A

SUPPORTING DATA

Table A.1: Depth of thermally affected region

Experiment	Measured depth (μm) (± 1σ)	Analytical model (μm)	FE model (μm)
I	19 ± 2.5	17	20
II	34 ± 1.5	42	37
III	58 ± 2.6	70	60
IV	18 ± 2.1	16	20
V	32 ± 1.4	40	37
VI	55 ± 3	68	60

Table A.2: Width of thermally affected region

Experiment	Measured width (μm) (± 1σ)	Analytical model (μm)	FE model (μm)
I	161± 5.1	144	190
II	242 ± 9	320	260
III	308 ± 9.6	390	340
IV	160 ± 7.5	140	190
V	220 ± 10	314	260
VI	258 ± 10.5	385	340

REFERENCES

[1] A. Aramcharoen, *et al.*, "Evaluation and selection of hard coatings for micro milling of hardened tool steel," *International Journal of Machine Tools and Manufacture*, vol. 48, pp. 1578-1584, 2008.

[2] D. Dornfeld, *et al.*, "Recent advances in mechanical micromachining," *CIRP Annals-Manufacturing Technology*, vol. 55, pp. 745-768, 2006.

[3] T. Masuzawa, "State of the art of micromachining," *CIRP Annals - Manufacturing Technology*, vol. 49, pp. 473-488, 2000.

[4] H. Weule, *et al.*, "Micro-cutting of steel to meet new requirements in miniaturization," *CIRP Annals - Manufacturing Technology*, vol. 50, pp. 61-64, 2001.

[5] X. Liu, *et al.*, "The mechanics of machining at the microscale: Assessment of the current state of the science," *Journal of Manufacturing Science and Engineering, Transactions of the ASME*, vol. 126, pp. 666-678, 2004.

[6] S. Min, *et al.*, "A study on initial contact detection for precision micro-mold and surface generation of vertical side walls in micromachining," *CIRP Annals - Manufacturing Technology*, vol. 57, pp. 109-112, 2008.

[7] T. Masuzawa and H. K. Toenshoff, "Three-dimensional micromachining by machine tools," *CIRP Annals - Manufacturing Technology*, vol. 46, pp. 621-628, 1997.

[8] G. Bissacco, *et al.*, "Micromilling of hardened tool steel for mould making applications," *Journal of Materials Processing Technology*, vol. 167, pp. 201-207, 2005.

[9] G. Bissacco, *et al.*, "Size effects on surface generation in micro milling of hardened tool steel," *CIRP Annals - Manufacturing Technology*, vol. 55, pp. 593-596, 2006.

[10] P. Li, *et al.*, "Performance evaluation of micromilling of hardened tool steel," in *Proceedings of ICOMM*, 2007, pp. 219-224.

[11] K. Maekawa, *et al.*, *Metal machining - theory and applications*: Butterworth-Heinemann, 2002.

[12] R. Singh and S. N. Melkote, "Experimental characterization of Laser-Assisted Mechanical Micromachining (LAMM) process," in *2005 ASME International Mechanical Engineering Congress and Exposition, IMECE 2005, November 5, 2005 - November 11, 2005*, Orlando, FL, United states, 2005, pp. 957-964.

[13] R. Singh and S. N. Melkote, "Characterization of a hybrid laser-assisted mechanical micromachining (LAMM) process for a difficult-to-machine material," *International Journal of Machine Tools and Manufacture*, vol. 47, pp. 1139-1150, 2007.

[14] T. Burakowshi and T. Wierzchon, *Surface engineering of metals*: CRC Press, 1999.

[15] W. M. Steen, *Laser material processing*: Springer-Verlag, 1998.

[16] G. Chryssolouris, *Laser machining - theory and practice*: Springer-Verlag, 1991.

[17] R. E. Wagner, "Laser drilling mechanics," *Journal of Applied Physics*, vol. 45, pp. 4631-4637, 1974.

[18] F. W. Dabby and U. C. Paek, "High- intensity laser- induced vaporization and explosion of solid material," *IEEE Journal of Quantum Electronics*, vol. 8, pp. 106-111, 1972.

[19] Y. Tian, *et al.*, "Laser-assisted milling of silicon nitride ceramics and inconel 718," *Journal of Manufacturing Science and Engineering, Transactions of the ASME*, vol. 130, pp. 0310131-0310139, 2008.

[20] S. Rajagopal, *et al.*, "Machining aerospace alloys with the aid of a 15 KW laser," *Journal of Applied Metal Working*, vol. 2, pp. 170-184, 1982.

[21] W. Konig and A. K. Zaboklicki, "Laser-assisted hot machining of ceramics and composite materials," National Institute of Standards & Technology, 1993.

[22] F. Klocke and T. Bergs, "Laser-assisted turning of advanced ceramics," in *Rapid Prototyping and Flexible Manufacturing, June 16, 1997 - June 16, 1997*, Munich, Germany, 1997, pp. 120-130.

[23] Y. Jeon and F. Pfefferkorn, "Effect of laser preheating the workpiece on micro end milling of metals," *Journal of Manufacturing Science and Engineering, Transactions of the ASME*, vol. 130, pp. 0110041-0110049, 2008.

[24] J. A. Shelton and Y. C. Shin, "Experimental evaluation of laser-assisted micromilling in a slotting configuration," *Journal of Manufacturing Science and Engineering, Transactions of the ASME*, vol. 132, pp. 0210081-0210089, 2010.

[25] J. F. Ready, *LIA Handbook of laser materials processing*: Laser Institute of America, 2001.

[26] N. Rizvi, *et al.*, "Laser micromachining - new developments and applications," in *Laser Applications in Microelectronic and Optoelectronic Manufacturing V, January 24, 2000 - January 26, 2000*, San Jose, CA, USA, 2000, pp. 261-271.

[27] J. Zhang, *et al.*, "Laser-induced plasma-assisted ablation of fused quartz using the fourth harmonic of a Nd+:YAG laser," *Applied Physics A: Materials Science and Processing*, vol. 67, pp. 545-549, 1998.

[28] J. Zhang, *et al.*, "High-speed machining of glass materials by laser-induced plasma-assisted ablation using a 532-nm laser," *Applied Physics A: Materials Science and Processing*, vol. 67, pp. 499-501, 1998.

[29] D. Hellrung, *et al.*, "High-accuracy micromachining of ceramics by frequency-tripled Nd:YAG-lasers," in *Proceedings of the 1999 Laser Applications in Microelectronic and Optoelectronic Manufacturing IV (LAMOM-IV), January 25, 1999 - January 27, 1999*, San Jose, CA, USA, 1999, pp. 348-356.

[30] H. Yang and C. T. Pan, "Excimer laser-induced formation of metallic microstructures by electroless copper plating," *Journal of Micromechanics and Microengineering*, vol. 12, pp. 157-161, 2002.

[31] W. Pfleging, *et al.*, "Rapid fabrication of microcomponents - UV-laser assisted prototyping, laser micro-machining of mold inserts and replication via photomolding," *Microsystem Technologies*, vol. 9, pp. 67-74, 2003.

[32] P. Stanley, *et al.*, "Influence of Femtosecond Laser Parameters on Fabrication of Photomask by Direct Ablation," *Lasers in Engineering*, vol. 13, pp. 13-23, 2003.

[33] I. V. Hertel, *et al.*, "Surface and bulk ultra-short pulsed laser processing of transparent materials," in *1st International Symposium on Laser Precision Microfabrication, June 14, 2000 - June 16, 2000*, Omiya, Japan, 2000, pp. 17-24.

[34] G. Dumitru, *et al.*, "Laser processing of hardmetals: Physical basics and applications," *International Journal of Refractory Metals and Hard Materials*, vol. 23, pp. 278-286, 2005.

[35] X. Luo, *et al.*, "Design of ultraprecision machine tools with applications to manufacture of miniature and micro components," *Journal of Materials Processing Technology*, vol. 167, pp. 515-528, 2005.

[36] K. Okazaki, "Micromachine tool to machine micro-parts," in *15th Annual Meeting of the ASPE*, Scottsdale, AZ, 2000.

[37] C.-J. Kim, *et al.*, "A static model of chip formation in microscale milling," *Journal of Manufacturing Science and Engineering, Transactions of the ASME,* vol. 126, pp. 710-718, 2004.

[38] M. P. Vogler, *et al.*, "Microstructure-level force prediction model for micro-milling of multi-phase materials," in *2001 ASME International Mechanical Engineering Congress and Exposition, November 11, 2001 - November 16, 2001*, New York, NY, United states, 2001, pp. 3-10.

[39] M. P. Vogler, *et al.*, "On the modeling and analysis of machining performance in micro-endmilling, part I: Surface generation," *Journal of Manufacturing Science and Engineering, Transactions of the ASME,* vol. 126, pp. 685-694, 2004.

[40] M. P. Vogler, *et al.*, "On the modeling and analysis of machining performance in micro-endmilling, part II: Cutting force prediction," *Journal of Manufacturing Science and Engineering, Transactions of the ASME,* vol. 126, pp. 695-705, 2004.

[41] G. Bissacco, *et al.*, "Modelling the cutting edge radius size effect for force prediction in micro milling," *CIRP Annals - Manufacturing Technology,* vol. 57, pp. 113-116, 2008.

[42] M. B. G. Jun, *et al.*, "Investigation of the dynamics of microend milling - Part I: Model development," *Journal of Manufacturing Science and Engineering, Transactions of the ASME,* vol. 128, pp. 893-900, 2006.

[43] X. Liu, *et al.*, "Model-based analysis of the surface generation in microendmilling - Part I: Model development," *Journal of Manufacturing Science and Engineering, Transactions of the ASME,* vol. 129, pp. 453-460, 2007.

[44] X. Liu, *et al.*, "Model-based analysis of the surface generation in microendmilling - Part II: Experimental validation and analysis," *Journal of Manufacturing Science and Engineering, Transactions of the ASME,* vol. 129, pp. 461-469, 2007.

[45] M. Malekian, *et al.*, "Tool wear monitoring of micro-milling operations," *Journal of Materials Processing Technology,* vol. 209, pp. 4903-4914, 2009.

[46] M. Rahman, *et al.*, "Micro milling of pure copper," *Journal of Materials Processing Technology,* vol. 116, pp. 39-43, 2001.

[47] J. C. Miao, *et al.*, "Review of dynamic issues in micro-end-milling," *International Journal of Advanced Manufacturing Technology,* vol. 31, pp. 897-904, 2007.

[48] R. Komanduri, *et al.*, "M.D. simulation of nanometric cutting of single crystal aluminum-effect of crystal orientation and direction of cutting," *Wear,* vol. 242, pp. 60-88, 2000.

[49] R. Komanduri, *et al.*, "Effect of tool geometry in nanometric cutting: A molecular dynamics simulation approach," *Wear,* vol. 219, pp. 84-97, 1998.

[50] E. Budak, *et al.*, "Prediction of milling force coefficients from orthogonal cutting data," *Journal of Manufacturing Science and Engineering, Transactions of the ASME,* vol. 118, pp. 216-224, 1996.

[51] C. R. Friedrich, *et al.*, "Micromilling development and applications for microfabrication," *Microelectronic Engineering,* vol. 35, pp. 367-372, 1997.

[52] C. R. Friedrich and V. P. Kulkarni, "Effect of workpiece springback on micromilling forces," *Microsystem Technologies,* vol. 10, pp. 472-477, 2004.

[53] T. Schaller, *et al.*, "Microstructure grooves with a width of less than 50 m cut with ground hard metal micro end mills," *Precision Engineering,* vol. 23, pp. 229-235, 1999.

[54] S. Filiz, *et al.*, "An experimental investigation of micro-machinability of copper 101 using tungsten carbide micro-endmills," *International Journal of Machine Tools and Manufacture,* vol. 47, pp. 1088-1100, 2007.

[55] J. Fleischer and J. Kotschenreuther, "The manufacturing of micro molds by conventional and energy-assisted processes," *International Journal of Advanced Manufacturing Technology,* vol. 33, pp. 75-85, 2007.

[56] S. Filiz, *et al.*, "Micromilling of microbarbs for medical implants," *International Journal of Machine Tools and Manufacture,* vol. 48, pp. 459-472, 2008.

[57] S. Lei, *et al.*, "Experimental investigation of thermo-mechanical characteristics in laser-assisted machining of silicon nitride ceramics," *American Society of Mechanical Engineers, Manufacturing Engineering Division, MED,* vol. 10, pp. 781-788, 1999.

[58] J. C. Rozzi, *et al.*, "Transient thermal response of a rotating cylindrical silicon nitride workpiece subjected to a translating laser heat source, Part I: Comparison of surface temperature measurements with theoretical results," *Journal of Heat Transfer,* vol. 120, pp. 899-906, 1998.

[59] S. Lei, *et al.*, "Deformation mechanisms and constitutive modeling for silicon nitride undergoing laser-assisted machining," *International Journal of Machine Tools and Manufacture,* vol. 40, pp. 2213-2233, 2000.

[60] P. A. Rebro, *et al.*, "Laser-assisted machining of reaction sintered mullite ceramics," *Journal of Manufacturing Science and Engineering, Transactions of the ASME,* vol. 124, pp. 875-885, 2002.

[61] F. E. Pfefferkorn, *et al.*, "Laser-assisted machining of magnesia-partially-stabilized zirconia," *Journal of Manufacturing Science and Engineering, Transactions of the ASME,* vol. 126, pp. 42-51, 2004.

[62] G. Germain, *et al.*, "Machinability and surface integrity for a bearing steel and a titanium alloy in laser assisted machining (pptimisation on LAM on two materials)," *Lasers in Engineering,* vol. 17, pp. 329-344, 2007.

[63] S. Skvarenina and Y. C. Shin, "Laser-assisted machining of compacted graphite iron," *International Journal of Machine Tools and Manufacture,* vol. 46, pp. 7-17, 2006.

[64] M. Anderson, *et al.*, "Laser-assisted machining of inconel 718 with an economic analysis," *International Journal of Machine Tools and Manufacture,* vol. 46, pp. 1879-1891, 2006.

[65] H. Attia, *et al.*, "Laser-assisted high-speed finish turning of superalloy inconel 718 under dry conditions," *CIRP Annals - Manufacturing Technology,* vol. 59, pp. 83-88, 2010.

[66] R. Bejjani, *et al.*, "Laser assisted turning of titanium metal matrix composite," *CIRP Annals - Manufacturing Technology,* vol. 60, pp. 61-64, 2011.

[67] P. Dumitrescu, *et al.*, "High-power diode laser assisted hard turning of AISI D2 tool steel," *International Journal of Machine Tools and Manufacture,* vol. 46, pp. 2009-2016, 2006.

[68] J. C. Rozzi, *et al.*, "Transient, three-dimensional heat transfer model for the laser assisted machining of silicon nitride: II. Assessment of parametric effects," *International Journal of Heat and Mass Transfer,* vol. 43, pp. 1425-1437, 2000.

[69] J. C. Rozzi, *et al.*, "Transient, three-dimensional heat transfer model for the laser assisted machining of silicon nitride: I. Comparison of predictions with measured surface temperature histories," *International Journal of Heat and Mass Transfer,* vol. 43, pp. 1409-1424, 2000.

[70] L. N. Lopez De Lacalle, *et al.*, "Plasma assisted milling of heat-resistant superalloys," *Journal of Manufacturing Science and Engineering, Transactions of the ASME,* vol. 126, pp. 274-285, 2004.

[71] S. M. Afazov, *et al.*, "Modelling and simulation of micro-milling cutting forces," *Journal of Materials Processing Technology,* vol. 210, pp. 2154-2162, 2010.

[72] W. Y. Bao and I. N. Tansel, "Modeling micro-end-milling operations. Part III: Influence of tool wear," *International Journal of Machine Tools and Manufacture,* vol. 40, pp. 2193-2211, 2000.

[73] W. Y. Bao and I. N. Tansel, "Modeling micro-end-milling operations. Part II: Tool run-out," *International Journal of Machine Tools and Manufacture,* vol. 40, pp. 2175-2192, 2000.

[74] W. Y. Bao and I. N. Tansel, "Modeling micro-end-milling operations. Part I: Analytical cutting force model," *International Journal of Machine Tools and Manufacture,* vol. 40, pp. 2155-2173, 2000.

[75] A. N. Samant and N. B. Dahotre, "Laser machining of structural ceramics-A review," *Journal of the European Ceramic Society,* vol. 29, pp. 969-993, 2009.

[76] J. Webster and M. Tricard, "Innovations in abrasive products for precision grinding," *CIRP Annals - Manufacturing Technology,* vol. 53, pp. 597-617, 2004.

[77] S. Malkin and T. W. Hwang, "Grinding mechanisms for ceramics," *CIRP Annals - Manufacturing Technology,* vol. 45, pp. 569-580, 1996.

[78] S. Malkin and J. E. Ritter, "Grinding mechanisms and strength degradation for ceramics," *Journal of Engineering for Industry,* vol. 111, pp. 167-174, 1989.

[79] I. Marinescu, *Handbook of advanced ceramics machining*: Taylor & Francis, 2007.

[80] H.-W. Hoffmeister and R. Wittmer, "Development and test of CVD-diamond microgrinding wheels," in *ICoPE2010 and 13th ICPE International Conference on Precision Engineering, July 28, 2010 - July 30, 2010*, Singapore, 2010, pp. 131-135.

[81] J. Gabler and S. Pleger, "Precision and micro CVD diamond-coated grinding tools," *International Journal of Machine Tools and Manufacture,* vol. 50, pp. 420-424, 2010.

[82] E. Westkaemper, "Grinding assisted by Nd:YAG lasers," *CIRP Annals - Manufacturing Technology,* vol. 44, pp. 317-320, 1995.

[83] C. H. Tsai and H. W. Chen, "The laser shaping of ceramic by a fracture machining technique," *International Journal of Advanced Manufacturing Technology,* vol. 23, pp. 342-349, 2004.

[84] C.-H. Tsai and C.-S. Liou, "Fracture mechanism of laser cutting with controlled fracture," *Journal of Manufacturing Science and Engineering, Transactions of the ASME,* vol. 125, pp. 519-528, 2003.

[85] E. M. Trent and P. K. Wright, *Metal cutting*: Butterworth-Heinemann, 2000.

[86] G. Boothroyd and W. A. Knight, *Fundamentals of machining and machine tools*: Taylor & Francis, 2005.

[87] B. M. Kramer and N. P. Suh, "Tool wear by solution: A quantitative understanding," *Journal of Engineering for Industry,* vol. 102, pp. 303-309, 1980.

[88] D. T. Quinto, "Challenging applications," *Cutting Tool Magazine,* vol. 59, 2007.

[89] H. G. Prengel, *et al.*, "State of the art in hard coatings for carbide cutting tools," *Surface and Coatings Technology,* vol. 102, pp. 183-190, 1998.

[90] A. S. More, *et al.*, "Tool wear and machining performance of cBN-TiN coated carbide inserts and PCBN compact inserts in turning AISI 4340 hardened steel," *Journal of Materials Processing Technology,* vol. 180, pp. 253-262, 2006.

[91] W. Konig, *et al.*, "Physically vapor deposited coatings on tools. Performance and wear phenomena," *Surface and Coatings Technology,* vol. 49, pp. 316-324, 1991.

[92] K. D. Bouzakis, *et al.*, "The influence of the coating thickness on its strength properties and on the milling performance of PVD coated inserts," *Surface and Coatings Technology,* vol. 174-175, pp. 393-401, 2003.

[93] J. A. Olortegui-Yume and P. Y. Kwon, "Tool wear evolution in multilayer coated inserts using topographic imaging," in *Transactions of the NAMRI/SME, May 23, 2006 - May 26, 2006*, Milwaukee, WI, United states, 2006, pp. 405-412.

[94] J. A. Olortegui-Yume, *et al.*, "Understanding tool wear of multilayer coated carbides in machining 1045 steel," in *Transactions of the NAMRI/SME, May 20, 2008 - May 23, 2008*, Monterrey, Mexico, 2008, pp. 525-532.

[95] P. J. Heaney, *et al.*, "Diamond coatings for micro end mills: Enabling the dry machining of aluminum at the micro-scale," *Diamond and Related Materials,* vol. 17, pp. 223-233, 2008.

[96] C. D. Torres, *et al.*, "Analyzing the performance of diamond-coated micro end mills," *International Journal of Machine Tools and Manufacture,* vol. 49, pp. 599-612, 2009.

[97] D. L. Wissmiller and F. E. Pfefferkorn, "Micro end mill tool temperature measurement and prediction," *Journal of Manufacturing Processes,* vol. 11, pp. 45-53, 2009.

[98] K. A. Bourne, *et al.*, "An acoustic emission-based method for determining contact between a tool and workpiece at the microscale," *Journal of Manufacturing Science and Engineering, Transactions of the ASME,* vol. 130, pp. 0311011-0311018, 2008.

[99] A. A. Sodemann and J. R. Mayor, "Parametric investigation of precision in tool-workpiece conductivity touch-off method in micromilling," in *37th Annual North American Manufacturing Research Conference, NAMRC 37, May 19, 2009 - May 22, 2009*, Greenville, SC, United states, 2009, pp. 565-572.

[100] K. Jemielniak and P. J. Arrazola, "Application of AE and cutting force signals in tool condition monitoring in micro-milling," *CIRP Journal of Manufacturing Science and Technology*, vol. 1, pp. 97-102, 2008.

[101] S. Y. Liang, *et al.*, "Machining process monitoring and control: The state-of-the-art," *Journal of Manufacturing Science and Engineering, Transactions of the ASME*, vol. 126, pp. 297-310, 2004.

[102] G. Byrne, *et al.*, "Tool condition monitoring (TCM) - the status of research and industrial application," *CIRP Annals - Manufacturing Technology*, vol. 44, pp. 541-567, 1995.

[103] M. Kumar, *et al.*, "An experimental technique to detect tool-workpiece contact in micromilling," *Journal of Manufacturing Processes*, vol. 12, pp. 99-105, 2010.

[104] A. C. Wijeyewickrema, *et al.*, "Drill wandering motion: Experiment and analysis," *International Journal of Mechanical Sciences*, vol. 37, pp. 495-509, 1995.

[105] H. C. Carslaw and J. C. Jaeger, *Conduction of heat in solids*: Oxford Science Publications, 1959.

[106] Z. M. Zhang, *Nano/microscale heat transfer*: McGraw-Hill, 2007.

[107] F. Cverna, *Thermal properties of metals*: ASM International, 2002.

[108] H. Woo and H. Cho, "Three-dimensional temperature distribution in laser surface hardening processes," *Proceedings of the Institution of Mechanical Engineers, Part B: Journal of Engineering Manufacture*, vol. 213, pp. 695-712, 1999.

[109] M. Kumar and S. Melkote, "Evaluation of cutting tool coatings for laser assisted micro milling," in *ICOMM*, Madison, WI, USA, 2010, pp. 297-302.

[110] E. G. Loewen and M. C. Shaw, "On analysis of cutting-tool temperatures," *Transactions of the ASME*, vol. 76, pp. 217-225, 1954.

[111] P. K. Wright, "Predicting the shear angle in machining from workmaterial strain-hardening characteristics," *Journal of Engineering for Industry*, vol. 104, pp. 285-292, 1982.

[112] Y. B. Guo and C. R. Liu, "Mechanical properties of hardened AISI 52100 steel in hard machining processes," *Journal of Manufacturing Science and Engineering, Transactions of the ASME,* vol. 124, pp. 1-9, 2002.

[113] E. R. Marsh, *Precision spindle metrology*: DEStech Publications, Inc., 2008.

[114] Y. Altintas, *Manufacturing automation*: Cambridge University Press, 2000.

[115] J. A. Arsecularatne, *et al.*, "Prediction of chip flow direction and cutting forces in oblique machining with nose radius tools," *Proceedings of the Institution of Mechanical Engineers, Part B: Journal of Engineering Manufacture* vol. 209, pp. 305-315, 1995.

[116] G. C. I. Lin, *et al.*, "Predicting cutting forces for oblique machining conditions," *Proceedings of the Institution of Mechanical Engineers,* vol. 196, pp. 141-148, 1982.

[117] B. A. Boley and J. H. Weiner, *Theory of thermal stresses*: John Wiley & Sons, 1960.

[118] M. Ferber, "Thermal shock testing of advanced ceramics," International Energy Agency, 2000.

[119] K. D. Bouzakis, *et al.*, "Ambient and elevated temperature properties of TiN, TiAlN and TiSiN PVD films and their impact on the cutting performance of coated carbide tools," *Surface and Coatings Technology,* vol. 204, pp. 1061-1065, 2009.

[120] J. Deng, *et al.*, "Wear mechanisms of PVD ZrN coated tools in machining," *International Journal of Refractory Metals and Hard Materials,* vol. 26, pp. 164-172, 2008.